A thesis submitted in fulfillment of the requirements

for the degree of Doctor of Philosophy

Year submitted 2025

Probing the Structure of Complex Functional Polymers Using Ion Mobility Mass Spectrometry and Molecular Dynamics Simulations

Sarajit Naskar

M.Sc. (Chemistry)

School of Chemistry and Physics, Faculty of Science

Queensland University of Technology, Australia

University of Mons, Belgium

Acknowledgements

I would like to sincerely express my gratitude to the reviewers for accepting the invitation to read and evaluate this thesis. I feel truly honored to share this experience with you.

I am deeply grateful to all my supervisors and mentors for their invaluable guidance and support throughout this journey. I would like to extend special thanks to Prof. Pascal Gerbaux (UMONs) and Dr. Julien De Winter for teaching me how to perform experiments, how to approach scientific questions, how to survey the literature, and for their continuous encouragement. At the beginning of my PhD, I knew very little about this instrument, and they patiently guided me through every step.

I am also very thankful to Prof. Christopher Barner-Kowollik (QUT) for his continuous support, guidance, and encouragement through regular meetings. His academic advice and personal support have been a source of strength throughout my doctoral studies.

I wish to thank Prof. Jérôme Cornil (UMONs), Dr. Andrea Minoia, and Dr. Vincent Lemaur for their supervision, guidance, and support in computational modelling and DFT. Before starting my PhD, I had no experience in molecular modelling, but they guided me through every step of my theoretical work and helped me develop a strong foundation.

My sincere gratitude also goes to Prof. Stephen Blanksby (QUT) for his continuous support, guidance, and valuable discussions.

I would also like to thank my dear friends Dr. Aidan Izuagbe and Dr. Fred Pashley-Johnson for synthesizing compounds, their valuable discussions, and their constant support through virtual calls. I am grateful to Dr. Quentin Duez, Dr. Philippe Savarino, Dr. Benjamin Tassignon, Thomas Robert, and Louis Groignet for their help in carrying out mass spectrometry experiments. I thank Dr. Antoine Nitelet for insightful discussions, suggestions, and guidance in chemistry. I am grateful to Pauline Blanckaert and Ruth Stella Kamguem Kamga for introducing me to French, and to my dear friend David Dellemme for his company both in the office and at the IUPAC Macro 2024 conference.

Contents

Abbreviation	Explanation
SCNP	Single-chain nanoparticle
CAD	collision-activated dissociation
IMS	Ion Mobility spectrometry
DLS	Dynamic light scattering
DOSY	Diffusion-ordered spectroscopy
HRMS	Higher-resolution mass spectrometry
IMS-MS	Ion mobility spectrometry mass spectrometry
ESI-MS	Electrospray ionization mass spectrometry
IR	Infrared
MS	Mass spectrometry
NMR	Nuclear magnetic resonance
CCS	Collisional cross sections
SANS	Small angle neutron scattering
SAXS	Small angle X-ray scattering
SEC	Size exclusion chromatography
SEM	Scanning electron microscopy
TEM	Transmission electron microscopy
ESI	Electrospray ionization
MALDI	Matrix-assisted laser desorption ionization
M_n	Number average molecular weight
LC	Liquid chromatography
SAR	Structure-activity relationship
RAFT	Reversible addition−fragmentation chain transfer
MD	Molecular dynamics

UPLC	Ultra-performance liquid chromatography
QM	Quantum-mechanical
FF	Force field
CD-MS	Charge detection mass spectrometry
CIU	Collision-induced unfolding
GC-MS	Gas- chromatography mass spectrometry
IMR	Ion molecule reaction
DFT	Density functional theory
TPE	Trifunctional photoactive ene
T_g	Glass transition temperature
TAG	Thermal gravimetric analysis
TM	Trajectory method
PA	Projection Approximation
TEMPO	2,2,6,6-tetramethylpiperidine-*N*-oxyl
EXP	Experimental
M_W	Weight average molecular weight
MWD	Molecular weight distribution
R_h	Hydrodynamic radius
cIMS	Cyclic ion mobility spectrometry
HM	High molecular weight
LM	Low molecular weight
Th	Theoretical
Bu	*Sec*-Butyl

Abstract

Nature achieves extraordinary functionality through macromolecules such as proteins and enzymes, which fold into precise three-dimensional structures that enable selective and efficient catalysis. Inspired by these systems, synthetic chemists have developed single-chain polymeric nanoparticles (SCNPs), in which individual polymer chains undergo intramolecular cross-linking and collapse into compact nanostructures. SCNPs represent a versatile class of biomimetic materials with applications in catalysis, drug delivery, sensing, and imaging. Among them, metallo-folded SCNPs—formed through coordination between metal ions and ligand sites along the polymer backbone—act as catalytic nanoreactors, closely mimicking enzymatic function while offering advantages in reusability and solubility tuning. However, progress in rational SCNP design has been hindered by their intrinsic heterogeneity: differences in chain length, monomer sequence, and functional group distribution lead to diverse folding pathways and structural outcomes that are not resolved by ensemble-averaged techniques such as dynamic light scattering (DLS), size exclusion chromatography (SEC), and diffusion-ordered NMR spectroscopy (DOSY NMR).

This thesis addresses this challenge by applying ion mobility–mass spectrometry (IMS-MS) as a molecular-level tool to characterize individual ionized SCNP precursor polymers and their collapsed forms in the gas phase. In IMS, ions drift through a neutral gas under an electric field, and their collisional cross section (*CCS*)—a rotationally averaged measure of ion–gas interactions reflecting overall size and shape—is extracted from mobility data. By integrating IMS-derived *CCS* values with atomistic molecular dynamics simulations (MD) and density functional theory (DFT) calculations, this work establishes the starting point for correlating gas-phase ion structures with solution-phase folding behavior in synthetic polymers.

Collectively, these results demonstrate that IMS-MS provides the molecular resolution necessary to characterize heterogeneity, folding pathways of precursor SCNPs. When ionized in the gas phase. The thesis establishes a validated experimental–computational toolbox for probing synthetic polymer folding at the single-chain level and offers design

principles for next-generation functional nanostructures that more closely mimic Nature's precision".

Introduction

Richard Feynman famously remarked *"The imagination of Nature is far, far greater than the imagination of Man."* Indeed, scientists have long turned to Nature for inspiration. Natural macromolecules, such as enzymes, achieve extraordinary functionality through their precise and dynamic three-dimensional (3D) architectures—featuring specific shapes and meticulously positioned functional groups on their surfaces or interiors.[1] Nature has demonstrated its skill of functional design through proteins, which power a wide range of biological processes from gene expression to enzymatic catalysis.[2] These remarkable molecules perform complex tasks within intricate biological environments with unmatched efficiency and selectivity. Their catalytic ability is owed to precision morphologies, a direct result of their sequence-defined primary structures composed of amino acids. This precise sequence enables controlled folding, resulting in catalytic pockets that stabilize the transition states of substrates undergoing biochemical transformations.[3]

Inspired by the folding behavior of proteins and enzymes, macromolecular chemists today aim to design synthetic single polymer chains that undergo intramolecular cross-linking and collapse into nanoparticles mimicking Nature's precision. These single-chain nanoparticles (SCNPs) hold immense promise as biomimetic materials and provide insight into protein folding processes. Their versatility spans applications in drug delivery,[4–7] sensing,[8,9] catalysis,[10] and imaging contrast agents,[11] owing to their diversity of structures and compaction behaviors.

The collapse of SCNPs can be modulated by external stimuli such as temperature, pH, solvent and metal ion complexation. For example, metallo-folded SCNPs collapse through complexation between metal ions and ligand moieties grafted along the polymer chain.[12,13] These complexed metal ions serve as catalytic centers, enabling SCNPs to

function as innovative, reusable catalysts. Among their most advanced applications is their role as catalytic nanoreactors, effectively mimicking enzymatic activity.[13] Current approaches aim to strategically incorporate metal ions at specific sites on the polymer chain via grafted ligands, seamlessly combining metal incorporation with chain collapse. Metallo-folded SCNPs have demonstrated impressive substrate specificity and product selectivity in reactions such as terminal alkyne coupling[14] and aldehyde-alcohol coupling.[15] Furthermore, their solubility can be fine-tuned by adjusting the polymer backbone, enhancing recovery and reuse, clear advantages over traditional metal complexes.[16,17]

However, conventional SCNPs synthesized from synthetic polymers are inherently polydisperse, with variations in sequence, chain length, and functional group positioning. Each individual chain may exhibit different catalytic behaviors, depending on the number of catalytic centers and the specific architecture of its catalytic pocket. Thus, a deep understanding of the structure-activity relationship of individual SCNPs is critical for identifying the most promising chain architectures.

Traditional SCNP characterization techniques, such as dynamic light scattering (DLS), size exclusion chromatography (SEC) and diffusion-ordered NMR spectroscopy (DOSY NMR), offer useful insights into the average hydrodynamic radius reduction. However, these methods cannot resolve the behavior of individual polymer strands within the diverse SCNP ensemble that inevitably arises from polydisperse precursors.

Addressing this limitation, the present PhD thesis focuses on developing a novel methodology to gain deep insight into the size and shape of SCNP parent or pre-polymers. Given that collapse processes involve significant structural changes from the precursor to the SCNP, we leverage the capabilities of ion mobility spectrometry (IMS) coupled with mass spectrometry (IMS-MS) to carefully determine the structure of SCNP precursor polymers with increasing complexity in the gas phase.[18–23] Mass spectrometry was chosen as the primary characterization tool in the current thesis for its unique ability to probe the size and shape of the complex polymer. Our approach centers on IMS-MS which selectively analyzes ionized species such as the metallo-folded complex polymer targeted in this project.

Critically, ion mobility spectrometry (IMS) measures the mobility of ions as they drift through a neutral gas under the influence of an electric field. From these mobility measurements, the collisional cross section (CCS) is derived. The CCS represents the rotationally averaged interaction area between an ion and the buffer gas molecules, and depends on the ion's overall size, shape, and charge distribution. Ions with different conformations spend different amounts of time inside the mobility cell: for example, a compact, tightly folded ion undergoes fewer collisions and therefore exhibits higher mobility (smaller CCS), while an extended or open conformation experiences more frequent collisions, leading to lower mobility (larger CCS). Thus, CCS provides a physically meaningful descriptor of molecular conformation in the gas phase and enables IMS to distinguish between different folded states of polymers and SCNPs. Comparing these experimental CCS values with theoretical estimates (CCS_{th}) obtained via atomistic simulations enables the elucidation of the structures of these ions at the molecular level. Furthermore, we investigate the energetic landscape underpinning SCNP formation using density functional theory (DFT), shedding light on the interactions driving nanoparticle folding.

Literature Review

Single chain polymeric nanoparticles

Single chain nanoparticles (SCNPs) are the simplest synthetic system by which chemists can mimic natural enzymes. SCNPs are single polymer chains that undergo intramolecular collapse to form nanoparticles upon the application of an external stimulus. These SCNPs are generally formed by intramolecular interactions. In general, SCNPs are prepared using high dilution[24] techniques to avoid intermolecular interactions.

Single-chain polymeric nanoparticles (SCNPs) stand at the forefront of synthetic nanomaterials designed to emulate the structural and functional sophistication of natural enzymes. These innovative entities are constructed from individual pre- or parent polymer chains – which are the focus of the current PhD thesis – that fold into compact, nanoscale architectures through intramolecular collapse, triggered by external stimuli such as light, temperature shifts, pH variation, or the introduction of specific chemical reagents. This

self-folding behavior enables SCNPs to achieve molecular-level precision in form and function, qualities that are highly sought after in catalysis, drug delivery, and molecular recognition.

The folding process is predominantly governed by strategically placed reactive or interactive functional groups along the polymer backbone, which drive the chain to collapse upon activation. To prevent the formation of undesired intermolecular crosslinks – an outcome that would compromise their monodisperse and unimolecular nature – SCNPs are typically synthesized under high-dilution conditions. This controlled environment ensures that the folding remains strictly intrachain, thereby preserving the discrete, single-molecule character that defines these materials.

Single-chain polymeric nanoparticles (SCNPs) can be systematically classified based on the underlying mechanism by which the polymer chain undergoes folding. Broadly, these mechanisms fall into two principal categories: *(i)* selective point folding and *(ii)* repeat unit folding.[25]

Selective point folding is a highly controlled approach wherein crosslinking sites are strategically positioned at specific locations along the polymer backbone. This precision enables the formation of SCNPs with well-defined and reproducible architectures, allowing for consistency in structural features across different synthetic batches. Such uniformity is particularly valuable when the nanoparticles are intended for applications that require tight control over size, shape, or functionality.

In contrast, *repeat unit folding* relies on a statistical distribution of cross linkable units along the polymer chain. Folding in this case emerges from the spontaneous interactions of these randomly placed functional groups, resulting in structurally diverse and morphologically irregular SCNPs. While less predictable, this approach can yield dynamic and adaptable materials with a wide range of properties.

Beyond these two foundational strategies, SCNPs are further distinguished by the chemical nature of the folding process, typically categorized into *(i)* homo-functional coupling (involving identical reactive groups), *(ii)* hetero-functional coupling (requiring complementary reactive pairs on the same chain), and *(iii)* crosslinker-mediated collapse (employing an external bifunctional agent). Each of these modes reflects a unique folding mechanism and chemistry, imparting distinct structural and functional characteristics to the resulting nanoparticles (refer to Figure 1).[26–28]

The following section briefly describes three different collapse methods:

i) Intrachain Homo-coupling: In the homo-coupling chain-collapse pathway, complementary reactive groups are introduced into the copolymer chain. Under dilute conditions, these groups undergo an intramolecular reaction (refer to Figure 1a).

ii) Intrachain hetero-coupling: Similar to the homo-coupling chain-collapse approach, this technique requires the simultaneous incorporation of two complementary functional groups within the same polymer chain, rather than a single functionality (refer to Figure 1b). As in the previous case, the reaction must be carried out under dilute conditions.

iii) Crosslinker-Induced Collapse: A bifunctional crosslinking agent is used in the crosslinker-induced chain-collapse technique to cause a functionalized polymer chain to fold intramolecularly into a unimolecular nanoparticle. The polymer is pre-functionalized with reactive groups, which are designed to selectively interact with two complementary end groups present on the crosslinker molecule (refer to Figure 1c). To suppress unwanted intermolecular crosslinking, the components are typically combined in a controlled manner often by the gradual addition of one reagent into the other under dilute conditions. This method offers two significant advantages: It simplifies the synthesis of the precursor polymers by avoiding complex orthogonal chemistries, and it enables the incorporation of extra functional motifs through the design of the crosslinker itself enhancing the chemical versatility and potential applications of the resulting SCNPs.
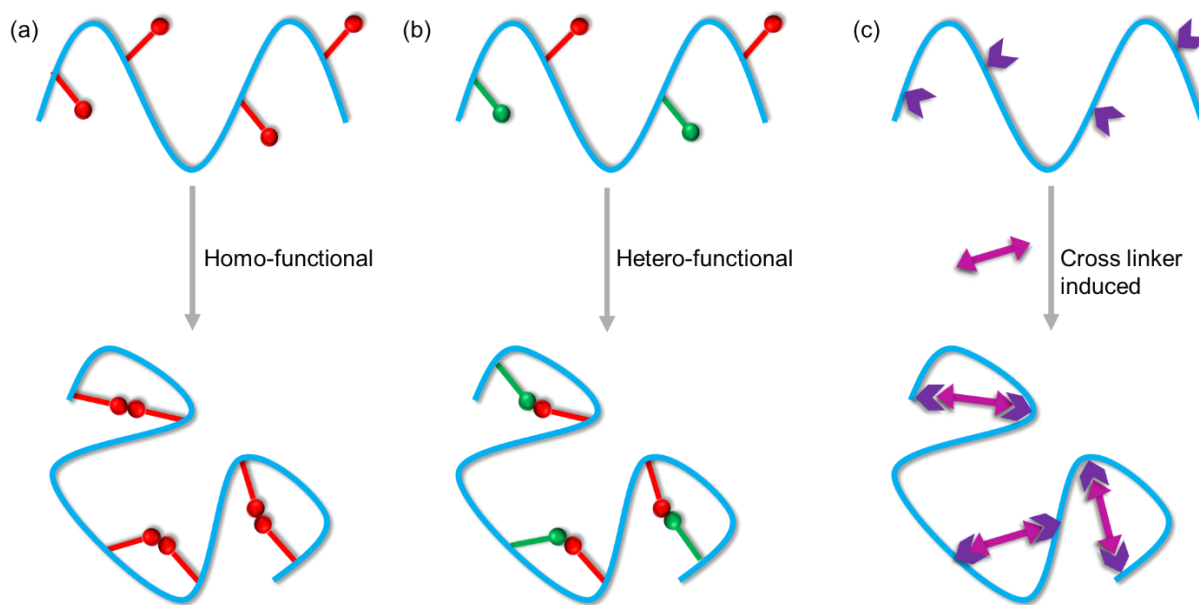
Figure 1. In SCNPs, there are three different forms of crosslinking: (a) Homo-functional, (b) Hetero-functional and (c) Crosslinker-induced collapse.

Nature employs a diverse array of orthogonal interactions to stabilize the folded structures of biomacromolecules, including covalent cross-links (such as disulfide bonds), non-covalent interactions (such as metal coordination, hydrogen bonding), and dynamic covalent interaction (such as acetal formation). Inspired by these natural design principles, the generation of single-chain polymeric nanoparticles (SCNPs) often mirrors these strategies, incorporating similar covalent and non-covalent motifs to drive and stabilize intramolecular folding.[1]

Therefore, reversible covalent (dynamic),[29,30] irreversible covalent[31–38] and non-covalent[39–46] cross linking are the most common methods to produce the folding of the polymer chain (refer to Figure 2a). The methods used to collapse the polymer chain play a critical role in the resulting structure and properties of the generated SCNPs. Both the size of the polymer and the properties of the SCNPs may be tuned by varying the nature of the intramolecular cross-linker. The methods used for the cross-linking are often based on the Friedel-Craft reaction,[31] free radical coupling,[36,37] photo-induced cycloaddition,[38] azide-alkyne[11,47–49] click reactions or thiol-ene[50,51], thiol-yne[52] click reactions,

photoinduced nitrile imine mediated tetrazole-ene[53] cyclo addition (NITEC), photodimerization of coumarin[54] and photodimerization of anthracene (refer to Table 1).[55]
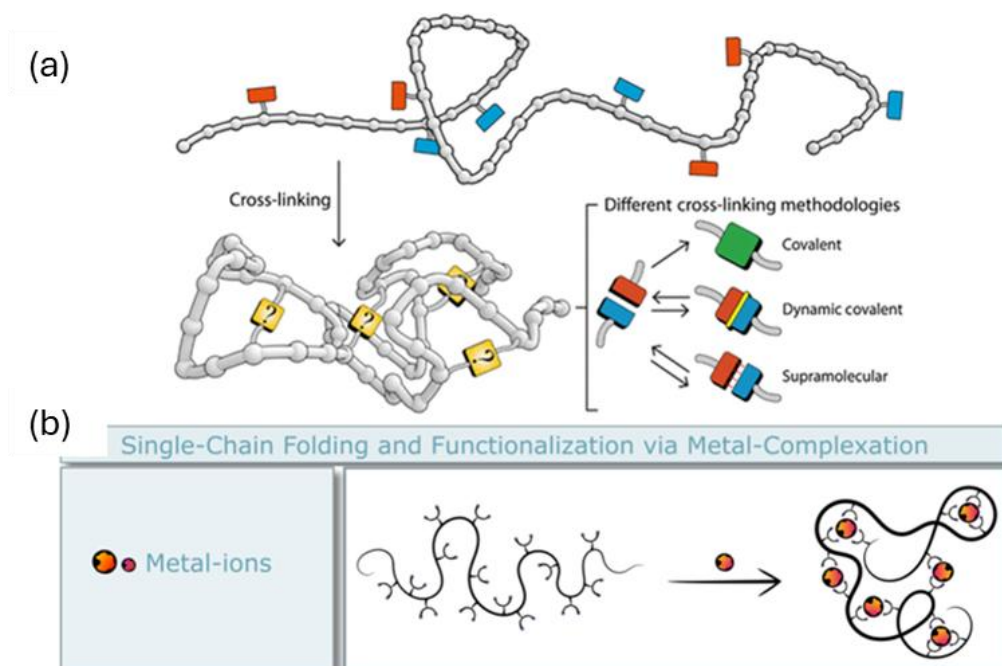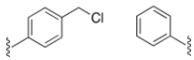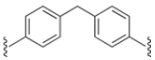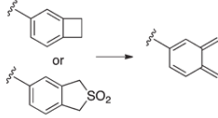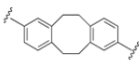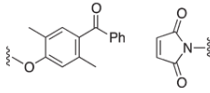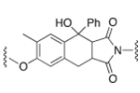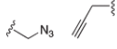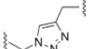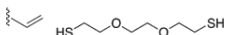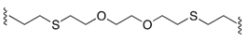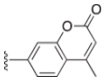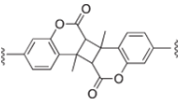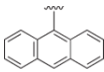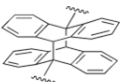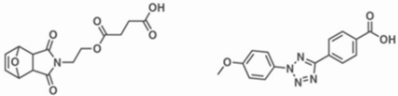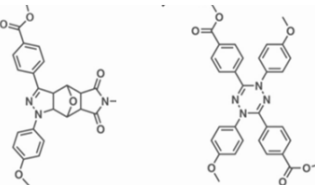
Figure 2. (a) Collapse of a single chain polymer into a nanoparticle via different cross-linking methodologies.[56] (b) SCNP formation by introducing metal ions in a polymer chain containing ligand moieties. Metal cations are responsible for both the folding and catalytic activity.[13] Reproduced with permission from references [13, 56].

Table 1. The chemistry of crosslinking reactions toward SCNPs

Before cross-linking	Structure of cross-link	Type of chemistry
		Friedel–Crafts alkylation
		Thermal [4 + 4] cycloaddition
		Photoinduced [4 + 2] cycloaddition
		Azide–alkyne "click" chemistry
		Thiol–ene "click" chemistry
		Photodimerization of coumarin
		Photodimerization of anthracene
		Tetrazole-ene cyclo addition

Numerous proteins present in the human body display enzymatic activity that is due to the presence of different type of metal ions, such as Zn in zinc-anhydrase,[57] Fe in hemoglobin,[58] and Cu in hemocyanin.[59] Therefore, to mimic the catalytic activity of biomolecules or to gain a better understanding of them, it is necessary to generate SCNPs with metal centers. Recently, Barner-Kowollik and coworkers introduced metallo-folded polymer chains (refer to Figure 2b) in which the metal centers are responsible for both the collapse of the chain and the resulting catalytic activity.[13]

In the following section, we delve into the fascinating realm of metallo-folded SCNPs, with a particular focus on systems incorporating Pd, Fe, and Cu. These metal centers not only drive the intramolecular folding through coordination chemistry, but also impart unique structural and functional properties to the resulting nanoparticles.

Metallo-folded SCNPs using Pd

Barner-Kowollik and coworkers reported one of the first and most significant examples of single-chain collapse caused by metal complexation.[60] Homotelechelic bis-triphenylphosphine (PPh₃) macromolecular groups that bind with a Pd(II) precursor were used in their investigation to accomplish polymer collapse, which results in the formation of large cyclic complexes (refer to Figure 3). Here, the phosphorus atoms at both ends of the polymer chain serve as ligand sites that bind to Pd centers, effectively folding the polymer into a well-defined single-chain polymeric nanoparticle (SCNP).
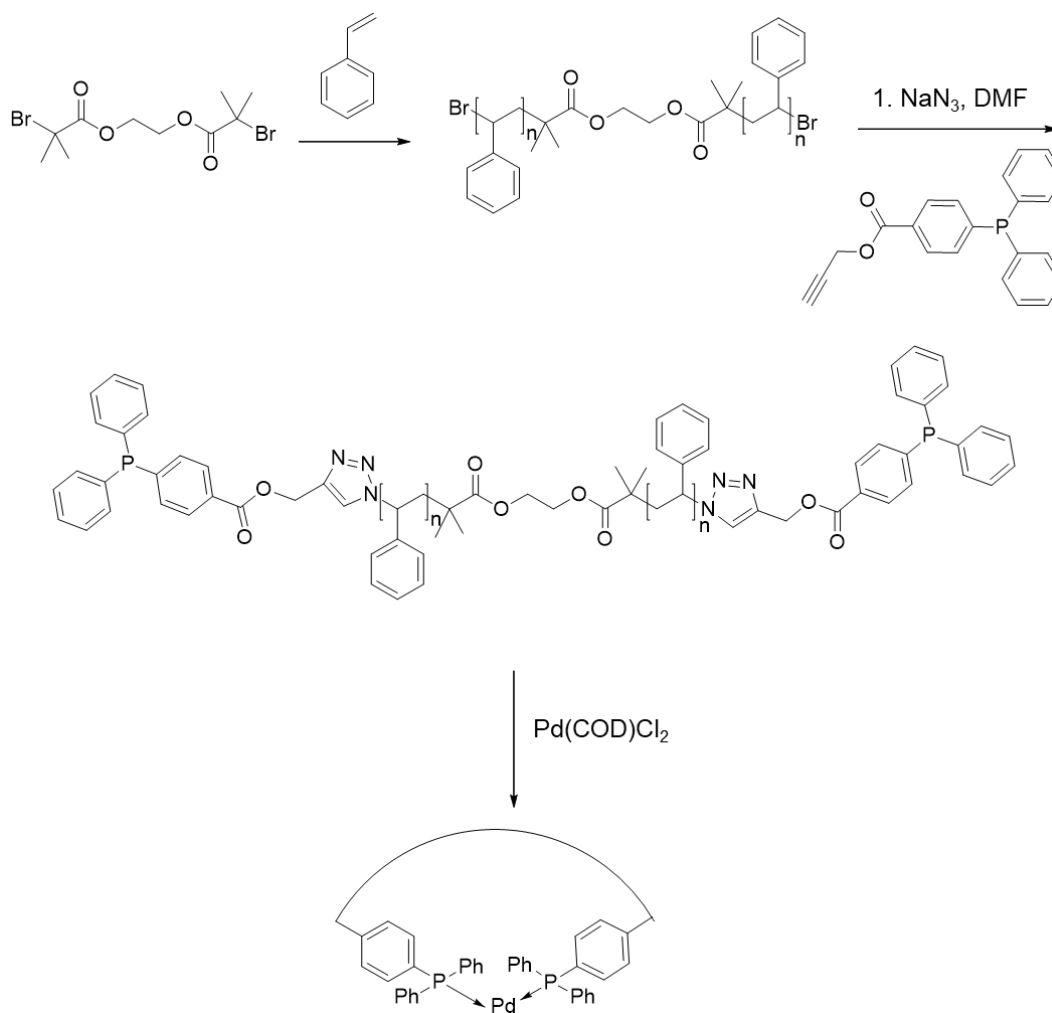
Figure 3. Pd complexation results in the formation of large cyclic complexes.[60] Reproduced with permission from reference [60].

The folding process was monitored using both ^{1}H and ^{31}P NMR spectroscopy, which revealed characteristic downfield shifts indicative of successful macrocyclization.

16

Complexation is evidenced by a significant downfield shift in the proton resonances of the aromatic protons of the triphenylphosphine moieties.[60,61] In addition, Pd-induced SCNP formation was investigated using dynamic light scattering (DLS), indicating a 26% reduction in hydrodynamic radius compared to the precursor polymer, evidencing the effective single-chain collapse. Complementary size exclusion chromatography (SEC) measurements featured the expected shift toward higher retention times, further confirming a decrease in hydrodynamic diameter. Together, these techniques provide compelling evidence of efficient Pd complexation and nanoparticle formation by the macroligands.

The team expanded the methods to prepare well-defined metal (Pd) induced single-chain nanoparticles (Pd(II)-SCNPs) using the repeat unit approach.[62] Using nitroxide-mediated random copolymerization, the precursor polymers were synthesized. Suitable functional groups were then introduced using post-polymerization modification. Here, triphenylphosphine (PPh_3) units embedded along the polymer backbone served as ligand sites that coordinate with Pd(II) ions (refer to Figure 4), driving the formation of compact and uniform SCNPs through efficient metal-ligand complexation.
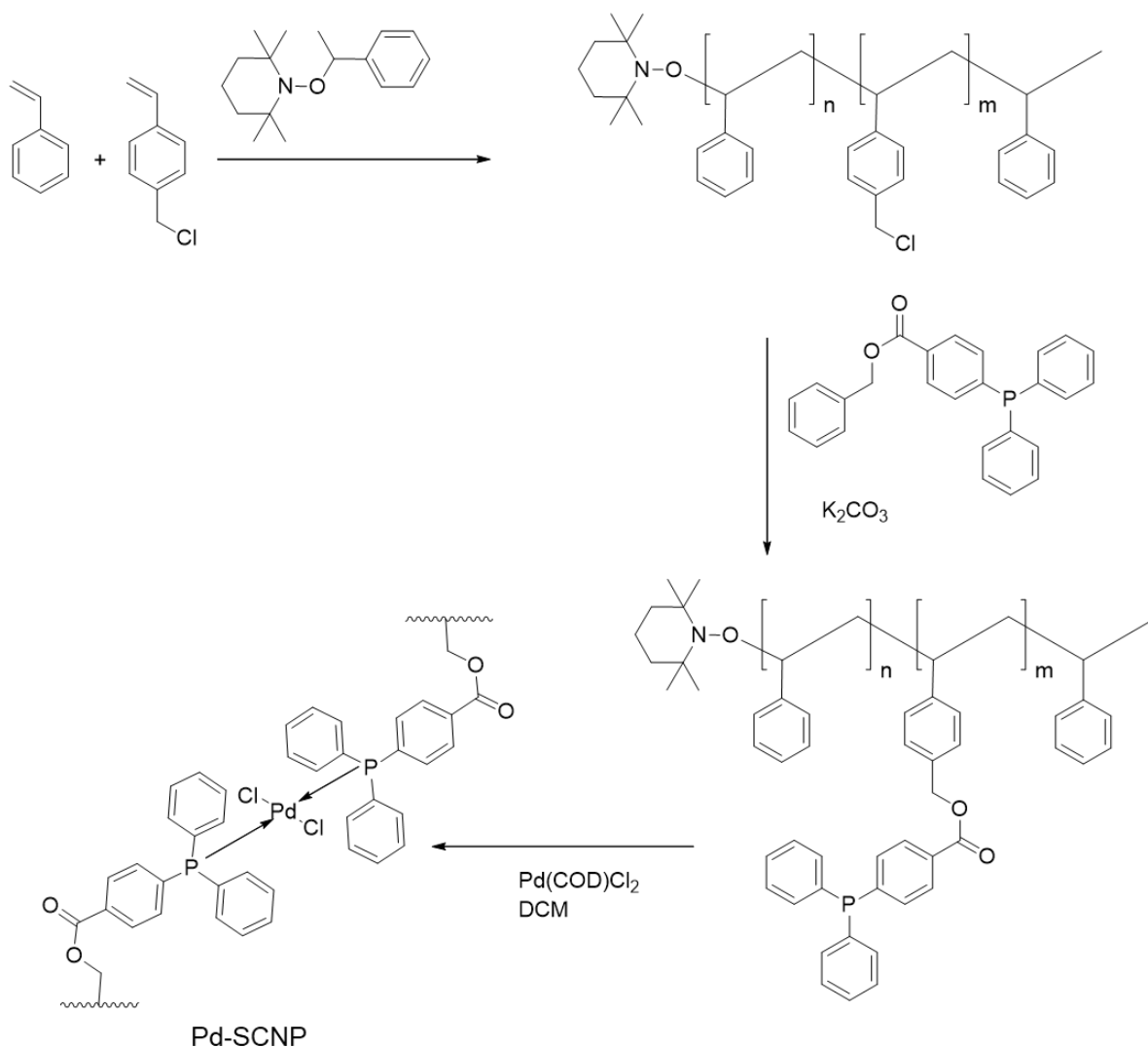
Figure 4. Pd complexation results in the formation of Pd-SCNPs.[62] Reproduced with permission from reference [62].

In contrast to the earlier approach – where cross-linking sites were positioned at the chain ends – this strategy distributes the phosphine groups uniformly along the entire polymer backbone, enabling the formation of a more compact and densely cross-linked structures. Metal induced intramolecular collapse was accomplished by the gradual, dropwise addition of the precursor polymer solution into a [Pd(COD)Cl$_2$] solution in dichloromethane, ensuring controlled complexation. To maximize cross-linking (assuming full coordination), a 1:2 ratio of Pd(II) ions to phosphine ligands was employed.

The folding process was carefully tracked using SEC, which showed a clear increase in retention time for the SCNPs with respect to the precursor polymer, indicating successful

compaction. Complementary DLS analysis confirmed a significant reduction in hydrodynamic diameter, *i.e.* from 8.8 nm (precursor polymer) to 5.4 nm (SCNP), providing further evidence of efficient intramolecular collapse. The formation of Pd complexes was additionally validated using ^{1}H and ^{31}P NMR spectroscopies, which revealed the expected chemical shift changes characteristic of successful metal coordination.

Metallo-folded SCNPs using Fe

Pu and coworkers introduced the formation of the SCNPs by Fe. Here, SCNPs are formed due to the coordination of the precursor polymer and the metal ions (refer to Figure 5).[63] Reversible addition−fragmentation chain-transfer (RAFT) polymerization was used for the synthesis of the precursor polymer.
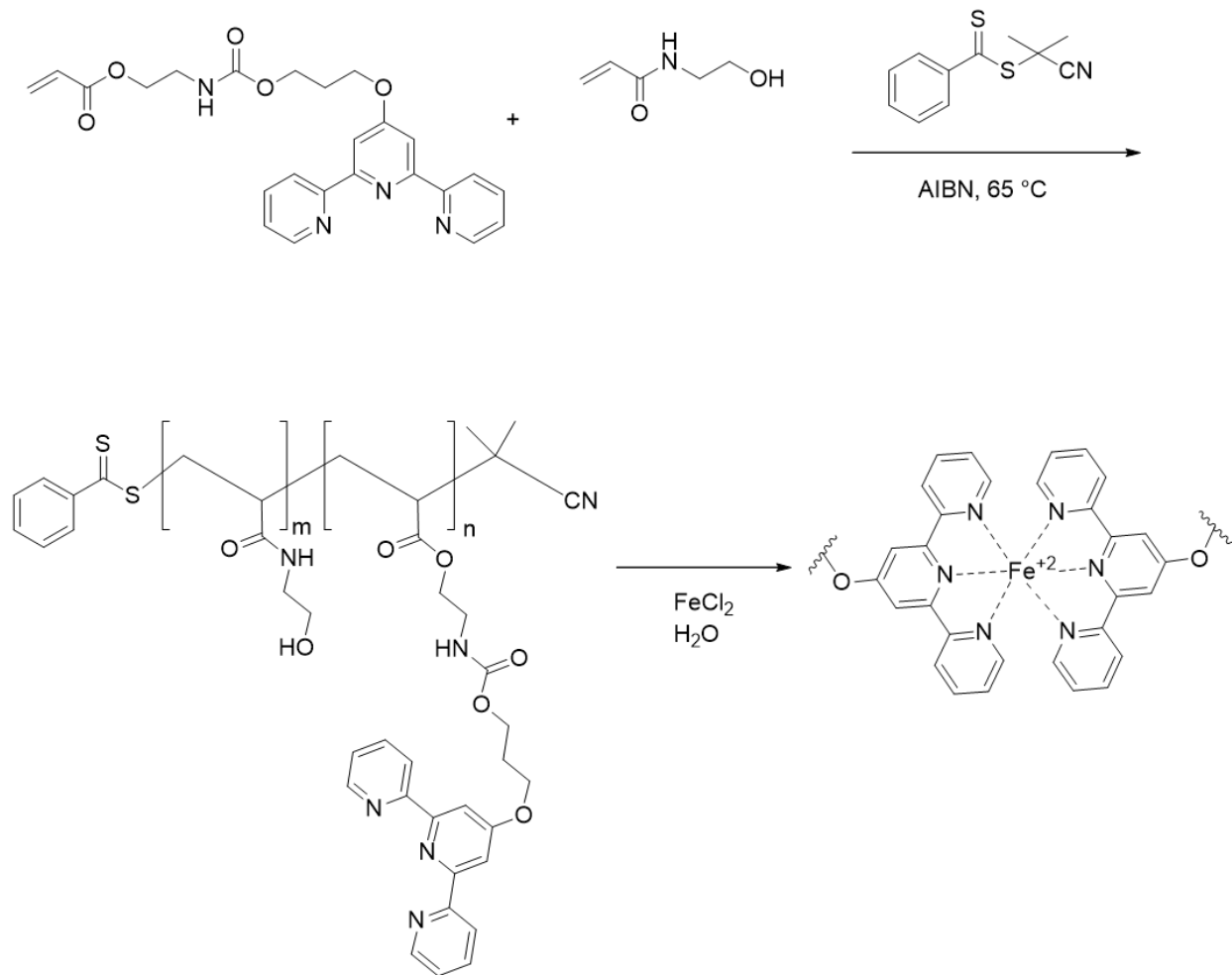
Figure 5. Fe complexation with terpyridine results in the formation of Fe-SCNPs.[63] Reproduced with permission from reference [63].

19

The aqueous solution of the polymer was added dropwise to a $FeCl_2$ solution under inert conditions, promoting SCNP formation via intramolecular collapse. Both viscosity measurements and dynamic light scattering (DLS) supported the successful formation of SCNPs. Specifically, the viscosity of the precursor (linear) polymer was significantly higher than that of the resulting SCNPs, which is attributed to the intermolecular interactions present in the linear precursor vanishing upon intramolecular folding. DLS analysis revealed a substantial decrease in hydrodynamic diameter, from 9.3 nm for the precursor polymer to 4.7 nm following Fe-induced SCNP formation. Furthermore, the hydrodynamic diameter of the precursor polymer was observed to be larger in DMF compared to water, clearly demonstrating that solvent environment also plays a critical role in determining the macromolecular architectures.

UV-Vis and ^1H NMR spectroscopic investigations revealed the formation of an octahedral metal complex as a result of Fe^{2+} coordinating with terpyridine. The glass transition temperature (T_g) of the Fe-SCNP increased, indicating reduced mobility of the chain due to intramolecular cross-linking. The formation and deformation of the SCNPs can be controlled by the addition of aqueous NaOH solution.[64]

Berda and colleagues[65] reported a SCNP mimicking a metalloenzyme. The active site of Fe_2-H_2ase inspired the development of a particular site-binding strategy based on the covalent binding of a single transition metal complex to a photo-crosslinkable polymer chain (refer to Figure 6). The precursor polymer was synthesized from 9-anthracenyl methacrylate (AMMA) with styrene and methyl methacrylate (MMA) monomer units using RAFT polymerization. The polymer exhibited a low dispersity (Đ = 1.08), indicating a narrow molecular weight distribution. Single-chain polymeric nanoparticles (SCNPs) were generated through intramolecular photodimerization of pendant anthracene moieties. The dimerization was carried out by irradiating a highly diluted solution of the polymer in tetrahydrofuran (THF) at 350 nm. Size exclusion chromatography (SEC) revealed a shift toward higher retention times after irradiation, suggesting a collapse of the polymer chains into more compact structures. Furthermore, a notable decrease in intrinsic viscosity was observed for the SCNPs compared to the precursor polymers, consistent with the formation of compact, intramolecularly cross-linked nanoparticles.
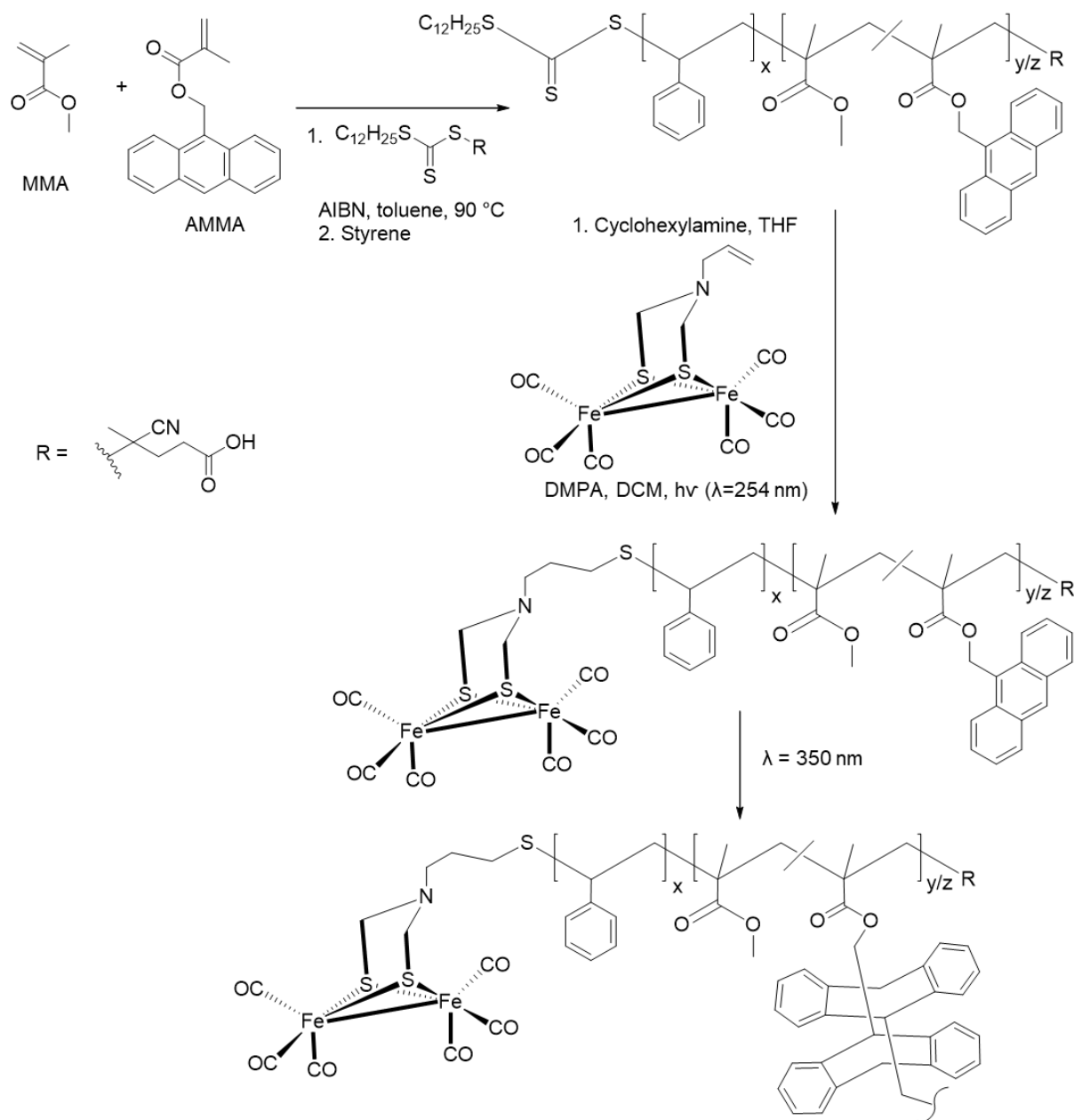
Figure 6. Creation of polymer-bound Fe_2-H_2ase model complex.[65] Reproduced with permission from reference [65].

Metallo-folded SCNPs using Cu

Water-soluble single-chain polymeric nanoparticles (SCNPs) exhibit key similarities to enzymes, particularly in terms of their structural compactness and functional versatility.[66] Owing to these similarities, researchers have sought to use SCNPs as model systems to better understand enzyme stabilization and construction mechanisms. In particular, two

key factors have been the focus of investigations: *(i)* electrostatic repulsion between side chains or end groups, and *(ii)* interplay between coordination-association interactions and coordination bond formation.

To probe these factors, Cai and co-workers designed an enzyme-inspired block copolymer synthesized via reversible addition–fragmentation chain transfer (RAFT) polymerization. The copolymer was constructed from two monomers, namely 2-hydroxypropyl methacrylamide and 2,4-imidazolylethyl acrylamide (refer to Figure 7). The resulting polymer was water-soluble under acidic conditions. Notably, the imidazole-containing monomer units exhibit pH-responsive behavior, undergoing reversible ionization depending on the solution pH. These imidazole units are capable of forming coordination bonds with transition metals such as Cu, leading to the formation of SCNPs.

Importantly, the formation of these Cu-induced SCNPs can be dynamically modulated by altering the pH of the solution. This pH-dependent coordination provides a tunable platform to mimic aspects of enzyme behavior, offering insights into the underlying principles of intramolecular folding and metal-mediated stabilization.
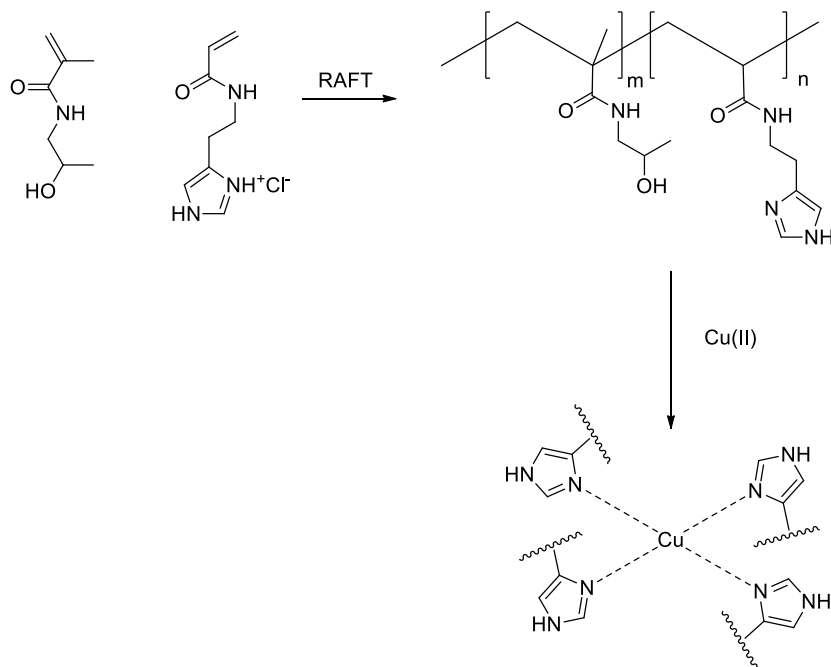
Figure 7. Cu complexation with imidazole results in the formation of Cu-SCNPs.[66] Reproduced with permission from reference [66].

The SCNPs formation was investigated using UV-Vis and ^{1}H NMR spectroscopies. A strong absorbance was observed in the UV-Vis spectroscopy at λ_{max} = 600 nm, and the intensity of the band was shown to increase with increasing pH. The pH-responsive character was investigated through an aqueous electrophoresis measurement, revealing that basic pH reduces interparticle electrostatic repulsion as the zeta potential (ζ) decreased. Using DLS, the folding was investigated at different pH. The copolymer was soluble in acidic conditions in the absence of metal ions (Cu(II)), and it showed phase separation already at pH $\geq$ 7.3. Although complete dehydration was observed at pH = 4.0, phase separation was not observed at pH $\leq$ 6.9, when Cu(II) ions were dissolved in solution. Thus, single-chain folding is likely caused by Cu(II)-coordination above pH 4.0. The DLS analysis at pH 4.0 revealed a 5.5 nm intensity-average hydrodynamic diameter and a unimodal distribution.

A further example was presented by Pomposo and colleagues (2014),[14] exploring how metal enzymes could be used as a guide for mimicking the catalytic activity using metallo-folded SCNPs. 2-(acetoxy)ethyl methacrylate (AEMA) and methyl methacrylate (MMA) repeat units were present in the random copolymer used in this investigation (M_n = 375 kDa, Đ = 1.4), along with a readily accessible β-ketoester group for complexing Cu(II) ions (refer to Figure 8a).

Single-chain collapse was accomplished using 1 mg mL^{-1} concentration of the precursor polymer in THF solvent at 300 K. As the concentration of Cu(OAc)$_2$ increases, the SEC or multi-angle light scattering (MALS) analysis monitored the slow decline in the particle radius of gyration. Initially, the hydrodynamic diameter of the precursor polymer was 26 nm. The radius gradually decreased due to SCNP formation upon the addition of Cu, ultimately reaching 15 nm at the maximum level of Cu absorption.

The amount of Cu in the SCNP was determined by thermal gravimetric analysis (TGA), and it was close to 26 mol% in relation to AEMA units. Moreover, X-ray Photoelectron Spectroscopy (XPS) was used to check whether Cu ion remains in the +2 oxidation state. IR spectroscopy was used to investigate the coordination of metal ions (Cu(II)), which revealed the C=C and C=O stretching bands for the enol tautomer bound to Cu(II) at 1515 and 1600 cm^{-1}, respectively.
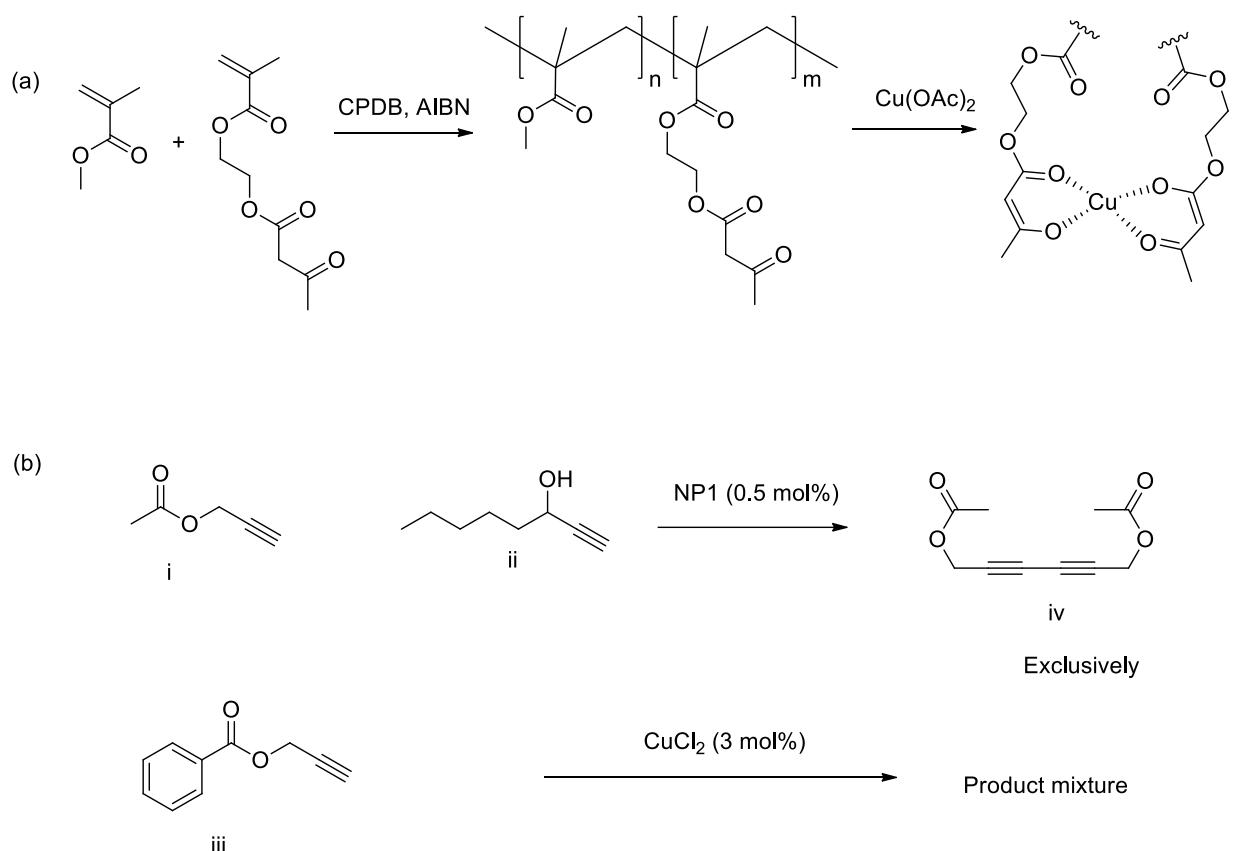
Figure 8. (a) Cu complexation with β-ketoester group results in the formation of Cu-SCNPs. (b) Cu-SCNP catalytic action in the oxidative coupling of terminal acetylenes.[14] Reproduced with permission from reference [14].

In order to assess the SCNPs' catalytic activity, terminal acetylenes were oxidatively coupled to generate 1,3-diyne, a structural motif that is needed as building block for the production of pharmacological intermediates, supramolecular materials, and acetylenic oligomers and polymers. In comparison to the conventional $CuCl_2$ catalyst used at 3 mol% in the presence of Et_3N (3 mol%), the SCNP were generated with a very low concentration of Cu(II) (0.5 mol%).

$CuCl_2$ did not show any selectivity since almost every substrate that was investigated in their study yielded the proper 1,3-diyne product. Compared to the $CuCl_2$ salt, the aforementioned Cu-SCNPs exhibit higher specificity and are nearly six times more effective. The SCNP exceptional specificity was further demonstrated in experiments including binary and ternary mixes of substrates i, ii, and iii (refer to Figure 8b). These trials produced the 1,3-diyne (iv) exclusively (refer to Figure 8b), with no signs of cross-coupling products (refer to Figure 8b). A mixture of three different reactants (i, ii, and iii)

was used to investigate catalytic activity. In the presence of the $CuCl_2$ catalyst, a mixture of products was obtained. However, the Cu-SCNP demonstrated remarkable selectivity by exclusively producing product iv (refer to Figure 8b).

The authors postulated that the SCNP's methyl methacrylate (MMA)-rich environment may aid in lowering the energy of the transition state of the reaction involving the acetate. The enhanced activity may be attributed to the presence of an active site or catalytic pocket, a hallmark of enzymatic systems, combined with the high local concentration of Cu(II) ions.

After di Lena and Bruns's group conducted studies on the use of metalloenzymes,[67,68] Pomposo and colleagues used Cu(II) salts to produce globular-shaped water-soluble SCNPs, which they used as catalysts for polymerization processes.[69] The parent polymers were prepared using RAFT polymerization. Various concentrations of 4-cyanopentanoic acid dithiobenzoate (CPADB) (the chain transfer reagent), were employed in the polymerization of hydrophilic oligo(ethylene glycol) methyl ether methacrylate (OEGMA) and hydrophobic 2-(acetoxy)ethyl methacrylate (AEMA) in 1,4-dioxane (percentage of AEMA inclusion is 12-33 mol%) (refer to Figure 9). The synthesized polymers were labeled as P1, P2, and P3 based on the number of incorporated monomer units. For example, P1 corresponds to n = 137, m = 95; P2 to n = 114, m = 45; and P3 to n = 301, m = 57.

Despite the somewhat hydrophobic AEMA content, P1 to P3 polymers were thoroughly characterized using SEC and ^{1}H NMR spectroscopy, which showed high molecular weights (M_w = 47.1 to 113.6 kDa), low dispersity ($Đ$ = 1.07 to 1.12), and also very good water solubility. At 25 °C, folding of the single polymeric chain was achieved by mixing 1 mg mL^{-1} of aqueous solution of Cu(OAc)$_2$ (with 0.5 equivalent with respect to per AEMA unit).

Size exclusion chromatography (SEC) showed that the polymer chains effectively collapse with longer retention times upon the addition of Cu to the solution. DLS further confirmed that intrachain coordination of the metal ion (Cu(II)) with an increase in Cu ion concentration results in a reduction of the average R_h (hydrodynamic radius). Based on the outcomes of small-angle neutron scattering (SANS) testing in D_2O, it was proposed

that the SCNP may have a spherical shape. The hydrophilic oligoglycols in the shell make the particles soluble in water, while the hydrophobic AEMA unit constitutes the center of the nanoparticle. According to IR and UV-Vis spectroscopies, Cu(II) ions formed the corresponding complex, in line with a widening of the resonances in the ^1H NMR spectra due to the Cu(II) paramagnetic nature.

P1: n = 137, m = 95
P2: n = 114, m = 45
P3: n = 301, m = 57
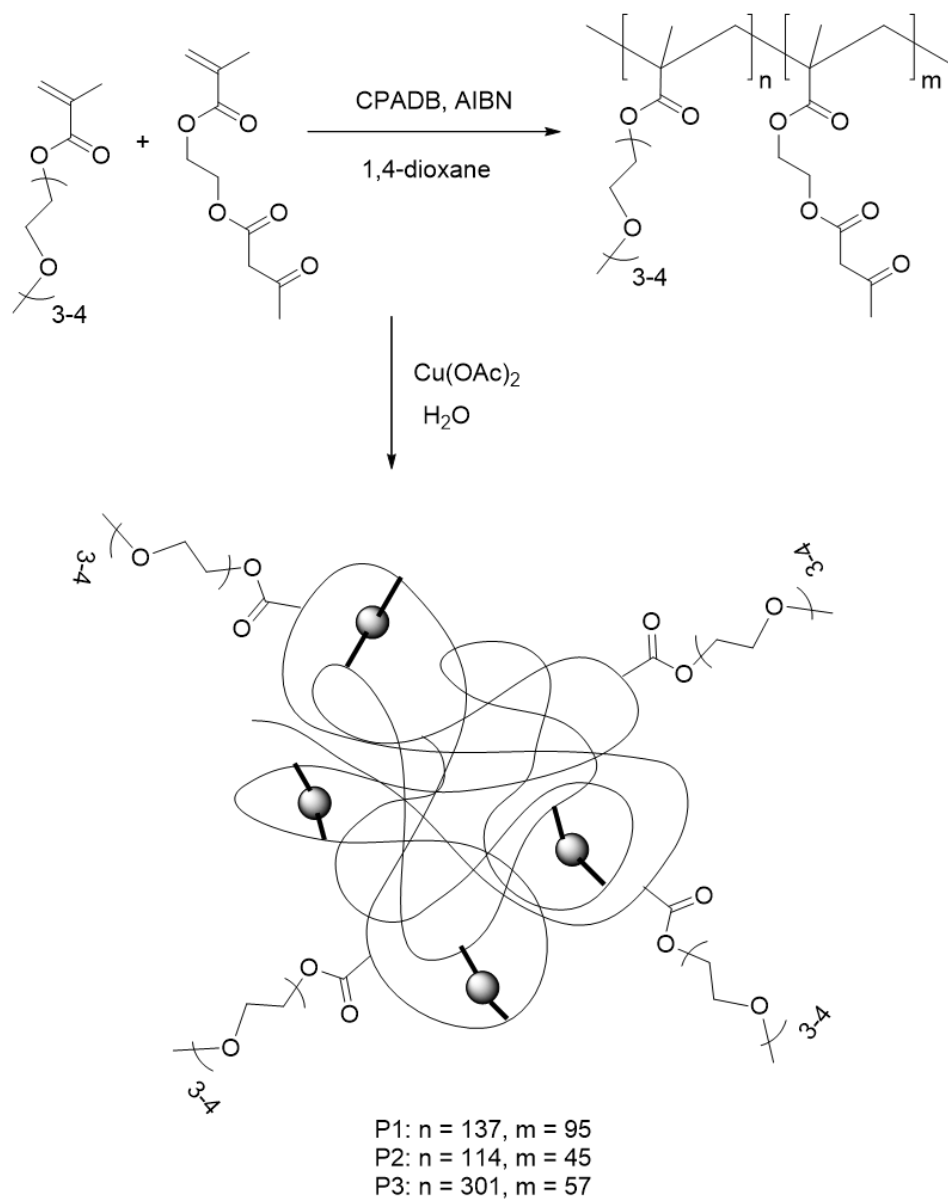
Figure 9. Cu complexation with acetate results in the creation of H_2O soluble Cu-SCNPs.[69] Reproduced with permission from reference [69].

These Cu-containing SCNPs were successfully employed to synthesize linear polyOEGMA (refer to Figure 9). In this system, polyOEGMA was prepared using the following components: Cu(II)-SCNPs served as the catalyst, L-ascorbic acid was used as the reducing agent, 2-cyano-2-propyl dithiobenzoate acted as the RAFT chain transfer agent, and 2-bromopropionitrile functioned as the atom transfer radical polymerization (ATRP) initiator. The resulting polymer exhibited a low polydispersity ($Đ$ = 1.1–1.2).

The authors proposed that the isolated metal ions (Cu) in the Cu(AEMA)$_2$ units were the cause of the elevated SCNP catalytic activity. Moreover, the catalysis was not considerably affected by SCNP concentrations in the range of 0.8-4 mg mL^{-1}.

Metallo-folded SCNPs using Ru

The ambition to imitate Nature most successful catalysts is one of the primary motivators in the SCNP field. High selectivity in catalytic processes can be achieved by using a collapsed single-chain of amphiphilic polymers, according to research by Palmans and colleagues.[70] They selected two polymers, *i.e.* P4, which is based on lauryl methacrylate, and P5, which is based on methacrylate of 1,3,5-benzene-tricarboxamide (BTAMA). The primary distinction between P4 and P5 is that the hydrophobic effect causes P4 to simply collapse, whereas P5 benzene tricarboxylic acid units form a highly ordered (chiral) structure due to the strong isolated hydrogen bonds among the units. Both polymers were made using RAFT polymerization technique. Polymer P4 was prepared using oligo(ethylene glycol) methyl ether methacrylate (OEGMA), lauryl methacrylate, and diphosphinostyrene (styrene-PPh$_2$) as the Ru-binding ligand. In contrast, polymer P5 was synthesized using methacrylate-functionalized 1,3,5-benzene-tricarboxamide (BTAMA) in place of lauryl methacrylate. The molecular weight of the synthesized polymers was (M_n) around 14 kDa and $Đ$ of less than 1.4 (refer to Figure 10).
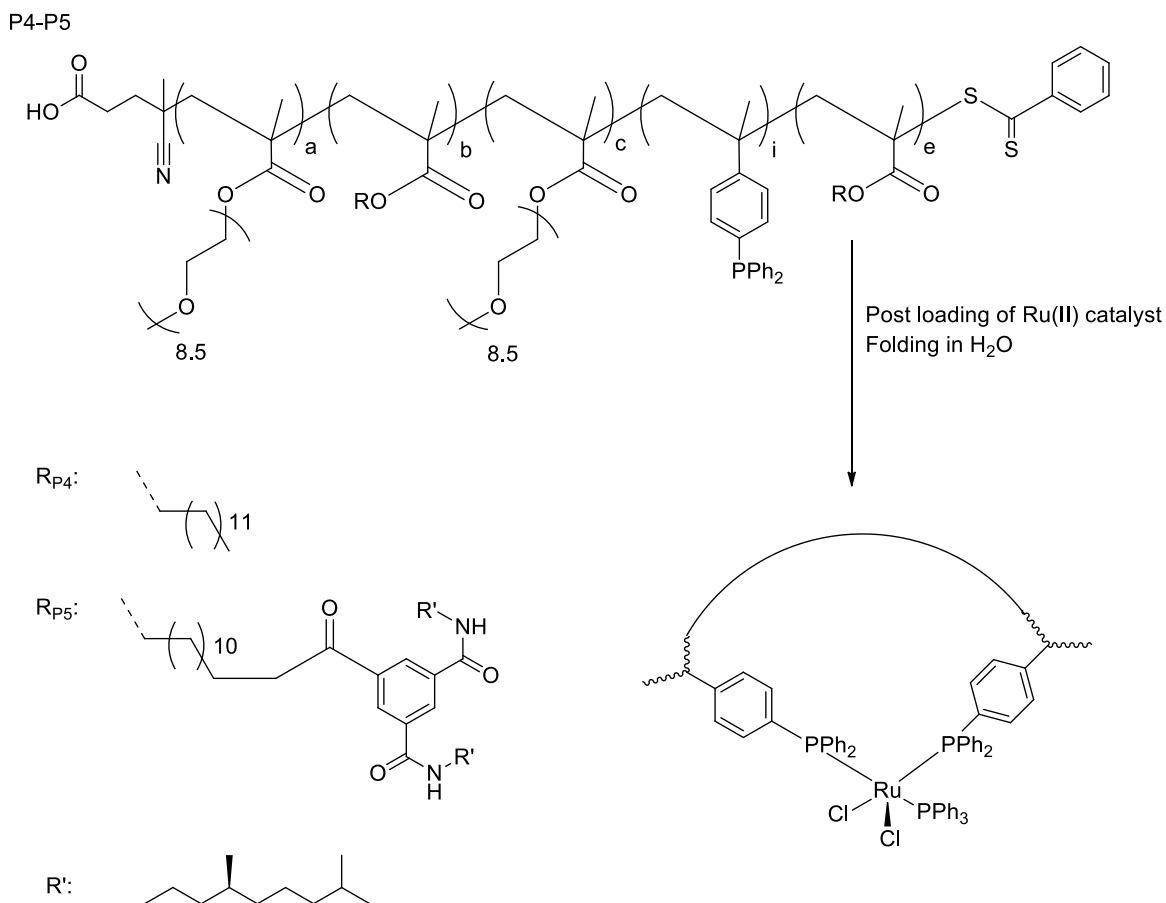
Figure 10. Ru complexation with triphenyl phosphine ligand results in the formation of catalytically active Ru-SCNPs, able to catalyze the oxidation of alcohols in aqueous medium.[70] Reproduced with permission from reference [70].

RuCl$_2$(PPh$_3$)$_3$ was added to the polymers using a post-encapsulation technique in order to form catalytic centers. Inductively Coupled Plasma – Atomic Emission Spectroscopy (ICP-AES) revealed that each polymer chain in both polymers included between two and three Ru centers. Additionally, DLS and Circular dichroism (CD) were used to characterize the polymers and the catalysts that accompanied them.

Tert-butyl hydroperoxide was used as the oxidant in the catalytic reaction to convert alcohols into ketones. The catalytic experiments using these SCNPs led to two important results: *(i)* the catalytic activity is directly proportional to the hydrophobicity of the substrates and *(ii)* P4 and P5 did not show any remarkable difference, indicating that an efficient reaction can be achieved with a hydrophobic pocket within the polymer (instead of the more well-defined structure provided by the benzene tricarboxylic acid units). In summary, the hydrophobic substrates embedded within the catalytically active, folded

28

polymers introduced by the Palmans and Meijer groups have demonstrated remarkable selectivity in aqueous environments for the oxidation of alcohols. Their studies moved the field towards synthetic enzymes by advancing our knowledge of how these polymers function and what components are required to generate selective reactions in water.

Photodynamic SCNPs

Reversible folding and unfolding are challenging, and photodynamic SCNP morphologies are still scarcely reported. When confined within constrained polymer environments, common photoreversible covalent chemistries such as coumarin dimerization, anthracene, and styrylpyrene tend to reach photostationary states heavily biased toward the dimer form, ultimately limiting their utility in truly reversible polymer folding.[71]

For example, Zhao and coworkers successfully generated SCNPs using coumarin photochemistry.[54] Coumarin-functionalized precursor polymers were synthesized via RAFT copolymerization (refer to Figure 11), enabling light-triggered, reversible dimerization through [2+2] cycloaddition. The resulting polymers exhibited well-defined characteristics with M_n = 110 and 104 kDa, low dispersity ($Đ$ = 1.1) and mol% of coumarin between 7 and 13 mol%, respectively. At dilute concentrations (1 mg·mL^{-1}), selective intramolecular chain collapse was induced at wavelengths above 310 nm, while exposure to light below 260 nm effectively reverses the dimerization, demonstrating precise photochemical control over polymer folding. UV-Vis spectroscopy was used to monitor the extent of [2+2] cycloaddition. A maximum [2+2] cycloaddition efficiency at 70% was observed, corresponding to a decrease in the intensity of the absorption peak associated with the coumarin units at 320 nm. Upon irradiation at wavelengths below 260 nm for two hours, only 38% of the original polymers could be recovered through the reversed process.
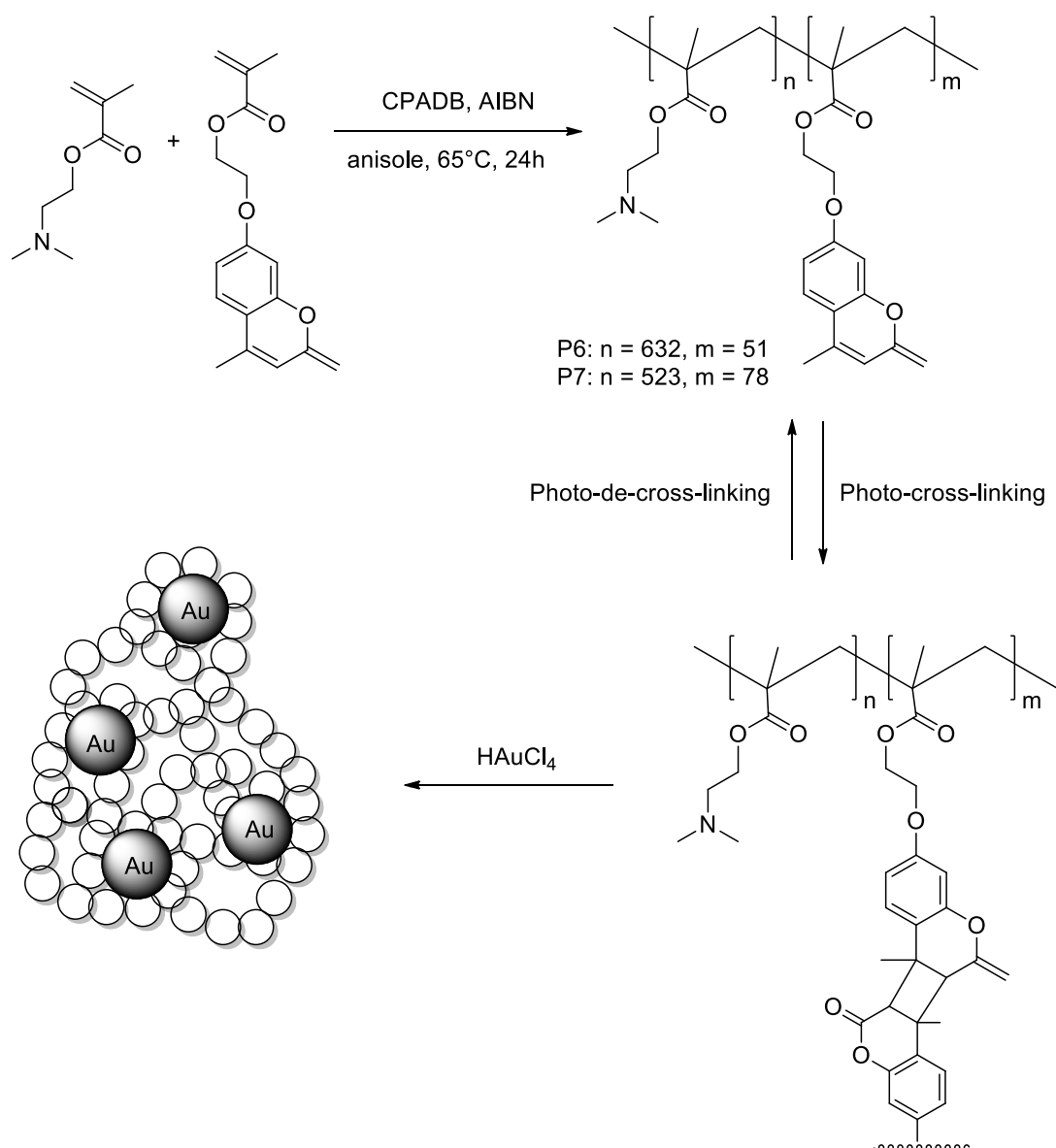
Figure 11. Photodynamically responsive SCNPs formed via [2+2] cycloaddition of coumarin units enable tunable gold nanoparticle (AuNP) formation.[54] Reproduced with permission from reference [54].

Size-exclusion chromatography (SEC) confirmed that increasing the degree of coumarin dimerization led to a clear reduction in polymer size, transitioning from extended single chains to compact, intramolecularly collapsed structures. Remarkably, despite variations in initial coumarin content, both polymers P6 and P7 converged to similar apparent molecular weights upon collapse. Notably, SEC elution profiles remained unchanged following exposure to light capable of reversing the crosslinks, suggesting that a dimerization degree of approximately 38% was sufficient to stabilize the globular SCNP

conformation. Differential scanning calorimetry (DSC) analysis revealed that enhanced cross-linking broadened the thermal transition and elevated the glass transition temperature (T_g), underscoring the structural and thermal consequences of coumarin-mediated folding. These SCNPs were employed as nanoreactors to modulate the creation of gold nanoparticles (AuNPs).[54] To initiate AuNP formation, $HAuCl_4$ was introduced into solutions containing spherical SCNPs with varying degrees of coumarin dimerization (0%, 27%, and 64%). Interestingly, the reaction kinetics diverged significantly from conventional methods, revealing a strong dependence on the polymer chain mobility and conformation dictated by the extent of coumarin cross-linking. Notably, as the cross-linking density increased, the reaction mixtures exhibited a progressively darker red colour indicating enhanced AuNP formation. This behavior was attributed not only to the compact architecture of the SCNPs, which promotes local accumulation of gold atoms, but also to the presence of tertiary amine groups within the polymer, which act dually as reducing agents and stabilizers, thereby facilitating the nucleation and growth of AuNPs within the confined nanoreactor environment.

Our group combined orthogonal folding and end-to-end ligation within a single polymer by leveraging the photodimerization of anthracene side chains and a styrylpyrene end group, enabling the controlled formation of SCNPs through different photoreactions (refer to Figure 12).[72]
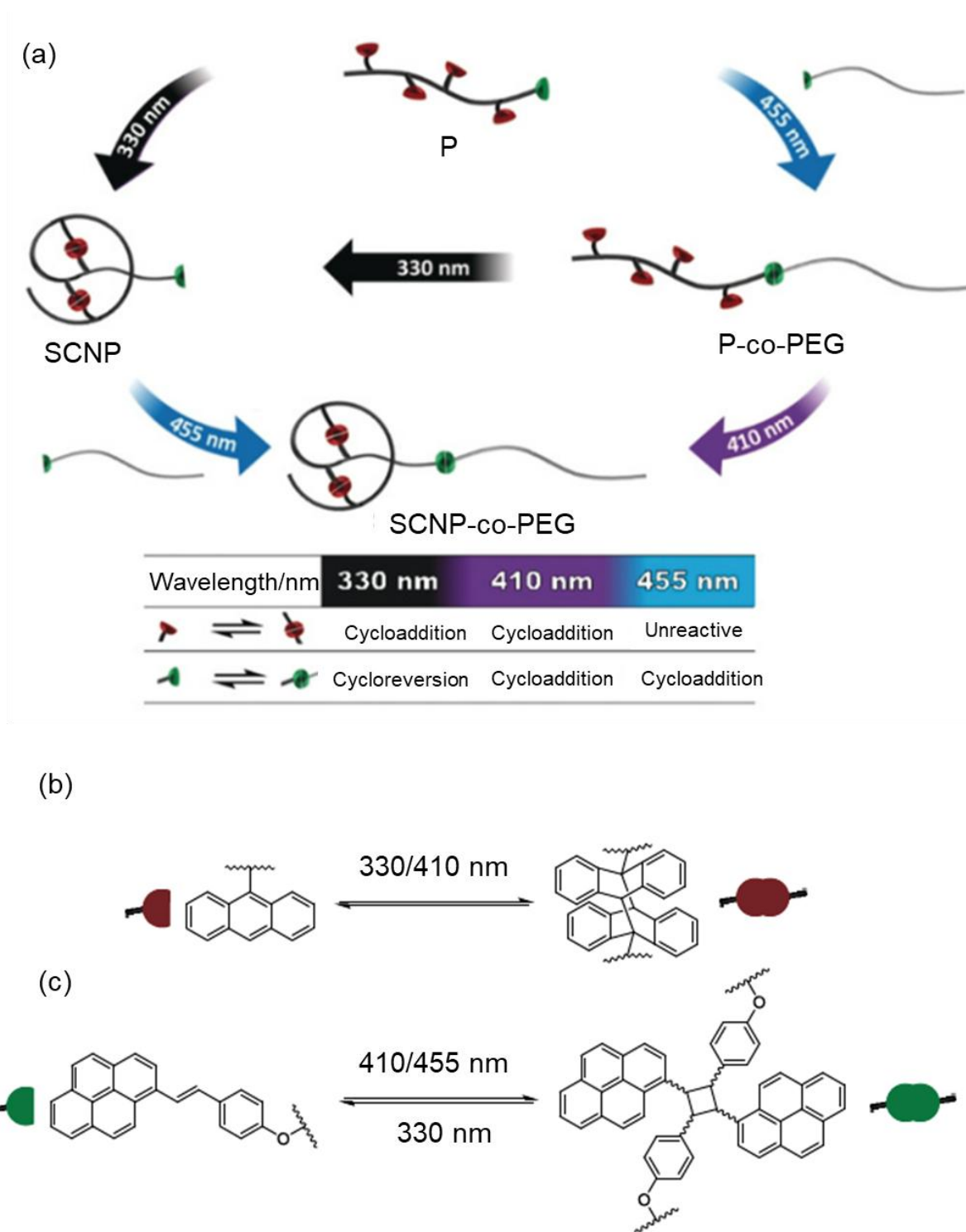
Figure 12. (a) Photochemically selective chain-end ligation; (b) Intramolecular chain collapse via [4+4] cycloaddition of anthracene units under 330 nm irradiation; and (c) Orthogonal [2+2] photodimerization of styrylpyrene at 455 nm.[72] Reproduced with permission from reference [72].

Anthracene dimerization produced SCNPs at 330 nm. Without causing anthracene dimerization, styrylpyrene end groups were used to achieve chain ligation to a PEG polymer at 455 nm. However, the chain ligation mediated by styrylpyrene end groups was reversed upon irradiation at 330 nm, while anthracene dimerization was predominant at this wavelength. Therefore, the two polymers were cleaved by reversing the styrylpyrene-mediated ligation under 330 nm light, and simultaneously, SCNPs were formed through anthracene dimerization. Since no additional bonds keep the two polymer chains close to one another, they can freely diffuse away from one another when exposed to 330 nm radiation. The reversible ligation is responsible for the reversible morphological regulation of a SCNP tertiary structure. However, the reversible ligation process does not result in any detectable unfolding or alteration of the compaction of SCNPs.

Only a few SCNP systems incorporate photoswitchable elements. Our group was among the first to report the unfolding of the SCNP triggered by visible light.[73] Wen *et al*. developed a light-responsive SCNP by photodimerizing stilbene units while integrating azobenzene pendant units capable of reversible *cis*/*trans* isomerization under 360 nm (UV) and 520 nm (visible) light, respectively.[74] Prior to irradiation, the SCNPs exhibited well-defined tubular morphologies, as observed by transmission electron microscopy (TEM). Upon UV exposure at 360 nm, these structures transformed into larger, spherical nanoparticles. Remarkably, this morphological change was fully reversible upon irradiation with visible light at 520 nm, restoring the original tubular form. These dynamic transformations were attributed to changes in polarity and the substantial shift in free volume resulting from azobenzene isomerization.[75,76] The tubular structures are based on the stacking of *trans*(*E*)-azobenzene units, driven by liquid crystalline (LC) phase behavior. Upon *cis*-isomerization under visible light, increased molecular disorder disrupted the LC alignment, leading to spherical morphologies and underscoring the responsiveness of these SCNPs to external light stimuli.

Mutlu *et al*. utilized bi-imine photoswitches, capable of reversible *Z*/*E* isomerization, as integral components of a linear polymer backbone.[77] Upon UV irradiation, the polymer underwent light-induced isomerization, triggering a metal induced collapse into a single-chain nanoparticle (SCNP) with significantly reduced hydrodynamic volume, as confirmed

by DOSY NMR, dynamic light scattering (DLS), and SEC. Interestingly, the process was fully reversible: thermal relaxation restored the bi-imine units to their stable *Z* isomer, regenerating the original linear polymer structure (refer to Figure 13). The photoinduced folding of the linear polymer was attributed to increased chain flexibility resulting from *E/Z* isomerization of the bis-imine units. Notably, the introduction of Pd ions capable of selectively coordinating with the *Z* isomer enabled a secondary folding mechanism via metal-ligand complexation, leading to further compaction into SCNPs. This metal coordination-driven collapse was clearly evidenced by both DLS and SEC, which revealed a marked reduction in hydrodynamic size. The combination of reversible photoswitching and metal coordination thus presents a compelling strategy for designing catalytically active SCNPs with tunable morphologies and stimuli-responsive catalytic behavior.
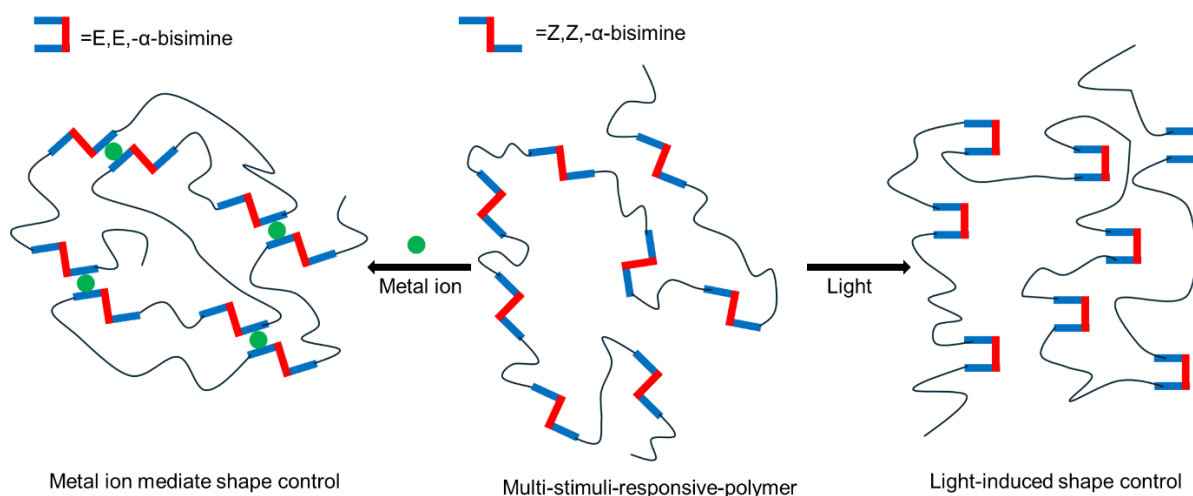
Figure 13. Two distinct SCNP topologies were achieved through the synergistic interplay of main-chain photoisomerization of a bis-imine photoswitch and metal coordination, enabling precise structural control at the single-chain level.[77] Reproduced with permission from reference [77].

Characterization of SCNPs becomes increasingly challenging as the molecular structures become more intricate and advanced. Alongside the synthetic efforts, advanced characterization of SCNPs and their precursors becomes critically important.

Since the early efforts in SCNP technology, size exclusion chromatography (SEC) has been essential for delivering qualitative size and molecular weight data. SEC – when combined with a viscometer or multi-angle light scattering (SEC-MALS) – enables the

determination of intrinsic viscosity and absolute molecular weight, providing critical insights into polymer-to-nanoparticle transitions. Complementary spectroscopic techniques including ultraviolet-visible (UV-Vis), infrared (IR), circular dichroism (CD), nuclear magnetic resonance (NMR) and fluorescence spectroscopy offer valuable evidence of structural and conformational changes during SCNP formation. Additionally, diffusion-ordered NMR spectroscopy (DOSY) and other 2D NMR techniques afford a deeper understanding of the dynamic transformation from linear chains to compact nanoparticle architectures. To investigate the morphology of nanoparticles derived from individual polymer chains, both microscopy and scattering techniques are essential. Solution-free methods such as transmission electron microscopy (TEM) and atomic force microscopy (AFM) provide morphological insights at the nanoscale. In parallel, solution-based scattering techniques including dynamic light scattering (DLS), small-angle neutron scattering (SANS), and small-angle X-ray scattering (SAXS) provide detailed information on particle size, shape, and internal structure in their native solvated states. Together, these complementary approaches enable a comprehensive and concise evaluation of the structural properties of SCNPs.

Characterization of SCNPs using Size Exclusion Chromatography (SEC)

Since its introduction by Moore in 1964,[78] size-exclusion chromatography (SEC) has become one of the most widely used techniques in polymer research. Molecules travel through the column at different rates depending on how well they can penetrate the pores of the stationary phase.[79] Polymer coils are effectively separated on the basis of their hydrodynamic radii (R_h).[80] Smaller chains usually enter particle pores and move through the pores of the column, but larger chains can elute faster and avoid pores. The molecular weight (MW) and molecular weight distribution (MWD) of the synthetic polymers can be determined using SEC, yet often with considerable uncertainty.

Size-exclusion chromatography (SEC) using standard calibration is one of the most widely used methods for qualitatively assessing SCNP formation.[81] In this method, a calibration curve is generated using a series of linear standards with well-separated and known molecular weights (MW). By interpolating the retention time of an injected sample along this curve, its apparent molecular weight can be estimated. Since the molecular weight of SCNPs cannot be accurately determined using linear polymer standards, SEC

primarily provides valuable qualitative information.[1] Due to the intrinsic compaction resulting from intramolecular cross-linking, SCNPs exhibit significantly smaller hydrodynamic radii compared to their linear polymer precursors. Consequently, the folding of linear polymers into SCNPs is typically associated with a shift in the SEC trace toward longer retention times.[82–85]

Our group synthesized a cysteine-functionalized monomer by esterifying protected cysteine N-(*tert*-butoxy-carbonyl)-S-trityl-L-cysteine with 2-hydroxyethyl methacrylate (HEMA).[86] Subsequent RAFT polymerization with poly(ethylene glycol) methacrylate (PEGMA) yielded a water-soluble precursor polymer, incorporating an average of four cysteine units. The resulting polymer exhibited a number-average molecular weight (M_n) of 7,000 g mol^{-1} and a low dispersity ($Đ$ = 1.2), making it an ideal scaffold for further functionalization (refer to Figure 14).
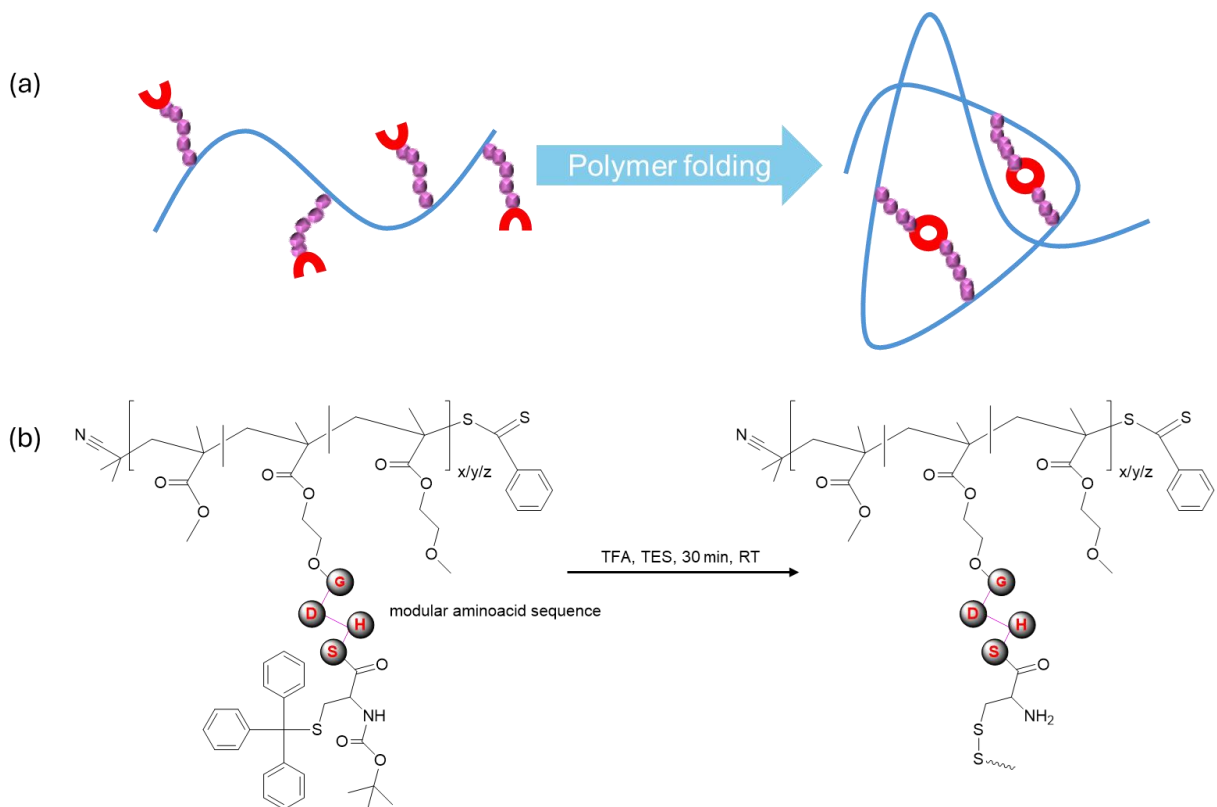
Figure 14. (a) Schematic representation of single polymer chain collapse driven by cysteine-terminal peptide side chains. (b) Deprotection of the precursor polymer simultaneously triggers intramolecular folding into well-defined SCNPs.[86] Reproduced with permission from reference [86].

The precursor polymer was dissolved in a trifluoroacetic acid (TFA) and triethylsilane (TES) mixture (9:1, *v/v*) to simultaneously trigger deprotection of acid-labile groups and promote disulfide bond formation. This reaction was performed at 298 K for 30 minutes under ambient air, conditions known to facilitate the oxidation of cysteine methylesters into disulfides. The collapse of single polymer chains into SCNPs was tracked by size exclusion chromatography (SEC). Upon removal of protective groups and intramolecular crosslinking, the hydrodynamic volume and consequently the molecular weight decreased significantly from M_p = 7,900 g·mol^{-1} for the precursor polymer to 7,000 g·mol^{-1} for the folded SCNP. The detection of a high-molecular-weight shoulder in the SEC trace indicated minor intermolecular crosslinking, a mild side reaction during the folding process (refer to Figure 15).
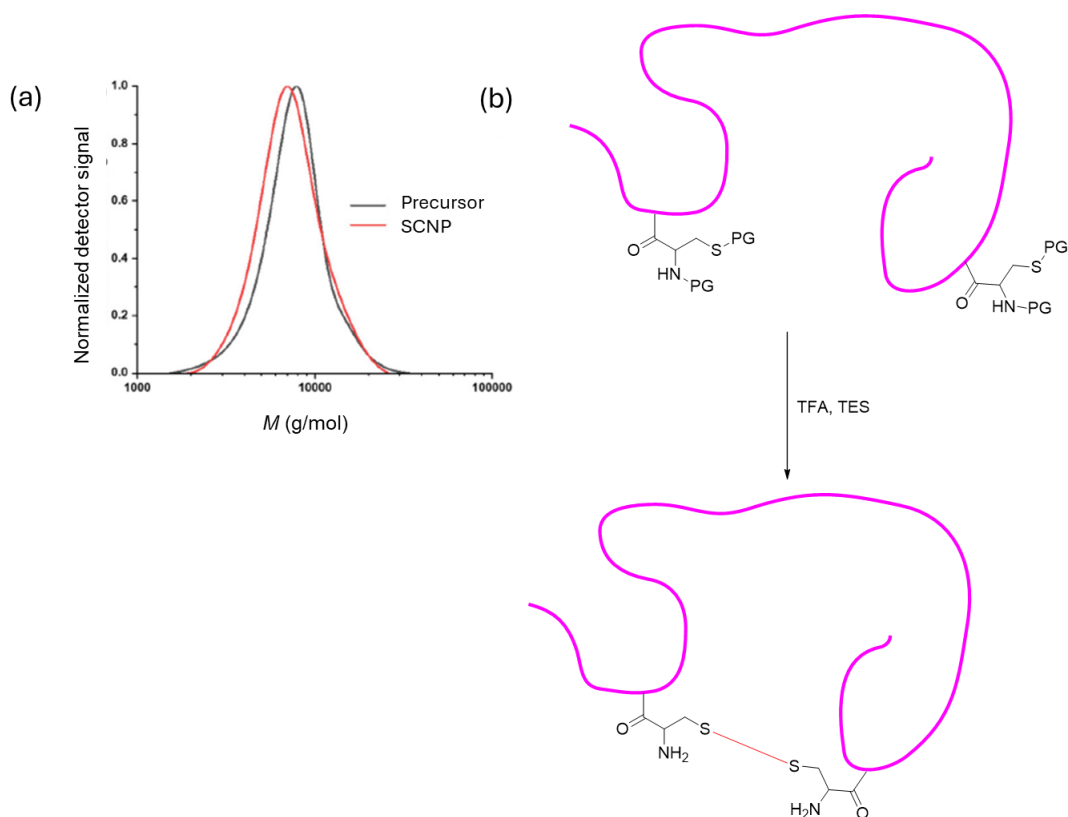
Figure 15. (a) Overlaid SEC chromatograms comparing the precursor polymer and the resulting single-chain nanoparticle (SCNP), highlighting the decrease of the hydrodynamic volume upon folding. (b) Schematic representation of SCNP formation driven by disulfide bridge crosslinking between cysteine residues.[86] Reproduced with permission from reference [86].

Here, the SEC chromatograms of the SCNPs and their precursor polymer nearly overlap, indicating minimal observable changes. Since SEC does not provide absolute molecular weight values and all measurements are relative, it is not a suitable technique for the definitive characterization of SCNPs.

Characterization of SCNPs using ^{1}H Nuclear Magnetic Resonance Spectroscopy (^{1}H NMR)

Researchers have employed NMR spectroscopy since the late 1940s, when the technology was first established.[87,88] Since the introduction of Fourier Transform (FT) NMR in the late 1960s, a wide range of experiments and pulse sequences has been developed to probe the dynamics, structure, and composition of molecules. Although early continuous-wave (CW) NMR instruments (1940s–1960s) relied on field scanning and did not permit modern pulse-sequence–based methods, the conceptual foundations established during that period still inform contemporary NMR analysis. When describing SCNPs, the same principles initially applied to small molecules continue to be highly useful. Single-chain polymer nanoparticles can be characterized using 1D and 2D spectroscopic techniques. SCNPs are typically formed through the use of either internal or external cross-linkers.[1] A standard one-dimensional (1D) ^{1}H NMR experiment is often the simplest method to monitor this transformation, as the appearance or disappearance of characteristic resonances in the NMR spectra can indicate the formation of cross-links. Moreover, since ^{1}H is highly abundant in nature, these experiments require only a small amount of material and can yield results faster than many conventional characterization techniques.

Recently, our group developed a metallo-folded single-chain nanoparticle (SCNP) using Cu(II) ions as key crosslinkers. The precursor polymer (P8) was prepared using RAFT polymerization of 2-((2-nitrobenzyl)oxycarbonyl)amino)ethyl methacrylate and poly(ethylene glycol) methyl ether methacrylate, as illustrated in Figure 16.[89] The SCNP formation was achieved by mixing 2 mg mL^{-1} polymer (P8) in acetonitrile with Cu(II) chloride dihydrate, followed by batch photochemical irradiation using a light-emitting diode (LED). This approach enabled precise control over metal-mediated folding,

resulting in well-defined metallo-SCNPs with potential for advanced catalytic and functional applications.
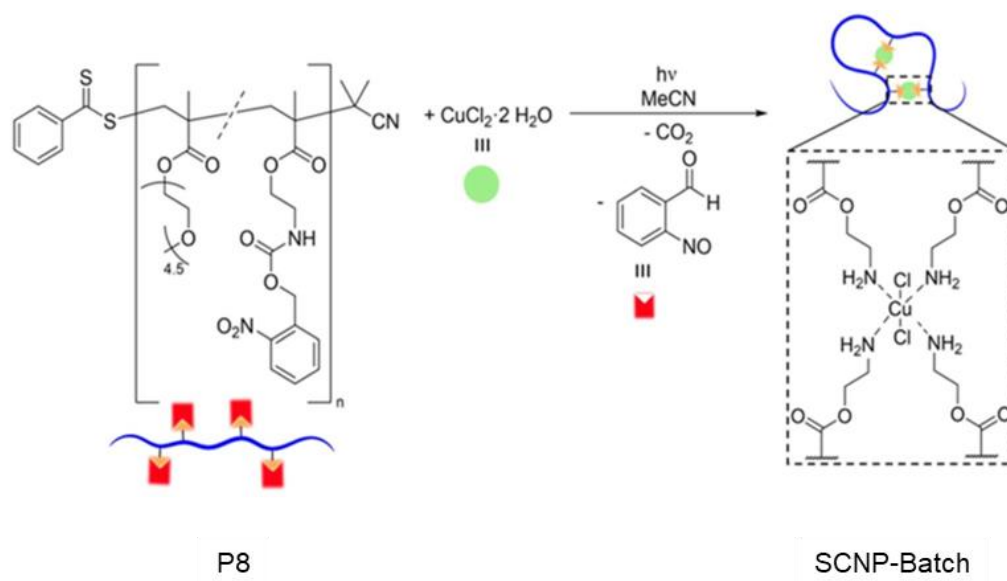
Figure 16. Schematic illustration of the photochemical synthesis of Cu(II)-folded SCNPs. The linear precursor polymer (P8) undergoes a batch irradiation process in the presence of Cu(II) ions, resulting in the formation of compact, metallo-crosslinked SCNP-Batch structures.[89] Reproduced with permission from reference [89].

^{1}H NMR spectroscopy was employed to characterize both the precursor polymer and the resulting SCNP. Key resonances corresponding to the photolabile *ortho*-nitrobenzyl protecting group—observed at δ = 8.20-7.45 ppm, 6.35-6.15 ppm, and 5.52-5.38 ppm disappeared upon irradiation, confirming substantial deprotection of the linear precursor (refer to Figure 17). However, while ^{1}H NMR spectroscopy clearly confirms the removal of protecting groups, it does not allow differentiation between the desired intrachain folding and unintended interchain crosslinking.
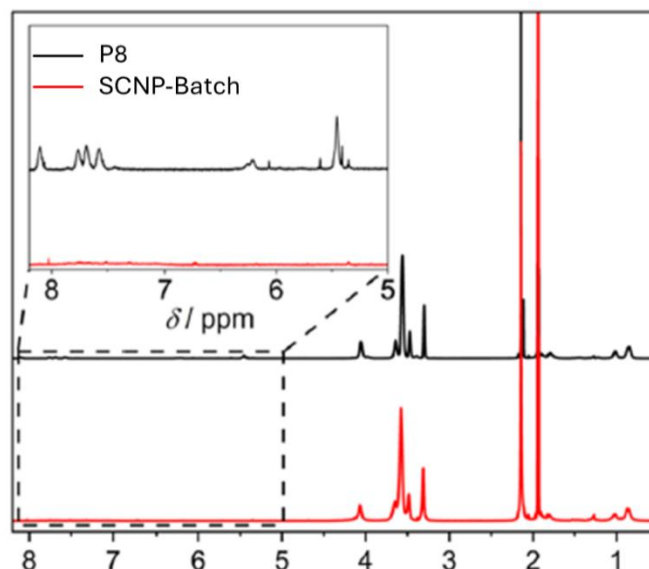
Figure 17. ¹H NMR spectra (600 MHz, CD₃CN, 298 K) comparing the linear precursor polymer (P8) and the metallo-folded SCNP-Batch, highlighting the disappearance of *ortho*-nitrobenzyl resonances following photochemical deprotection and intramolecular folding.[89] Reproduced with permission from reference [89].

Characterization of SCNPs using Dynamic Light Scattering (DLS)

Dynamic light scattering (DLS) is a highly effective technique for investigation of the particle sizes in solution at the nanoscale making it particularly valuable for characterizing single-chain nanoparticles (SCNPs), which typically form in the nanometer range. Dynamic light scattering has been widely employed in SCNP research to evaluate particle size and size distribution. For example, Barner-Kowollik and co-workers showcased the utility of DLS by investigating the collapse and functional modification of random copolymers composed of styrene and 4-chloromethyl styrene, underscoring DLS as a reliable tool for probing SCNP formation and behavior.[38]

Dynamic light scattering (DLS) was also employed to investigate the formation of the metallo-folded SCNP described in the previous section.[89] Measurements conducted in acetonitrile revealed a notable reduction in the solvodynamic diameter (D_h), examined from number-averaged size distributions from D_h = 6.4 nm for the precursor polymer (P8) to D_h = 3.1 nm for SCNP-Batch, consistent with the expected compaction upon folding (refer to Figure 18). It is worth noting, however, that DLS data for particles of such a small size should be interpreted with caution due to their inherently low scattering intensity.[1]

40
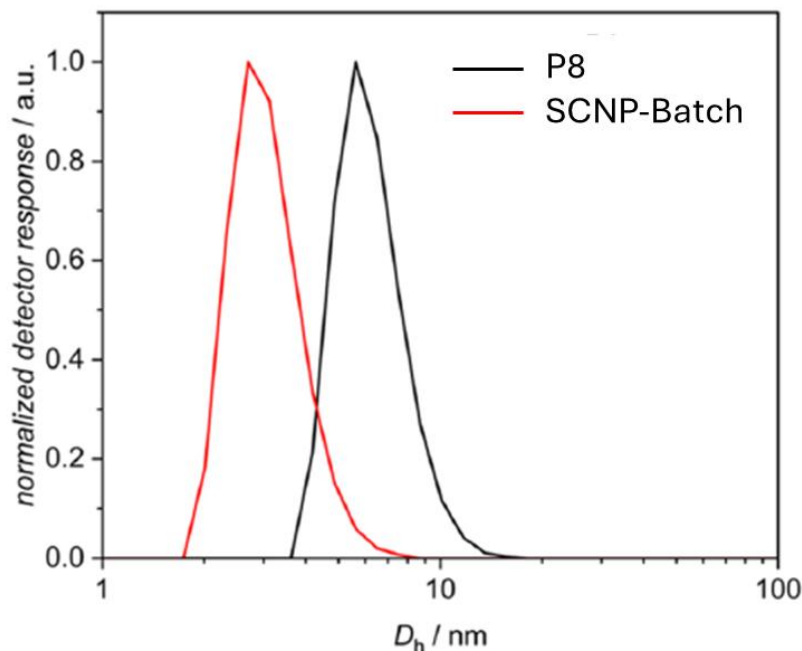
Figure 18. Number-weighted DLS size distributions in acetonitrile, comparing the metallo-folded SCNP-Batch (red) with the linear precursor polymer (*i.e.* marked by P8 represent by black (refer to Figure 16)), highlighting the significant reduction in hydrodynamic diameter upon intramolecular folding.[89] Reproduced with permission from reference [89].

However, since SCNPs are isolated macromolecules and typically very small (often less than 10 nm in diameter), their scattering intensity is low and often difficult to distinguish from background noise. As a result, DLS is not a suitable technique for the accurate characterization of SCNPs, as it cannot provide structural information.

Characterization of SCNPs using Electrospray Ionization Mass Spectrometry (ESI-MS) and Tandem Mass Spectrometry (MS/MS)

Sir J.J. Thomson's investigations into the nature of positively charged particles at the end of the 19th century laid the foundation for the development of modern day mass spectrometers.[90] In the following decades, Francis William Aston advanced this emerging technique, enabling the differentiation of isotopes in various gases.[91] However, it was the critical importance of isotope separation for the Manhattan Project during World War II that significantly accelerated research in the field. By the 1950s, mass spectrometers had become commercially available. The development of Electrospray ionization (ESI) revolutionized mass spectrometry by enabling the gas-phase ionization of large

molecules while preserving their structural integrity. ESI-MS allows for the determination of average molecular weight, identification of end groups, and assessment of the charge states of ions derived from macromolecules. Tandem mass spectrometry (MS/MS), which relies on the fragmentation of mass-selected ions, has become one of the most versatile characterization tools for probing the primary structure of a wide range of compounds. MS/MS is a powerful technique for identifying the sequence of proteins, peptides, and polymers through controlled fragmentation processes.[92]

Recently, macromolecular chemists started to introduce high resolution mass spectrometry for the characterization of SCNPs.[93] For example, Barner-Kowollik and colleagues investigated the formation of SCNPs from poly(methyl methacrylate-*stat*-glycidyl methacrylate) in the presence of a strong Lewis acid $B(C_6F_5)_3$. Specifically, $B(C_6F_5)_3$ acts as a catalyst, enabling SCNPs formation via the ring opening of the epoxide that ultimately leads to intramolecular crosslinking and compaction. These authors used ESI coupled to mass spectrometry to directly analyze SCNPs directly from a solution. A typical resulting mass spectrum is presented in Figure 19. In the recorded mass spectrum, it is very difficult to identify SCNP ions since the mass spectrum is constituted by ions from single chain nanoparticles and precursor polymers, including different charge states. By focusing on a specific region, refer to Figure 20, it is nevertheless possible to attribute the most abundant ions to ionized SCNPs constituted by methyl methacrylate monomer units as shown in Figure 20.
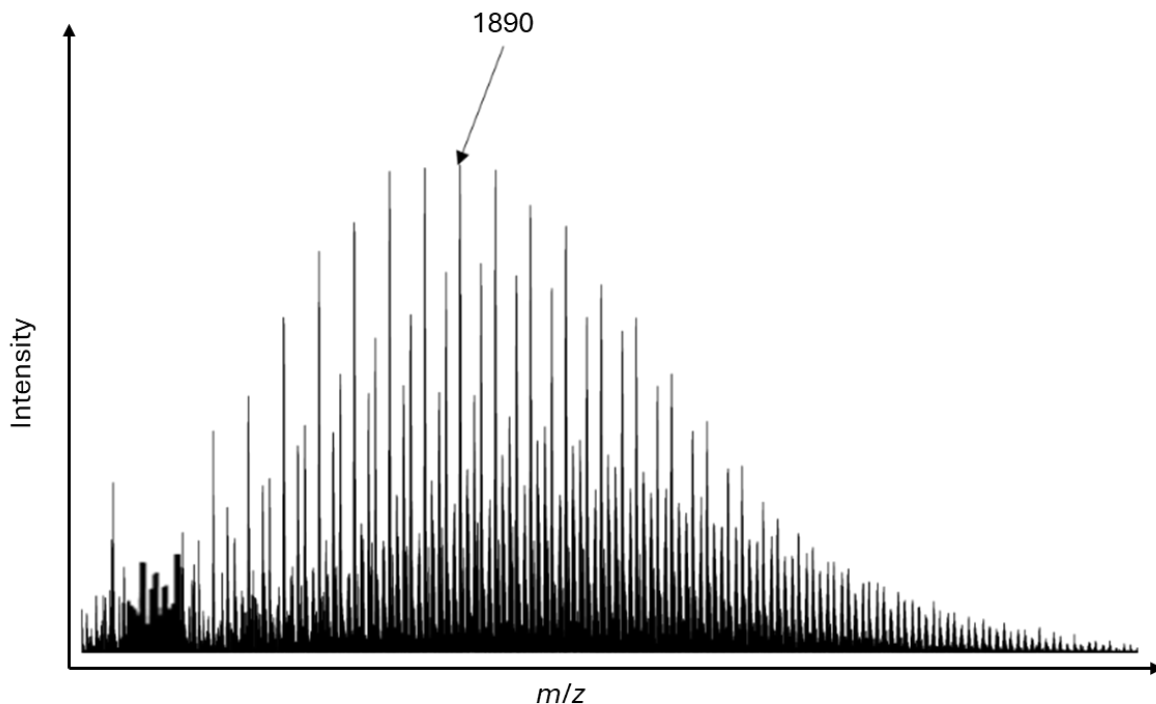
Figure 19. Electrospray ionization mass spectrometry (ESI-MS) analysis of single-chain polymeric nanoparticles (SCNPs) derived from the precursor polymer poly(methyl methacrylate-stat-glycidyl methacrylate)[93] in the presence of the Lewis acid $B(C_6F_5)_3$ revealed that SCNP formation occurred via epoxide ring opening followed by intramolecular crosslinking. The most intense peak was observed at *m/z* 1890. Reproduced with permission from reference [93].

Therefore, the formation of SCNPs can be confirmed via such an analysis. However, it is very difficult to predict the structure of SCNPs from this single-stage mass measurement.
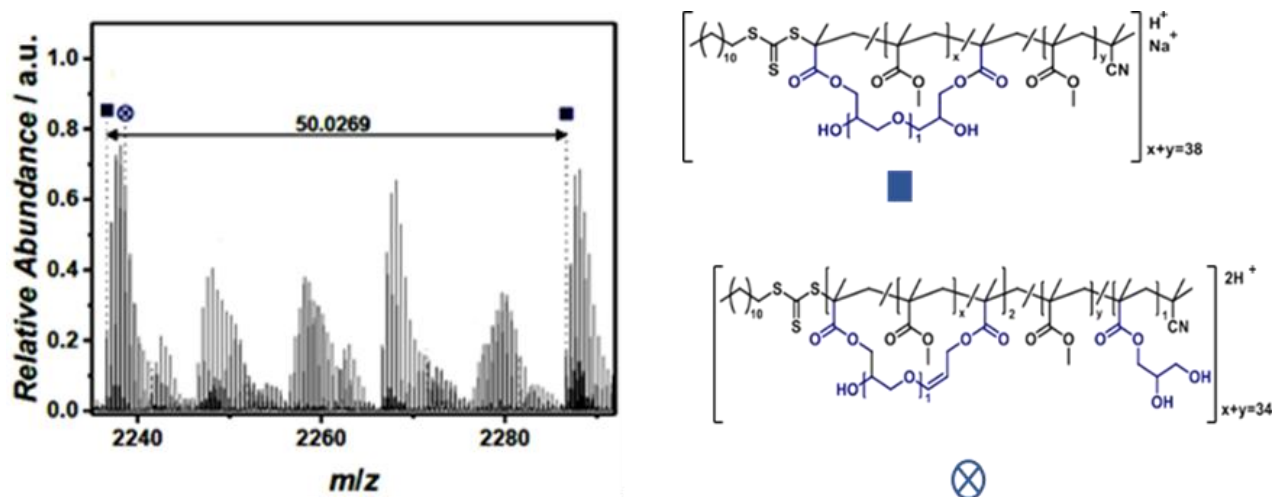
Figure 20. (Left) Zoomed (*m/z* 2235 to *m/z* 2292) of the positive mode Electrospray mass spectrum of SCNPs produced from the precursor polymer poly(methyl methacrylate-stat-glycidyl methacrylate).[93] Here the squares and cross circles

43

identify the peaks of the most abundant SCNP ions. The *m/z* difference between two peaks (marked by squares) is 50.0269 u, corresponding to the mass of the methyl methacrylate repeating unit. (Right) Chemical structures of the most abundant SCNP ions.[93] Reproduced with permission from reference [93].

Recently, several research teams attempted to study SCNP using state-of-the-art mass spectrometry.[93,94] In these experiments, SCNPs were extracted from solution to the gas phase of the mass spectrometer using electrospray ionization. Mass spectrometry can provide accurate information on the mass and the charge of gaseous ionized SCNP through single stage mass spectrometry analysis, *i.e.* recording of a mass spectrum. However, ESI-MS does not provide information about the conformation or shape of SCNPs. To gain deeper insight into the conformational properties and overall shape of these ions, ion mobility spectrometry (IMS) can be integrated into the mass spectrometry workflow. IMS has been introduced to the mass spectrometry toolbox and is particularly efficient in studying the 3D structures of gas phase ions. IMS is to-date scarcely used for the investigation of SCNP or their pre-polymers.[93]

Tandem mass spectrometry (MS/MS)

In mass spectrometry-based analyses, precursor ions are typically isolated and subjected to multiple collisions with rare gas atoms to produce an MS/MS spectrum, which is then analyzed based on the *m/z* values of the resulting fragments.[95] This technique, known as collision-induced dissociation (CID), imparts sufficient internal energy to induce the cleavage of covalent bonds. In the case of peptides, protonation typically occurs at the amide bonds along the peptide backbone. Upon collisional activation, these protonated amide linkages become more labile and prone to cleavage, resulting in the formation of a series of homologous fragment ions. For example, the MS/MS spectrum shown in Figure 21b displays successive peptide fragment ions such as PE, PEP, and so on. The objective of this method is to generate a series of peptide fragments that differ by the mass of a single amino acid, thereby enabling the deduction of the amino acid sequence of the precursor peptide.[92]
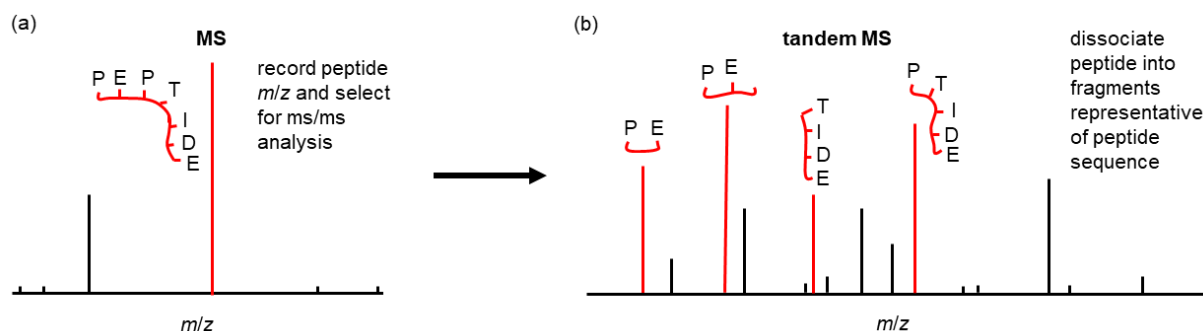
Figure 21. A modern proteomics experiment using mass spectrometry (MS) typically follows a defined sequence of steps: (a) The mass spectrometer separates the charged peptides based on their mass-to-charge ratio (*m/z*). (b) In tandem mass spectrometry (MS/MS), the most abundant peptide cations are selected for fragmentation. The resulting fragment ions are then analyzed according to their *m/z* values to generate MS/MS spectra, which are used for peptide identification and sequencing.[92] Reproduced with permission from reference [92].

Ion mobility mass spectrometry

Ion mobility experiments record the time taken by ions to transit through a cell filled with an inert gas under the influence of an electric field (refer to Figure 22). More accurately, since ions experience collisions with the buffer gas (generally nitrogen or helium), the combination between the acceleration by the electric field and the deceleration by collisions will affect the drift time of the ions.
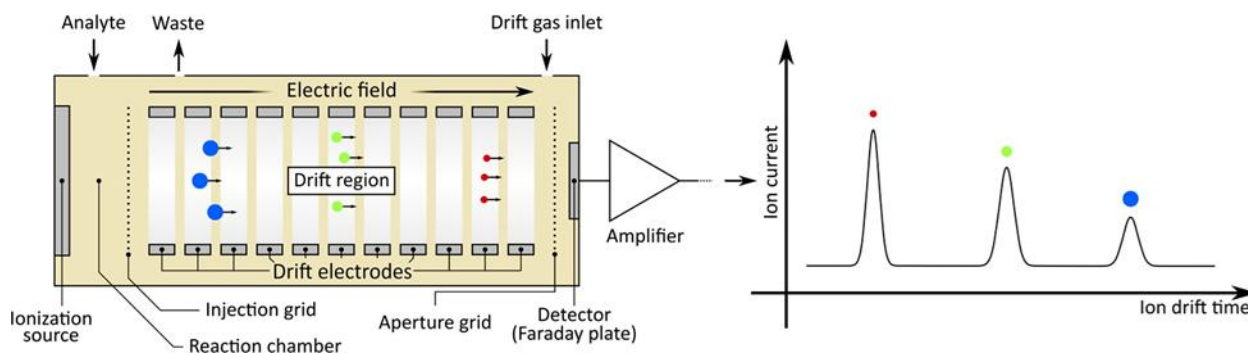
Figure 22. Ions move through the drift tube during IMS separation, smaller ions move faster and larger ions move slower (Left). Resulting ion mobility separation spectrum (Right).[96] Reproduced with permission from reference [96].

Specifically, different ions will experience different numbers of collisions with the buffer gas inside the drift tube. More compact ions experience fewer collisions with the buffer gas and less compact ions face a high number of collisions with the buffer gas. Thus, more compact ions move faster compared to the less compact ions during their flight

through the drift tube (refer to Figure 22). The drift time is directly correlated with the structure or conformation of the ions. Collision cross sections (*CCS*) can subsequently be determined from the drift time measurements. Several types of ion mobility mass spectrometry are used for analysis, including drift-time IMS, aspiration IMS, field-asymmetric waveform IMS, trapped IMS and traveling-wave IMS.[97,98] However, providing a full description of these methodologies is beyond the scope of this introduction.

The spatial organization of gaseous ions can be directly investigated using ion mobility spectrometry coupled with mass spectrometry (IMS-MS). The measured ion mobility (*K*) depends on the ion charge (*z*) and its collision cross section (*CCS*) as well as experimental parameters such as temperature (*T*) and the nature of buffer gas employed. When operated in the low-field regime, where the electric field minimally perturbs ion trajectories, the Mason–Schamp equation defines the relationship between *K* and *CCS*:

$$K = \frac{3ze}{16N} \left(\frac{2\pi}{\mu k_B T} \right)^{1/2} \frac{1}{\Omega}$$

N is the buffer gas number density, μ is the reduced mass of the ion–gas pair, k_B is the Boltzmann constant, and Ω is rotationally averaged collision cross section (*CCS*). This equation illustrates the dependence of ion mobility on the *CCS*, temperature, ion mass, buffer gas identity, and charge state.

Since *CCS* directly reports an ion's three-dimensional structure, IMS is a powerful method for assessing ion size, shape, and conformation in the gas phase. Importantly, the Mason–Schamp equation applies only in the low-field regime. At higher electric field strengths—such as those used in high-field asymmetric waveform ion mobility spectrometry (FAIMS) or when operating beyond the low-field limit—ion mobility becomes field-dependent, and the Mason–Schamp relationship no longer holds.

Ion mobility spectrometers were first coupled to mass spectrometers (IMS-MS) in 1962 to separate ions according to both their mobilities and mass-to-charge ratios.[84] IMS is typically coupled to MS in order to: *(i)* study the three-dimensional structures of gaseous ions; *(ii)* separate isomeric ions, species with identical masses but different spatial configurations that cannot be distinguished by MS alone; and *(iii)* enhance the sensitivity and resolution of traditional mass spectrometry. A key advantage of IMS-MS lies in its compatibility with atomistic theoretical techniques, such as molecular dynamics (MD)

simulations, which allow detailed investigation of both equilibrium structures and conformational dynamics of ions.

The connection between structure and mobility is further strengthened by algorithms that calculate theoretical CCS values (CCS_{th}) from simulated ion structures, enabling direct comparison between experimental data and computational models, providing deeper insights into ion behavior and structure in the gas phase.

Ion mobility–mass spectrometry (IMS-MS) holds a unique and valuable position in the study of synthetic polymers. Due to their inherent dispersity, synthetic polymers generate a diverse range of homologous ions with varying chain lengths, often detected in multiple charge states.[99–101] This characteristic makes them particularly well-suited for IMS analysis. IMS enables the structural interrogation of polymer ions across the entire macromolecular distribution, providing insight into conformational trends as a function of polymer length and charge state.

As a result, collision cross sections of single chain nanoparticle ions can be directly obtained using IMS-MS. In the last decade, Gerbaux and coworkers, amongst others, exploited the combination between ion mobility and mass spectrometry to characterize different polymer architectures such as cyclic vs linear polymers, copolymers and dendrimers.[102] However, the CCS represents the rotationally averaged interaction area between an ion and the buffer gas molecules. It essentially provides information about the overall size and shape of the ions. However, CCS does not give insight into the positions of functional groups, the orientation of end groups, or the specific interactions present within the molecules. Comparing experimental CCS values with theoretical predictions generated using computational chemistry—particularly Molecular Dynamics simulations—can offer such molecular-level descriptions and help identify candidate structures of the detected ions.[103]

In molecular structure calculations, ions and molecules populate both local and global minima on their potential energy surfaces. Quantum mechanical (QM) approaches provide a rigorous framework for mapping these surfaces because they treat electrons explicitly, offering higher accuracy than classical force-field methods. In quantum mechanical calculations,[104] molecular geometries are optimized by systematically adjusting bond lengths, angles, and torsional coordinates until a minimum-energy

structure is identified. Although QM calculations have been successfully applied to a wide range of gas-phase ions, their computational cost increases steeply with system size, making routine studies of systems containing more than ~150 atoms challenging, stable structures and collision cross sections are often calculated using a force field-based method.[105] Here, systems are described as a collection of spheres with a chemical identity connected by springs. Collision cross sections may further be determined using many different well-known methods such as for example the trajectory method, exact hard sphere scattering, diffuse trajectory method, or projection approximation.[106] Generally, the trajectory method is used because it accounts for the long-range interaction energy of the ions. A large number of input structures were analyzed, and the obtained results matched the experimental data very well.[107] Here, long-range interaction forces are considered via Lennard-Jones potentials, enabling the description of charge and temperature effects. In practice, collision cross sections from a large number of snapshots extracted from the MD simulations are considered and compared with the experimental results. Average collision cross sections at different temperatures are also often calculated to assess the extent of conformational changes induced by temperature.[108] In these studies, molecular dynamics (MD) simulations were employed to investigate the gas-phase structures of polymer ions across varying degrees of polymerization (*DP*) and charge states. By comparing the theoretical collision cross-section (*CCS*) values derived from the simulated structures with experimental measurements, the conformational landscape of these ions can be elucidated, providing deeper insight into their structural evolution. For a detailed description of molecular dynamics simulations of single-chain polymeric nanoparticles, please refer to Chapter 2 of the book *Single-Chain Polymer Nanoparticles* by Prof. José A. Pomposo (ISBN: 978-3-527-80641-6).[109]

The Bowers group was among the pioneers in applying IMS-MS to the study of synthetic polymers and biomolecules.[110–114] IMS-MS has since emerged as a powerful structural analysis tool for probing the gas-phase conformations of biomolecules and polymer ions. A detailed examination of polymer structures investigated by IMS–MS can be found in "Gas-Phase Structure of Polymer Ions: Tying Together Theoretical Approaches and Ion Mobility Spectrometry," *Mass Spectrometry Reviews* 2023, 42 (4), 1129–1151.

For researchers interested in solution-phase chemistry, the absence of solvent in the mass spectrometer can be a significant concern. How accurately does gas-phase data reflect the behavior of molecules in solution? The analyte can be introduced into the mass spectrometer through various techniques, including electrospray ionization (ESI).[115] ESI is a "soft" ionization method that gently transfers intact analyte molecules from the solution into the gas phase. A key question addressed by the Bowers group was how closely the resulting gas-phase structures resemble their solution-phase geometries, and what types of structures are produced by an ESI source. To investigate this, they selected ubiquitin as a model protein due to its small size and well-characterized nature.[114]

The Bowers group examined the Electrospray ionization (ESI) mass spectra of ubiquitin under both positive and negative ion mode conditions, using a variety of solution environments (refer to Figure 23). Ubiquitin, as a sequence-defined biomolecule with a well-defined three-dimensional structure, can be considered as a sequence-defined single-chain nanoparticle. In the positive ion mode, they tested four different solvent conditions. (a) In a 1:1 water–methanol mixture with 1% acetic acid, the dominant peaks correspond to ubiquitin ions with charge states of +11, +12, and +13, indicating an excess of 11–13 protons. (b) In a 1:1 water–methanol mixture without acetic acid, the major peaks correspond to charge states of +7 and +8. (c) In pure water, the dominant peak corresponds to the +7 charge state. (d) In water with 1% acetic acid, the spectrum is similar to condition (c), with the +7 charge state being dominant. Subsequently, they conducted experiments in the negative ion mode under two solvent conditions, *i.e.,* (e) a 1:1 water–methanol mixture and (f) pure water. In both cases, they observed ubiquitin ions with charge states of –7 and –8, corresponding to deprotonated species (refer to Figure 23).
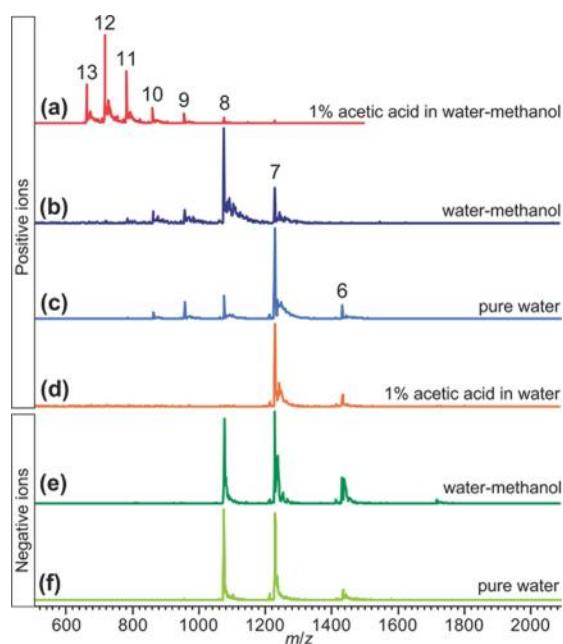
Figure 23. Mass spectra of ubiquitin in both positive and negative ion modes were obtained under different ESI solution conditions. In positive ion mode, spectra were recorded using: (a) 1% acetic acid in a 1:1 water–methanol mixture; (b) 1:1 water–methanol; (c) pure water; and (d) 1% acetic acid in water. In negative ion mode, spectra were recorded using: (e) 1:1 water–methanol and (f) pure water. In the positive ion mode spectra, the charge states of ubiquitin are indicated by the numbers above the peaks.[114] Reproduced with permission from reference [114].

Ubiquitin contains four arginine residues, seven lysine residues, one histidine, and an N-terminal amino group. As a result, it can exist in highly protonated forms, up to 13 positive charges in the case of full protonation and highly deprotonated forms, with a maximum of 8 negative charges. The charge states of the ions are denoted as $[M + zH]^{z+}$ in positive ionization mode and $[M − zH]^{z−}$ in negative ionization mode.

The native structure of ubiquitin (referred to as the N state) has been well-characterized by X-ray crystallography and NMR spectroscopy (refer to figure 24).[116–119] This structure is tightly folded and incorporates both α-helical and β-sheet secondary structure elements (refer to Figure 24). Even in the presence of substantial amounts of organic solvents, the native conformation remains remarkably stable in aqueous solution and does not denature. The N state persists across a broad pH range, including the conditions used in experiments (b) through (f). However, under acidic conditions with high methanol content, specifically in experimental condition (a) ubiquitin undergoes conformational

reorganization into a less compact, partially folded form known as the A state (refer to Figure 24).[120–122]
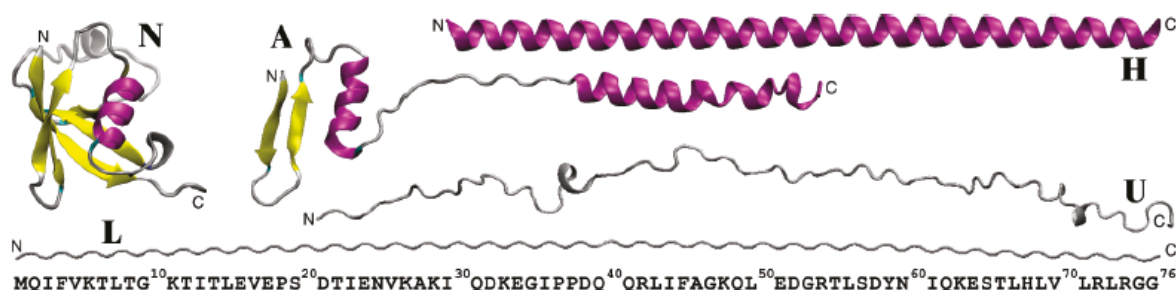
Figure 24. The sequence of the 76-residue protein ubiquitin and its various conformational states are illustrated. H represents a hypothetical fully α-helical conformation; U denotes an unfolded conformation observed in molecular dynamics (MD) simulations of $[M + 13H]^{13+}$ in a solvent-free environment; L corresponds to a hypothetical fully linear conformation; N indicates the native state, as determined by X-ray crystallography and NMR; and A refers to the unfolded state observed only under acidic conditions with high methanol concentrations.[123] The unbolded letters *N* and *C* denote the N- and C-termini of each structure, respectively, with all structures oriented such that the N-terminus is on the left and the C-terminus on the right.[114] Reproduced with permission from reference [114].

Ion mobility spectra as a function of charge state (z) are shown in Figure 25 for various m/z-selected ubiquitin ions, $[M ± zH]^{±z}$. The primary features of the arrival time distributions (*ATD*s) appear across all spectra between 40 and 100 ms. However, as seen in Figure 25, the drift times are normalized by helium pressure, drift voltage, and ion charge (z). As a result, the drift time becomes directly proportional to the collision cross section[124,125] and is reported in units of $Å^2$.

Highly charged ubiquitin ions (z = 10–13) produce one or two pronounced peaks in the 1700–2000 $Å^2$ range. In contrast, lower charge state ions (z = ±6, ±7, and ±8) display sharp peaks centered around 1000 $Å^2$ (refer to Figure 25). Intermediate charge states (z = 8–11) exhibit broad peaks in the 1300–1700 $Å^2$ range, indicating the presence of multiple unresolved conformers. These charge state dependent trends are consistently observed across all solution conditions used in this study.
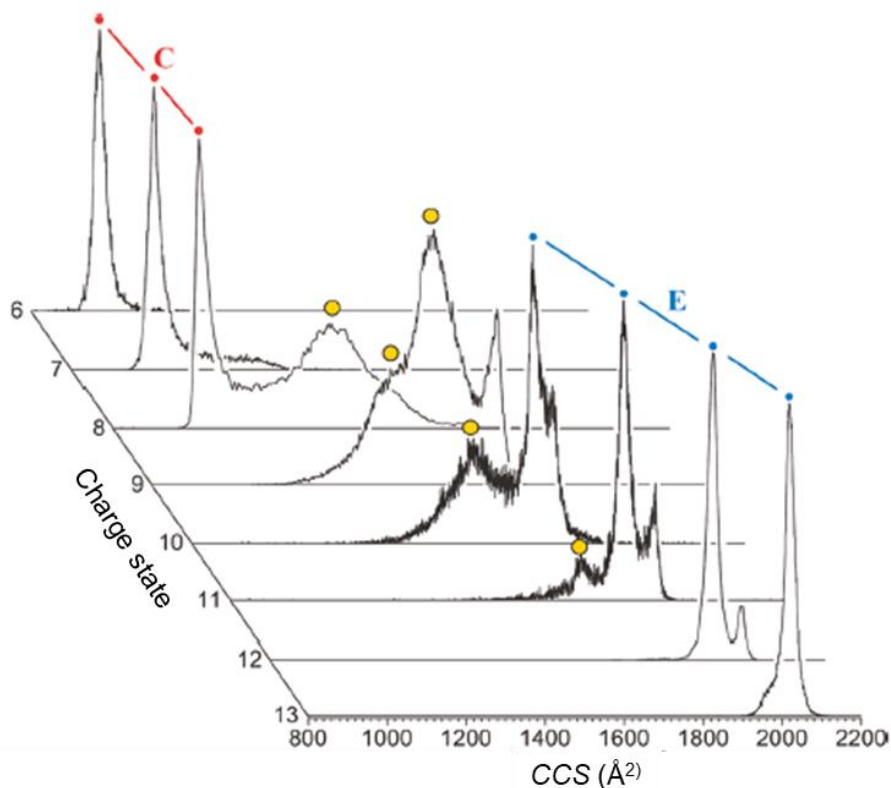
Figure 25. Charge state dependent ion mobility spectra of mass-selected, positively charged ubiquitin ions are shown. In each case, the drift times (x-axis) are normalized by ion charge, helium pressure, and drift voltage, making them directly proportional to the collision cross sections, which are reported in units of $Å^2$. This normalization enables direct comparison of spectral features across different charge states.[114] Reproduced with permission from reference [114].

All spectra display ion drift times between 40 and 100 ms. A set of strong peaks, labeled family C (highlighted in red), appears at approximately 1000 $Å^2$ and corresponds to ions with charge states of +6 to +8. For charge states of +10 and higher, a second set of intense, sharp peaks labeled E (highlighted in blue) is observed in the 1600–2000 $Å^2$ range. Broad features associated with intermediate charge states and cross sections are marked by a large yellow dot. The solvent conditions used for acquiring the spectra are as follows: pure water for z = +6 and +7, a 1:1 water–methanol mixture for z = +8 and +9, and 1% acetic acid in a 1:1 water–methanol mixture for z = +10 to +13.

In the IM-MS experiment, the experimental collision cross section (CCS_{exp}) was compared to the dimensions of known ubiquitin structures. A collision cross section of 1150 $Å^2$ in helium corresponds to the native structure (N) depicted in Figure 24 (protein data bank

(PDB) ID: 1D3Z, geometry #1).[117] However, upon solvent removal, this structure does not correspond to a minimum on the potential energy surface. By optimizing the geometry in vacuum using the Assisted Model Building and Energy Refinement (AMBER) force field,[126] a 10% reduction in cross section (to 1010 Å^2) is achieved, without disrupting the secondary and tertiary structure, as shown in Figure 24. This compaction in the $z = 0$ geometry arises solely from side-chain rearrangement and annealing of unstructured C-terminal residues after solvent removal.

According to AMBER simulations, the addition of 6, 7, or 8 positive charges to this $z = 0$ structure results in an increase in CCS of approximately 5%, yielding values in the range of 1050–1070 Å^2, while still preserving the native-like secondary and tertiary structures. In contrast, the collision cross section of the unfolded A state, following solvent removal and annealing is significantly larger, approximately 1690 Å^2, indicating a much less compact conformation than the native form (refer to Figure 24).[123]

Research Problem and Thesis Overview

Even though the use of metallo-folded SCNPs as nanoreactors is still in its infancy,[12,13] major challenges in the field have already been identified. First, most SCNPs are synthesized via polymerization of co-monomers and ligand-grafted co-monomers, resulting in complex samples containing many chains varying by composition, position of ligands, and chain length. Depending on their chemical architecture and cross-linked network, it can be envisioned that SCNPs will collapse into many different 3-dimensional arrangements, exhibiting different catalytic activities. Polydisperse SCNPs are therefore characterized by a distribution at two levels, *i.e.*, chain composition and compactness, clearly limiting the analogy between SCNPs and enzymes. To effectively mimic enzymes and avoid the high versatility of structures, the synthesis of monodisperse sequence-defined SCNPs with designed catalytic pockets is proposed as one of the next major steps in the field.[13]

As outlined in recent reviews, the structural characterization of SCNPs remains challenging.[127–129] The goal of the current thesis is to investigate whether ion mobility–mass spectrometry (IM-MS), coupled with molecular dynamics (MD) simulations is an effective technique for the characterization of single-chain polymeric nanoparticle (SCNP) precursor (or parent) polymers. Traditionally, SCNPs and their precursor polymers are characterized by using conventional techniques such as nuclear magnetic resonance (NMR) spectroscopy, dynamic light scattering (DLS), and size-exclusion chromatography (SEC). Solution-phase characterization methods only provide averaged data over the entire sample and do not allow to examine the structural features of individual chains. A mass spectrometry (MS) approach would solve these issues by enabling the analysis of isolated species in the gas phase. More recently, our group has also explored the use of electrospray ionization mass spectrometry (ESI-MS) for SCNP characterization.[130] However, to date, the application of IM-MS to SCNP and parent polymer analysis has not been reported.

Our group developed a visible-light-induced, photo-switchable single-chain polymeric nanoparticles (SCNPs). The design of these SCNPs is based on azobenzene cross-linkers incorporated into a polystyrene backbone bearing pendent phosphine and hydroxy

functionalities (refer to Scheme 1). The resulting system is of particular significance due to its potentially remote light control catalytic nature, exhibiting high catalytic activity in the intramolecular hydroamination of an alkyne with an amine. Importantly, the catalytic performance of these SCNPs is envisaged to be remotely regulated by light, wherein morphological changes within the SCNP internal architecture govern accessibility to the active sites.
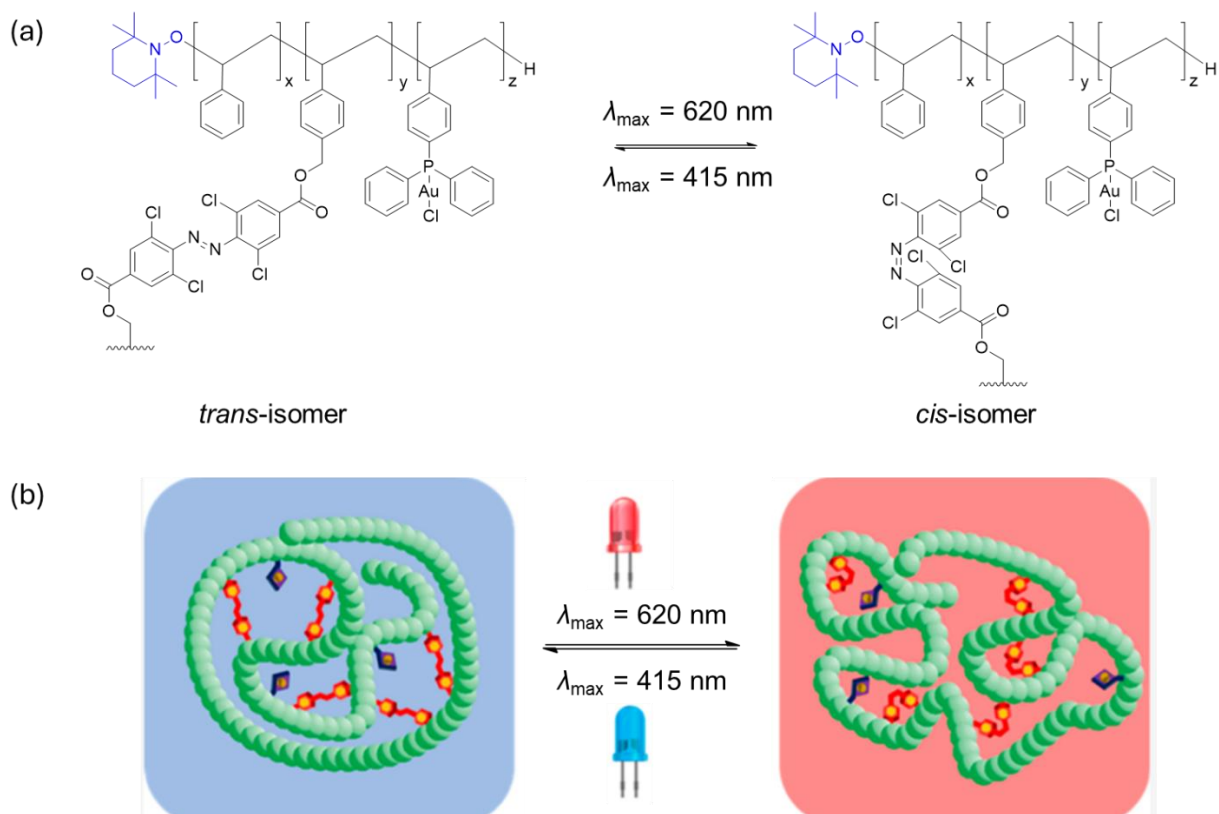
Scheme 1. Light induced catalytically active SCNPs: (a) chemical structure of the SCNPs and (b) morphological compaction of the SCNPs due to light induced *cis-trans* isomerization of the azobenzene unit.[131] Reproduced with permission from reference [131].

SCNPs are complex systems, and therefore it was initially very challenging to apply IM-MS directly to them. As a result, the current PhD thesis does not investigate SCNPs themselves, but rather SCNP precursor polymers. Specifically, a bottom-up approach was adopted, investigating precursor polymer systems of increasing complexity. Our SCNP precursors are primarily based on polystyrene – as are the SCNPs shown in Scheme 1 – and the investigation thus began with polystyrene polymers bearing different end groups, specifically a 2,2,6,6-tetramethylpiperidine-N-oxyl (TEMPO)-terminated polystyrene

(TEMPO-PS) and *sec*-butyl-terminated polystyrene (BU-PS) (refer to Scheme 2). This strategy helps to unravel the complexity of the precursor polymers and provides valuable insights (folding process, position of the functional group and charged center) that contribute to a deeper understanding of SCNPs.

Following the very promising results from the initial study of polystyrene polymers, the approach was applied to more complex pre-polymer systems that precede the SCNPs shown in Scheme 1, including copolymers of styrene (STY) and STY-CH_2-OH monomers, and eventually to the full SCNP precursor polymers that were ultimately transformed into SCNPs. The precursors were composed of various monomers, such as STY, STY-CH_2-OH, STY-PPh_2 and AuCl attached STY-PPh_2 (refer to Scheme 2), featuring a wide range of degrees of polymerization (*DP*) and compositions. The study clearly demonstrates that IM-MS, coupled with MD simulations, is a powerful technique for characterizing SCNP precursors. It also provides in-depth insight into the chain collapse process of the precursor SCNPs.[131]
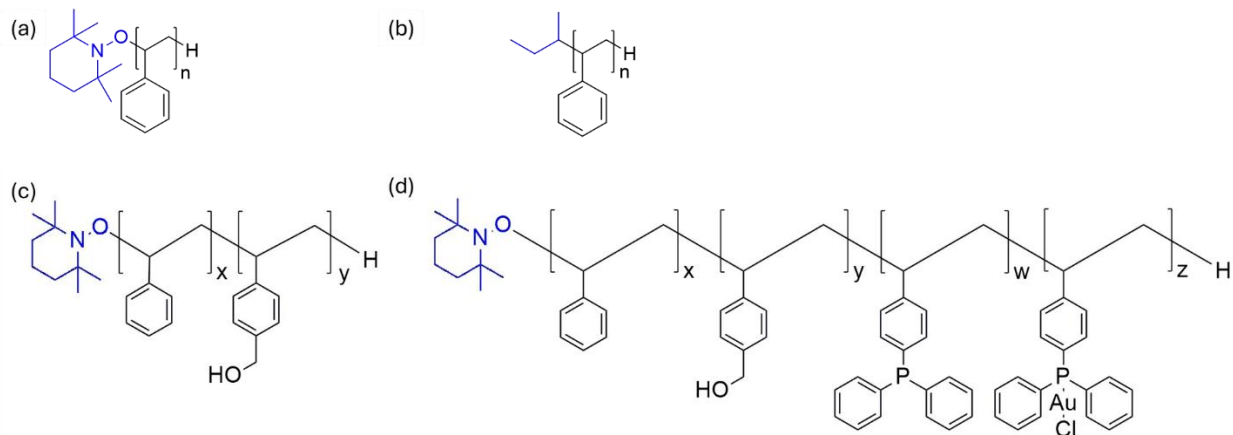
Scheme 2. Chemical structures of the precursor polymers: (a) TEMPO-(styrene)$_x$, (b) BU-(styrene)$_x$, (c) TEMPO-(styrene)$_x$-(styrene-CH_2-OH)$_y$ and (d) TEMPO-(styrene)$_x$-(styrene-CH_2-OH)$_y$-(styrene-PPh_2)$_w$-(styrene-PPh_2-AuCl)$_z$. Here, TEMPO refers to the 2,2,6,6-tetramethylpiperidine-N-oxyl end group[124,125] and BU refers to the *sec*-butyl end group.

After the successful application of ion mobility–mass spectrometry (IM-MS) and molecular dynamics (MD) simulations to SCNP precursors containing metal ions, the methodology was further extended to a different class of SCNPs generated via photochemical

reactions, namely photochemically-compacted SCNPs. Specifically, IM-MS and MD simulations were employed to investigate the folding process as well as the separation of stereoisomers arising from [2+2] cycloadditions of a trifunctional photoactive ene (TPE) molecules (refer to Scheme 3).[132] This task proved to be extremely challenging, as the resulting coexisting stereoisomers were very similar in size (refer to Scheme 3), making their separation difficult. The ion mobility resolution of the employed Waters Synapt G2-*Si* mass spectrometer was insufficient to distinguish these isomers. Therefore, the investigation employed cyclic ion mobility spectrometry (cyclic-IMS). Following the cyclic-IMS experiments, a large number of density functional theory (DFT) calculations were performed alongside MD simulations. Ultimately, the dominant stereoisomer was successfully identified using a combination of IM-MS, cyclic-IMS, DFT, and MD simulations. The separation of stereoisomers also provides insight into the molecular folding that occurs during the intramolecular [2+2] photocycloaddition reaction. This reaction drives the photochemical formation of SCNPs from TPE molecules, thereby offering a deeper understanding of the SCNP folding process.
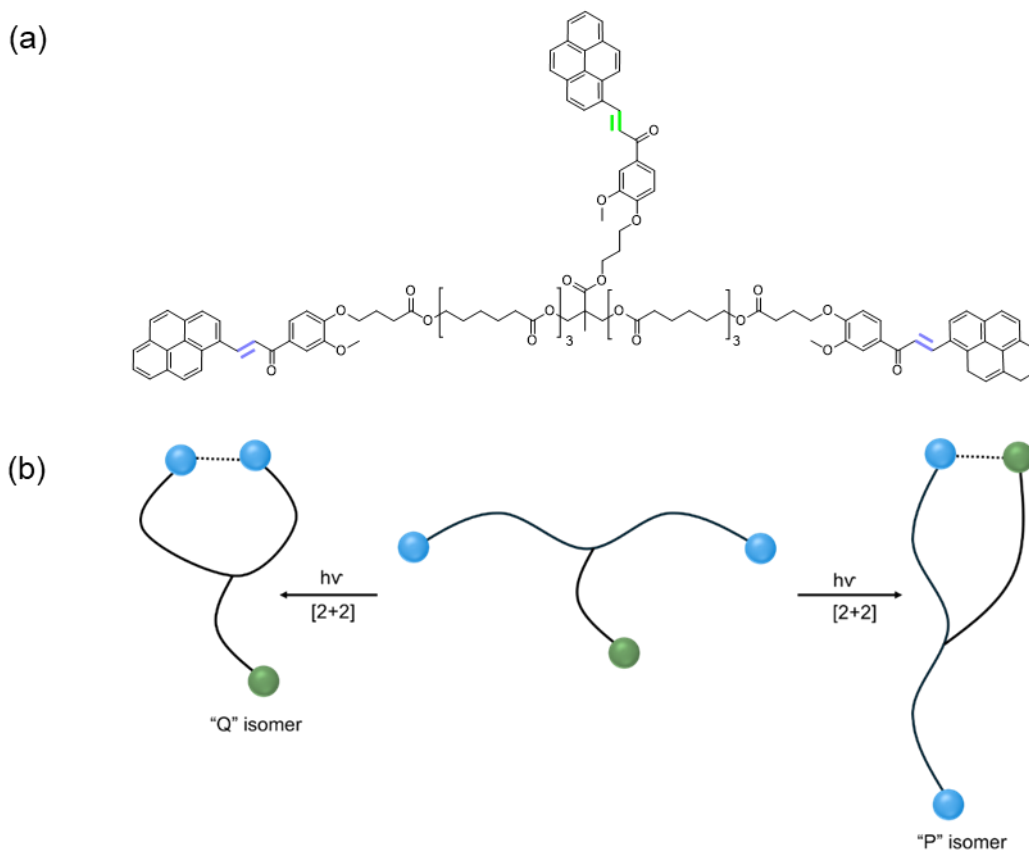
Scheme 3. Structure of the investigated trifunctional photoactive ene (TPE): (a) chemical structure of the trifunctional photoactive ene molecule; (b) graphical representation of the two distinct isomers formed from the trifunctional photoactive ene as a result of the [2+2] photocycloaddition reaction.[132]

The current PhD thesis thus opens a new chapter in the characterization of single-chain polymeric nanoparticle (SCNP) precursor polymers (parent polymers) by employing ion mobility spectrometry–mass spectrometry (IMS-MS) and molecular modelling. We investigated the three-dimensional structure of the precursor SCNPs, the position of the charge centers, the location of metal ions, and the stability of different isomers to obtain detailed information about their structure prior to folding. In addition, the current PhD thesis applied the developed methodologies to a small molecule folding systems consisting of three photoreactive enes able to undergo a [2+2] cycloaddition.

Statement of Contribution of Co-Authors

The following is the suggested format for the required declaration provided at the start of any thesis chapter which includes a co-authored publication, whether published or unpublished. This is a requirement for all Theses by Publication; and for any Theses by Monograph where the relevant published papers are incorporated into the body of the thesis or comprise a chapter within the thesis.

The authors listed below have certified that:

1. *they meet the criteria for authorship and that they have participated in the conception, execution, or interpretation, of at least that part of the publication in their field of expertise;*
2. *they take public responsibility for their part of the publication, except for the responsible author who accepts overall responsibility for the publication;*
3. *there are no other authors of the publication according to these criteria;*
4. *potential conflicts of interest have been disclosed to (a) granting bodies, (b) the editor or publisher of journals or other publications, and (c) the head of the responsible academic unit, and*
5. *they agree to the use of the publication in the student's thesis and its publication on the* [QUT's ePrints site](#) *consistent with any limitations set by publisher requirements.*

In the case of this chapter:

Please state the publication title and date of publication or status: Polystyrene Chain Geometry Probed by Ion Mobility Mass Spectrometry and Molecular Dynamics Simulations

Published on 16 September 2024

Contributor	Statement of contribution*
Sarajit Naskar	Designed and conducted experiments, analyzed data, and wrote the manuscript
Co-first author's name (if applicable)	
Andrea Minoia	Supervised the project and guided the manuscript preparation
Quentin Duez	Guided the data analysis
Aidan Izuagbe	Synthesized one of the polymer (TEMPO-PS)
Julien De Winter	Guided the experimental analysis and data analysis
Stephen J. Blanksby	Supervised the project and guided the manuscript preparation
Christopher Barner-Kowollik	Supervised the project and guided the manuscript preparation
Jérôme Cornil	Supervised the project and guided the manuscript preparation
Pascal Gerbaux	Supervised the project and guided the manuscript preparation

Polystyrene Chain Geometry Probed by Ion Mobility Mass Spectrometry and Molecular Dynamics Simulations

Determining the structure and morphology of precursor polymers to SCNPs using ion mobility spectrometry (IMS) experiments is a critical aspect of the current PhD thesis. We intend here to introduce IMS-MS as an original and powerful method for tracking the structural morphology of precursor SCNPs. The current work thus investigates the precursor polymers of single-chain nanoparticle characterization with ion mobility–mass spectrometry (IM-MS) and molecular dynamics (MD) simulations, yielding valuable insights into polymer folding and nanostructure characterization.

The high sensitivity of mass spectrometry-based methods enables the monitoring of the collapse of precursor SCNPs in the presence of ions. IMS provides unprecedented insights into the structure and conformational changes of collapsed precursor SCNPs. Throughout the study, the influence of key instrumental parameters—such as solvent, ionization conditions, and temperature—was carefully evaluated to ensure the reliability and reproducibility of the results.

The starting polymer for the investigation in the current chapter – polystyrene (PS) – is a thermoplastic polymer commonly used in various applications due to its bulk properties. Designing functional polystyrenes with well-defined structures for targeted applications is of significant interest due to the rigid and apolar nature of the polymer chain, including for SCNPs. Progress is to date hindered by the limitations of current analytical methods in defining at the atomistic-level the folding of the polymer chain. The integration of ion mobility spectrometry and molecular dynamics simulations is highly beneficial in addressing these challenges. However, data on gas-phase polystyrene ions is rarely reported in the literature. We herein investigate the gas phase structure of polystyrene ions with different end groups to establish how the nature and the rigidity of the monomer unit affects the charge stabilization. We find that – in contrast to polar polymers in which the charges are located deep in the ionic globules – the charges in the PS ions are rather located at the periphery of the polymer backbone leading to singly and doubly charged PS ions adopting dense elliptic-shaped structures. Molecular dynamics (MD) simulations indicate that the folding of the PS rigid chain is controlled by phenyl ring interactions with the charge ultimately remaining excluded from the core of the globular ions, whereas the folding of polyether ions is initiated by the folding of the flexible polyether chain around typically a sodium ion that remains deeply enclosed in the core of the ions.

Introduction

Polystyrene is a thermoplastic polymer commonly used in various applications such as packaging, insulation, medical devices and electronics, due to its bulk properties such as transparency, low density, rigidity, low thermal conductivity, and low electrical conductivity.[133] Designing functional polystyrenes for targeted applications such as drug encapsulation,[134] cell targeting, and catalysis is of significant interest due to the rigid and apolar nature of the polymer chain. However, progress is hindered by the limitations of current analytical methods in defining the atomistic-level folding and intramolecular crosslinking of the polymer chain. The integration of ion mobility spectrometry (IMS) and molecular dynamics (MD) simulations is highly beneficial in addressing these challenges. However, data on gas-phase polystyrene ions is rarely reported in the literature. While mass spectrometry analyses of polystyrene samples have been conducted, often utilizing

Ag$^+$ to aid cationisation[135,136,137,138] the 3D structure(s) of the resulting ions are far less understood. Bowers and co-workers[139] were one of the few groups to explore the 3D structure of polystyrene ions (with alkali and silver ions) using a combination of IMS-MS and molecular dynamics computations. Based on their investigation of oligomers ($DP <$ 7) across a range of cationization agents, they proposed a "V" shape for all ion types, including for silver cationized polymers, where the shape is induced by a cationic stacking of styrene moieties.[139]
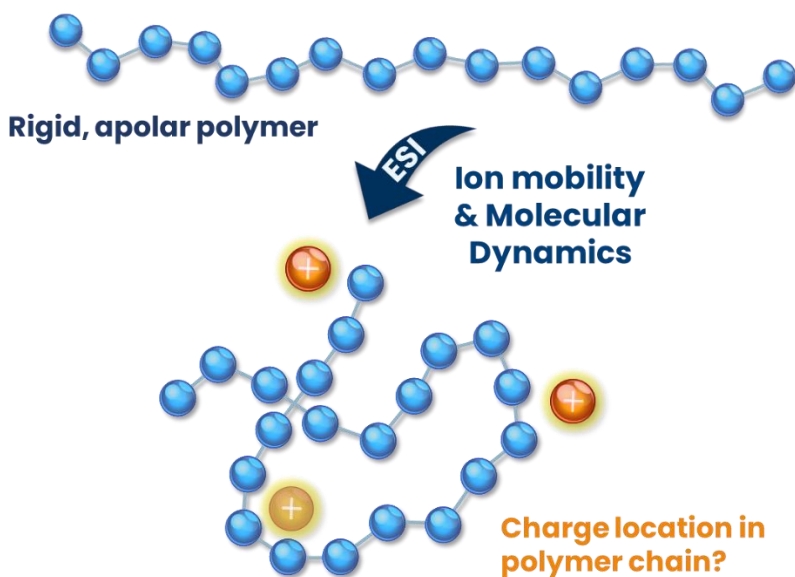
Scheme 1. Folding of polystyrene (PS) chains upon Electrospray Ionization : the primary objective of this joint experimental and theoretical investigation is to decipher at the atomistic-level the internal structure of gaseous PS ions.

Herein, as depicted in Scheme 2, we critically extend these investigations to much larger polystyrenes and to higher charge states using the unique combination between IMS-MS and MD, with particular emphasis on the impact of the apolar and rigid nature of the polystyrene chain on the charge stabilization in the gas phase of the mass spectrometer.

The experimental and theoretical methodologies are described in the annexes.

Results and Discussion

Three polystyrene samples – refer to Scheme 2 – containing different end groups, namely TEMPO-PS (M_n = 3,400 g mol^{-1} and $Đ$ = 1.2), low molecular weight BU-PS, *i.e.* BU-PS$_{LM}$ (here LM is used to indicate low molecular weight, $Đ$ = 1.01 – M_n = 580 g mol^{-1}) and high

molecular weight BU-PS, *i.e.* BU-PS$_{HM}$ (here HM is used to indicate high molecular weight, Đ = 1.03 – M_n = 3,270 g mol^{-1}), have been selected to investigate the influence of the nature of the end group and the chain length on the gas phase structure of the PS ions. The selection of the polymer end-groups is motivated by the fact that the TEMPO residue is anticipated to participate in the charge localization by catching a proton unlike the butyl residue. Synthesized TEMPO-PS polymer has been fully characterized using NMR and SEC (refer to Figure 1). The synthesis and initial characterization was conducted by Dr. Aiden Izuagbe from our team.
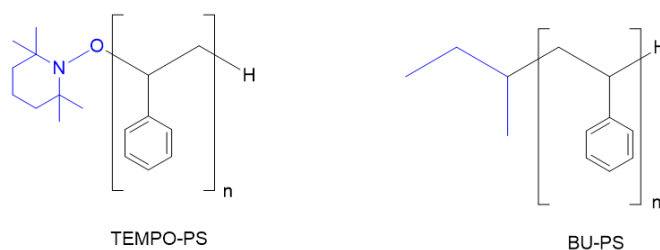
TEMPO-PS   BU-PS

Scheme 2. Chemical structures of the polystyrene samples used in the present investigation, TEMPO-PS : (M_n = 3,400 g mol^{-1} and Đ = 1.2) and BU-PS$_{LM/HM}$ (M_n = 580 g mol^{-1} and Đ = 1.01 and M_n = 3,270 g mol^{-1} and Đ = 1.03).
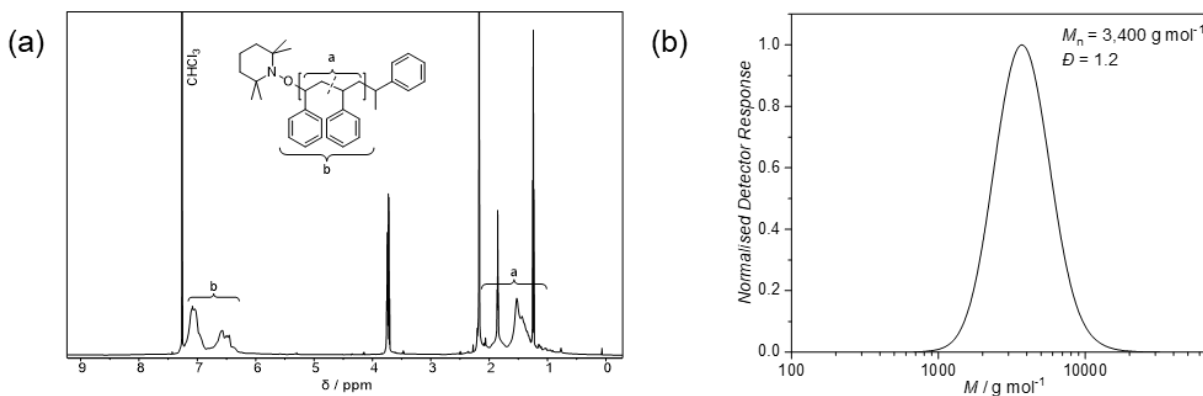
Figure 1. TEMPO-PS characterization : (a) ^{1}H NMR spectrum (600 MHz, CDCl$_3$); (b) SEC elugram (THF/PS calibration standards).

^{1}H-NMR Spectroscopy was used to characterize the TEMPO-PS polymer (refer to Figure 1). Characteristic resonances between (δ = 7.21 – 6.21 ppm) are attributed to the aromatic hydrogen atoms of the styryl group. Resonances between (δ = 2.36 – 0.82 ppm) are assigned to the aliphatic hydrogen atoms of the polymer backbone. The number average molecular weight of the polystyrene polymer was determined using Size

Exclusion Chromatography (SEC) and found to be 3,400 g mol^{-1} with a low dispersity of 1.2.[131]

MALDI-ToF is a widely used and valuable technique for polymer characterization. Therefore, in the initial stage of this study, a polystyrene sample was analyzed using MALDI-ToF. This investigation confirmed the successful synthesis of the polymer and provided information about its molecular weight. The synthesized TEMPO-PS polymer was characterized using MALDI-ToF experiments with two different matrices (refer to Figure 2). Mass spectrometry experiments on TEMPO-PS involved cationization and protonation events depending on the experimental conditions. DCTB and DHB matrices,[140,141] together with AgNO$_3$ as the cationization agent,[142] allow characterizing TEMPO-PS by MALDI-ToF. AgNO$_3$ was used as the cationization agent in the presence of DCTB matrix (refer to Figure 2). In this case, intact polymer ions were not identified as the labile TEMPO end group was dissociated creating two different ions, $[\text{H-(styrene)}_{n-1}\text{-CH=CH-C}_6\text{H}_5 + \text{Ag}]^+$ and $[\text{H-(styrene)}_{n-2}\text{-CH}_2\text{C(C}_6\text{H}_5)\text{=CH}_2 + \text{Ag}]^+$ (refer to Table 1).[143] The $[\text{H-(styrene)}_{n-1}\text{-CH=CH-C}_6\text{H}_5 + \text{Ag}]^+$ and $[\text{H-(styrene)}_{n-2}\text{-CH}_2\text{C(C}_6\text{H}_5)\text{=CH}_2 + \text{Ag}]^+$ ions were produced by the irreversible fragmentation of the alkoxyamine bond via beta hydrogen elimination and the dissociation of the TEMPO-PS, respectively.
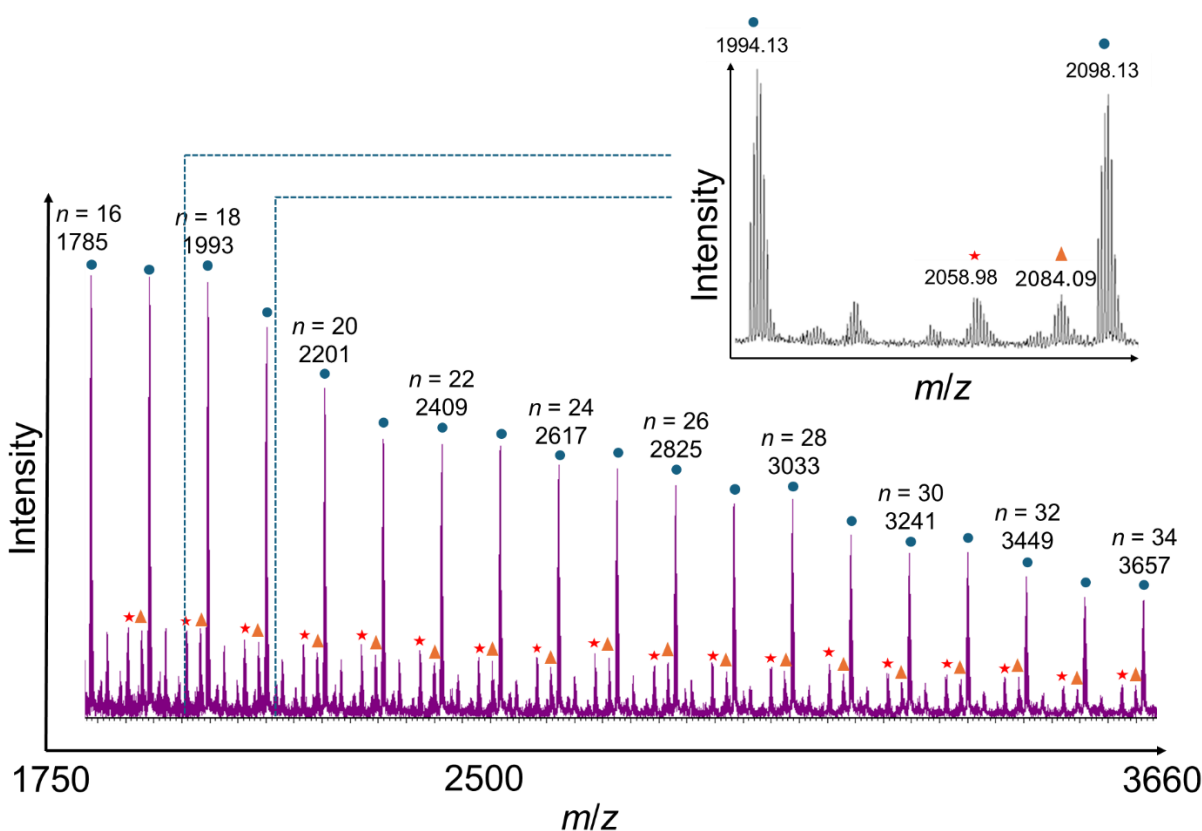
Figure 2. MALDI analysis of TEMPO-PS (0.1 mg mL^{-1}) in tetrahydrofuran/acetonitrile (1 : 9) using DCTB as the matrix and AgNO$_3$ (0.4 mg mL^{-1}) as the cationizing agent. Blue circles correspond to [H-(styrene)$_{n-2}$-CH$_2$C(C$_6$H$_5$)=CH$_2$, Ag]$^+$ ions, orange triangles are used to label [H-(styrene)$_{n-1}$-CH=CH-C$_6$H$_5$, Ag]$^+$ ions, and red stars correspond to [H-(styrene)$_{n-2}$-CH$_2$C(C$_6$H$_5$)=CH$_2$, Ag]$^+$ AgNO$_3$ ions.

Table 1. Possible structures of the different ions of TEMPO-PS (0.1 mg mL^{-1}) in tetrahydrofuran/acetonitrile (1 : 9), identified by MALDI analysis with DCTB matrix and AgNO$_3$ (0.4 mg mL^{-1}) as the cationization agent

Ion structure		n	Monoisotopic peak (m/z)
[H-(styrene)$_{n-2}$-CH$_2$C(C$_6$H$_5$)=CH$_2$, Ag]$^+$	●	17	2098.13
[H-(styrene)$_{n-1}$-CH=CH-C$_6$H$_5$, Ag]$^+$	▲	19	2084.09
[H-(styrene)$_{n-2}$-CH$_2$C(C$_6$H$_5$)=CH$_2$, Ag]$^+$. AgNO$_3$	★	19	2162.98

During the MALDI-ToF experiment, TEMPO-PS underwent dissociation in the presence of the DCTB matrix and AgNO$_3$ as the ionization agent. As a result, intact TEMPO-PS ions were not detected. Subsequently, TEMPO-PS was analyzed using DHB as the matrix. No cationization agent was required in the case of the DHB matrix as DHB matrix

has sufficient acidity to promote the protonation of the nitrogen atom of the TEMPO end group. In this case, intact polymer ions, *i.e.* ([H-(styrene)$_n$-TEMPO + H]$^+$, were identified by MALDI-ToF (refer to Figure 3).
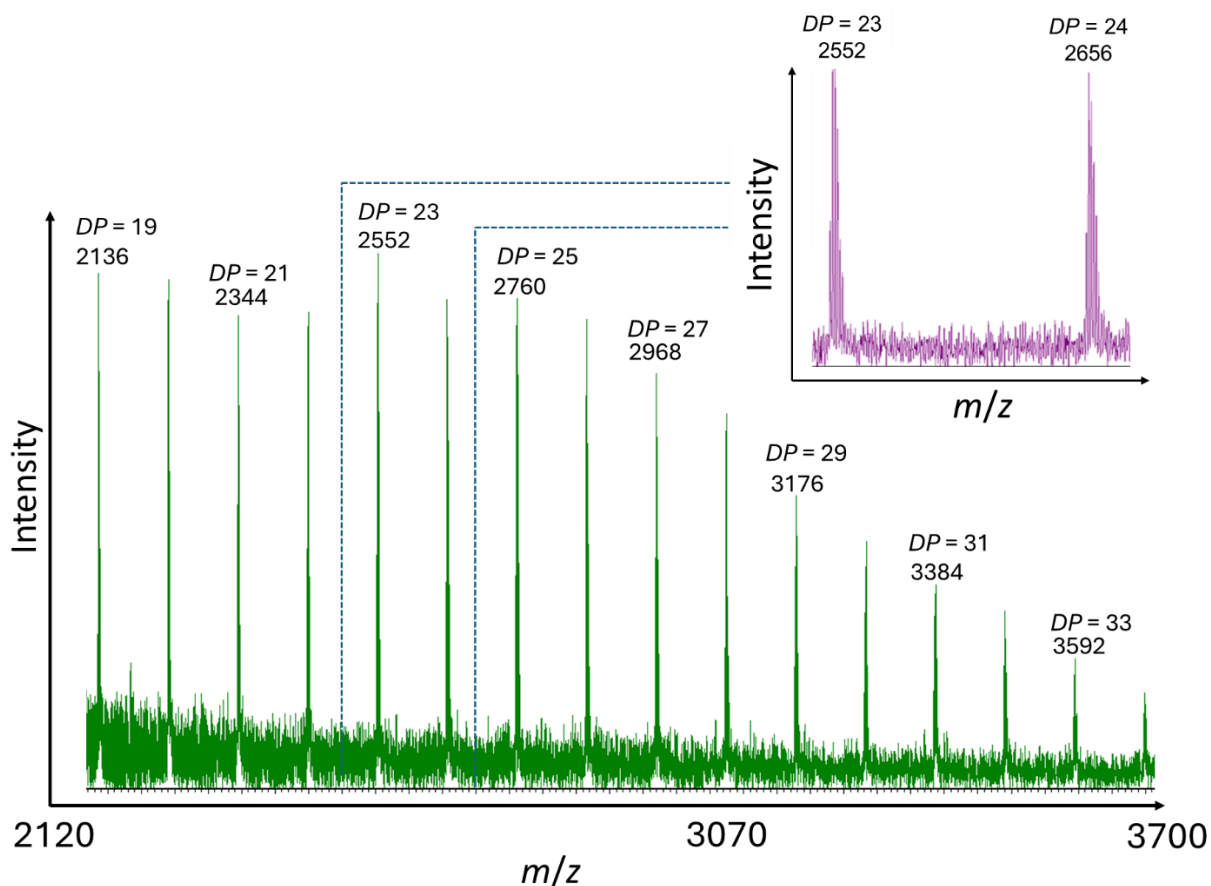
Figure 3. MALDI analysis of TEMPO-PS (0.1 mg mL^{-1} in tetrahydrofuran) using DHB matrix and without any cationizing agent, singly charged intact polymer ions (*DP* = 19-34) are identified without any fragmentation.

In the case of TEMPO-PS, the TEMPO end group is polar, containing both nitrogen and oxygen atoms. These heteroatoms facilitate protonation during the ionization process, thereby aiding the formation of polymer ions. Thus, the end group plays a critical role in the ionization of the polymer. To investigate the effect of the end group, a polystyrene sample with a non-polar end group was selected. For this purpose, a commercially available polystyrene with a *sec*-butyl end group (BU-PS) was used.

In addition to the nature of the end group, molecular weight also influences the ionization behavior and charge state of the polymer. Therefore, BU-PS samples with two different

molecular weights were selected for this investigation (refer to Table 2). The commercially available high molecular weight BU-PS (denoted as BU-PS$_{HM}$) formed singly charged ions during MALDI-ToF experiments in the presence of AgNO$_3$ as the ionizing agent and DCTB as the matrix. In this case, the polymer ions formed due to coordination of the polymer chain with silver ions (refer to Figure 4). Molecular weight and dispersity of all these polymer samples are gathered in Table 2.

Table 2. Molecular weight and dispersity of the polystyrene samples (TEMPO-PS and BU-PS) used in the study, The BU-PS$_{LM/HM}$ polymers were supplied by Agilent Technologies, Diegem, Belgium. The molar mass and dispersity of the BU-PS polymer were provided by Agilent Technologies.

| Polymer	M_n (g mol^{-1})	Đ
TEMPO-PS	3,400 (SEC)	1.2 (SEC)
BU-PS$_{LM}$	580	1.01
BU-PS$_{HM}$	3.270	1.03
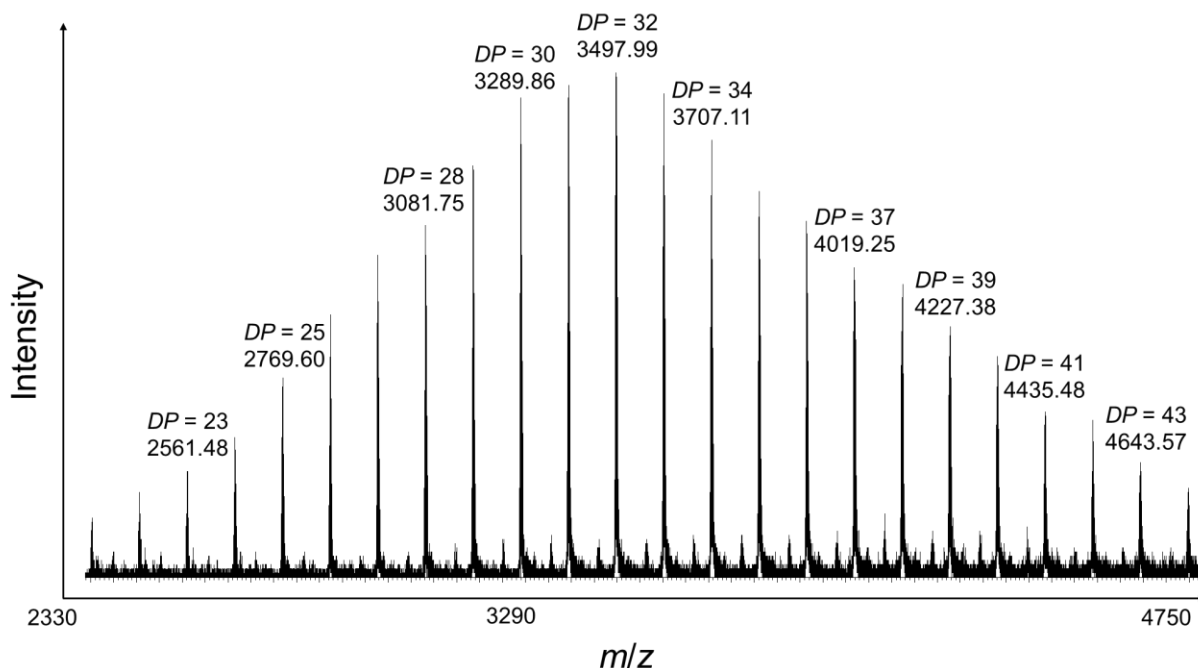
Figure 4. MALDI analysis of BU-PS$_{HM}$ (0.1 mg mL^{-1}) in tetrahydrofuran/acetonitrile (1 : 9) using DCTB as the matrix and AgNO$_3$ (0.4 mg mL^{-1}) as the cationizing agent. Singly charged intact polymer ions (*DP* = 21-44) are identified without any fragmentation.

After analyzing the high molecular weight BU-PS, the commercially available low molecular weight BU-PS (denoted as BU-PS$_{LM}$) was also analyzed using MALDI-ToF in the presence of DCTB as the matrix. The low molecular weight BU-PS was detected as singly charged ions during MALDI-ToF experiments with AgNO$_3$ as the ionizing agent. In this case, the polymer coordinates with one silver ion, resulting in singly charged species (refer to Figure 5).

While TEMPO-PS underwent dissociation under the same MALDI-ToF conditions (using DCTB matrix and AgNO$_3$), BU-PS produced intact polymer ions. This highlights the influence of the end group and molecular weight on the ionization behavior of polymers.
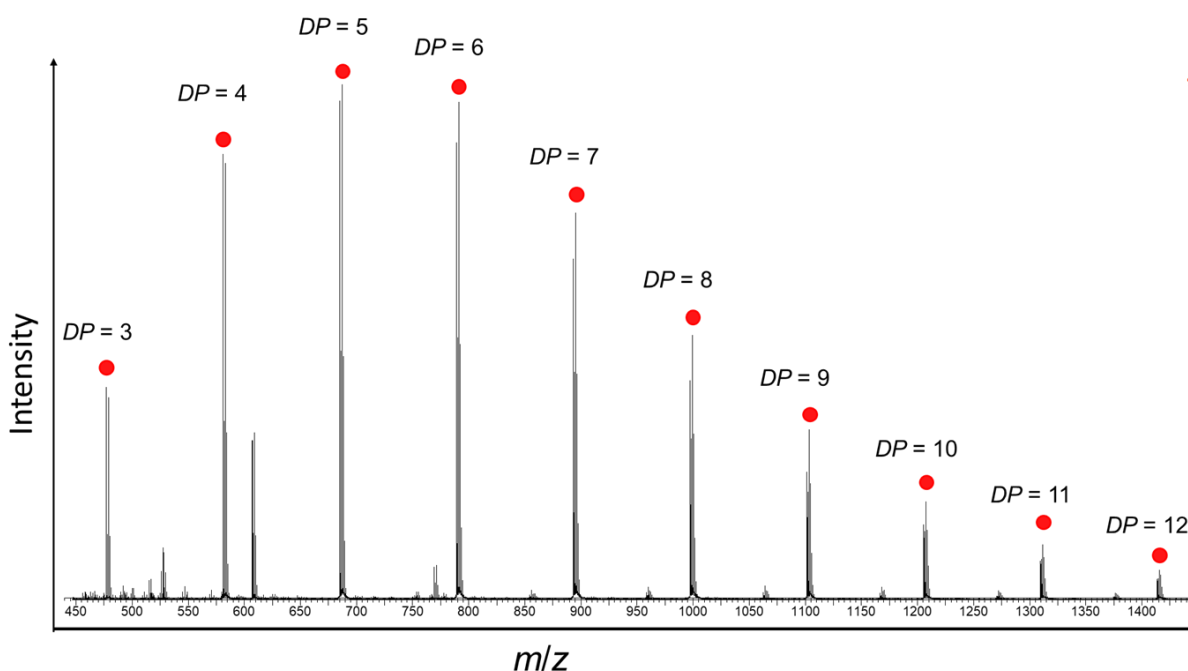
Figure 5. MALDI analysis of BU-PS$_{LM}$ (0.1 mg mL^{-1}) in tetrahydrofuran/acetonitrile (1 : 9) using DCTB as the matrix and AgNO$_3$ (0.4 mg mL^{-1}) as the cationizing agent. Singly charged intact polymer ions (*DP* = 3-12) were identified without any fragmentation.

The MALDI-ToF experiments on different polystyrene samples provided several important insights. The polarity of the end group plays a significant role in the ionization

process, and the nature of the polymer ions (*i.e.* whether they remained intact or fragmented) is influenced by the choice of matrix and ionization agent.

Both polymer samples were also analyzed using ESI-MS. Unlike MALDI-ToF, ESI is a soft ionization technique, thereby minimizing the risk of polymer ion fragmentation and enabling the detection of intact polymer ions.

1. ESI-MS analysis of PS

The polystyrene samples were thus analyzed using electrospray ionization mass spectrometry (ESI-MS) to assess their ionization behavior and establish a foundation for the subsequent IM-MS analysis. Polystyrene is best analyzed by mass spectrometry, either using MALDI or ESI, in the presence of Ag^+ ions because of favorable interactions between the π-electrons of the aromatic rings and the silver cations.[144] TEMPO-PS contains a polar TEMPO end group, which is prone to protonation during the ionization process. TEMPO-PS was analyzed under two different experimental conditions: *(i)* without any ionization agent and *(ii)* in the presence of $AgNO_3$ as an ionization agent. When analyzed without any ionization agent, the TEMPO end group was protonated during ionization, resulting in the formation of singly charged $[\text{TEMPO-PS} + \text{H}]^+$ ions (refer to Figure 6a). In contrast, in the presence of $AgNO_3$, TEMPO-PS produced two types of polymer ions: singly charged $[\text{TEMPO-PS} + \text{H}]^+$ and doubly charged $[\text{TEMPO-PS} + \text{H} + \text{Ag}]^{2+}$ (refer to Figure 6b).

Subsequently, high molecular weight BU-PS was also analyzed using ESI-MS. In this case, the end group is non-polar and cannot undergo protonation. However, in the presence of $AgNO_3$ as an ionization agent, doubly charged $[\text{BU-PS}_{HM} + 2\text{Ag}]^{2+}$ ions were detected (refer to Figure 6c).
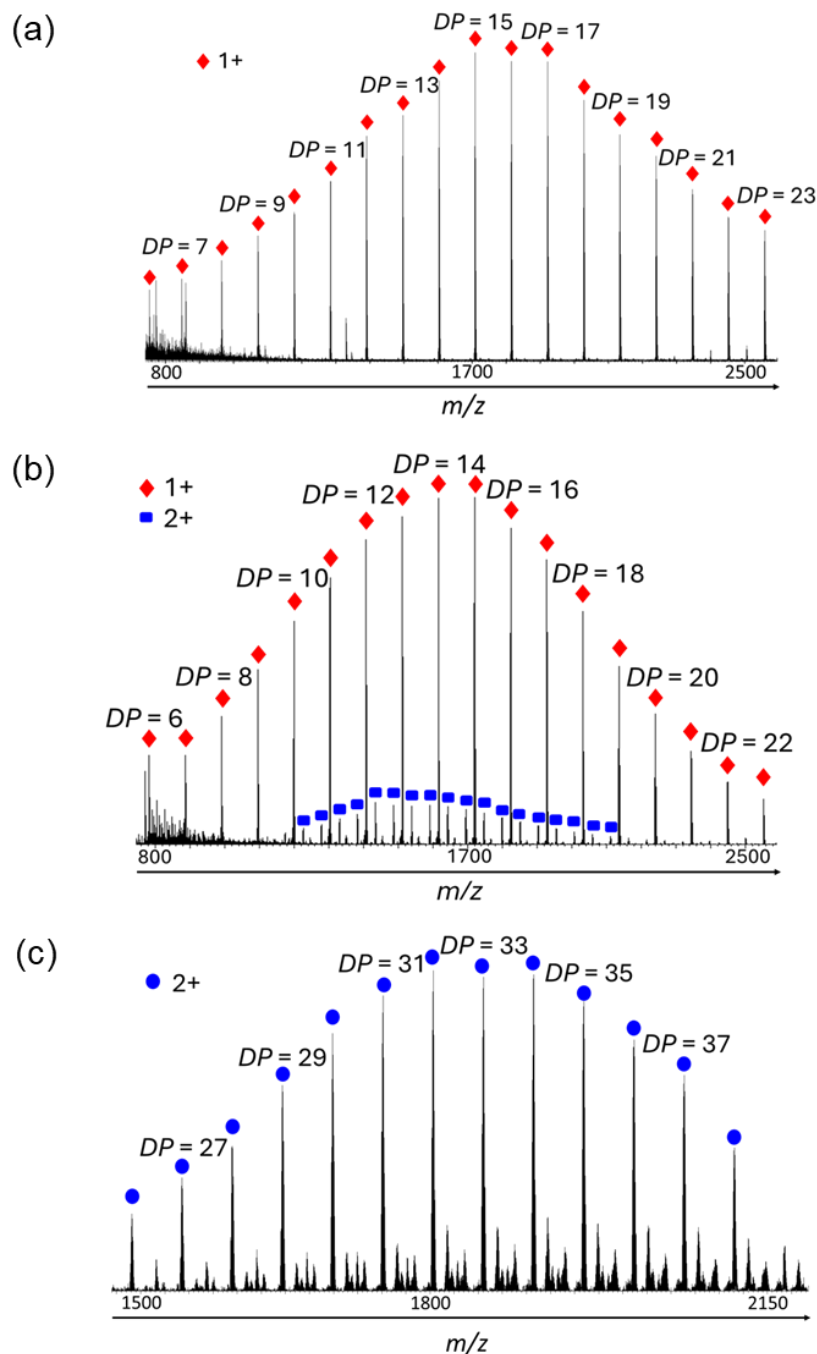
Figure 6. ESI-MS mass spectra of (a) TEMPO-PS (0.01 mg mL^{-1}) in acetonitrile/acetone 80/20 ,(b) TEMPO-PS (0.01 mg mL^{-1}) in acetonitrile/acetone 80/20 with AgNO$_3$ (0.0002 mg mL^{-1}) and (c) BU-PS$_{HM}$ (0.01 mg mL^{-1}) in 80/20 acetonitrile/acetone with AgNO$_3$ (0.0002 mg mL^{-1}). Red diamonds correspond to [TEMPO-PS + H]$^+$, blue squares represent the [TEMPO-PS + H + Ag]$^{2+}$ and blue circles correspond to [BU-PS$_{HM}$ + 2Ag]$^{2+}$ ions. The values reported on the top of the peaks correspond to the *DP* of the corresponding polymer ions.

Termination of the PS with the TEMPO group provides a basic site for protonation under positive ionization ESI conditions and thus enables localization of at least one charge and even facilitates ionization without the addition of a cationization agent. The TEMPO-PS ESI-ToF mass spectrum is presented in Figure 6a and features a symmetrical peak distribution centered at m/z 1823 (DP = 16), with the 104 u mass difference between two consecutive signals that is typical of singly charged (+1) PS ions. These ions are assigned to [TEMPO-PS + H]$^+$ ions based on the comparison between the isotope distribution with the theoretical one (refer to Figure 7). TEMPO-PS was further analyzed by ESI-ToF in presence of AgNO$_3$ as a source of Ag$^+$ cationization agent in Figure 6b and 7. Besides [TEMPO-PS + H]$^+$ ions, already detected in Figure 6a, 2+ ions are detected for DP = 21-44 and are clearly ascribed as [TEMPO-PS + H + Ag]$^{2+}$ ions (refer to Figure 7 for the isotopic distribution analysis).

BU-PS$_{LM/HM}$ was also subjected to ESI-ToF analysis in presence of AgNO$_3$ as the source of cationizing agent. As expected, no protonated BU-PS was detected due to the absence of proton binding site. Nevertheless, as seen in Figure 6c and Figure 8, abundant doubly and singly charged ions are detected and correspond to [BU-PS$_{HM}$ + 2Ag]$^{2+}$ and [BU-PS$_{LM}$ + Ag]$^+$ ions , respectively. Note here that BU-PS$_{LM}$ mostly contains chains with DP = 3-13, whereas BU-PS$_{HM}$ contains chains with DP = 26-38. Again, the ion charge states and the ion compositions for both the 1+ and 2+ Bu-PS$_{LM/HM}$ ions have been established based on the comparison between the experimental isotopic distributions and the simulated ones (refer to Figures 8 and 9).
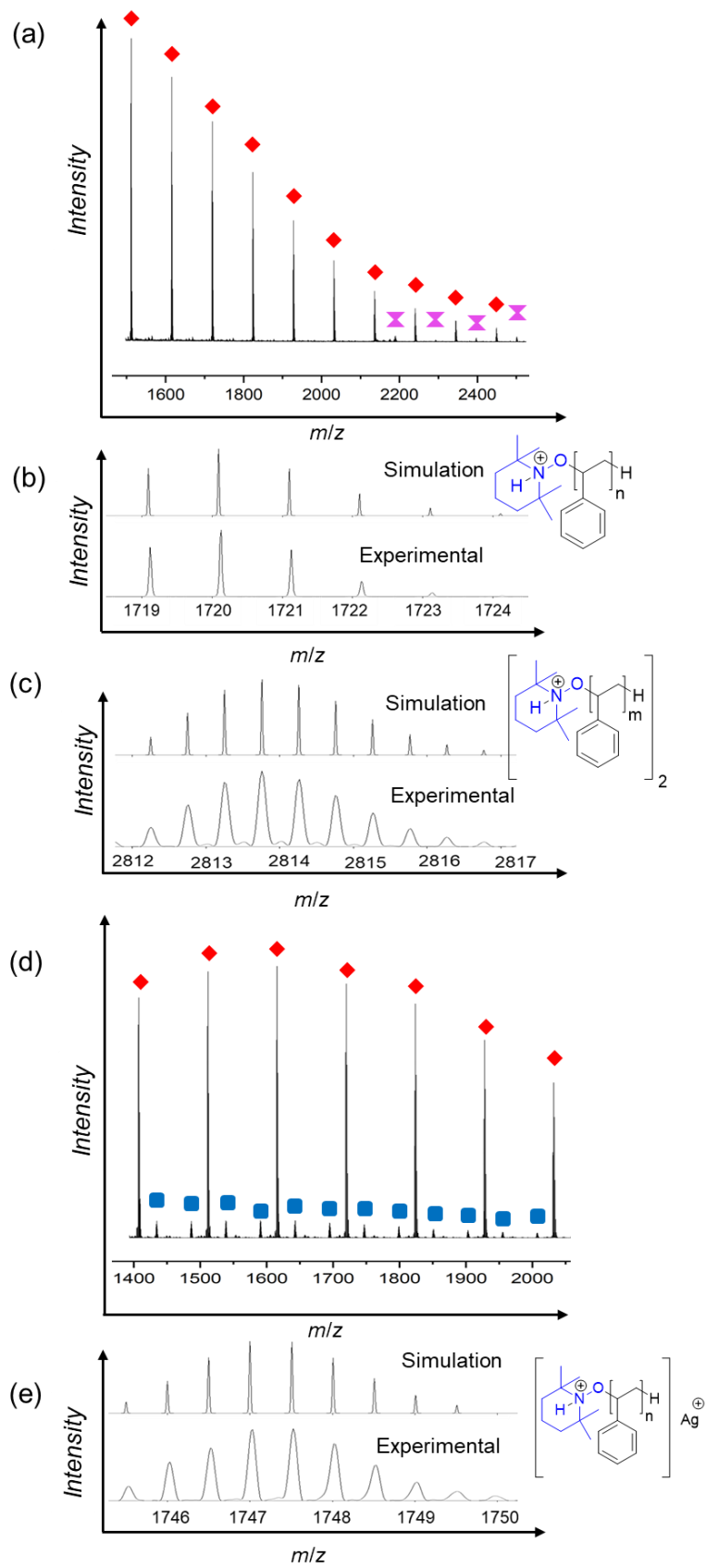
Figure 7. Electrospray analysis of TEMPO-PS (0.01 mg mL^{-1}) in acetonitrile/acetone 80/20 without (a-c) and with (d-e) cationizing (Ag$^+$) agent (0.0002 mg mL^{-1}): (a) and (d) present partial views of the ESI mass spectra highlighting the presence of [TEMPO-PS + H]$^+$ (red diamonds), [TEMPO-PS + H + Ag]$^{2+}$ (blue rectangles) ions and [2 TEMPO-PS + 2 H]$^{2+}$ adduct ions (pink diabolos). (b), (c) and (e) present the comparison between experimental and simulated isotope patterns for [TEMPO-PS + H]$^+$ (*DP* = 15), [2 TEMPO-PS + 2H]$^{2+}$ (*DP* = 51) ions and [TEMPO-PS + H + Ag]$^{2+}$ (*DP* = 31).

After the analysis of high molecular weight BU-PS, the low molecular weight BU-PS sample, referred to as BU-PS$_{LM}$, was also analyzed using ESI-MS. In the presence of AgNO$_3$ as the ionization agent, BU-PS$_{LM}$ produced only singly charged ions, [BU-PS$_{LM}$ + Ag]$^+$(refer to Figure 8a). Since the end group is non-polar, it did not lead to ion formation via protonation. Therefore, the polymer ions were generated through complexation of a single silver ion. The isotopic distribution of these ions—both experimental and simulated—match exactly (refer to Figure 8b).
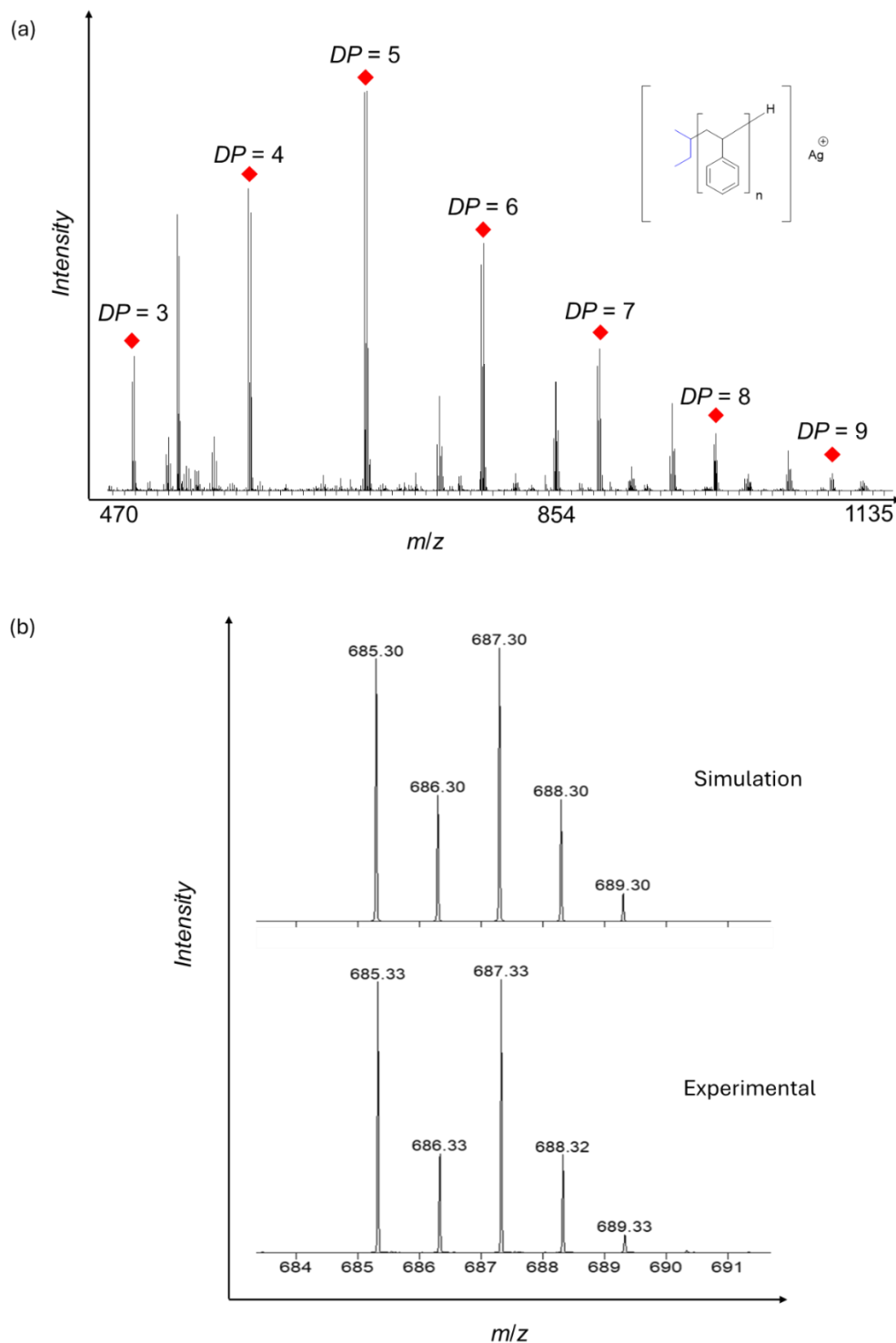
Figure 8. Electrospray analysis of BU-PS$_{LM}$ (MW = 580 g mol^{-1}, 0.01 mg mL^{-1} in acetonitrile/acetone: 80/20) with AgNO3 (0.0002 mg mL^{-1}) as a cationizing agent : (a) partial view of the ESI mass spectrum highlighting the presence of [BU-PS$_{LM}$ + Ag]$^+$ and (b) comparison between experimental and simulated isotope patterns for singly charged BU-PS$_{LM}$ ([BU-PS$_{LM}$ + Ag]$^+$, (DP = 5)).

After the identification of the polymer ions and their charge states, the isotopic distribution was analyzed and compared with the simulated spectrum to ensure that the identified ions corresponded to the correct polymer species. High molecular weight BU-PS generated doubly charged ions, [BU-PS$_{HM}$ + 2Ag]$^{2+}$. The isotopic distribution of these ions was also examined and compared with the simulated spectrum. The experimental spectrum matches perfectly with the simulated one, confirming that the identified ions are indeed the expected polymer ions (refer to Figure 9).
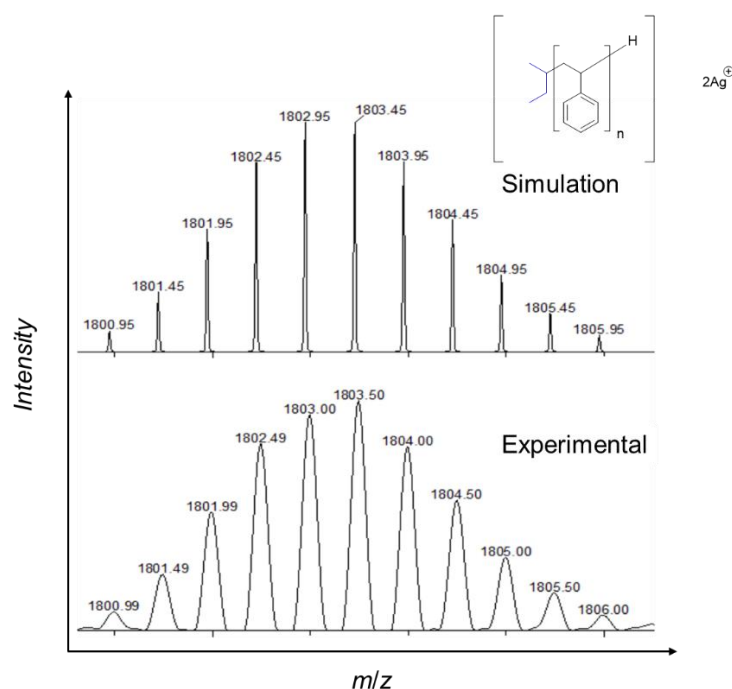
Figure 9. Electrospray analysis of BU-PS$_{HM}$ (0.01 mg mL^{-1} in acetonitrile/acetone: 80/20) with AgNO$_3$ (0.0002 mg mL^{-1}) as a cationizing agent : comparison between experimental and simulated isotope patterns for doubly charged BU-PS$_{HM}$ ([BU-PS$_{HM}$ + 2Ag]$^{2+}$, (*DP* = 32)).

2. IMS experiments on gaseous TEMPO-PS and BU-PS ions

After analyzing all polystyrene samples using ESI-ToF mass spectrometry, the investigation was extended to the advanced and highly promising technique of ion mobility–mass spectrometry (IM-MS), for polymer characterization. All PS ions, *i.e.*, [TEMPO-PS + H]$^+$, [TEMPO-PS + H + Ag]$^{2+}$, [BU-PS$_{LM}$ + Ag]$^+$ and [BU-PS$_{HM}$ + 2Ag]$^{2+}$ ions, have been subjected to ion mobility experiments to investigate the influence of the

nature of the end-group (TEMPO vs BU), of the chain length, of the charge state (1+ vs 2+), and of the cationizing agent (H^+ vs Ag^+) on the gas phase structure of the polymer ions.

The effects of the end group, chain length, charge state, and ionization agent have been investigated experimentally by *(i)* analyzing for all the ions the symmetry of the Arrival Time Distribution (*ATD*), *(ii)* determining the ion CCS_{exp}, and *(iii)* monitoring the CCS_{exp} evolution over the mass range (*DP* = 6-23 for [TEMPO-PS + H]$^+$, *DP* = 21-44 for [TEMPO-PS + H + Ag]$^{2+}$, *DP* = 3-13 for [BU-PS$_{LM}$ + Ag]$^+$ and *DP* = 26-38 for [BU-PS$_{HM}$ + 2Ag]$^{2+}$). Asymmetrical *ATD* would reveal the presence of non-interconverting gas phase structures,[102] whereas plotting the *CCS* evolution as a function of mass (*m/z*) – the so-called trend line analysis – enables *(i)* assessing the global 3D structure of the ions (sphere vs cylinder, for instance)[145,146] and *(ii)* detecting subtle modifications in the structure of macroions, typically the transition between extended and folded structures upon mass increase.[147] Charged polymer ions often adopt globular conformations in the gas phase, for which the evolution of *CCS* as a function of the mass is described by a power law, *i.e. CCS = A M^B* where *M* is the molecular weight, B is ~2/3 that of the characteristic value for a spherical evolution and A is related to the ion density.[146] Polymer ions with B ~ 2/3 are compact with the spherical structure being considered as the densest arrangement, while ions with B > 2/3 are increasingly extended, with a value of B ~1 characteristic of fully extended structures growing linearly with the number of monomer units (or the mass). Based on theoretical calculations, we recently demonstrated that extended objects such as helices have their B parameter tending to 1 as their mass (or length) tends to infinity, but at a different rate depending on the chemical nature of the side chains.[147,148]

Figures 10-13 contain the IMS data for [TEMPO-PS + H]$^+$, [TEMPO-PS + H + Ag]$^{2+}$, [BU-PS$_{LM}$ + Ag]$^+$ and [BU-PS$_{HM}$ + 2Ag]$^{2+}$ ions. As shown in Figures 11-13, sharp and symmetrical arrival time distributions (*ATD*) have been recorded for all the 1+ and 2+ ions, indicating the presence of unique ion structures or structures that are interconverting very fast over the sampled mass ranges, as also confirmed by the quasi constant *CCS* resolution (*R*~40, that is the instrument resolution[149]) for all the analyzed ions (refer to

Figure 14). For TEMPO-PS ions, the *CCS*/*Mass* evolutions for both the 1+ and 2+ ions are fitted by $CCS_{exp} = A\,M^B$, as shown in Figure 10a/b, with the B values determined at 0.69 and 0.70, respectively, indicating that the 3D structures cannot be considered as fully spherical (B = 2/3). Indeed, the B value is really sensitive to the 3D structure, implying that slight differences in the B value could indicate strong modifications in the structures.[145] For example, we recently determined a B value at 0.72 for helical anionic peptoid ions (*DP* = 3 – 15).[146]
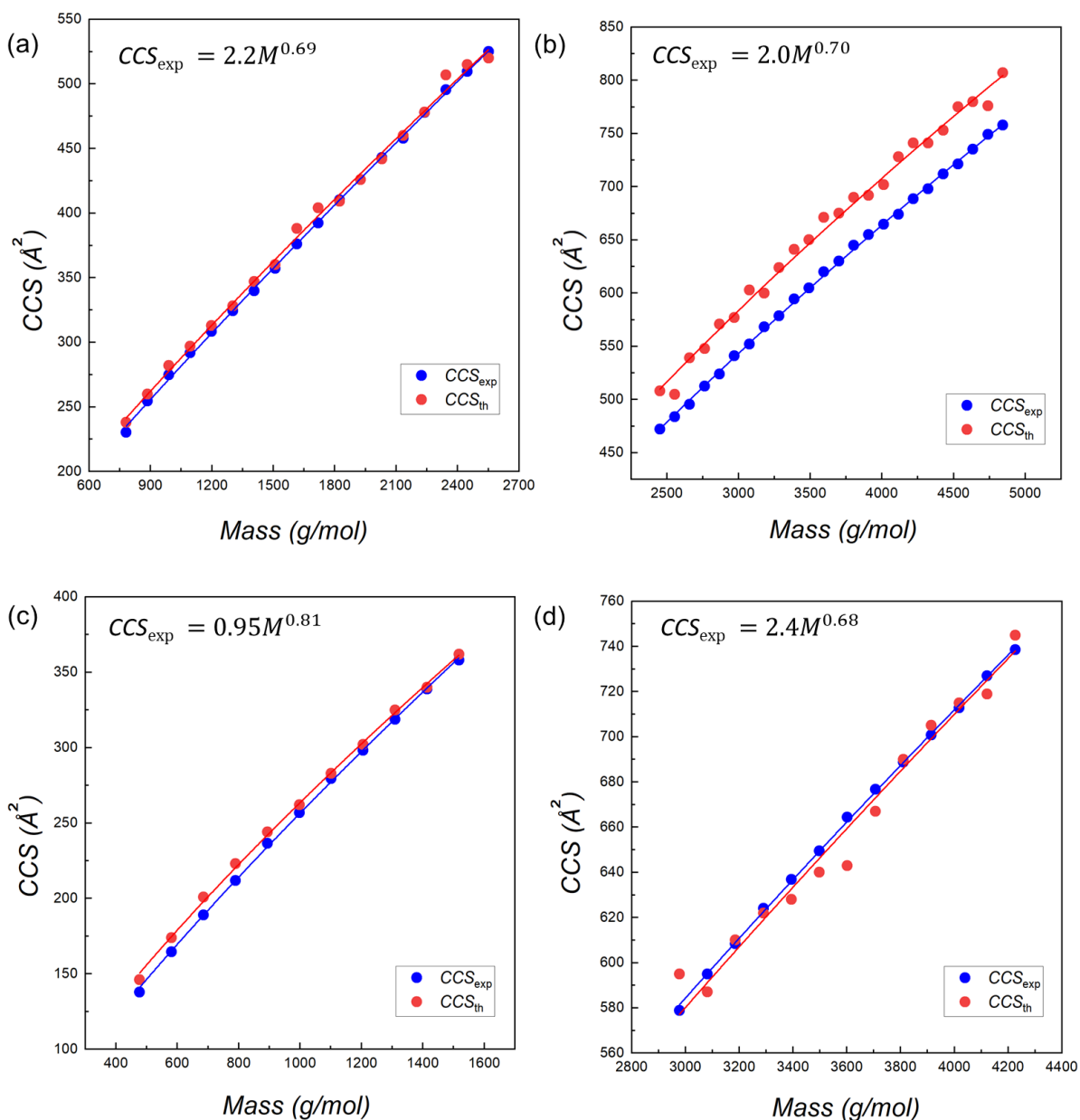
Figure 10. Ion mobility mass spectrometry analysis of TEMPO-PS and BU-PS$_{LM/HM}$: trend line analysis (*CCS* evolution with *mass*) of (a) [TEMPO-PS + H]$^+$, (b) [TEMPO-PS + H + Ag]$^{2+}$, (c) [BU-PS$_{LM}$ + Ag]$^+$ and (d) [BU-PS$_{HM}$ + 2Ag]$^{2+}$. The blue curves and the fitting equations correspond to the experimental *CCS* evolutions. The red curves correspond to the theoretical (MD) *CCS* evolutions.

Ion mobility spectrometry–mass spectrometry (IM-MS) measures the time required for ions to travel from the ion source to the detector through the mobility cell under the influence of an electric field. Within the mobility cell, ions are separated based on their mobility; therefore, different ions take different amounts of time to traverse the cell. By subtracting the time spent traveling from the analyzer to the detector from the total arrival time, the resulting value is referred to as the drift time. The collision cross section (*CCS*) is calculated from these drift times. The nature of the arrival time distribution (*ATD*) spectrum is highly informative, as it reveals whether a single ion species or multiple ion species are present within a given time frame. Here, the *ATD* spectra of polystyrene ions are shown for selected degrees of polymerization (refer to Figures 11, 12, and 13).
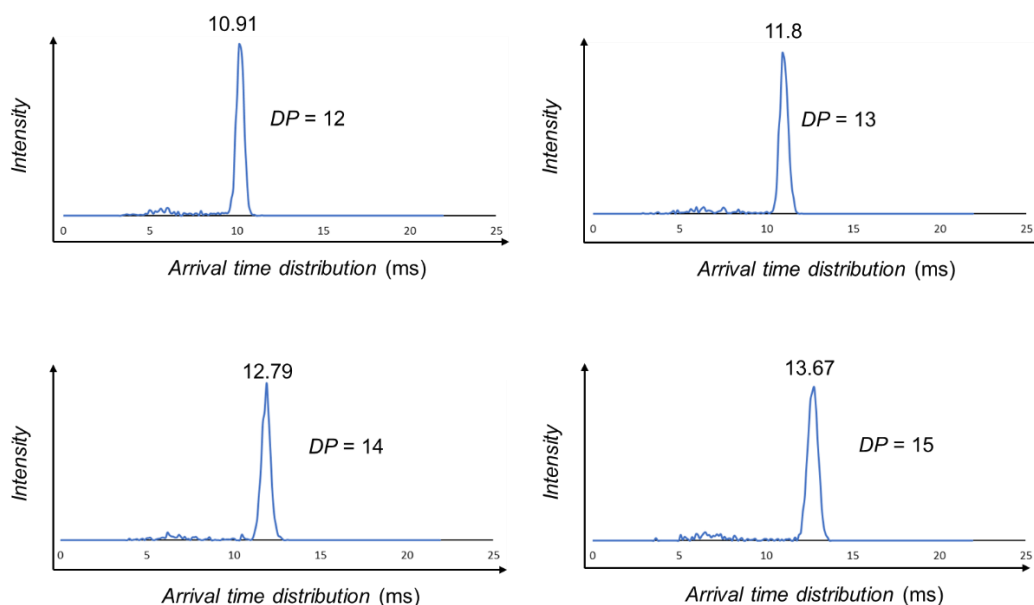
Figure 11. Ion mobility mass spectrometry analysis of 0.01 mg mL^{-1} in acetonitrile/acetone (80/20) TEMPO-PS (Waters Synapt G2-*Si* mass spectrometer) : arrival time distribution (*ATD*) of selected) [TEMPO-PS + H]$^+$ ions (*DP* = 12-15).
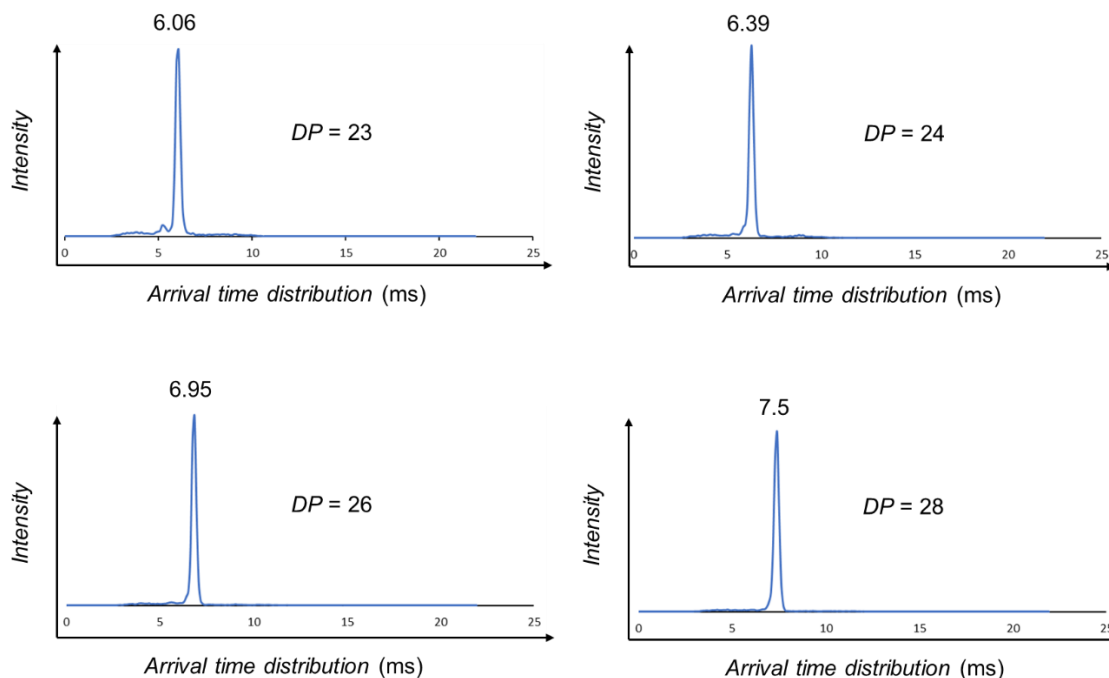
Figure 12. Ion mobility mass spectrometry analysis of 0.01 mg mL^{-1} in acetonitrile/acetone (80/20) TEMPO-PS with AgNO$_3$ (0.0002 mg mL^{-1}) as a cationizing agent (Waters Synapt G2-*Si* mass spectrometer) : arrival time distribution (*ATD*) of selected [TEMPO-PS + H + Ag]$^{2+}$ ions (DP = 23, 24, 26 and 28).
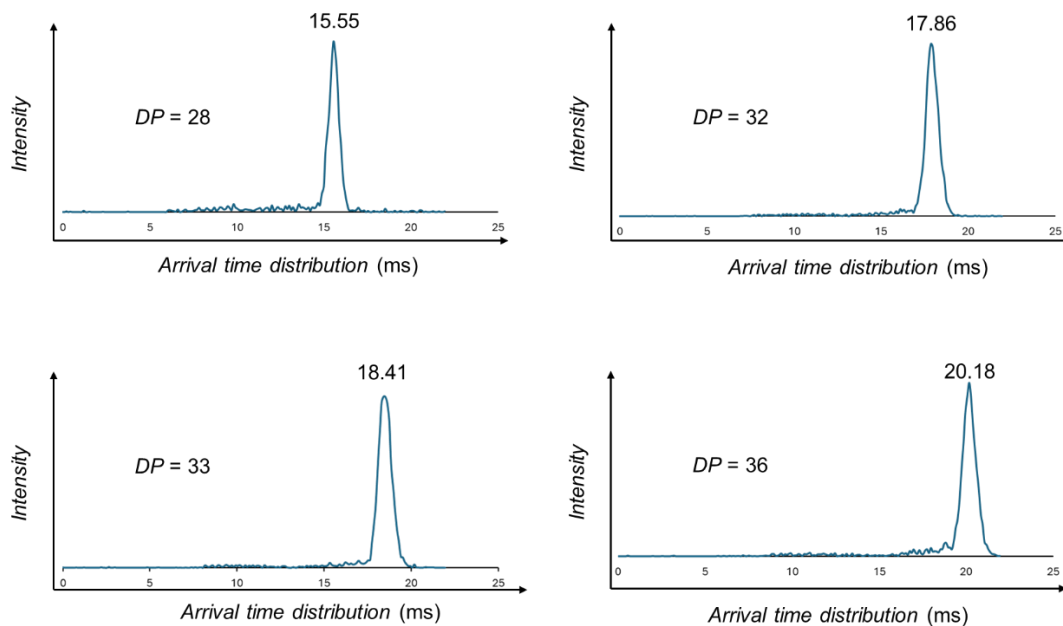
Figure 13. Ion mobility mass spectrometry analysis of 0.01 mg mL^{-1} in acetonitrile/acetone (80/20) BU-PS$_{HM}$ with AgNO$_3$ (0.0002 mg mL^{-1}) as the cationizing agent (Waters Synapt G2-*Si* mass spectrometer) : arrival time distribution (*ATD*) of selected [BU-PS$_{HM}$ + 2Ag]$^{2+}$ ions (*DP* = 28, 32, 33 and 36).
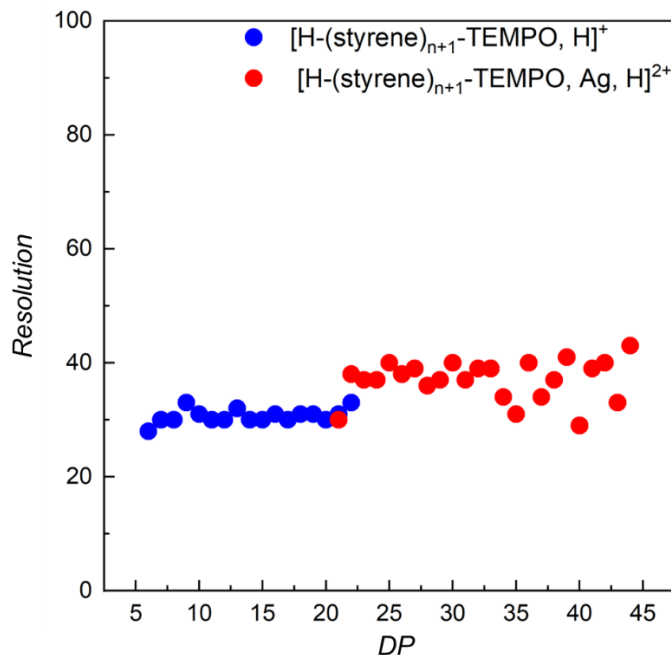
Figure 14. Ion mobility mass spectrometry analysis of TEMPO-PS (Waters Synapt G2-*Si* mass spectrometer) : evolution of the *CCS* resolution (*R = CCS/Δ50%CCS*) over the *DP* range for TEMPO-PS 1+ ions with proton and 2+ ions with proton and silver ion. Note that the maximal Waters Synapt *CCS* resolution is close to 40.

By approximating globular proteins as spheres, Ruotolo et al.[150] established that the ion density can be determined using *equation 1* based on *CCS* trend line analysis. Doing so, *i.e.,* by assuming that the PS ions were quasi spherical, we obtained ρ_{CCS} = 0.40 Da Å^{-3} and 0.47 Da Å^{-3} for respectively [TEMPO-PS + H]$^+$ and the [TEMPO-PS + H + Ag]$^{2+}$ ions. Based on the reported density of bulk polystyrene, 0.96-1.05 g cm^{-3} say 0.57-0.62 Da Å^{-3},[151] ρ_{CCS} are thus calculated by far lower for both the 1+ and 2+ ions. This indicates, in conjunction with the determined B parameters, that the 1+ and 2+ ions do not adopt spherical structures in the gas phase.

$$\rho_{CCS} = \frac{3}{4}\sqrt{\frac{\pi}{A^3}} \ (Da/\text{Å}^3) \ \textit{equation 1}$$

Polyether and polyester polymer ions are characterized by the charge(s) positioned deep in the core of the ion structure with the flexible (and polar) polymer chain folded around the cationizing particle(s).[152] In the case of PS ions, we may imagine that the silver ion stabilization by the phenyl rings also induces the PS chain folding with the silver ion(s)

incorporated within the globular ion. We thus analyzed [BU-PS$_{LM}$ + Ag]$^{+}$ and [BU-PS$_{HM}$ + 2Ag]$^{2+}$ ions, in which the butyl group is not participating in any cationization or protonation process. As shown in Figures 10c and 10d, the fitting process affords B = 0.81 and ρ_{CCS} = 1.43 Da Å^{-3} (A = 0.95), B = 0.68 and ρ_{CCS} = 0.33 Da Å^{-3} (A = 2.48) for 1+ and 2+ BU-PS$_{LM/HM}$ respectively, values that clearly deviate from the bulk PS density.

A wealth of important information regarding polymer folding, as well as the size and shape of the ions, was obtained from the IM-MS investigations. These findings demonstrate that IM-MS is a highly suitable technique for the characterization of precursor SCNPs. However, to gain deeper insight into the polymer collapse process and the three-dimensional structures of the polymer ions across a range of degrees of polymerization (*DP*), IM-MS must be combined with molecular dynamics (MD) simulations.

3. Molecular modeling and theoretical *CCS* calculation

3.1 Polystyrene ion shape analysis

Atomistic simulations constitute an efficient approach to generate accurate information about the ion structure with a description at the atomistic level. *CCS* is used here to identify the best structure candidates amongst a set of generated ion geometries, upon direct comparison between the *CCS*$_{exp}$ and *CCS*$_{th}$.[153] Using Molecular Dynamics simulations, we optimized the structures of all gaseous 1+ and 2+ PS ions detected in the ESI experiments. In the case of the protonated polymers, we first used DFT calculations to establish the preferential position of the added proton on the TEMPO end group. As shown in Figure 15, the *N*-protonation is favored over the *O*-protonation, with a stabilization energy of ~32 kcal mol^{-1}.

E = 0 kcal mol^{-1} E = 32 kcal mol^{-1}
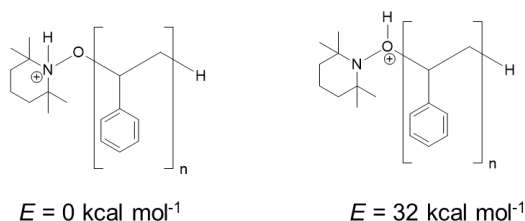
Figure 15. DFT calculations were performed using B3LYP functional and 6-31G** basis set for the determination of the energetically more stable protonation center in TEMPO-PS. Protonation at the nitrogen center of TEMPO was found to be 32 kcal mol^{-1} more stable than protonation at the oxygen center.

CCS_{th} were calculated from the atomistic simulations using the Trajectory Method implemented in Collisdoscope[154] and then compared with the CCS_{exp} in Figure 10. For [TEMPO-PS + H]$^+$, [BU-PS$_{LM}$ + Ag]$^+$ and [BU-PS$_{HM}$ + 2Ag]$^{2+}$ ions, the CCS_{th} values are in very good agreement with the experimental ones, whereas, in the case of [TEMPO-PS + H + Ag]$^{2+}$ ions, the CCS_{th} values are consistently overestimated by ~9% compared to the experimental ones.[154] Since the CCS_{th} curve is parallel to the CCS_{exp} evolution for the [TEMPO-PS + H + Ag]$^{2+}$ ions, there is most likely a systematic error made theoretically for these systems. For di-cations, a parameter that is not accounted for by our calculations is the screening of the Coulomb repulsion between the two cations by the intervening medium. The description of such screening would require exploring the use of more complex polarizable force fields, which is beyond the scope of the present work. The screening effects are expected to condense further the ions and to be more pronounced when there is a large separation between the ions (*i.e.,* a wider polarizable medium). This is actually the case for the [TEMPO-PS + H + Ag]$^{2+}$ compared to the [BU-PS$_{HM}$ + 2Ag]$^{2+}$ ions (refer to Figure 16 and 17), in line with the fact that the cross sections are overestimated for the former ions.

Figure 16. Molecular Dynamics simulations (PCFF force field, 300 K, 25 ns) of TEMPO-PS ions : (a) snapshot of the last frame of the MD for [TEMPO-PS + H]$^+$ (DP = 23); (b) snapshot of the last frame of the MD for [TEMPO-PS + H + Ag]$^{2+}$ (DP = 33). The coloured styrene rings are involved in the cation-π interaction; (c) evolution of the distance between the charged center (H$^+$ or Na$^+$) and the center-of-mass (COM) normalized by the ion radius of gyration (R_g) for [TEMPO-PS + H]$^+$ (blue dots) and [PEG + Na]$^+$ (red dots) (PEG stands for polyethylene glycol, refer to Figure 18 for the optimized ion structure); (d) evolution of the distance between the H$^+$ (cyan dots) and Ag$^+$ (green dots) and the center-of-mass (COM) normalized by the ion radius of gyration (R_g) for [TEMPO-PS + H + Ag]$^{2+}$. Refer also Figure 19 for the evolution of the inter-charge distance for [TEMPO-PS + H + Ag]$^{2+}$ ions.

Figure 16 shows the optimized structures of [TEMPO-PS + H]$^+$ (DP = 23) and [TEMPO-PS + H +Ag]$^{2+}$ (DP = 33), as typical examples selected for the 1+ and 2+ series of ions. We observe that both the 1+ and 2+ ions appear as compact structures with the protonated TEMPO end group located on the edge of the folded chain. For the 1+ ions,

this is clearly different from the situation encountered with a classical (traditional) polymer such as Na^+-cationized polyethers and polyesters, where the Na^+ ion is stabilized deeply into the core of the globular structure,[152] refer to Figure 18 for a typical polyethylene glycol (PEG) ion. To illustrate this particularity, the distance between the charged center (protonated TEMPO or Na^+) and the center-of-mass of the ion for, respectively, [TEMPO-PS + H]$^+$ or [PEG + Na]$^+$ ions, has been divided by the radius of gyration (R_g) of the ion to generate normalized data for increasing DP. As shown in Figure 16c, the normalized distance is between 0.1 and 0.4 for the [PEG + Na]$^+$ ions but increases up to ~1 for the [TEMPO-PS + H]$^+$ ions, implying that the charged end group clearly remains at the surface of the ion structure over the investigated DP range. As shown in Figure 16b for the [TEMPO-PS + H + Ag]$^{2+}$ ions, the protonated TEMPO remains on the surface of the ion and the added Ag^+ cation is located at a diametrically opposite position (Figure 16d), although also at the surface of the ion. The H^+ or Ag^+ distance remains nearly constant around 15-20 Å over the whole investigated DP range (that extends from DP = 21 to 44) to minimize the electrostatic repulsion between both charged centers (refer to Figure 19). Again these [TEMPO-PS + H + Ag]$^{2+}$ ions appear as compact structures. In a recent study related to gas phase dendrimer ions,[145] the so-called solvent-accessible surface area ($SASA$) has been introduced to estimate the effective ion density to be compared to the CCS-determined density (ρ_{CCS}).[155] $SASA$ corresponds to the total area of the ion envelope and, in our simulations, helium is considered as the probing atom (refer to experimental section). The respective molecular volume (V_{SASA}) can subsequently be used to determine the ion effective density, namely ρ_{SASA}, that is only equal to ρ_{CCS} for hard spheres.[145] We determined the $SASA$ for all the [TEMPO-PS + H]$^+$ and [TEMPO-PS+ H + Ag]$^{2+}$ ions, see Tables 3 and 4, and calculated an average $<\rho_{SASA}>$ = 0.62 Da Å^{-3} and 0.65 Da Å^{-3} for respectively the 1+ and 2+ ions. These calculated effective densities (0.62-0.65 Da Å^{-3}) lie close to the bulk PS density (0.57-0.62 Da Å^{-3}),[151] revealing that the ion folding ends up with dense PS ions, whose high density is mainly caused by the PS chain compaction (refer to Table 3-4). Therefore, molecular dynamic simulations assist in obtaining deep knowledge about the 3-dimensional shape of the polymer chain for a broad range of the DP in addition to the IM-MS. Detailed information regarding the size and shape of the polymer ions was obtained through IM-MS and molecular dynamics

(MD) simulations. These studies also provided insights into the effects of polarity and the nature of the end group on the behavior of polymer ions. It was observed that the end group consistently remains at the edge of the ion aggregate. The charged center is stabilized by interactions with the styrene rings and is also located near the periphery of the polymer ion aggregate. Therefore, it was anticipated that IM-MS, coupled with molecular dynamics (MD) simulations, would be a highly effective technique for investigating the size, shape, and collapse behavior of precursor SCNPs.
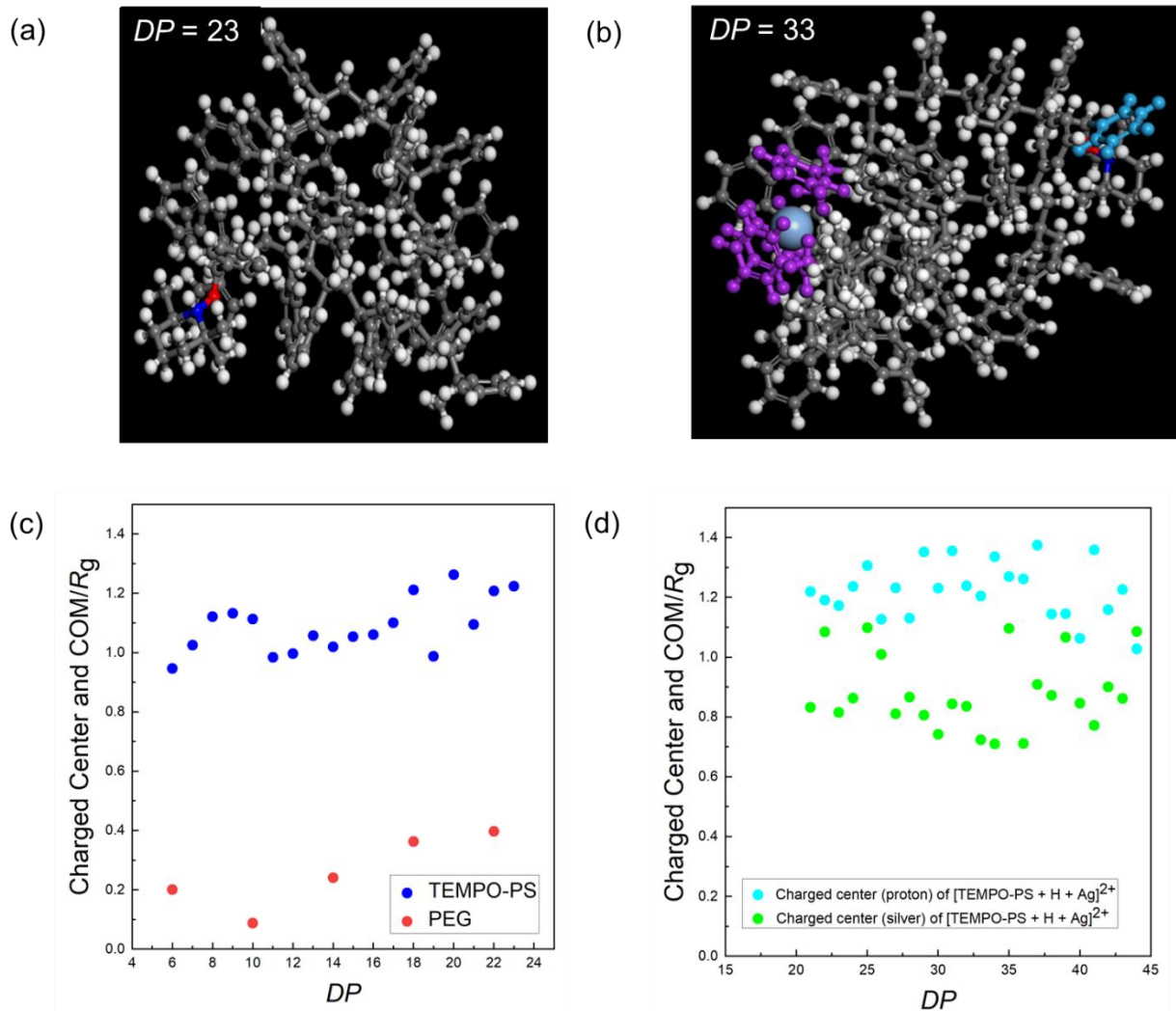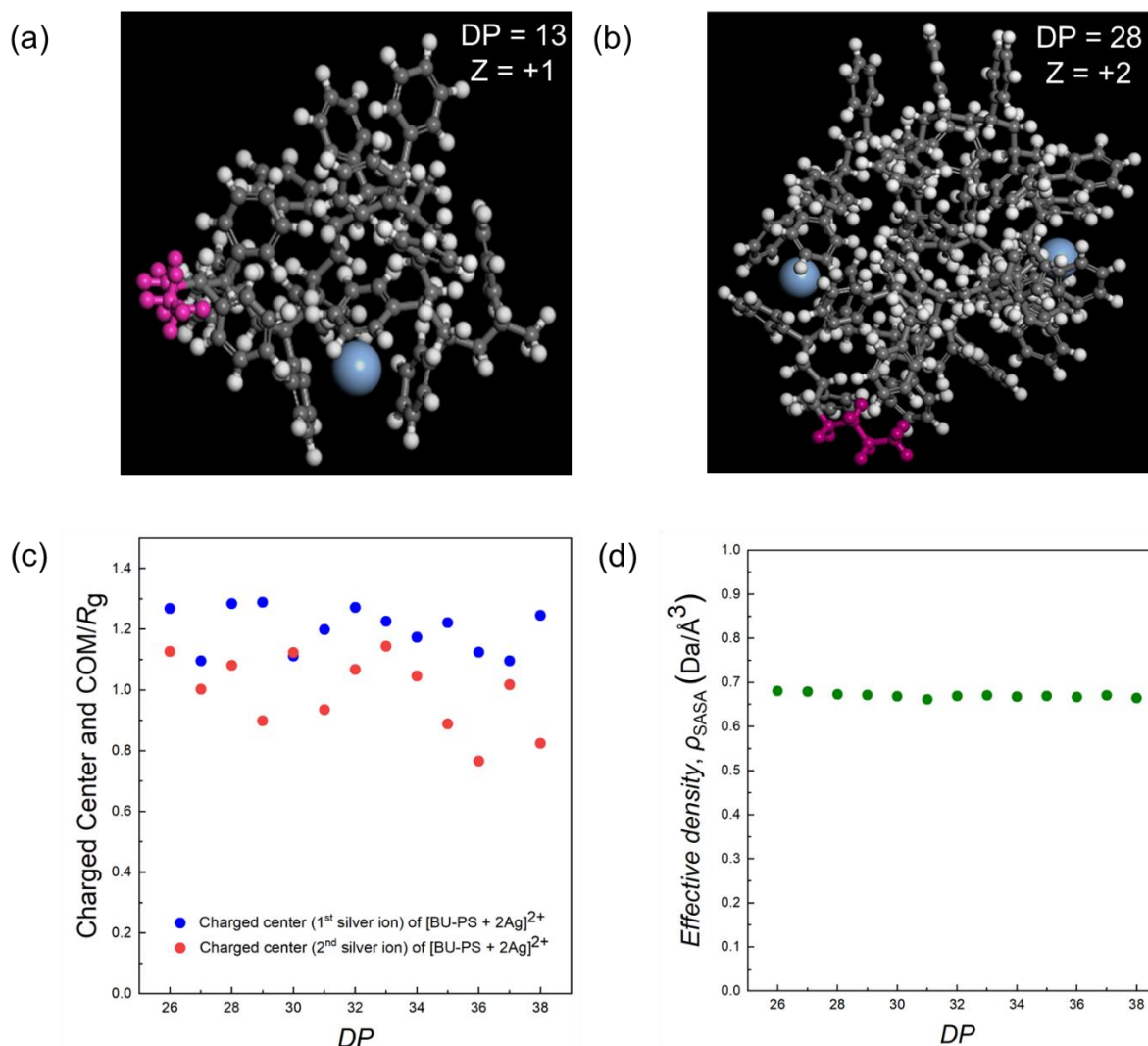

Figure 17. Molecular Dynamics simulations (PCFF force field, 300 K, 25 ns) of BU-PS ions : (a) snapshot of the last frame of the MD for $[BU\text{-}PS_{LM} + Ag]^+$ (DP = 13); (b) snapshot of the last frame of the MD for $[BU\text{-}PS_{HM} + 2Ag]^{2+}$ (DP = 28); (c) evolution of the distances between the charged centers (Ag^+ ions) and the center-of-mass (COM) normalized by the ion radius of gyration (R_g) for $[BU\text{-}PS + 2Ag]^{2+}$; blue and red dots correspond to both silver ions; (d) evolution of the effective density, $\rho_{SASA,}$ from DP = 26 to DP = 38 for $[BU\text{-}PS_{HM} + 2Ag]^{2+}$.

In the case of polystyrene, the charged center consistently remains at the edge of the ion aggregate. This behavior is attributed to the non-polar nature of polystyrene, which lacks strong interactions with the charged species. In contrast, for a polar polymer such as polyethylene glycol (PEG), the charged center is located at the center of the ion aggregate. PEG contains multiple polar oxygen atoms that strongly interact with the charged center, effectively stabilizing it within the core of the polymer ion aggregate (refer to Figure 18).
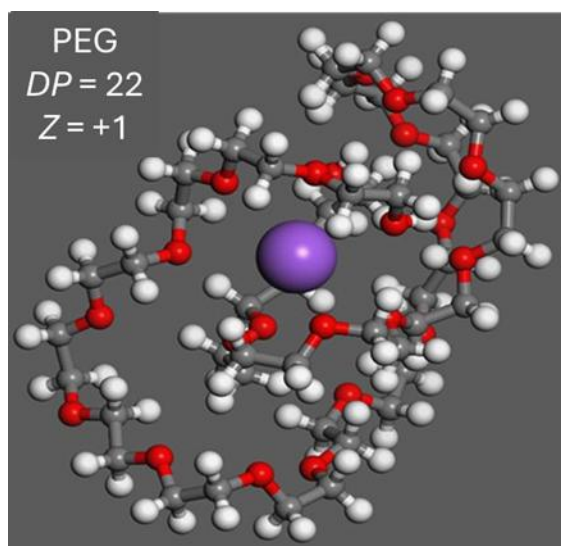
Figure 18: Molecular Dynamics simulations (PCFF force field, 300 K, 25 ns) of singly charged polyethylene glycol ions with sodium : snapshot of the last frame of the MD for [Polyethylene glycol + Na]$^+$ (DP = 22), with the sodium ion present in the center of the polymer ion.

In the case of doubly charged polymer ions, such as [TEMPO-PS + H + Ag]$^{2+}$, two charged centers are present: the protonated TEMPO group and the silver ion. Both charged centers are located at the edge of the ion aggregate, and the distance between them remains consistently in the range of 15–20 Å across all degrees of polymerization (refer to Figure 19).
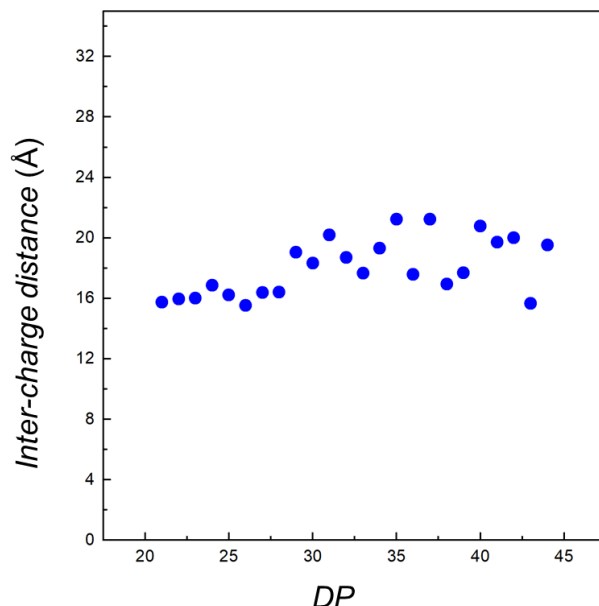
Figure 19. Molecular Dynamics simulations (PCFF force field, 300 K, 25 ns) of TEMPO-PS ions : Evolution of the inter-charge distance in [TEMPO-PS + H + Ag]$^{2+}$ ions.

TEMPO-PS produced two different types of ions: singly charged ions [TEMPO-PS + H]$^+$ and doubly charged ions [TEMPO-PS + H + Ag]$^{2+}$. The solvent-accessible surface area (*SASA*) was calculated for both ion types across the full range of degrees of polymerization (*DP*). Subsequently, the volume corresponding to the *SASA* (V_{SASA}) was determined, and the density (ρ_{SASA}) of the polymer ions was calculated (refer to Tables 3 and 4).

Table 3. Ion mobility mass spectrometry and Molecular Dynamics simulations (PCFF force field, 300 K, 25 ns) of [TEMPO-PS + H]$^+$ ions : experimental and theoretical collision cross sections, Solvent Accessible Surface Area (He atom as the probe), the volume V_{SASA} corresponds to the volume delimited by the *SASA* and allows calculating an effective density, ρ_{SASA}.

			[TEMPO-PS + H]$^+$			
DP	*m/z*	CCS_{exp} (Å^2)	CCS_{th} (Å^2)	*SASA* (Å^2)	V_{SASA} (Å^3)	ρ_{SASA} (Da Å^{-3})
6	782	230	238	910	1293	0.60
7	886	255	263	1020	1459	0.61
8	990	275	286	1077	1641	0.60
9	1094	292	319	1272	1797	0.61
10	1198	308	325	1169	1928	0.62

11	1302	324	333	1247	2101	0.62
12	1406	340	350	1351	2254	0.62
13	1510	357	369	1455	2434	0.62
14	1615	376	386	1578	2605	0.62
15	1719	392	407	1666	2764	0.62
16	1823	410	410	1648	2872	0.63
17	1927	426	437	1738	3060	0.63
18	2031	443	449	1843	3262	0.62
19	2135	458	467	1908	3410	0.63
20	2239	478	492	2015	3615	0.62
21	2343	495	500	2037	3772	0.62
22	2447	510	508	2052	3863	0.63
23	2551	525	537	2214	4049	0.63

Table 4. Ion mobility mass spectrometry and Molecular Dynamics simulations (PCFF force field, 300 K, 25 ns) of $[TEMPO\text{-}PS + H + Ag]^{2+}$ ions : experimental and theoretical collision cross sections, solvent Accessible Surface Area (He atom as the probe), the volume V_{SASA} corresponds to the volume delimited by the $SASA$ and allows calculating an effective density, ρ_{SASA}.

$[TEMPO\text{-}PS + H + Ag]^{2+}$						
DP	m/z	CCS_{exp} (Å^2)	CCS_{th} (Å^2)	SASA (Å^2)	V_{SASA} (Å^3)	ρ_{SASA} (Da Å^{-3})
21	1225.18	470	508	2262	3715	0.66
22	1277.21	481	505	2301	3862	0.66
23	1329.24	493	539	2612	4093	0.65
24	1381.27	511	548	2611	4226	0.65
25	1433.3	522	571	2665	4353	0.66
26	1485.33	540	577	2780	4533	0.66
27	1537.36	551	603	2934	4715	0.65
28	1589.39	567	600	2959	4873	0.65
29	1641.42	578	624	3102	5062	0.65
30	1693.45	594	641	3072	5161	0.66
31	1745.48	604	650	3262	5376	0.65
32	1797.51	620	671	3203	5501	0.65
33	1849.54	630	675	3330	5630	0.66
34	1901.57	645	690	3457	5819	0.65

35	1953.6	655	692	3390	5964	0.66
36	2005.63	665	702	3693	6178	0.65
37	2057.66	675	728	3644	6308	0.65
38	2109.69	689	741	3854	6456	0.65
39	2161.72	699	741	3877	6619	0.65
40	2213.75	713	753	3966	6785	0.65
41	2265.78	723	775	4180	6991	0.65
42	2317.81	737	780	3936	7040	0.66
43	2369.84	751	776	4299	7275	0.65
44	2421.87	760	807	4373	7460	0.65

The charged center always stays at the edge of the ion aggregate, for doubly charged ions, the two charged centers maintain a constant distance throughout the DP range observed when examining the optimized geometries of [Bu-PS$_{LM}$ + Ag]$^+$ and [BU-PS$_{HM}$ + 2Ag]$^{2+}$ ions, as shown in Figure 17 and gathered in Tables 5-6. Indeed, for the 1+ ions (DP = 3-13), the Ag$^+$ cation remains at the surface of the globular ions while, for the 2+ ions, both Ag$^+$ ions are diametrically positioned at the surface of the globular ion with a quasi-constant distance of ~18-20 Å from DP 26 to 38 (refer to Figure 20) and an effective density staying constant at 0.65 Da Å^{-3} (Figure 17d). All the detected ions can therefore be considered as highly compact and fully folded structures.

Low molecular weight BU-PS formed singly charged ions [BU-PS + Ag]$^+$, while high molecular weight BU-PS formed doubly charged ions [BU-PS + 2Ag]$^{2+}$. The solvent accessible surface area ($SASA$) were calculated for both series of ions across the DP range. Subsequently, the volume corresponding to the $SASA$ (V_{SASA}) was determined, and finally, the density (ρ_{SASA}) of the polymer ions was calculated (refer to Tables 5 and 6). The densities obtained from these calculations were compared with the reported density of bulk polystyrene density (0.57-0.62 Da Å^{-3}).[151]

Table 5. Ion mobility mass spectrometry and Molecular Dynamics simulations (PCFF force field, 300 K, 25 ns) of [BU-PSLM + Ag]⁺ ions : experimental and theoretical collision cross sections, solvent Accessible Surface Area (He atom as the probe), the volume V_{SASA} corresponds to the volume delimited by the *SASA* and allows calculating an effective density, ρ_{SASA}.

		[BU-PS$_{LM}$ + Ag]$^+$				
DP	*m/z*	CCS_{exp} (Å^2)	CCS_{th} (Å^2)	*SASA* (Å^2)	V_{SASA} (Å^3)	ρ_{SASA} (Da Å^{-3})
3	477.19	138	146	541	685	0.70
4	581.26	165	174	642	837	0.69
5	685.33	189	201	769	1014	0.68
6	789.4	212	223	876	1182	0.67
7	893.46	237	244	914	1320	0.68
8	997.52	257	262	1045	1501	0.66
9	1101.59	280	283	1083	1636	0.67
10	1205.66	298	302	1235	1821	0.66
11	1309.71	319	325	1381	2001	0.65
12	1413.79	339	340	1456	2126	0.67
13	1517.87	358	362	1545	2316	0.66

Table 6. Ion mobility mass spectrometry and Molecular Dynamics simulations (PCFF force field, 300 K, 25 ns) of [BU-PSHM + 2Ag]$^{2+}$ ions : experimental and theoretical collision cross sections, solvent Accessible Surface Area (He atom as the probe), the volume V_{SASA} corresponds to the volume delimited by the *SASA* and allows calculating an effective density, ρ_{SASA}.

		[BU-PS$_{HM}$ + 2Ag]$^{2+}$				
DP	*m/z*	CCS_{exp} (Å^2)	CCS_{th} (Å^2)	*SASA* (Å^2)	V_{SASA} (Å^3)	ρ_{SASA} (Da Å^{-3})
26	1488.78	582	595	2538	4376	0.68
27	1540.83	598	587	2660	4540	0.68
28	1592.86	611	610	2857	4734	0.67
29	1644.89	627	622	2961	4901	0.67
30	1696.93	639	628	3123	5079	0.67
31	1748.96	652	640	3168	5288	0.66
32	1800.99	667	643	3183	5384	0.67
33	1853.02	679	667	3263	5527	0.67
34	1905.06	691	690	3350	5708	0.67

35	1957.09	703	705	3392	5852	0.67
36	2009.14	715	715	3453	6028	0.67
37	2061.16	729	719	3494	6147	0.67
38	2113.68	741	745	3566	6364	0.66

As far as the doubly charged polymer ions, $[BU\text{-}PS + 2Ag]^{2+}$ contains two silver ions as charged centers. Both charged centers are located at the edges of the ion aggregate, and the distance between them remains constant at 18–20 Å throughout the entire *DP* range (refer to Figure 20).
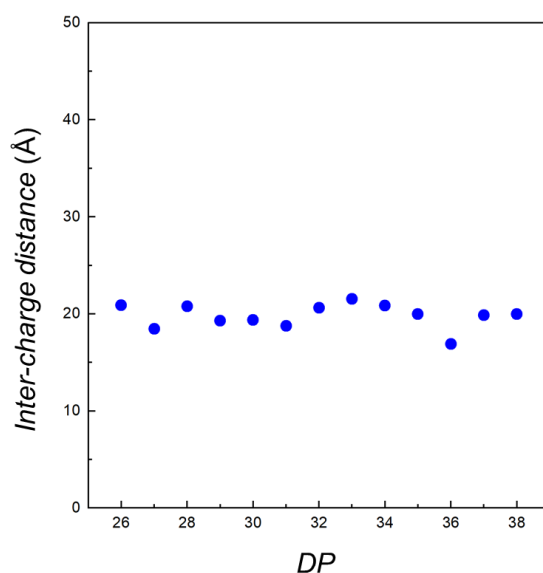
Figure 20. Molecular Dynamics simulations (PCFF force field, 300 K, 25 ns) of BU-PS ions : evolution of the inter-charge distance in $[BU\text{-}PS_{HM} + 2Ag]^{2+}$.

Globally, a globular ion with an egg-like shape represents the best structure to account for the experimental and theoretical data that can be summarized as follows: *(i)* regardless of the charge state and the chain ends, the PS chain folds into the most compact structure with a constant effective density (ρ_{SASA}) close to the bulk PS density; *(ii)* the charge(s) is (are) excluded from the PS core and remain(s) at the surface of the globular ions; and *(iii)* the inter-charge distance in 2+ ions remains constant ~15-20 Å

over the entire investigated *DP* range for both Ag⁺/H⁺ (refer to Figure 19) and Ag⁺/Ag⁺ pairs (refer to Figure 20).

3.2 Polystyrene ion molecular structure analysis

In addition to establishing the global shape of the ions, MD simulations also allow analyzing the ion structure at the atomistic level by examining the intramolecular interactions responsible for the chain folding.
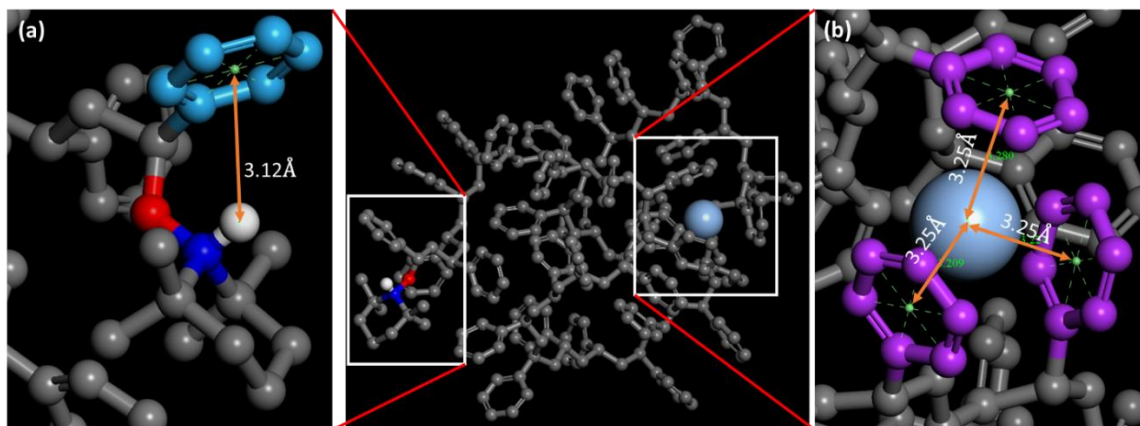
Figure 21. Molecular Dynamics simulations (PCFF force field, 300 K, 25 ns) of [TEMPO-PS + H + Ag]²⁺ ions (*DP* = 33). Snapshot of the last frame of the MD with enlarged views of the charged centers : (a) proton-π interaction around the TEMPO end group and (b) cation-π interaction involving the Ag⁺ ion and three phenyl rings of the PS backbone.

As featured in Figure 21, protonated TEMPO is stabilized by a cation (H⁺) - π interaction involving only the first styrene residue, with a proton - phenyl ring distance at ~3.1 Å whatever the charge state of the polymer ion. On the other hand, the silver ions (1+ and 2+ ions) are strongly interacting with three phenyl rings in a cage arrangement with distances around 3.25 Å between Ag⁺ and the geometrical center of the phenyl rings.[144,156] Using DFT calculations, we optimized the geometry of a model complex associating three benzene molecules to a single Ag⁺ cation. As shown in Figure 22, in the optimized geometry, the silver cation is located in the center of the benzene triad with cation-benzene distances around 2.9 Å, thus corroborating our MD calculations. DFT also

allows determining the interaction energy that stabilizes the folded polymer ions. DFT was used for the investigation of the interaction energy between styrene and silver ion.
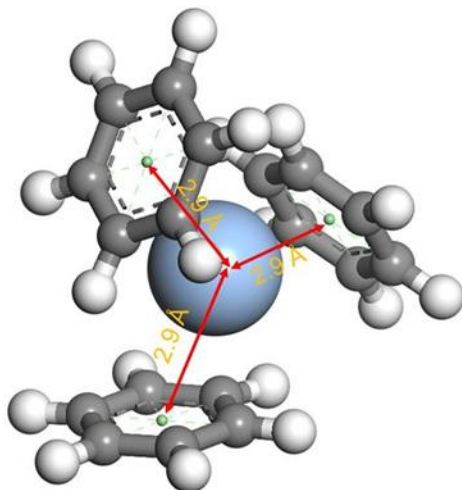
Figure 22. Cation-π interaction between 3 benzene rings and silver ion in [TEMPO-PS + H + Ag]$^{2+}$ as established by DFT calculations using the B3LYP functional, a cc-pVTZ basis set for carbon and hydrogen, a LANL2DZ basis set for silver ion and the van der Waals corrections GD3BJ. Here 2.9 Å corresponds to the distance between the geometrical center of phenyl ring and the silver ion.

Another aspect to be discussed is the spatial arrangement of the PS backbone within the globular ions or, in other words, to determine whether there is a preferred three-dimensional folding for the polymer chain. We examined the folding of the polymer backbone within the optimized [BU-PS + 2Ag]$^{2+}$ ions whose CCS_{th} are reported in Figure 10c. As sketched in Figure 23, we identified two different scaffolds that are described as U-folding and S-folding in the following discussion. The U-folding terminology reflects that the polymer backbone adopts a loop-like structure with one silver cation lying around in the middle of the chain and the second one associating the two extremities of the linear polymer, see Figure 23a. The S-folding is characterized by a spatial arrangement with two loops and one Ag+ cation at each extremity of the backbone, see Figure 23b. Both scaffolds are randomly observed over the entire *DP* range without any trend, implying that the chain randomly folds during the MD simulations.

94
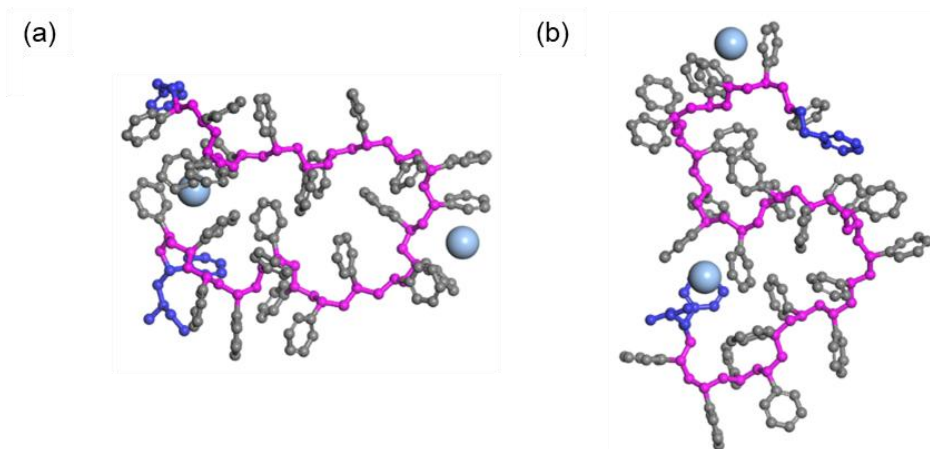
Figure 23. Molecular Dynamics simulations (PCFF force field, 300 K, 25 ns) of [BU-PS + 2Ag]$^{2+}$ ions (DP = 26) : snapshots of the last frame of the MD featuring U-shape and S-shape folding for the PS backbone. As described in the main text, these two geometries have been obtained from different input geometries presented in Figure S18. Here, blue is used to indicate the end groups and pink for the polymer backbone : a) "U" shape structure for [BU-PS + 2Ag]$^{2+}$ ions (DP = 26), and b) "S" shape structure for [BU-PS + 2Ag]$^{2+}$ ions (DP = 26).

As for a typical example, in Figure 23, U-folding and S-folding are generated by MD simulations from two different input structures for DP = 26 (refer to Figure 24 for the input structures). Moreover, these ions, both characterized by CCS_{th} = 584/585 Å^2, are not experimentally distinguishable and are likely to coexist in the gas phase.
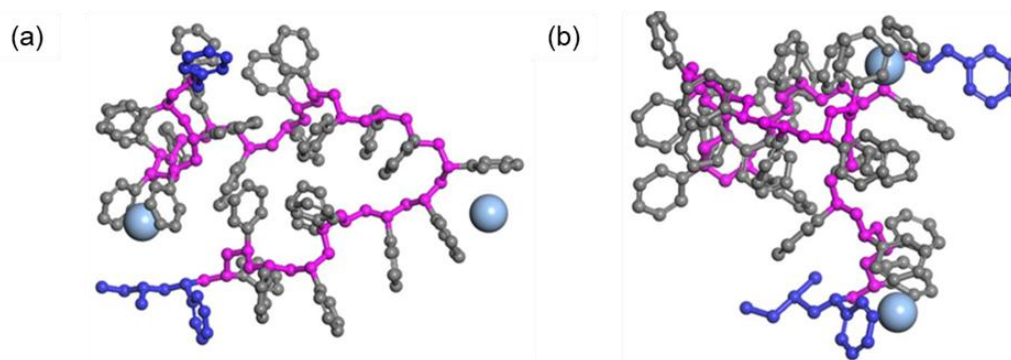
Figure 24. "U" and S-shape folding for [BU-PS + 2Ag]$^{2+}$ (DP = 26): a) input structure for Molecular Dynamics simulations (PCFF force field, 300 K, 25 ns) that drives the U-shape folding of the polystyrene backbone; and b) input structure for Molecular Dynamics simulations that drives the S-shape. The final structures generated after MD are presented in Figure 23.

3.3 Polystyrene ion vs polyether ion folding in the gas phase: what is the role of the charge?

There is thus an intrinsic difference between the gas phase structures of [PS + Ag]$^+$ ions and [PEG + Na]$^+$ ions since the Na$^+$ ion is located close to the center of mass of the globular ions (Figures 16c and 18) whereas the Ag$^+$ ion (or protonated TEMPO) remains mostly at the surface of the globular ions. For the BU-PS$_{HM/LM}$ 1+ and 2+ ions, we also noticed that the butyl end-group is invariably excluded from the PS core of the globular ions, see Figure 17 for typical examples. To understand the folding mechanism of [BU-PS + Ag]$^+$ ions, we performed 36 MD simulations starting from three different linear input structures for DP = 44, *i.e.*, with the Ag$^+$ positioned close to the butyl end group, near the middle of the chain and close to the hydrogen atom end-group, refer to Figure 25. In order to obtain a statistical relevant folding mechanism, each input geometry was submitted to 12 independent MD runs to generate 12 independent equilibrated geometries. We then evaluated the relative position of the Ag$^+$ in the equilibrated structures by calculating the distance between the charged center and the center-of-mass normalized by the radius of gyration (R_g), see Table 7. We noticed *(i)* that the Ag$^+$ ion does not diffuse along the polymeric chain (refer to Figure 26); and *(ii)* that, in all folded structures, the Ag$^+$ ion is stabilized at the surface of the coiled chain, as the ratio between the charged/center-of-mass distance normalized by the radius of gyration is systematically around 0.7 and 0.8. The same methodology has been applied to the case of the [PEG + Na]$^+$ ion (DP = 44) folding, starting from two initial uncoiled states where the Na$^+$ ion was placed near the beginning and into the middle of the polymeric chain (refer to Figure 27). Regardless of the initial geometry, all MD simulations ended up with coiled chains where the sodium cation is stabilized at the core of the polyether globule at an average position (distance between the sodium ion and the center-of-mass (COM) normalized by the ion radius of gyration) of ~ 0.4, refer to Table 7.

Figure 25. MD simulations (PCFF force field, 300 K, 2 ns) of [BU-PS + Ag]$^+$ ions (DP = 44): influence of the position of the charge center (Ag$^+$) in the input geometry on the output geometry. For the BU-PS ion, the Ag$^+$ ion is sandwiched phenyl rings located (a) close to the *sec*-butyl end-group (PS$_{BU}$), (b) near the middle of the chain (PSmiddle) and (c) close to the H end-group (PS$_H$). The geometries shown in (a)–(c) were used as inputs for the MD simulations, in which the charged center was placed at different positions along the polymer chain. The styrene unit holding the silver ion was marked in green. At the end of the simulation, the charged center was always retained by the marked styrene unit.

Table 7. MD simulations (PCFF force field, 300 K, 2 ns) of [BU-PS + Ag]$^+$ ions (DP = 44) and [PEG + Na]$^+$ ions (DP = 44) : influence of the position of the charged center (Ag$^+$/Na$^+$) in the input geometry to the output geometries. Statistical average and standard deviation of the charged center in the globular ion by calculating the distance between the charged center and the center-of-mass (COM) divided by the radius of gyration.

Position of the charged center (Ag$^+$/Na$^+$) in the input geometry of [BU-PS + Ag]$^+$ ions (DP = 44) and [PEG + Na]$^+$ ions (DP = 44)	Statistical average of the distance between the charged center and the center-of-mass (COM) divided by the radius of gyration (R_g)	Standard deviation (SD)
PS$_{BU}$	0.77	0.20
PSmiddle	0.78	0.18

PS$_H$	0.74	0.14
PEG	0.42	0.02

When examining frame-by-frame MD trajectories for both the [BU-PS + Ag]$^+$ and [PEG + Na]$^+$ ions (DP = 44), we realized that the folding mechanisms are intrinsically different for both families of ions. In the case of PS ions, as illustrated in Figure 26, the charge does not participate in the folding process, and coiling is initiated by the phenyl ring interaction in the middle of the chain on the way to PS-only core, from which the butyl end group and the silver ion are excluded, leading to the final compaction of the ions. In Figures 28 and 29, similar behaviors were detected during the MD starting from the input geometries presenting the Ag$^+$ ion in the middle or at the other extremity of the PS backbone, revealing that the ion folding is mostly driven by π-π interactions rather than by the charge stabilization. The MD simulations helped to visualize the folding processes of both polar and non-polar polymers (refer to Figure 26 and Figure 28-30). Based on the analysis of the polystyrene samples, it became clear that IM-MS, when combined with molecular dynamics simulations, is a highly valuable technique for polymer characterization.

Figure 26. Molecular Dynamics simulations (PCFF force field, 300 K, 2 ns) of [BU-PS + Ag]$^+$ ions (DP = 44) with the Ag$^+$ ion initially positioned close to the *sec*-butyl end-group of the PS backbone (PS$_{BU}$) : snapshots at different times of

the trajectory revealing that the folding process is mostly initiated by π-π interactions between phenyl rings with the charge and the *sec*-butyl end group remaining at the surface of the equilibrated structure. The styrene residues highlighted in green pinpoint the initial and final positions of the Ag$^+$ ion.

The folding process of the non-polar polymer BU-PS ions was examined, where the styrene ring responsible for coordinating the silver ions was highlighted in green. The positions of the silver ions and the marked styrene rings were monitored throughout the folding process. Initially, the silver ion was located between the marked styrene rings, near the *sec*-butyl end group. During the entire folding process, the silver ion remains coordinated by the marked styrene units, and the charged center consistently stays at the edge of the polymer ion aggregate.

Following the investigation of the non-polar polymer, the folding process of a polar polymer, polyethylene glycol (PEG), was examined. In this case, a sodium ion (Na$^+$) was initially placed either at one end of the polymer chain (refer to Figure 27a) or at the center of the chain (refer to Figure 27b), and its position was tracked throughout the folding process. The sodium ion consistently remains at the core of the polymer ion aggregate.

These two investigations clearly demonstrate that the position of the charged center is governed by the nature of interactions between the polymer chain and the charged ion.
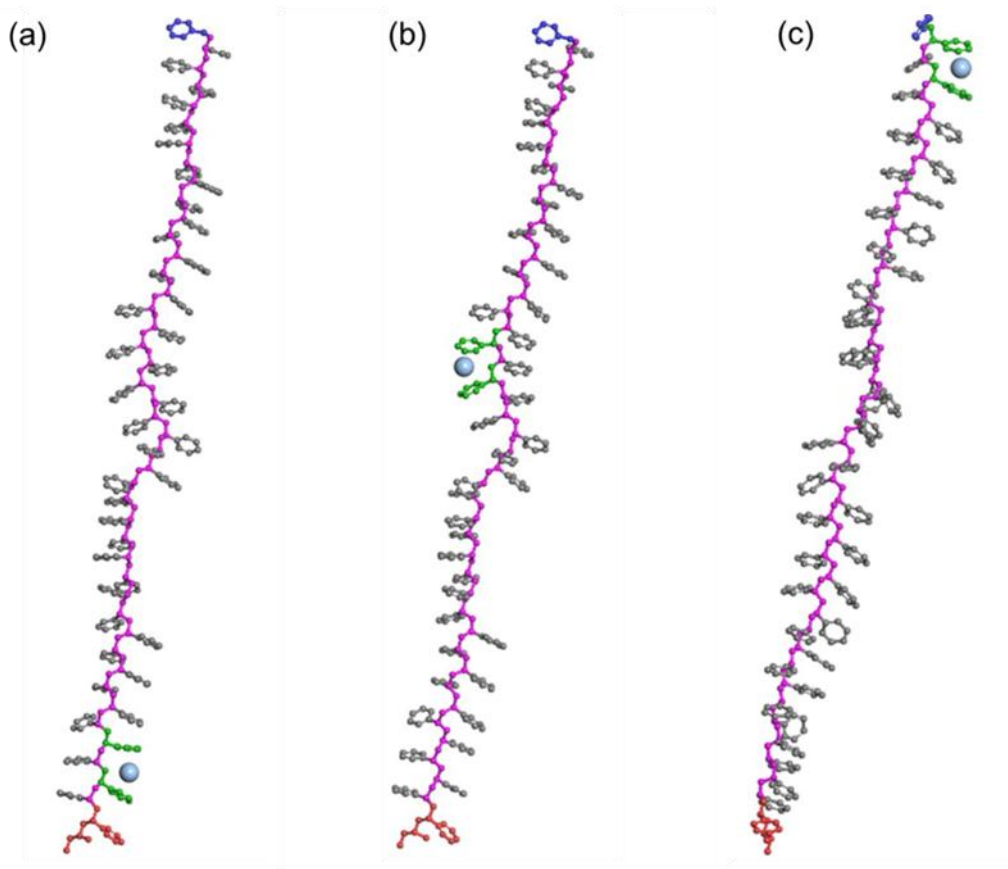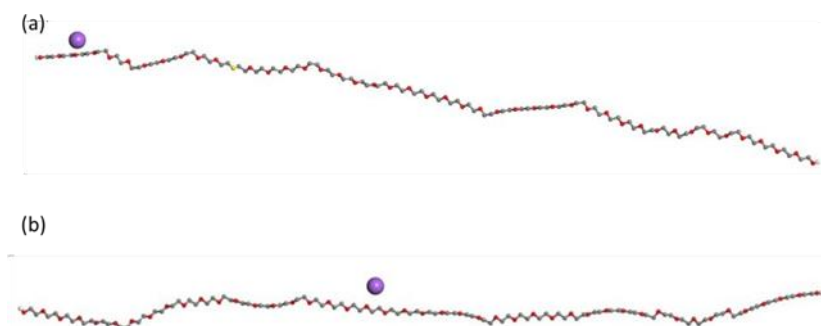

Figure 27. MD simulations (PCFF force field, 300 K, 2 ns) of [PEG + Na]$^+$ ions (*DP* = 44) : influence of the position of the charge center (Na$^+$) in the input geometry on the output geometries. (a) The Na$^+$ ion is positioned close to oxygen atoms located near the end-group and (b) the Na$^+$ ion is positioned at the middle of the polymer chain.
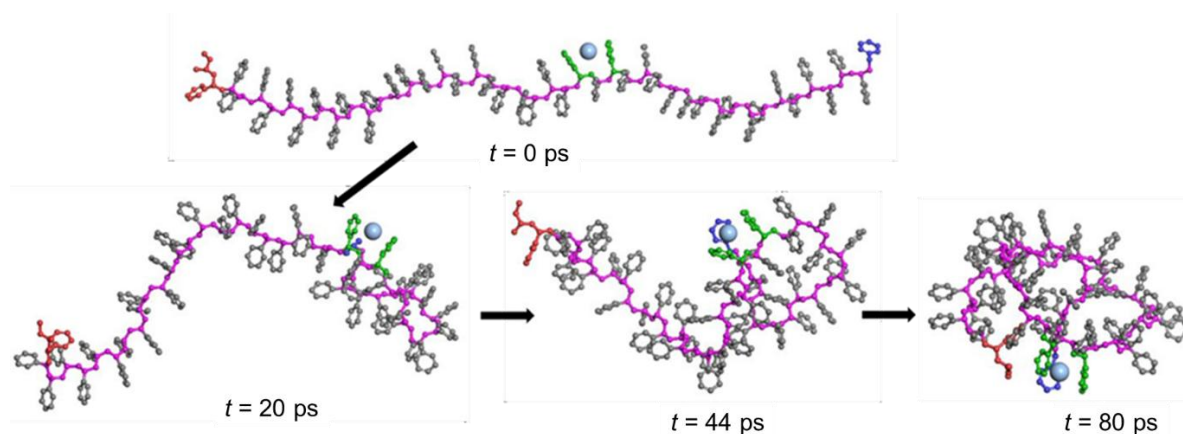
Figure 28. Molecular Dynamics simulations (PCFF force field, 300 K, 2 ns) of [BU-PS + Ag]$^+$ ions (*DP* = 44) with the Ag$^+$ ion initially positioned at the middle of the PS backbone (PS$_{middle}$) : snapshots at different points of the trajectory revealing that the folding process is mostly initiated by π-π interactions between phenyl rings with the charge and the *sec*-butyl end group (blue) remaining at the surface of the equilibrated structure. The styrene residues highlighted in green correspond to the initial and final positions of the Ag$^+$ ion.
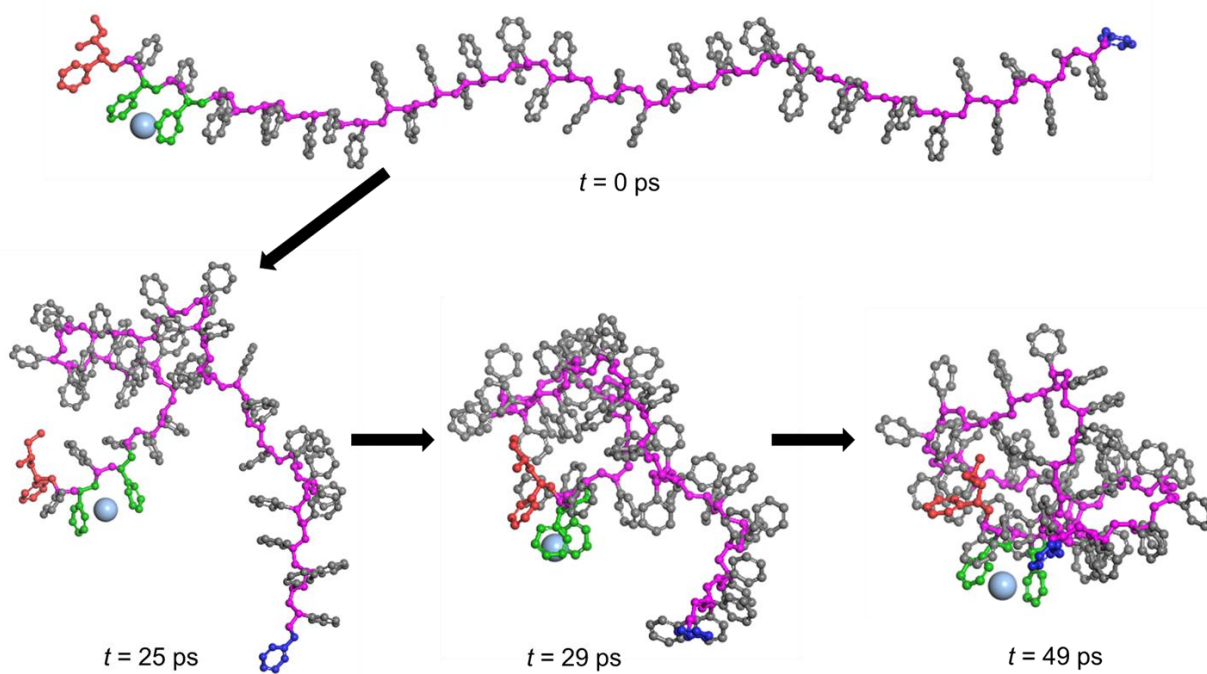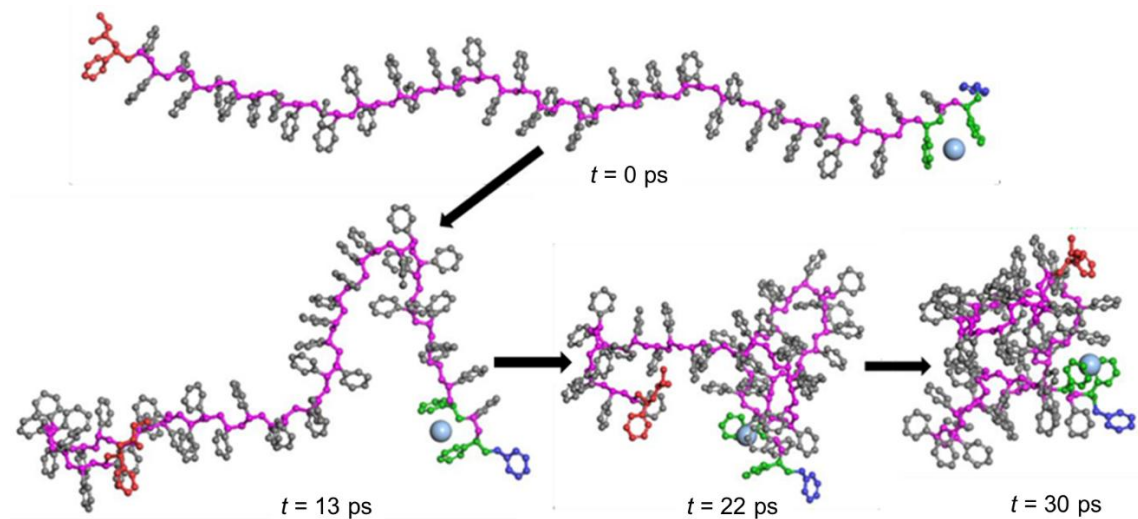

Figure 29. Molecular Dynamics simulations (PCFF force field, 300 K, 2 ns) of [BU-PS + Ag]$^+$ ions (*DP* = 44) with the Ag$^+$ ion initially positioned at the extremity of the PS backbone (PS$_H$) : snapshots at different points of the trajectory revealing that the folding process is mostly initiated by π-π interactions between phenyl rings with the charge and the *sec*-butyl end group (blue) remaining at the surface of the equilibrated structure. The styrene residues highlighted in green correspond to the initial and final position of the Ag$^+$ ion.

On the other hand, for the [PEG+Na]$^+$ ions, see Figure 30, the folding of the chain is triggered by the stabilization of the Na$^+$ ion by the flexible polymer chain. When the cation

is fully stabilized by the polyether chain, the rest of the polyether chain progressively collapses around the initial nucleus to generate a globular dense structure with the Na^+ ion settled deep in the core of the ion. Such a behavior is also allowed by the greater flexibility of the PEG chain compared to the PS backbone.
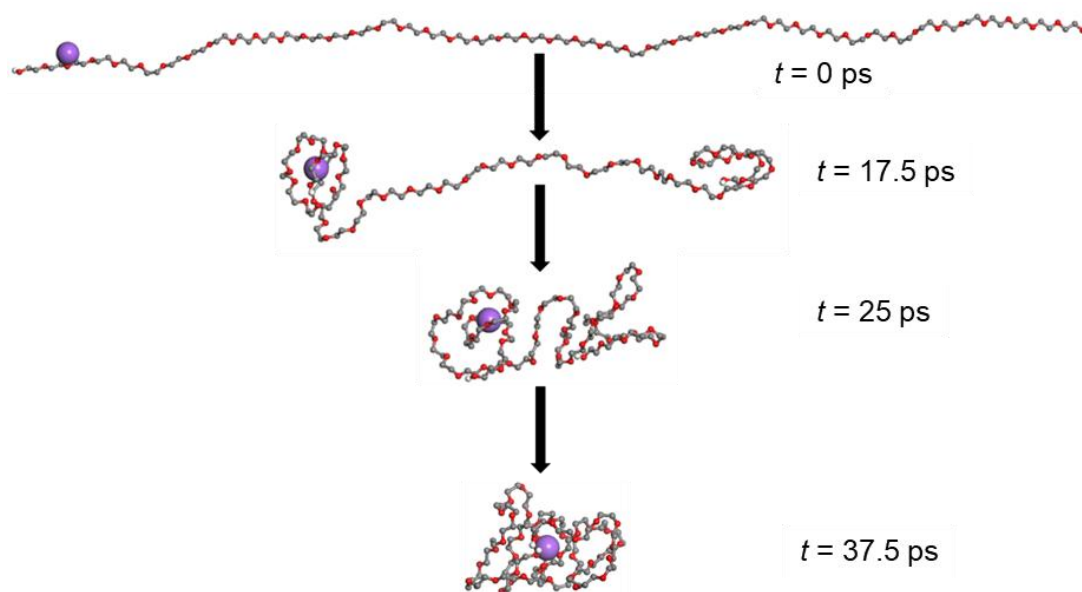
Figure 30. Molecular Dynamics simulations (PCFF force field, 300 K, 2 ns) of [PEG + Na]$^+$ ions (*DP* = 44) with the Na^+ ion initially positioned close to the extremity of the PEG backbone : snapshots at different points of the trajectory revealing that the folding process is mostly initiated by Na^+-dipole interactions between the oxygen atoms and the charge, generating globular ions with the Na^+ ion deeply settled in the PEG core, here position of the Na^+ ion at the end of dynamics does not depends on the position of the Na^+ ion in the input structure.

Conclusions

A combination between IMS-MS and molecular dynamics simulations has been used to investigate the structure of polymer ions constituted by rigid and apolar monomer units, *i.e.* styrene residues, and hydrophilic or hydrophobic end groups, *i.e.,* TEMPO and *sec*-butyl end-groups. Experimental and theoretical *CCS* were determined to establish the 3D shape of 1+ and 2+ PS ions. Trend line analyses (*CCS* vs *mass* plots) have been shown to be inefficient in predicting the exact shape of the ions. Experimental *CCS* became much more structure informative when compared to theoretical data generated using molecular dynamics simulations at the atomistic level of the ion structure. By computing the solvent accessible surface area (*SASA*), we initially established that the PS backbone is densely

packed within elliptic-shaped ions, with an effective density close to the bulk PS density. We further established that the charges (1+ and 2+ ions) are systematically positioned close to the surface of the folded ions, at variance with polyether ions in which the sodium ions are settled deep in the core of the ion structure. We also demonstrated by performing MD simulations starting from different input structures that the PS backbone can fold in different structures, generating U- and S-shapes, possessing quasi-identical theoretical *CCS* that cannot be distinguished by experiment. Such a behavior is reminiscent of solution phase processes where random coils are often involved to account for the hydrodynamic volumes of floppy polymers. Finally, to account for the intrinsic differences between the PS and the PEG ions, we used MD simulations to demonstrate that the folding of the PS rigid chain is induced by phenyl ring interactions with the charge ultimately remaining excluded from the core of the globular ions, whereas the folding of polyether ions is initiated by the folding of the flexible polyether chain around the sodium ion that remains deeply settled in the core of the ions. Critically, compared to literature results, our data reveal that in large PS structures charges – typically the silver cations – are not merely sandwiched between two phenyl rings but ligated in 3-dimensions inducing the overall collapse of the tertiary structure.

This investigation yielded several important findings. It revealed how polymer folding is influenced by the polarity of the end group and how the location of the charge center affects the three-dimensional structure of the collapsed polymer ions. These insights provided a deeper understanding of the polymer collapse process. After gaining a thorough understanding of the shape and 3D structure of the polystyrene samples, the technique could now be applied to more complex systems first to copolymers composed of styrene (STY) and STY-CH_2-OH monomers, and finally to even more complex precursor SCNPs incorporating STY, STY-CH_2-OH, and STY-PPh_2-AuCl monomers (refer to Chapter 2). Our group has previously reported an azobenzene-containing photo-switchable SCNP.[131] This SCNP is composed of STY, STY-CH_2-OH, and STY-PPh_2-AuCl monomers and exhibits catalytic activity. Their catalytic activity can potentially be linked to the position and accessibility of the metal center. Therefore, understanding the three-dimensional shape and the position of functional groups is critical for controlling the

catalytic activity. In this context, IM-MS coupled with MD simulations is an excellent technique to elucidate the three-dimensional structure.

Annexes

Polystyrene Chain Geometry Probed by Ion Mobility Mass Spectrometry and Molecular Dynamics Simulations

*based on Naskar et al, "Polystyrene Chain Geometry Probed by Ion Mobility Mass Spectrometry and Molecular Dynamics Simulations." J.Am.Soc.Mass Spectrom., 35 (**2024**) 2408-2419.*

Experimental Section

HPLC grade tetrahydrofuran (>99.8%), acetonitrile (>99.9%), acetone (>99.8%), methanol (>99.8%), toluene (>99.8%), chloroform (>99.9%) solvents were purchased from Chem-Lab (Zedelgem, Belgium). Silver nitrate (>99%) and sodium iodide were purchased from VWR (Leuven, Belgium) and used without any further purification. Polyethylene glycol was acquired from Sigma-Aldrich and utilized as IMS-MS calibrant. TEMPO-PS (2,2,6,6-tetramethylpiperidine-*N*-oxyl end group - $Đ$ = 1.2 – M_n = 3,400 g mol^{-1}) was prepared according to literature,[131] whereas BU-PS$_{LM}$ and BU-PS$_{HM}$ (*sec*-butyl end group - $Đ$ = 1.03 – M_n = 3,270 g mol^{-1} (BU-PS$_{HM}$) and $Đ$ = 1.01 – M_n = 580 g mol^{-1} (BU-PS$_{LM}$)) were purchased from Agilent Technologies (GPC or SEC Calibration Kits). LM and HM in subscript stand for low mass and high mass, respectively. Agilent BU-PS Standards are prepared by living anionic polymerization with a *sec*-butyl initiating substituent that is attached to the CH$_2$ group of styrene.[157]

Ion Mobility Experiments

Polystyrene stock solutions of 1.0 mg mL^{-1} were prepared in acetone and acetonitrile (20:80, *v/v*). TEMPO-PS was analyzed with and without AgNO$_3$ as cationizing agent. BU-PS$_{LM/HM}$ were only analyzed using AgNO$_3$ as cationization agent, because the lack of the basic functional groups precludes significant protonation under ESI conditions. The AgNO$_3$ solution (10.0 mg mL^{-1}) was prepared in THF and acetonitrile (1:9, *v/v*) and 2 µL of the cationization agent solution and 1 mL of the polystyrene solution were combined.

The PS solutions (with and without AgNO$_3$) have been 100x diluted with acetone and acetonitrile (20:80, *v/v*) before ESI analysis.

MS spectra and *CCS* measurements were performed on a Waters Synapt G2-*Si* mass spectrometer. The solutions were infused at a flow rate of 5 µL min^{-1} with a capillary voltage of 3.1 kV, a source temperature of 100 °C and a desolvation temperature of 150 °C. The standard IMS-MS parameters were : wave height = 40 V, wave velocities = 350 or 600 or 800 m s^{-1}, mass range = *m/z* 50-4,000; N$_2$ flow rate = 60 mL min^{-1}, He flow rate = 180 mL min^{-1} and trap bias = 45.0 V. A pre-established calibration procedure[158] was used to convert the experimentally determined arrival time distributions to $^{TW}CCS_{N2 \rightarrow He}$,[159] which will be referred to as *CCS*$_{exp}$. We performed our experiments in an N$_2$ drift gas; however, the *CCS* calibration was carried out using He. Therefore, the reported *CCS* values are based on the He calibration.

Molecular Dynamics Simulations

All calculations were carried out for a run lasting 25 ns with 1 fs time step in the *NVT* ensemble at 300 K (as temperature does not create much effect due to the high pressure in the IMS chamber) with the Materials Studio software (BIOVIA, San Diego, CA).[160] The PCFF force field was used and validated by the fact that the calculated effective density of TEMPO-PS (0.62-0.66 Da/Å^3) is in good agreement with the reported density of bulk polystyrene (0.57-0.62 Da/Å^3).[151] At first, a geometrical optimization was performed starting from a linear polymer chain (without charge) using the forcefield assigned algorithm for charge assignment. The final geometry was further reoptimized after addition of a charge (H$^+$ for TEMPO-PS and Ag$^+$ for BU-PS) to the optimized polymer chain. For the 2+ ions, a second geometry optimization was performed after addition of the second charge (Ag$^+$) to the polymer chain. A quenched dynamics was then executed for 20 ns using 1 fs timestep and 100 Å van der Waals and electrostatic interaction cutoff at 300 K. A MD run was then performed starting from the most stable structure obtained from the quenched dynamics until the calculated radius of gyration reaches equilibrium. The *CCS* calculations were carried out by taking average of 400 frames utilizing the trajectory method[161] (TM) model implemented within the Collidoscope software.[154] We

also determined the Solvent Accessible Surface Area ($SASA$) and this value against the molecular volume (V_{SASA}) used to estimate the effective density of the PS ions. Note that V_{SASA} was estimated only from the last frame of the dynamics with the Materials Studio 7.0 "Atom Volumes & Surfaces"[160] module using He as the probe. This implies that the $SASA$ value also includes the contribution of the He atom, as an additional layer covering the ion surface. The $SASA$ value reflects the rugosity of the surface except for the small surface irregularities that are too small to be probed by the helium atom. For the investigation of the folding process of PS and PEG ions with DP = 44, we performed a geometry optimization starting from a linear polymer chain (without charge) using the forcefield assigned charges. After that we performed a second geometry optimization after adding a charge at different positions. Finally, we run a NVT MD simulation for 2 ns at 300 K, using 1 fs timestep and 100 Å van der Waals and electrostatic interaction cutoff.

Density Functional Theory (DFT) Calculations

Calculations were performed at the Density Functional Theory (DFT) level using a 6-31G** double zeta basis set and the B3LYP functional, as implemented in the Gaussian 09 (D01 revision) suite, to determine the most favorable protonation center for the TEMPO end group.[162] To describe cation Ag^+-π interactions, the B3LYP functional has been used together with a cc-pVTZ basis set for carbon and hydrogen and a LANL2DZ basis set for silver ion,[163] respectively. To properly describe the dispersion interactions, Grimme's empirical dispersion correction GD3BJ was applied.[164]

Statement of Contribution of Co-Authors

The following is the suggested format for the required declaration provided at the start of any thesis chapter which includes a co-authored publication, whether published or unpublished. This is a requirement for all Theses by Publication; and for any Theses by Monograph where the relevant published papers are incorporated into the body of the thesis or comprise a chapter within the thesis.

The authors listed below have certified that:

1. *they meet the criteria for authorship and that they have participated in the conception, execution, or interpretation, of at least that part of the publication in their field of expertise;*
2. *they take public responsibility for their part of the publication, except for the responsible author who accepts overall responsibility for the publication;*
3. *there are no other authors of the publication according to these criteria;*
4. *potential conflicts of interest have been disclosed to (a) granting bodies, (b) the editor or publisher of journals or other publications, and (c) the head of the responsible academic unit, and*
5. *they agree to the use of the publication in the student's thesis and its publication on the QUT's ePrints site consistent with any limitations set by publisher requirements.*

In the case of this chapter:

Please state the publication title and date of publication or status: Ion mobility mass spectrometry coupled with molecular dynamics simulations: in-depth structural analysis of polystyrene-based Au-containing copolymers

Published on 28 March 2025

Contributor	Statement of contribution*
Sarajit Naskar	Designed and conducted experiments, analyzed data, and wrote the manuscript
Co-first author's name (if applicable)	
Aidan Izuagbe	Synthesized all polymers
Vincent Lemaur	Guided the molecular dynamics simulation
Quentin Duez	Guided the experiments and data analysis
Andrea Minoia	Guided the molecular dynamics simulation
Julien De Winter	Guided the experiments and data analysis
Stephen J. Blanksby	Supervised the project and guided the manuscript preparation
Jérôme Cornil	Supervised the project and guided the manuscript preparation
Christopher Barner-Kowollik	Supervised the project and guided the manuscript preparation
Pascal Gerbaux	Supervised the project and guided the manuscript preparation

Ion Mobility Mass Spectrometry Coupled with Molecular Dynamics Simulations: In-depth Structural Analysis of Polystyrene-based Au-Containing Copolymers

The main objective of the current thesis is to apply ion mobility–mass spectrometry (IM-MS) as a tool for the characterization of single chain polymeric nanoparticles (SCNPs) starting from the precursor polymers and copolymers. After the successful characterization of polystyrene ions bearing various end groups across a wide range of degrees of polymerization (*DP*) in Chapter 1, we will here proceed further toward complexity by submitting to our IMS/MD combination copolymer ions, composed of styrene (STY) and hydroxyl-functionalized styrene (STY-CH$_2$-OH) monomers. These copolymers exhibit a wide variety of compositions, with the number of STY-CH$_2$-OH units ranging from zero to six. All compositional variants will be thoroughly analyzed over a broad range of *DP*s. After gaining in-depth knowledge of the three-dimensional shape of the copolymer ions, the position of the functional groups, and their folding behavior, the IM-MS/MD combination will be applied to the characterization of an even more intricate copolymer on the way to SCNPs, namely copolymers constituted by styrene, styrene-

CH$_2$-OH and styrene-PPh$_2$-AuCl monomers, and bearing a TEMPO unit as the initiator end group.

Herein, IM-MS – coupled with molecular dynamics (MD) simulations – will be demonstrated to be a powerful technique to probe the three-dimensional structure and the position of functional groups within complex copolymer ions.

Introduction

Our team recently reported the synthesis and characterization of polystyrene-based gold containing photo-switchable copolymers and their subsequent folding into SCNPs.[131] The chains are decorated with pendent phosphine ligands complexed with catalytically active gold motifs (AuCl unit). ^{1}H Nuclear Magnetic Resonance (NMR) spectroscopy and size exclusion chromatography (SEC) were used to characterize the pre-polymers as well as evidence the formation of the SCNPs.[131]

In the bottom-up approach toward the use of IMS-MS/MD for prepolymer and ultimately SCNP precursor characterization, we investigated in Chapter 1 the gas phase structure of polystyrene ions with different end groups to establish how the nature and the rigidity of the monomer unit affect the charge stabilization. We demonstrated that – in contrast to polar polymers wherein the charges are located deep in the ionic globules – the charges in the PS ions are rather located at the periphery of the polymer backbone leading to singly and doubly charged PS ions adopting dense elliptic-shaped structures.[165]

In the present chapter, we move one step further towards detailed SCNP characterization using the IMS-MS/MD combination by examining in detail the conformation of gaseous Au-functionalized SCNP pre-copolymer ions containing three styrene derivatives, *i.e.* styrene, styrene-CH$_2$-OH and styrene-PPh$_2$-AuCl, refer to Scheme 1. The examined copolymer – with its chain distribution and statistical incorporation of the three monomer units – is a highly information rich system, where each chain is part of a unique subset of identical chains, making is a highly worthwhile system to carefully characterize well beyond the standard analysis methodologies used for SCNP pre-polymer analysis. We submit that while the current analysis is conducted in the gas phase, important learnings

about the copolymer structure can be deduced, including on the all-important chain folding geometry. While the coil geometry in solution will certainly be affected by the solvent, gas phase methods provide detailed insight into chain conformations. We believe that only via the combination of a range of analytical techniques applied to a specific polymer system – including both solution and gas phase – can an encompassing picture of its folding geometry be established. Finally, the current study does not seek to sequence each polymer chain to determine the order of the co-monomer units, but rather provides overarching composition formation and folding for subsets of identical chains.
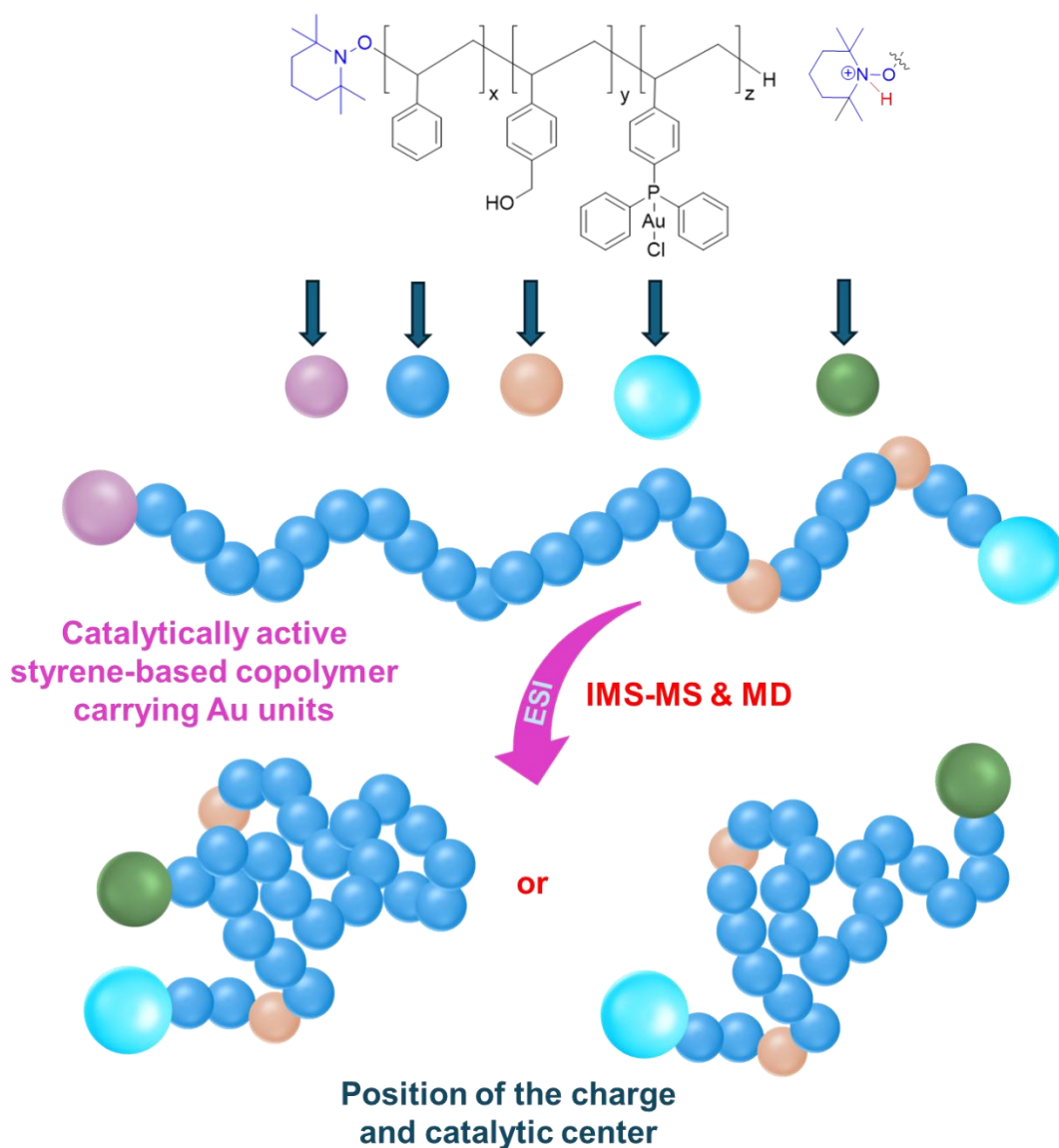
Scheme 1. Establishing the folding of complex copolymer ions using the IMS-MS/MD approach.

The experimental and theoretical methodologies are described in the annexes.

Results and Discussion

The copolymers, *i.e.* TEMPO-(styrene)$_x$-(styrene-CH$_2$-OH)$_y$ (M_n = 3,200 g mol^{-1} and Đ = 1.2, determined via SEC, refer to Figure A1, prepared by Dr. Aiden Izuagbe) and TEMPO-(styrene)$_x$-(styrene-CH$_2$-OH)$_y$-(styrene-PPh$_2$)$_w$-(styrene-PPh$_2$-AuCl)$_z$ (M_n = 2400 g mol^{-1} and Đ = 1.1, determined via SEC, refer to Figure A2), are presented in Scheme 2. We defined the 2,2,6,6-tetramethylpiperidine-*N*-oxyl end group (TEMPO) as "E", the styrene residue as "S", and the styrene-CH$_2$-OH residue as "B", whereas "Au" is assigned to the styrene-PPh$_2$-AuCl moiety. Note also that some free styrene-PPh$_2$ have also been detected and were marked as "P". Herein, the degree of polymerization (*DP*) will be defined as the sum of the numbers of all different monomer units (x + y + w + z) in the copolymers.
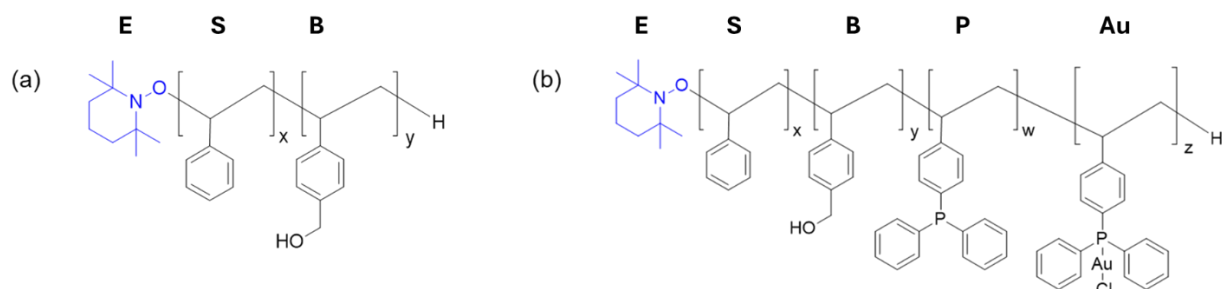
Scheme 2. The abbreviation used in the current study alongside the chemical structures of the selected copolymers: (a) TEMPO-(styrene)$_x$-(styrene-CH$_2$-OH)$_y$ and (b) TEMPO-(styrene)$_x$-(styrene-CH$_2$-OH)$_y$-(styrene-PPh$_2$)$_w$-(styrene-PPh$_2$-AuCl)$_z$.

1. ESI-MS analysis of the copolymers

Figures 1 and 2 present the ESI mass spectra recorded for both copolymers. Singly charged ions (+1) are predominantly detected as proton adducts, such as [TEMPO-(styrene)$_x$-(styrene-CH$_2$-OH)$_y$ + H]$^+$ and [TEMPO-(styrene)$_x$-(styrene-CH$_2$-OH)$_y$-(styrene-PPh$_2$)$_w$-(styrene-PPh$_2$-AuCl)$_z$ + H]$^+$. From Figure 1, we observe that the TEMPO-

(styrene)$_x$-(styrene-CH$_2$-OH)$_y$ copolymers are mostly detected as [E-S$_x$-B$_0$ + H]$^+$ (red circles), [E-S$_x$-B$_1$ + H]$^+$ (blue triangles) and [E-S$_x$-B$_2$ + H]$^+$ (green squares) ions. The ion compositions have been confirmed based on the measured *m/z* values and by comparison between experimental and simulated isotope patterns (refer to Figure A3 for selected examples). Beside these dominant monomer combinations, less abundant ions with different compositions are also detected, typically [E-S$_x$-B$_{3-6}$ + H]$^+$.
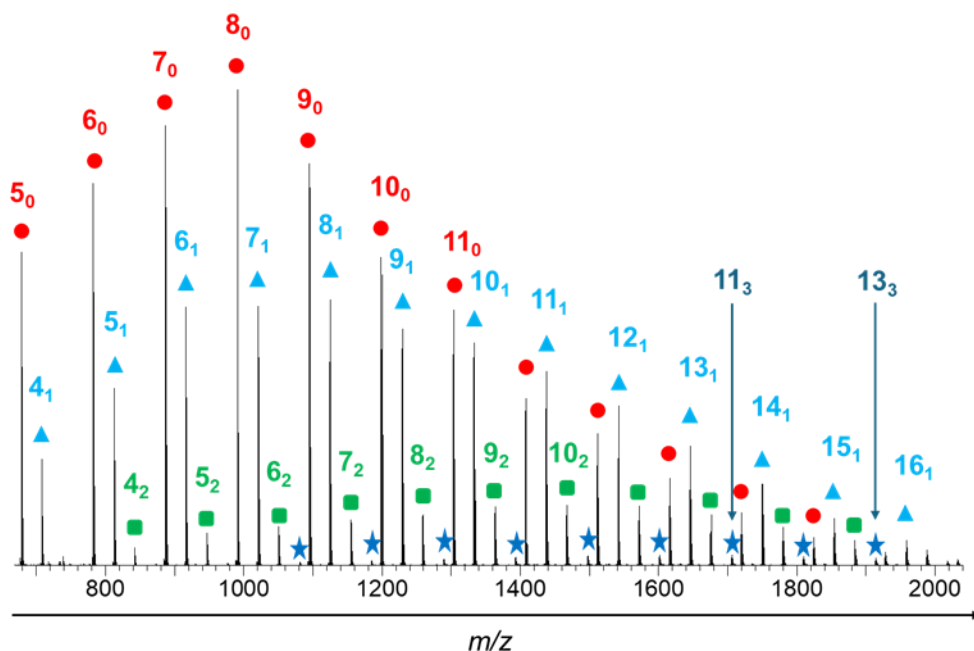
Figure 1. ESI-MS mass spectrum of TEMPO-(styrene)$_x$-(styrene-CH$_2$-OH)$_y$ (0.01 mg mL^{-1}) in acetonitrile/ tetrahydrofuran (80/20) (*v/v*). Red circles correspond to [E-S$_x$-B$_0$ + H]$^+$ ions (exemplified as x$_0$ in the figure), light blue triangles represent [E-S$_x$-B$_1$ + H]$^+$ ions (x$_1$), green squares correspond to [E-S$_x$-B$_2$ + H]$^+$ ions (x$_2$) ions and blue stars indicate [E-S$_x$-B$_3$ + H]$^+$ ions (x$_3$) ions.

The ESI-MS analysis of the second copolymer, *i.e.* TEMPO-(styrene)$_x$-(styrene-CH$_2$-OH)$_y$-(styrene-PPh$_2$)$_w$-(styrene-PPh$_2$-AuCl)$_z$, affords a more complex mass spectrum presented in Figure 2. This copolymer is mostly detected as [E-S$_x$-B$_0$-P$_0$-Au$_0$ + H]$^+$ (purple triangles), [E-S$_x$-B$_0$-P$_0$-Au$_1$ + H]$^+$ (green stars), [E-S$_x$-B$_1$-P$_0$-Au$_1$ + H]$^+$ (red squares), and [E-S$_x$-B$_4$-P$_1$-Au$_0$ + H]$^+$ (blue circles) ions. The ion compositions have been confirmed based on the measured *m/z* values and by comparison between experimental and simulated isotope patterns (refer to Figures A4-5 for selected examples). Beside these dominant monomer combinations, less abundant ions with different compositions are also

detected, typically $[E-S_x-B_{1-2}-P_0-Au_{0-1} + H]^+$, $[E-S_x-B_2-P_2-Au_0 + H]^+$ and $[E-S_x-B_4-P_1-Au_{0-1} + H]^+$.
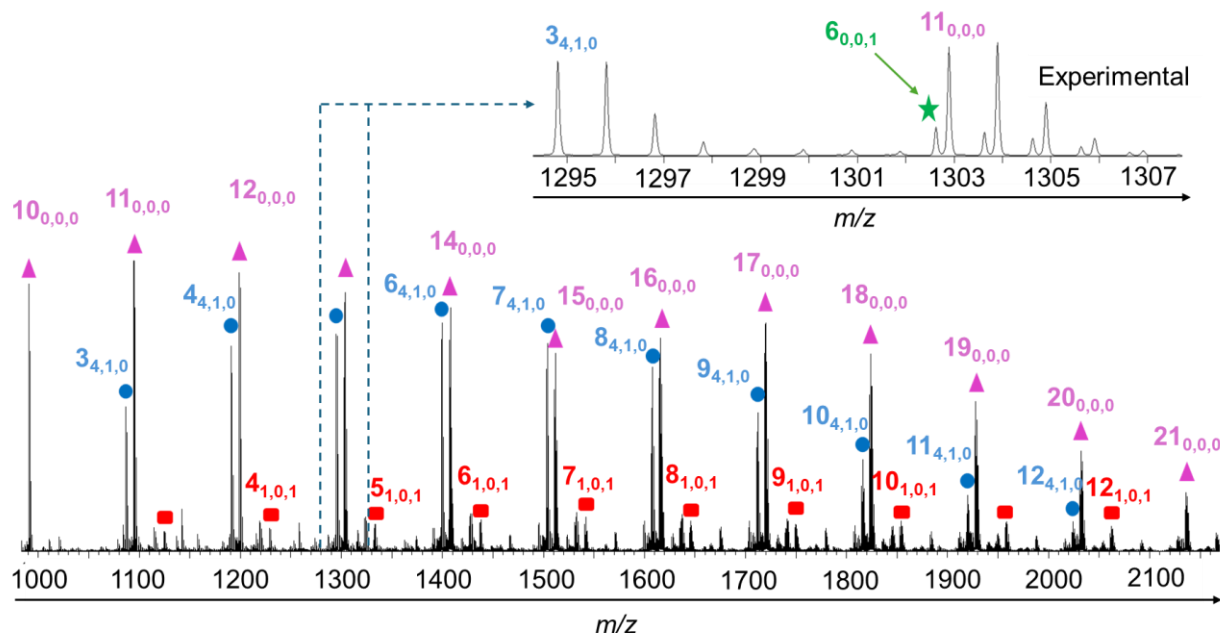
Figure 2. ESI-MS mass spectra of TEMPO-(styrene)$_x$-(styrene-CH$_2$-OH)$_y$-(styrene-PPh$_2$)$_w$-(styrene-PPh$_2$-AuCl)$_z$ (0.01 mg mL^{-1}) in acetonitrile/ tetrahydrofuran (80/20) (*v/v*). Blue circles correspond to $[E-S_x-B_4-P_1-Au_0 + H]^+$ ions (exemplified as $x_{4,1,0}$ in the Figure), purple triangles represent $[E-S_x-B_0-P_0-Au_0 + H]^+$ ions ($x_{0,0,0}$), green stars correspond to $[E-S_x-B_0-P_0-Au_1 + H]^+$ ions ($x_{0,0,1}$) ions and red squares indicate $[E-S_x-B_1-P_0-Au_1 + H]^+$ ions ($x_{1,0,1}$) ions.

2. IMS-MS experiments on gaseous copolymer ions

Ion mobility experiments have been performed on all detected copolymer ions, and the experimental collisional cross sections (CCS_{exp}) have been determined. We further analyzed the symmetry of the Arrival Time Distribution (*ATD*) for all ions to exclude the existence of non-interconverting gas phase structures (refer to Figure A6 for selected examples). Facing the large dataset of determined CCS_{exp}, we decided to use the "*CCS vs DP*" graphical representation (the so-called trend line analysis) for data visualization. Figure A7a presents the evolution of the CCS_{exp} *vs DP* for the $[E-S_x-B_y + H]^+$ ions (*DP* = x + y), whereas Figure A7(b-f) features the data for the detected $[E-S_x-B_y-P_w-Au_z + H]^+$ ions (*DP* = x + y + w + z). From Figures A6 and A7a, for a given *DP*, we respectively observed that the impact of the copolymer sequence heterogeneity on the CCS_{exp} is very

limited and that the incorporation of 1 to 6 styrene-CH_2-OH residue(s) in the polymer backbone does not significantly influence the CCS_{exp}. For the second copolymer, *i.e.,* TEMPO-(styrene)$_x$-(styrene-CH_2-OH)$_y$-(styrene-PPh_2)$_w$-(styrene-PPh_2-AuCl)$_z$, the incorporation of styrene-PPh_2 and/or styrene-PPh_2-AuCl units in the copolymer backbone strongly impacts the CCS_{exp} due to their bulkiness. Thus, it is challenging to establish the influence of these residues on the 3D structures, *i.e.* the folding, of the copolymer ions only based on comparison of CCS_{exp} and molecular modeling appears mandatory to generate candidate structures for an atomistic description of the ion folding.

3. Molecular modeling and theoretical *CCS* calculation for [E-S_x-B_y + H]$^+$ ions

When investigating copolymers, the comonomer arrangement along the polymer backbone, *i.e.* their sequence, determines the behavior of individual chains; in the context of copolymer ion folding, the impact of the sequence on the ion *CCS* deserves to be discussed. From Figure A6, we can infer that the expected sequence heterogeneity for a given composition does not translate into broad or asymmetrical *ATD* characteristics of different ion structures. To further assess whether alternating, block or random copolymers behave differently upon ionization and desolvation, we generated two copolymers, namely [E-S_6-B_6 + H]$^+$ ions (*DP* = 12) and [E-S_{12}-B_6 + H]$^+$ ions (*DP* = 18) presenting higher proportions of B monomers than the detected ones (see Figure 1). We executed MD simulations on a large diversity of hypothetical sequences and calculated the corresponding CCS_{th}. As shown in Figure A8, for the [E-S_6-B_6 + H]$^+$ ions and the [E-S_{12}-B_6 + H]$^+$ ions, the CCS_{th} ranges expand from 365 to 385 Å^2 and from 455 to 490 Å^2, respectively. Since the CCS_{FWHM} (FWHM stands for *Full Width Half Maximum* – 50%) resolution of our Waters Synapt G2-*Si* is 40, *i.e.* $R_{CCS} = CCS/\Delta^{50\%}CCS = 40$, $\Delta^{50\%}CCS \sim$ 9 and $\sim$ 12 Å^2 would characterize the *CCS* distribution for both ion compositions, respectively. When analyzing Figure A8, we predict that for the considered hypothetical copolymer ions, the Waters Synapt G2-*Si* mass spectrometer would be able to discriminate different sequences, even if most of the different sequences will be hidden under a given *CCS* distribution centered $\sim$ 375 and 475 Å^2, respectively for the [E-S_6-B_6 + H]$^+$ ions and the [E-S_{12}-B_6 + H]$^+$ ions.

To obtain atomistic insights into our experimental results, we selected one specific copolymer composition ([E-S_{22}-B_1 + H]$^+$ ions (*m/z* 2581.6)) for the theoretical modelling and created three different sequences, namely E-B_1-S_{22}, E-S_{11}-B_1-S_{11} and E-S_{22}-B_1. In these sequences, the alcohol moiety is positioned close to the TEMPO end group, in the middle of the chain and at the extremity of the chain, respectively. The CCS_{exp} has also been measured around 540 Å^2 with a $\Delta^{50\%}CCS$ ~ 17 Å^2 and a R_{CCS} ~ 32, as shown in Figure 3. The MD geometries are characterized by CCS_{th} at 530±8, 543±8 and 554±7 Å^2, respectively, for the E-S_{11}-B_1-S_{11}, E-S_{22}-B_1 and E-B_1-S_{22} ions. Interestingly, the sequences with the styrene-CH_2-OH moiety lying away from the TEMPO end group fit the experimental values, whereas the [E-B_1-S_{22} + H]$^+$ ions appear less folded, *i.e.* with higher *CCS*.
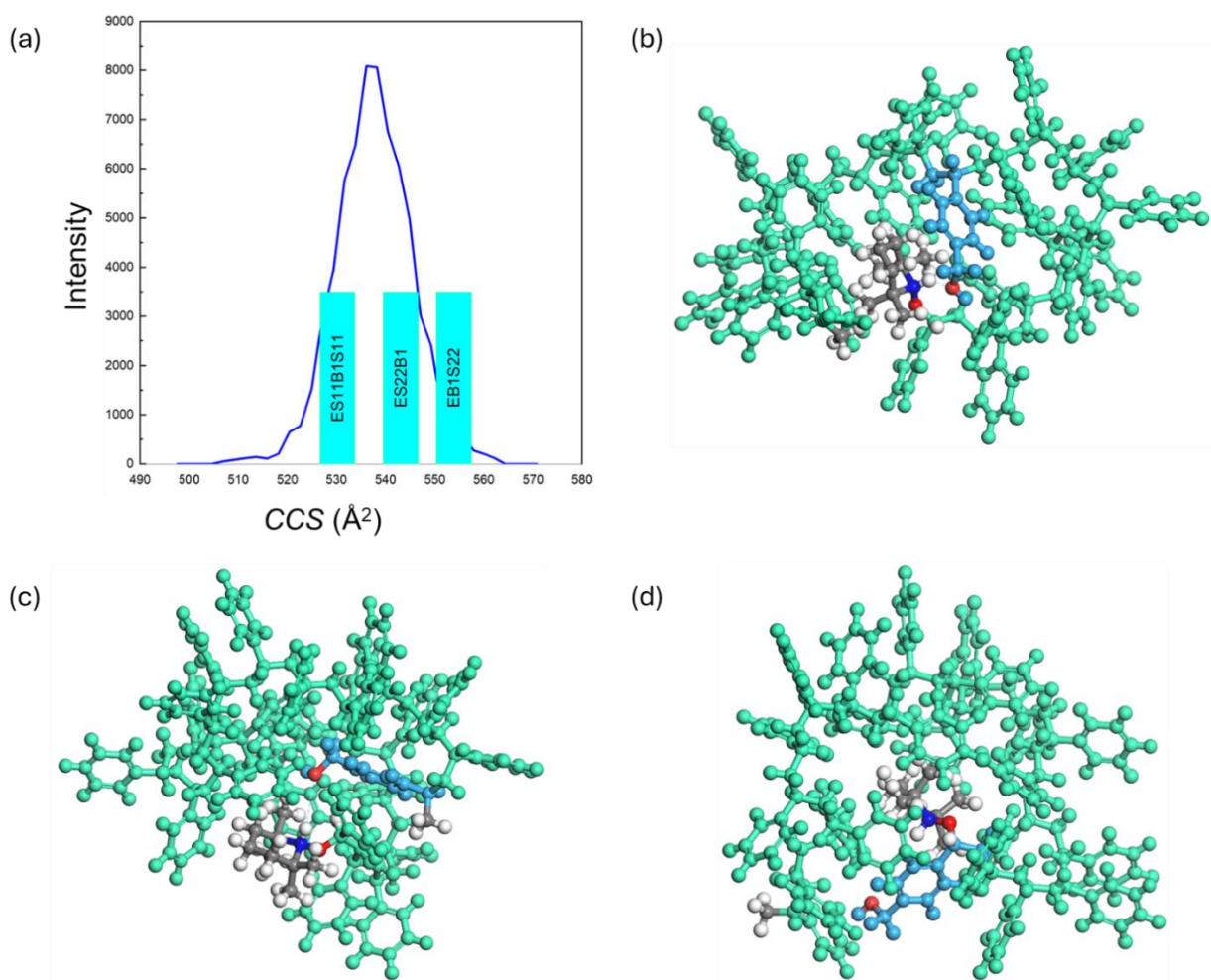
Figure 3. Ion mobility mass spectrometry analysis and Molecular Dynamics simulations of [TEMPO-(styrene)$_{22}$-(styrene-CH$_2$-OH)$_1$ + H]$^+$ ions presenting three different sequences, namely E-S$_{11}$-B$_1$-S$_{11}$, E-S$_{22}$-B1 and E-B$_1$-S$_{22}$: (a) experimental *CCS* distribution and theoretical *CCS*$_{th}$ for the [*M*+H]$^+$ ions; (b-c-d) snapshots of the last frame of the MD simulations for (b) E-S$_{11}$-B$_1$-S$_{11}$ (*CCS*$_{th}$ = 530 Å^2), (c) E-S$_{22}$-B$_1$ (*CCS*$_{th}$ = 543 Å^2) and (d) E-B$_1$-S$_{22}$ (*CCS*$_{th}$ = 554 Å^2) ions.

From the MD simulations (refer to Figure 3), we detected strong H-bonds associating protonated TEMPO (H atom) and the styrene-CH$_2$-OH group (O atom) for the more compact E-S$_{11}$-B$_1$-S$_{11}$ (3b) (1.69Å ± 0.11Å) and E-S$_{22}$-B$_1$ (3c) ions (1.60Å ± 0.08Å), whereas this H-bond is not present when the styrene-CH$_2$-OH group is directly attached to the TEMPO initiator in the E-B$_1$-S$_{22}$ ions (3d) (4.96Å ± 0.40Å). The strong H-bonds between the protonated TEMPO and the styrene-CH$_2$-OH group have also been measured for other copolymer compositions which have been experimentally identified (refer to Figure A9 and Figure A10). This has been confirmed on model systems using Density Functional Theory (DFT) calculations which point to a hydrogen bond length of 1.81 Å and an interaction energy between the two subunits involved in the hydrogen bond of 8.1 kcal/mol.

We further exposed to MD simulations all detected [E-S$_x$-B$_1$ + H]$^+$ ions by selecting the E-S$_x$-B$_1$ sequence, *i.e.,* with the styrene-CH$_2$-OH group at the extremity of the copolymer chain. As featured in Figure A11, we found an excellent agreement between *CCS*$_{th}$ and *CCS*$_{exp}$ over the whole investigated mass range (*m/z* = 750 – 2750), allowing us to propose the optimized geometries as promising candidates for the detected ions. In the previous chapter related to the TEMPO-initiated polystyrene (PS) ions, we reported that the folding of the PS rigid chain is controlled by phenyl ring interactions with the charge ultimately remaining excluded from the core of the globular ions. From the structures presented in Figure 3, we observe that protonated TEMPO is associated with the styrene-CH$_2$-OH group through a strong H-bond. To better understand its role on the structure of the copolymer, the distance between the charged center (protonated TEMPO) and the center-of-mass of the ion has been divided by the radius of gyration (*R*$_g$) for all [E-S$_x$-B$_1$ + H]$^+$ ions (x = 5-22) to generate normalized data for increasing *DP (= x+1)*. As shown in Figure 4, the normalized distance is ~0.8 for *DP* = 6 and decreases continuously upon chain elongation to reach ~0.3 for *DP* = 23, revealing that, when an H-bond is present,

the charged end group is progressively integrated at the center of the ions (refer to Figure 4) with increasing *DP*.
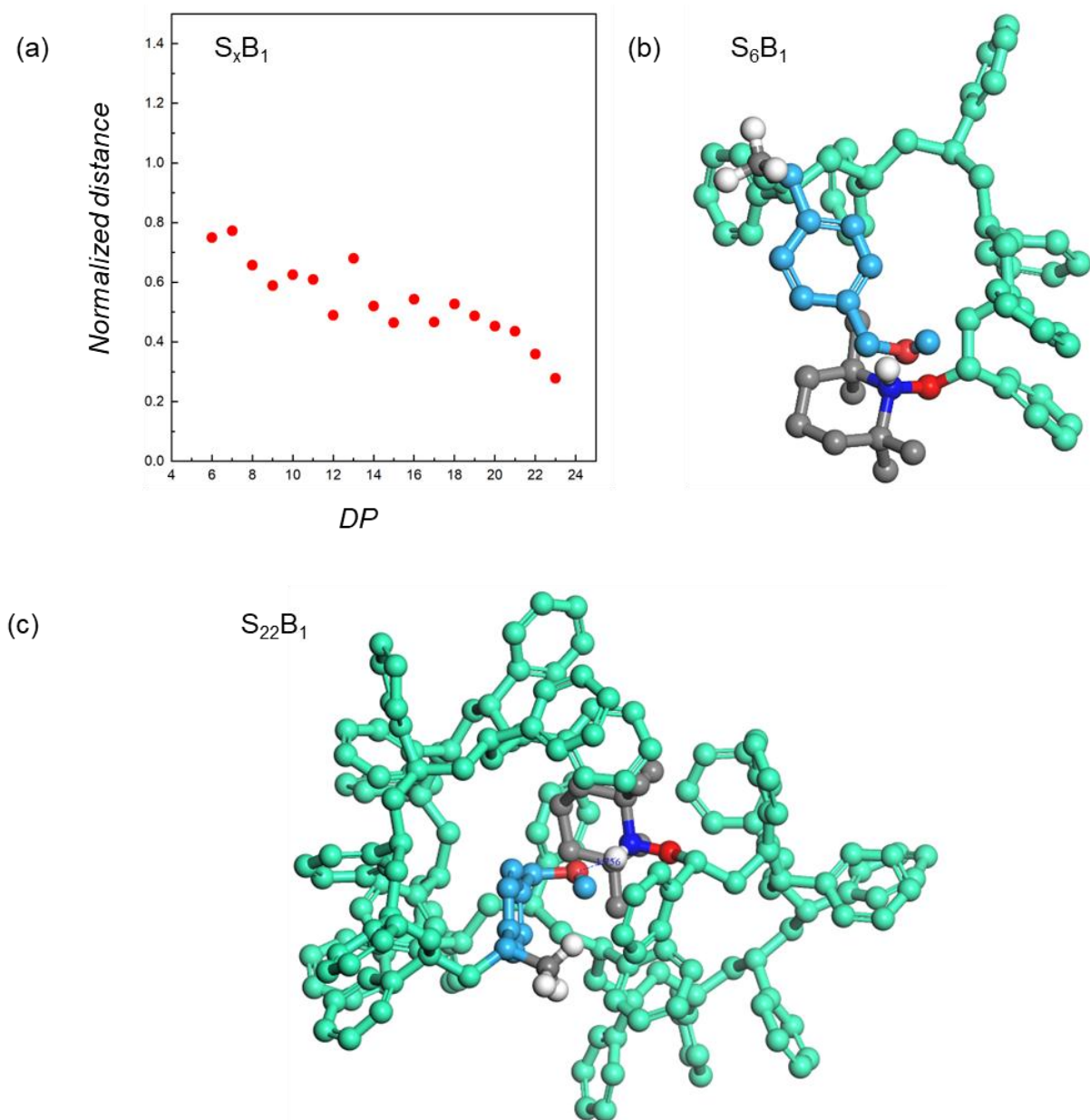
Figure 4. Molecular Dynamics simulations (PCFF force field, 298K, 25 ns) of [TEMPO-(styrene)$_x$-(styrene-CH$_2$-OH)$_1$ + H]$^+$ions: (a) represents the evolution of the distance between the charged center and the center-of-mass (COM) normalized by the ion radius of gyration (R_g) that is marked by normalized distance. (b) presents a snapshot of the last frame of the MD for [TEMPO-(styrene)$_6$-(styrene-CH$_2$-OH)$_1$ + H]$^+$ ions (*DP* = 7).). (c) presents a snapshot of the last frame of the MD for [TEMPO-(styrene)$_{22}$-(styrene-CH$_2$-OH)$_1$ + H]$^+$ ions (*DP* = 23).

In the previous chapter on the gas phase structure of PS ions,[165] we used MD simulations to demonstrate that the folding of the PS rigid chain is induced by phenyl ring interactions, with the charge ultimately remaining excluded from the core of the globular ions, whereas the folding of polyether ions is initiated by the folding of the flexible polyether chain around the sodium ion that remains deeply settled in the core of the ions. The data of Figure 4, *i.e.* polymer ions with the charge remaining localized in the core of the ions upon *DP* increase, prompted us to examine frame-by-frame MD trajectories for the E-S_{22}-B_1, E-B_1-S_{22} and E-S_{11}-B_1-S_{11} ions. As shown in Figures 5 and A12, the chain folding again appears to be triggered by the phenyl ring interactions for all ions. For the more compact [E-S_{22}-B_1 + H]$^+$ (CCS_{th} = 543 Å^2) and [E-S_{11}-B_1-S_{11} + H]$^+$ (CCS_{th} = 530 Å^2) ions, once created, there is the appearance of a H-bond between protonated TEMPO and styrene-CH_2-OH that further stabilizes them in the core of the globular ions, see Figure 5 for a typical example. However, for the less compact [E-B_1-S_{22} + H]$^+$ (CCS_{th} = 554 Å^2) ions (refer to Figure A12b) the direct proximity of the TEMPO end-group and the styrene-CH_2-OH first residue does not allow to form an H-bond so that the protonated TEMPO remains at the surface of the globular ion.
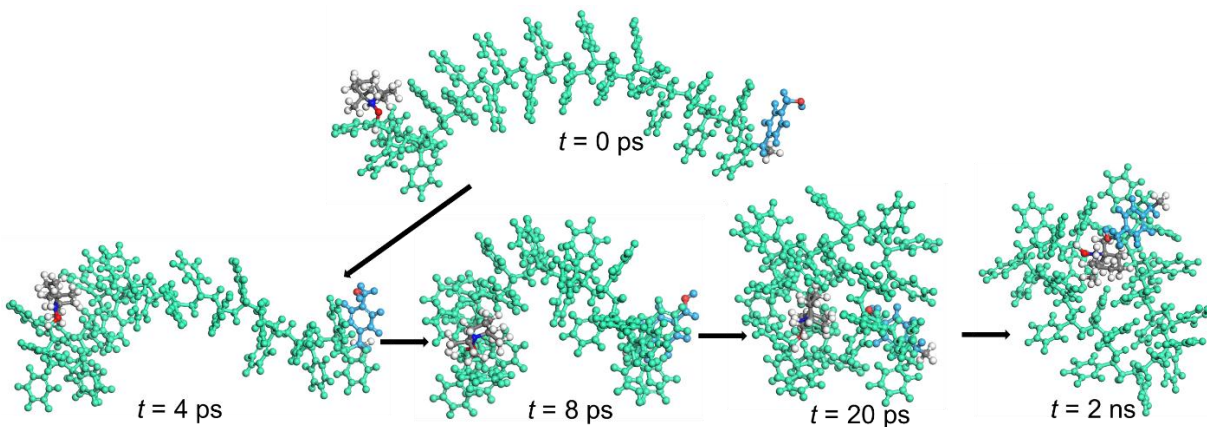
Figure 5. Molecular Dynamics simulations (PCFF force field, 300 K, 2 ns) of [E-S_{22}-B_1 + H]$^+$ ions (*DP* = 23): snapshots at different times of the trajectory revealing that the folding process is mostly initiated by π-π interactions between phenyl rings with the H-bonded protonated TEMPO and styrene-CH_2-OH ultimately incorporated in the core of the equilibrated structure. The styrene-CH_2-OH and the TEMPO residues are highlighted in grey and blue for visualization.

4. Molecular modeling and theoretical *CCS* calculations for $[E-S_x-B_y-Au_z + H]^+$ ions

In our bottom-up approach, we further examined selected TEMPO-(styrene)$_x$-(styrene-CH$_2$-OH)$_y$-(styrene-PPh$_2$-AuCl)$_z$ copolymer ions via our IMS-MS/MD approach, namely the $[E-S_x-B_y-Au_z + H]^+$ ions detected in the ESI mass spectrum presented in Figure 2. PCFF was used in the previous chapter.[165] However, due to the absence of the Au descriptors in the PCFF force field, we turned to Universal Force Field (UFF) for the TEMPO-(styrene)$_x$-(styrene-CH$_2$-OH)$_y$-(styrene-PPh$_2$-AuCl)$_z$ copolymer ions. As described in Annexes (refer to Figure A13), we tested whether UFF was able to reproduce the CCS_{exp} and CCS_{PCFF} by calculating, using both UFF and PCFF, the CCS_{th} for TEMPO-initiated polystyrene homopolymer ions (DP = 8-17) and TEMPO-initiated styrene/styrene-CH$_2$-OH copolymer ions (DP = 8-19). The three different *CCS, i.e.* CCS_{exp}, CCS_{UFF} and CCS_{PCFF} being nearly identical over the investigated DP-ranges for both copolymer ions, we consider that both force fields are able to generate reliable molecular structures without any further validation or parametrization.

We were thus interested in the comparison between the $[E-S_x-B_1-Au_0 + H]^+$ (Figure 1) and the $[E-S_x-B_0-Au_1 + H]^+$ (green stars in Figure 2) ions to question the impact of the bulky Au-containing group on the ion structure. To start our MD simulations, we created $[E-S_x-B_0-Au_1 + H]^+$ input structures by positioning the gold-containing residue at the extremity of the PS backbone, *i.e.* by formally replacing the styrene-CH$_2$-OH group within the $[E-S_x-B_1-Au_0 + H]^+$ ions. As shown in Figure 6a, for both ion series the CCS_{exp} and CCS_{th} are nicely fitting. Obviously, the *CCS* of the Au-containing ions are larger for a given *DP* due to the presence of the bulky triphenylphosphine ligand. As featured in Figure 6b, for the specific case of the $[E-S_{13}-Au_1 + H]^+$ ions, an H-bond is formed between the protonated TEMPO end group and the chlorine atom of the distal triphenylphosphine-AuCl moiety (refer to Figure A14), associating hereby both extremities of the polymer backbone. This is reminiscent of the styrene/styrene-CH$_2$-OH case, except that the N-H••O-H bond is here replaced by a N-H••Cl bond. A second difference is the position of the charged center in the globular ions. Indeed, as shown in Figure 6c, from *DP* = 7 to 16, the charged center remains at the surface of the ion globule because of the steric hindrance created

by the PPh_3 unit, which prevents the charged center from getting incorporated in the center of the globular ion, as also sketched in Figure 6b. MD simulations indicate that the H-bond distance remains between 2.5 and 3 Å (refer to Figure A15). We also calculated this H-bond length using the same DFT approach on model systems as before except that the gold atom is described using the LANL2DZ basis set. The average N-H••Cl H-bond length amounts to 2.2 Å, and the corresponding interaction energy between the styrene-PPh_2-AuCl and the protonated TEMPO units was estimated as 15.4 kcal/mol, twice that calculated for the styrene-CH_2-OH/TEMPO interaction (8.12 kcal/mol).
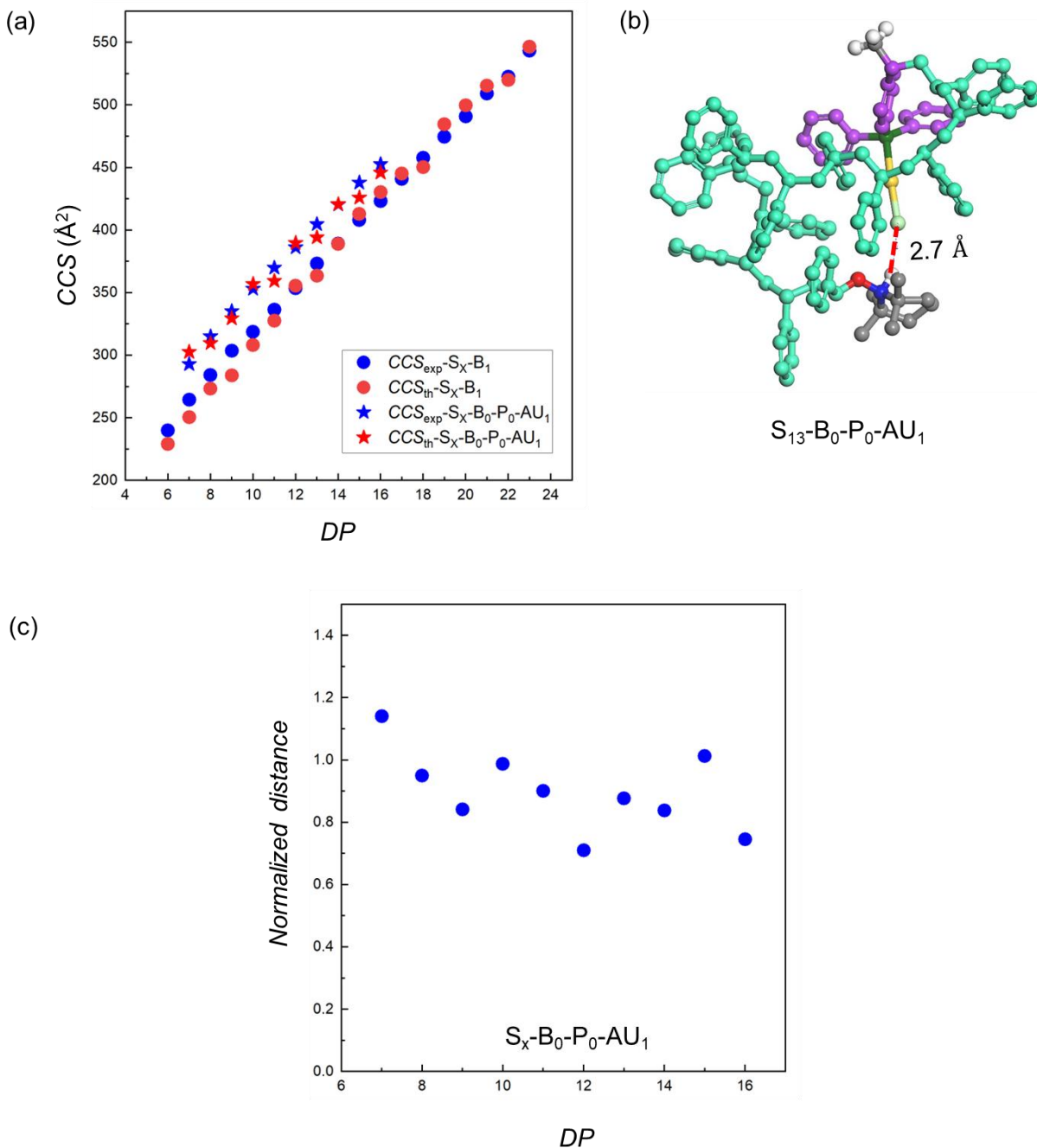
Figure 6. Ion mobility mass spectrometry analysis and Molecular Dynamics simulations (UFF/PCFF force field, 298K, 25 ns) of $[E-S_x-B_1 + H]^+$ (PCFF force field) and $[E-S_x-Au_1 + H]^+$ ions (UFF force field): (a) comparison between the CCS_{exp} and CCS_{th} over the full DP range, (b) snapshot of the last frame of the MD (UFF force field, 298K, 25 ns) for $[E-S_{13}-Au_1 + H]^+$ ions revealing the presence of an H-bond between protonated TEMPO and the chlorine atom of the triphenylphosphine-AuCl moiety, and (c) represents the evolution of the distance between the charged center and the center-of-mass (COM) normalized by the ion radius of gyration (R_g) that is marked by normalized distance.

As shown in Figure 2, copolymer ions combining the three different monomers, *i.e.* styrene, styrene-CH_2-OH and styrene-PPh_2-AuCl, were also detected upon ESI analysis, with the specific case of [E-S_x-B_y-Au_1 + H]$^+$ ions (y = 1 and 2). We determined their CCS_{exp} and CCS_{th} that are compared in Figure 7 and we once again observed excellent agreement between the experimental and theoretical values.
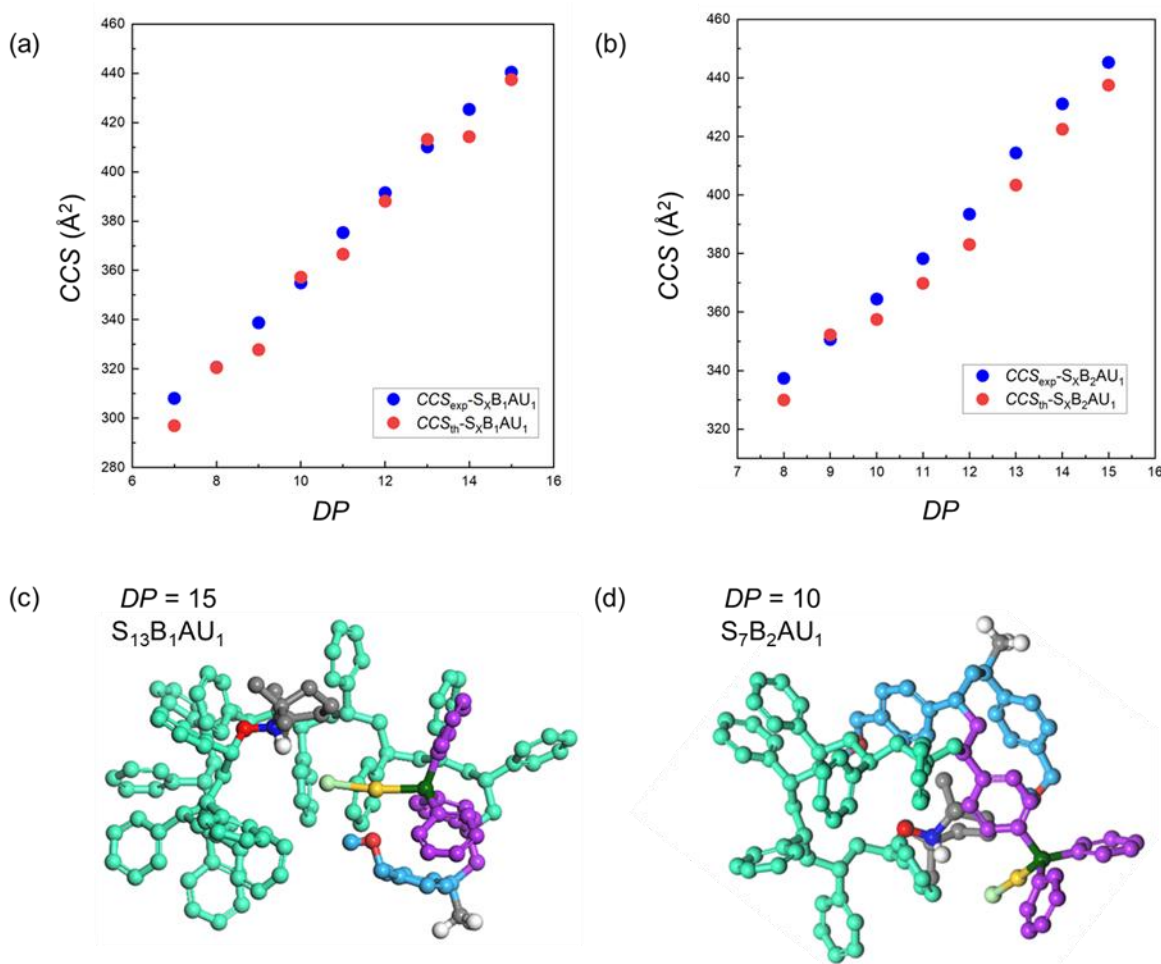
Figure 7. Ion mobility mass spectrometry analysis and Molecular Dynamics simulations of [E-S_x-B_1-Au_1 + H]$^+$ and [E-S_x-B_2-Au_1 + H]$^+$ ions: (a-b) comparison between the CCS_{exp} and CCS_{th} over the full DP range, and (c-d) snapshots of the last frame of the MD (UFF force field, 298K, 25 ns) for [E-S_{13}-B_1-Au_1 + H]$^+$ and [E-S_7-B_2-Au_1 + H]$^+$ ions, respectively.

The hydroxyl/chloride groups of the styrene-CH_2-OH/styrene-PPh_2-AuCl monomer units are thus H-bonded with protonated TEMPO (NH group) via the charged center (refer to Figure 8). When the chlorine atom rather than the hydroxyl group is involved in a hydrogen bond, the DFT results demonstrate that the ion is significantly more stabilized. Although

depending on the composition, there may be also additional weak hydrogen bonds (refer to Figure A14).
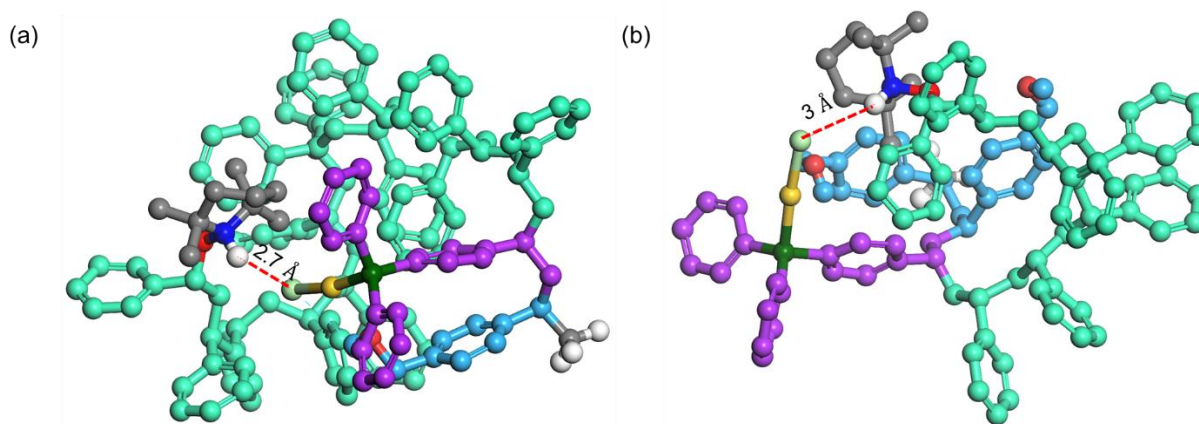
Figure 8. Molecular Dynamics simulations (UFF force field, 298K, 25 ns) of [TEMPO-(styrene)$_x$-(styrene-CH$_2$-OH)$_y$-(styrene-PPh$_2$-AuCl)$_z$ + H]$^+$ ions, snapshot of the last frame of the MD : (a) *DP* = 15 (x = 13, y = 1, z = 1) and (b) *DP* = 10 (x = 7, y = 2, z = 1),) where the hydrogen bond and the bonding distance are represented in red. Here, the styrene monomer unit is indicated by dark green, the styrene-CH$_2$-OH is indicated by light blue, styrene-PPh$_2$ represent by the plum and the end group is indicated by grey.

Conclusions

The macromolecular architecture and coil folding of gaseous polystyrene complex copolymer ions have been examined using molecular dynamics simulations in conjunction with IMS-MS on the way to SCNP characterization. We examined the conformation of gaseous Au-functionalized copolymer ions consisting of three different monomer units in detail, *i.e.* styrene, styrene-CH$_2$-OH and styrene-PPh$_2$-AuCl. All copolymers were prepared via nitroxide mediated radical polymerization (NMP) using TEMPO as the initiator. All copolymer ions correspond to [*M*+H]$^+$ ions with the proton anchored on the nitrogen atom of the TEMPO end group.

The styrene/styrene-CH$_2$-OH ions were shown to be stabilized by a strong H-bond established between protonated TEMPO and the oxygen atom of the styrene-CH$_2$-OH group and the charge center gradually migrates from the surface of the ion structure toward the center of the ion aggregate as the *DP* increases. On the other hand, an N-H••Cl H-bond, associating protonated TEMPO to the chlorine atom, was also detected

via MD simulations and confirmed through DFT calculations for the styrene/styrene-CH_2-OH/styrene-PPh_2-AuCl ions. Due to the steric hindrance of the PPh_3 unit, the charged center of the gold copolymer remains at the surface of the globular ions, pointing to a strong impact of the chemical structure of the subunits on the three-dimensional conformation of the SNCP pre-polymers and hence on their resulting properties.

This investigation yielded several important findings. It demonstrated how polymer folding is influenced by the polarity of the end group and how the location of the charge center affects the three-dimensional structure of the collapsed polymer. These insights provided a deeper understanding of the polymer collapse process. After establishing a detailed understanding of the shape and 3D structure of polystyrene samples, the methodology was extended to more complex systems—first to copolymers composed of styrene (STY) and STY-CH_2-OH monomers, and ultimately to precursor SCNPs incorporating STY, STY-CH_2-OH, and STY-PPh_2-AuCl monomers.

Our group has previously reported an azobenzene-containing, photo-switchable SCNP composed of STY, STY-CH_2-OH, and STY-PPh_2-AuCl monomers, which exhibits catalytic activity.[131] The catalytic function is directly linked to the position and accessibility of the metal center. Consequently, understanding the three-dimensional shape and spatial distribution of functional groups is essential for controlling catalytic activity. In this context, IM-MS combined with MD simulations provides a powerful approach to elucidate the three-dimensional structure.

The primary focus of this thesis, however, is the investigation of precursor SCNPs. A bottom-up approach was adopted, beginning with polystyrene, then gradually increasing polymer complexity by incorporating additional monomers stepwise, ultimately culminating in the precursor SCNP.

The next step should be the analysis of the folded SCNPs via the methodology described herein, which includes a comparison of their catalytic ability in different solvents.[131]

Annexes

Ion Mobility Mass Spectrometry Coupled with Molecular Dynamics Simulations: In-depth Structural Analysis of Polystyrene-based Au-Containing Copolymers

*based on Naskar et al, "Ion Mobility Mass Spectrometry Coupled with Molecular Dynamics Simulations: In-depth Structural Analysis of Polystyrene-based Au-Containing Copolymers." Polym.Chem., 16 (**2025**) 2143-2153.*

Experimental Section

HPLC grade tetrahydrofuran (>99.8%), acetonitrile (>99.9%) and acetone (>99.8%) solvents were purchased from Chem-Lab (Zedelgem, Belgium). Sodium iodide was purchased from VWR (Leuven, Belgium) and used for ESI-MS calibration. Polyethylene glycol was acquired from Sigma-Aldrich and utilized as IMS-MS calibrant. TEMPO-(styrene)$_x$-(styrene-CH$_2$-OH)$_y$ (2,2,6,6-tetramethylpiperidine-*N*-oxyl end group - *Đ* = 1.2 – M_n = 3,200 g mol^{-1}) and TEMPO-(styrene)$_x$-(styrene-CH$_2$-OH)$_y$-(styrene-PPh$_2$)$_w$-(styrene-PPh$_2$-AuCl)$_z$ (2,2,6,6-tetramethylpiperidine-*N*-oxyl end group - *Đ* = 1.1 – M_n = 2,400 g mol^{-1}) were synthesized according to reference.[131]

Ion Mobility Experiments

1.0 mg mL^{-1} solutions of the copolymer were obtained by dissolving it in acetonitrile and tetrahydrofuran (80:20, *v/v*). The stock solutions were 100x diluted with acetonitrile and tetrahydrofuran (80:20, *v/v*) before ESI analysis. MS spectra and *CCS* measurements were performed on a Waters Synapt G2-*Si* mass spectrometer. The solutions were infused at a flow rate of 5 μL min^{-1} with a capillary voltage of 3.1 kV, a source temperature of 100 °C and a desolvation temperature of 150 °C. The standard IMS-MS parameters were : wave height = 40 V, wave velocities = 350 or 600 or 800 m s^{-1}, mass range = *m/z* 50 – 4000; N$_2$ flow rate = 60 mL min^{-1}, He flow rate = 180 mL min^{-1} and trap bias = 45.0 V. A pre-established calibration procedure[158] was used to convert the experimentally determined arrival time distributions to $^{TW}CCS_{N2 \rightarrow He}$,[159] which will be referred to as CCS_{exp}.

Molecular Dynamics (MD) Simulations

All MD simulations were performed with the Materials Studio software (BIOVIA, San Diego, CA).[160] For the TEMPO-(styrene)$_x$-(styrene-CH$_2$-OH)$_y$ copolymer, the PCFF force field was used and validated by the fact that the calculated effective density of TEMPO-polystyrene (0.62-0.66 Da/Å^3) is in good agreement with the reported density of bulk polystyrene (0.57-0.62 Da/Å^3).[165] For the TEMPO-(styrene)$_x$-(styrene-CH$_2$-OH)$_y$-(styrene-PPh$_2$-AuCl)$_z$ copolymer, we switched to the UFF force field since the parameters for gold are not available in PCFF. Both the PCFF and UFF force field were found to provide similar collisional cross sections for chains without styrene-PPh$_2$-AuCl units, thus validating our choice of using the UFF force field to model the behavior of polymer chains including the styrene-PPh$_2$-AuCl units. Force field assigned atomic charges were used for the simulations with the PCFF force field, while Gasteiger charges[166] were used in combination with the UFF force field. At first, geometry optimization was performed starting from a linear polymer chain (without charge). After adding a charge (H$^+$) to the optimized polymer chain, the geometry underwent additional optimization; the TEMPO group is chosen as the proton carrier due to the presence of the basic nitrogen atom.[165] Next, a quenched dynamics (frames quenched every 5 ps) was run for 20 ns at 300 K, with a 1 fs timestep, and a cutoff of 100 Å for the van der Waals and electrostatic interactions. The most stable structure obtained from the quenched dynamics was then used as the starting point for a 25 ns-long MD run (*NVT* ensemble; constant number of particles, *N*, volume, *V*, and temperature (*T* = 300 K) and using a 1 fs time step). From this MD trajectory, 500 structures were extracted and used to obtained an average theoretical *CCS*$_{th}$ computed by using the trajectory method[161] (TM) model implemented within the Collidoscope software.[154]

Density Functional Theory (DFT) Calculations

Density Functional Theory (DFT) calculations were performed using the Gaussian 09 (D01 revision)[162] suite to estimate the strength of the interactions between the fragments which are interacting through an hydrogen bond in the polymer.[167] In practice, the interaction energies have been estimated as the energy difference between the energy of the assembly made of the two interacting fragments and the energy of the isolated molecules. All the geometry optimization calculations were conducted using the B3LYP functional combined to the 6-31G** double zeta basis set for C, H, N, O, Cl, P and LANL2DZ basis set for gold.[168] To properly describe the dispersion interactions, Grimme's empirical dispersion correction GD3BJ was applied.[164] In all cases, the interaction energies have been corrected from the basis set superposition error (BSSE) through the use of the Counterpoise method.[169] Note that, in all DFT calculations, the complex structure of the macromolecules has not been considered, as only the two interacting fragments were taken into account.

1D NMR Spectroscopy Measurements

^{1}H and ^{31}P spectra were recorded on a Bruker Avance III HD 600 MHz spectrometer, equipped with a BBO-Probe (5 mm) with z-gradient (^{1}H 600.13 MHz). All measurements were carried out in deuterated solvents. The chemical shift (δ) is reported in parts per million (ppm) relative to the residual solvent protons. The measured coupling constants were calculated in Hertz (Hz). MESTRENOVA 11.0 software was used to analyze the spectra.

Size Exclusion Chromatography

The SEC measurements were conducted on a PSS SECurity2 system consisting of a PSS SECurity Degasser, PSS SECurity TCC6000 Column Oven (35 °C), PSS SDV Column Set (8x150 mm 5 µm Precolumn, 8x300 mm 5 µm Analytical Columns, 100000 Å, 1000 Å and 100 Å) and an Agilent 1260 Infinity Isocratic Pump, Agilent 1260 Infinity Standard Autosampler, Agilent 1260 Infinity Diode Array and Multiple Wavelength Detector (A: 254 nm, B: 360 nm), Agilent 1260 Infinity Refractive Index 5 Detector (35 °C).

HPLC grade THF, stabilized with BHT, is used as eluent at a flow rate of $1 \, mL \cdot min^{-1}$. Low disperse linear poly(styrene) (M_n $266 \, g \cdot mol^{-1}$ to $2.52 \cdot 10^6 \, g \cdot mol^{-1}$) standards (PSS ReadyCal) were used as calibrants. All samples were passed over $0.22 \, \mu m$ PTFE membrane filters. Molecular weight and dispersity analysis was performed in PSS WinGPC UniChrom software (version 8.2).

General Procedure for NMP of Styrene Based Monomers

Styrene (1.27 g, 12.21 mmol, 133 eqv), styryl alcohol (0.25 g, 1.84 mmol, 20 eqv) and NMP initiator, 2,2,6,6-Tetramethyl-1-(1-phenylethoxy)piperidine, (0.024 g, 0.092 mmol, 1 eqv) were added to a Schlenk tube. Dry toluene was added (0.8 mL) and the combined solution was subjected to four freeze pump thaw cycles. The Schlenk tube was subsequently placed into an oil bath heated to 135 °C and left to stir for 90 minutes. The reaction mixture was quenched upon exposure to atmosphere and cooling in liquid nitrogen and concentrated under reduced pressure, redissolved in a minimal amount of dichloromethane and precipitated three times into cold methanol. The precipitate was centrifuged and dried at 40 °C in a vacuum oven affording TEMPO-(styrene)$_x$-(styrene-CH$_2$-OH)$_y$ as an off white powder.

A styrene based, triphenylphosphine containing polymer was synthesized according to the same general NMP procedure[170,171] to synthesize TEMPO-(styrene)$_x$-(styrene-CH$_2$-OH)$_y$, with modified stoichiometry and a reaction duration of 45 minutes. Styrene (0.18 g, 1.77 mmol, 66 eqv), styryl alcohol (0.035 g, 0.27 mmol, 10 eqv), 4-(diphenylphosphino) styrene (0.039 g, 0.13 mmol, 5 eqv) and nitroxide initiator (0.007 g, 0.027 mmol, 1 eqv) combined in dry toluene (0.4 mL).

The resulting phosphine polymer (0.025 g, 0.012 mmol) was dissolved in dry dichloromethane (0.2 mL) and ethanol (0.4 mL), and HAuCl$_4$ • 3H$_2$O (0.006 g, 0.015 mmol) was dissolved separately in ethanol (0.4 mL) and added dropwise to the first solution. The combined reaction mixture was subsequently stirred at room temperature for 1.5 hours. After stirring the solvent was removed under reduced pressure and the resulting light-yellow solid was redissolved in a minimal amount of dichloromethane and

precipitated once into ice cold methanol and then dried at 40 °C in a vacuum oven affording TEMPO-(styrene)$_x$-(styrene-CH$_2$-OH)$_y$-(styrene-P-Ph$_2$-AuCl)$_z$.

TEMPO-(styrene)$_x$-(styrene-CH$_2$-OH)$_y$ Copolymer analysis by SEC and ^{1}H NMR
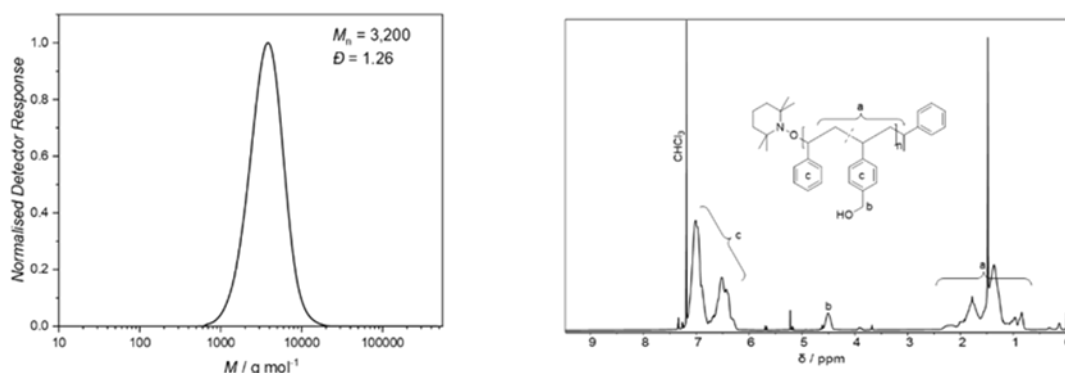
Figure A1. SEC and ^{1}H NMR spectrum of TEMPO-(styrene)$_x$-(styrene-CH$_2$-OH)$_y$, (Đ = 1.2 – M_n = 3,200 g mol^{-1}), styrene-CH$_2$-OH monomer unit present at 14 mol % with respect to styrene monomer unit.

^{1}H-NMR Spectroscopy was used to characterize the TEMPO-(styrene)$_x$-(styrene-CH$_2$-OH)$_y$ (refer to Figure A1). Characteristics resonances between (δ = 7.23 – 6.28 ppm) are attributed to the aromatic hydrogen atoms of the styryl groups. Benzylic hydrogens belonging to the alcohol containing styryl units are characterized by a distinct resonance at (δ = 4.69 – 4.45 ppm). The resonances between (δ = 2.47 – 0.81 ppm) represent the aliphatic hydrogens belonging to the backbone of the polymer. The number average molecular weight of the polymer was determined using Size Exclusion Chromatography (SEC) and found to be 3,200 g mol^{-1} with a low dispersity of 1.26.

TEMPO-(styrene)$_x$-(styrene-CH$_2$-OH)$_y$-(styrene-PPh$_2$-AuCl)$_z$ analysis by SEC and ^{1}H NMR
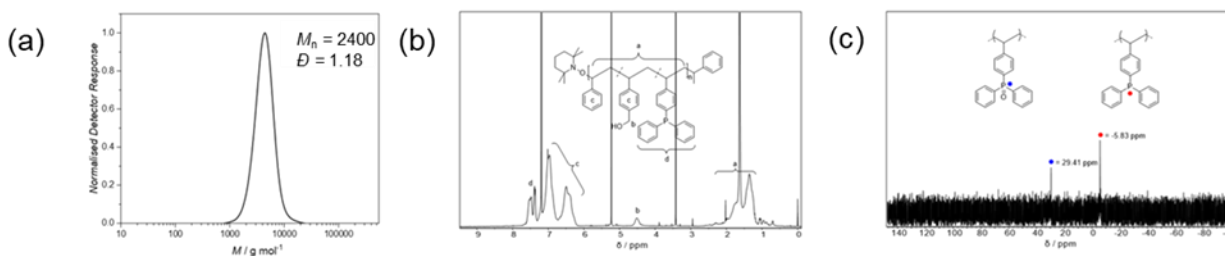
Figure A2. SEC and ^{1}H NMR analysis of TEMPO-(styrene)$_x$-(styrene-CH$_2$-OH)$_y$-(styrene-PPh$_2$-AuCl)$_z$, ($Đ$ = 1.15 – M_n = 2,400 g mol^{-1}). Styrene-CH$_2$-OH monomer unit present at 9 mol % and styrene-PPh$_2$-AuCl monomer unit present 12 mol % with respect to the styrene monomer unit.

^{1}H-NMR Spectroscopy was used to characterize the TEMPO-(styrene)$_x$-(styrene-CH$_2$-OH)$_y$-(styrene-P-Ph$_2$-AuCl)$_z$ (refer to Figure A2). Resonances between ($δ$ = 7.85 – 7.34 ppm) are attributed to the aromatic hydrogens of gold complexed triphenylphosphine. The ^{31}P-NMR spectrum further corroborated the complexation of gold to phosphine showing a resonance at ($δ$ = 32.36 ppm). Characteristics resonances between ($δ$ = 7.2 – 6.22 ppm) are attributed to the aromatic hydrogen atoms of the styryl groups. Benzylic hydrogens belonging to the alcohol containing styryl units are characterized by a distinct resonance at ($δ$ = 4.73 – 4.42 ppm). The resonances between ($δ$ = 2.59 – 0.77 ppm) represent the aliphatic hydrogens belonging to the backbone of the polymer. The number average molecular weight of the polymer was determined using Size Exclusion Chromatography (SEC) and found to be close to 2,400 g mol^{-1} with a low dispersity of $Đ$ = 1.15.

Ion mobility Experiments

Tetrahydrofuran and acetonitrile (20:80, *v/v*) were used to prepare copolymer stock solutions containing 1.0 mg mL^{-1}. Without the use of a cationizing agent, the copolymers were examined. Before ESI analysis, the copolymer solutions were diluted 100 times with tetrahydrofuran and acetonitrile (20:80, *v/v*).

Using a Waters Synapt G2-*Si* mass spectrometer, MS spectra and *CCS* measurements were taken. The solutions were infused at a rate of 5 µL min^{-1}, with a source temperature of 100 °C and a desolvation temperature of 150 °C, and a capillary voltage of 3.1 kV. The standard IMS-MS parameters were as follows: trap bias = 45.0 V, N$_2$ flow rate = 60 mL min^{-1}, He flow rate = 180 mL min^{-1}, mass range = *m/z* (50-4,000), wave height = 40 V and wave velocities = 350, 600, or 800 m s^{-1}. A pre-recognized calibration procedure[158] was used to transform the experimentally determined arrival time distributions to $^{TW}CCS_{N2→He}$,[159] which will be represented to as *CCS*$_{exp}$.

Molecular Dynamics Simulations

    a) Details procedure of *CCS* calculations

All calculations were performed with the Materials Studio software (BIOVIA, San Diego, CA).[160] For TEMPO-(styrene)$_x$-(styrene-CH$_2$-OH)$_y$ copolymer, PCFF force field was used and validated by the fact that the calculated effective density of TEMPO-polystyrene (0.62-0.66 Da/Å^3) is in good agreement with the reported density of bulk polystyrene (0.57-0.62 Da/Å^3).[151] For the TEMPO-(styrene)$_x$-(styrene-CH$_2$-OH)$_y$-(styrene-PPh$_2$-AuCl)$_z$ copolymer, we switched to the UFF force field since the parameters for gold are not available in PCFF (refer to the specific section in Annexes "Universal Force Field (UFF) Validation" and Figure A13). Force field assigned atomic charges were used for the simulations with the PCFF force field, while Gasteiger charges[166] were used in combination with the UFF force field. At first, geometry optimization was performed starting from a linear polymer chain (without charge). After adding a charge (H$^+$) to the optimized polymer chain, the geometry underwent additional optimization; the TEMPO group is chosen as the proton carrier due to the presence of the basic nitrogen atom. Subsequently, a quenched dynamics (frames quenched every 5 ps) was run for 20 ns at 300 K, with a 1 fs timestep, and a cutoff of 100 Å for the van der Waals and electrostatic interactions. The most stable structure obtained from the quenched dynamics was then used as the starting point for a 25 ns-long MD run (*NVT* ensemble; constant number of particles, *N*, volume, *V*, and temperature (*T* = 300 K) and using a 1 fs time step). From this MD trajectory, 500 structures were extracted and used to obtained an average theoretical *CCS*$_{th}$ computed by using the trajectory method (TM)[161] model implemented within Collidoscope software.[154]

    b) Details procedure for the investigation of the folding process

Since the folding process occurs on short timescales one must save snapshots very frequently to visualize it. In practice, instead of running a 25 ns-long MD with frames saved every 5 ps, we performed shorter MDs (2 ns-long) with snapshots saved every 0.5 ps, keeping all the other MD parameters constant.
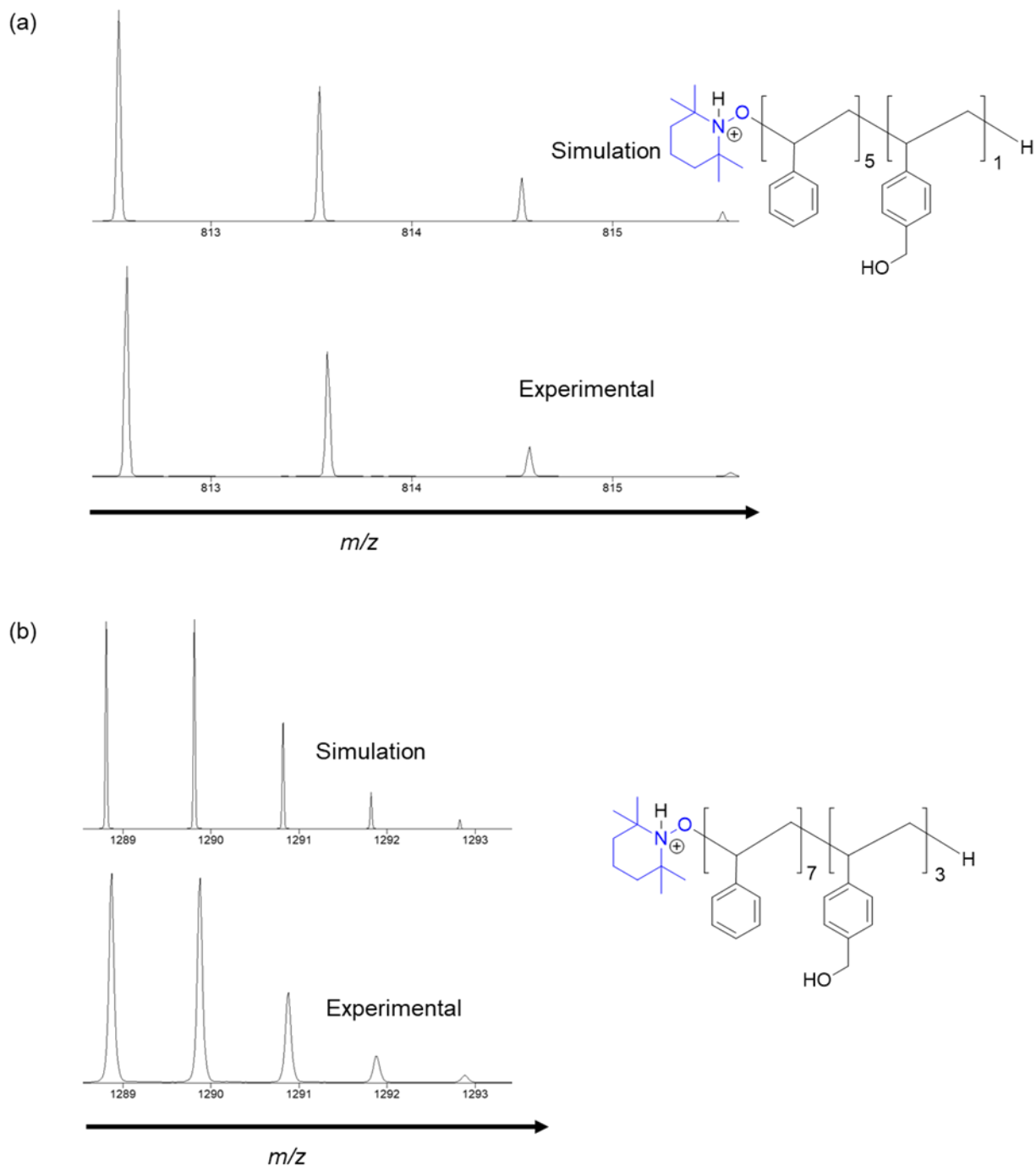
Figure A3. ESI-MS mass spectra of TEMPO-(styrene)$_x$-(styrene-CH$_2$-OH)$_y$ (0.01 mg mL^{-1}) in acetonitrile/ tetrahydrofuran (80/20) (v/v); Comparison between experimental and simulated isotope patterns: (a) [TEMPO-(styrene)$_5$-(styrene-CH$_2$-OH)$_1$ + H]$^+$ (DP = 6) and (b) [TEMPO-(styrene)$_7$-(styrene-CH$_2$-OH)$_3$ + H]$^+$ (DP = 10) ions, as selected examples.
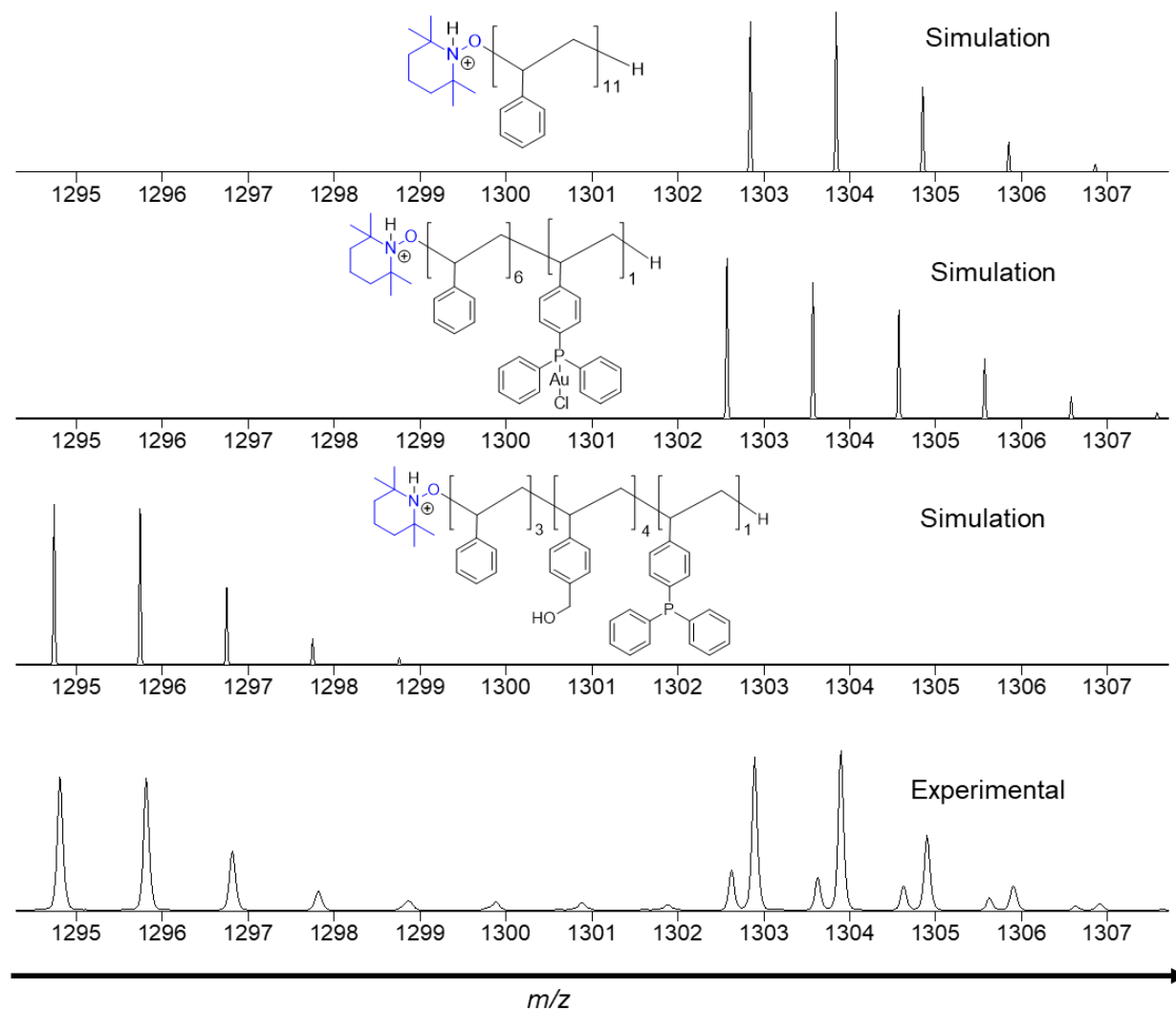
Figure A4. ESI-MS mass spectra of TEMPO-(styrene)$_x$-(styrene-CH$_2$-OH)$_y$-(styrene-PPh$_2$)$_w$-(styrene-PPh$_2$-AuCl)$_z$ (0.01 mg mL^{-1}) in acetonitrile/tetrahydrofuran (80/20) (*v/v*). Comparison between experimental and simulated isotope patterns.
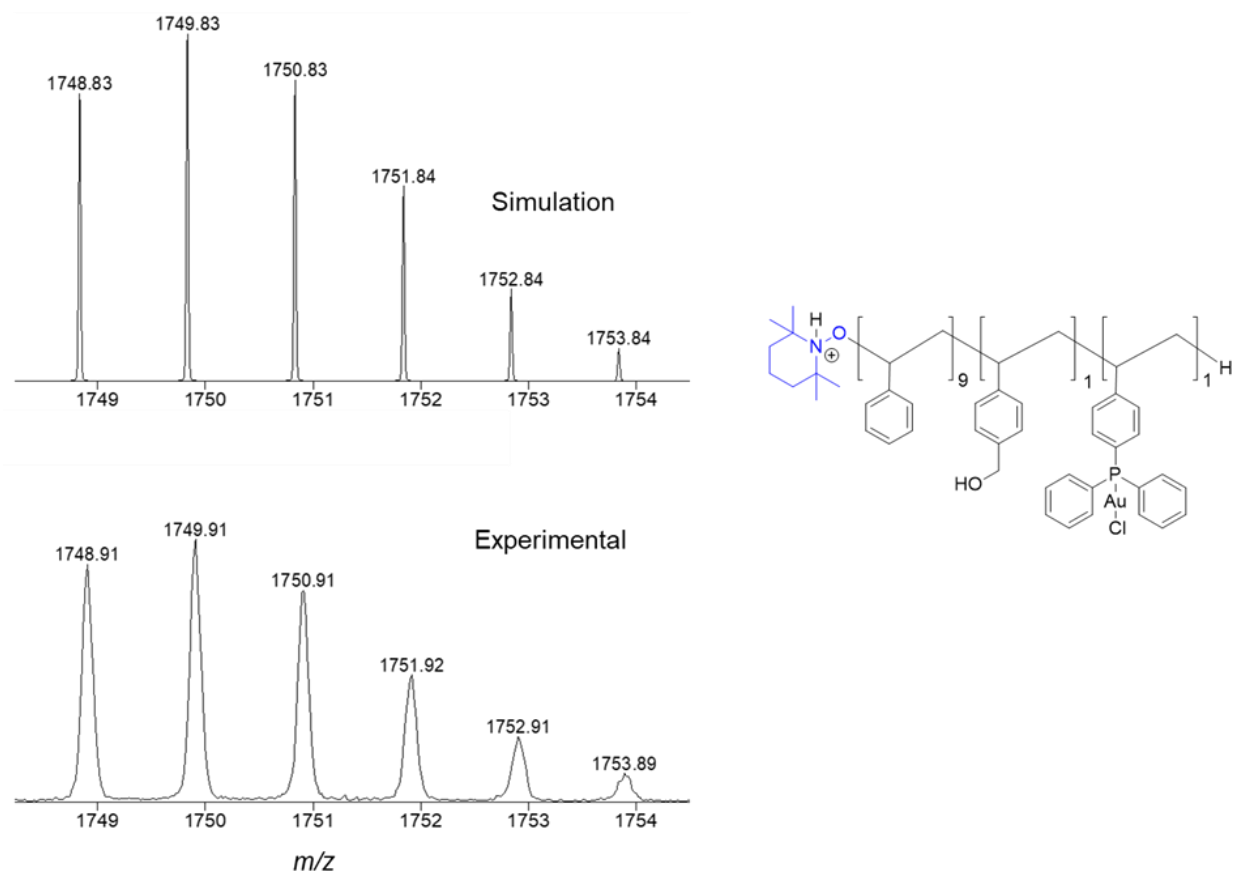
Figure A5. ESI-MS mass spectra of TEMPO-(styrene)$_x$-(styrene-CH$_2$-OH)$_y$-(styrene-PPh$_2$-AuCl)$_z$ (0.01 mg mL^{-1}) in acetonitrile/tetrahydrofuran (80/20) (*v/v*). Comparison between experimental and simulated isotope patterns and structure of the ion.
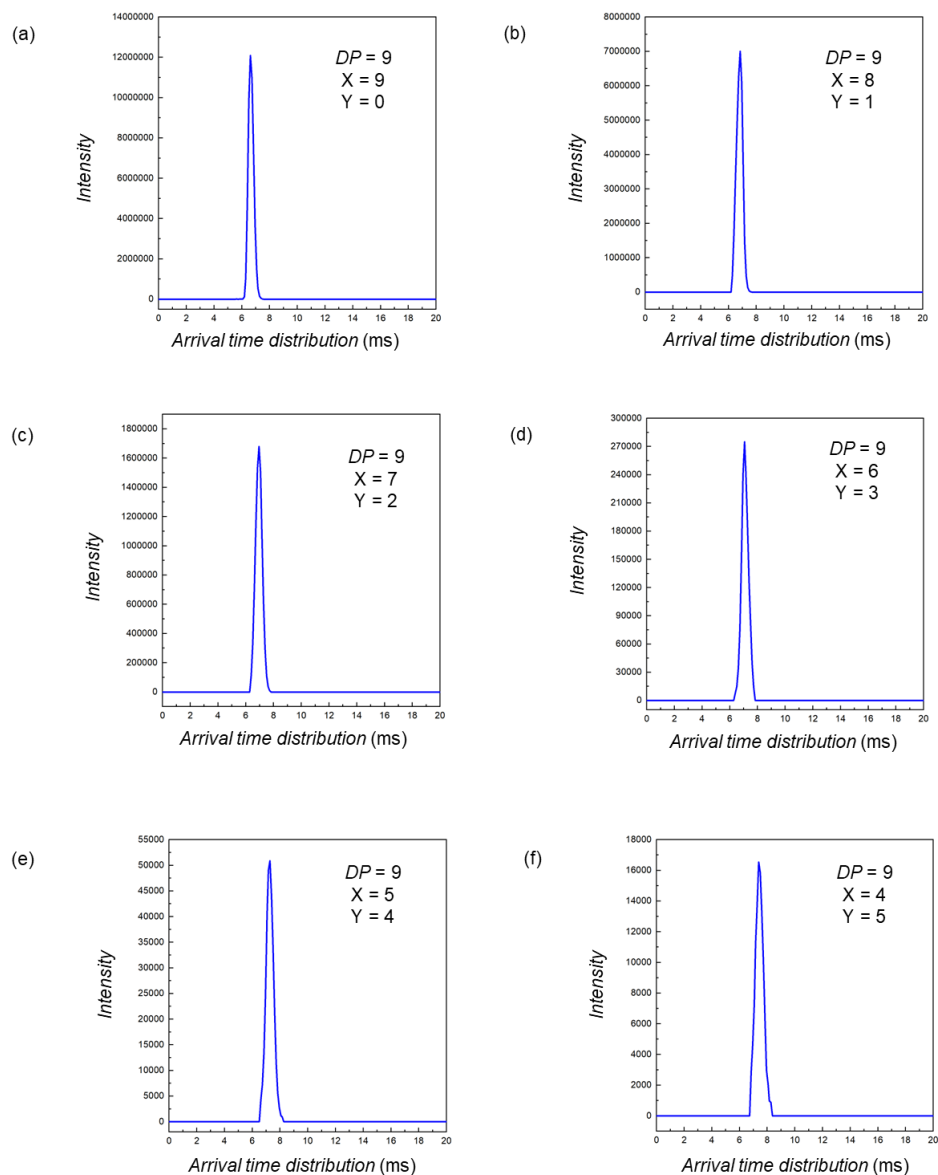
Figure A6. Ion mobility mass spectrometry analysis of the copolymer (0.01 mg mL^{-1}) in acetonitrile/tetrahydrofuran (80/20) (*v/v*) using Waters Synapt G2-*Si* mass spectrometer; arrival time distribution (*ATD*) of selected [TEMPO-(styrene)$_x$-(styrene-CH$_2$-OH)$_y$ + H]$^+$ ions: (a) x = 9, y = 0; (b) x = 8, y = 1; (c) x = 7, y = 2; (d) x = 6, y = 3; (e) x = 5, y = 4; (f) x = 4, y = 5; here total *DP* = 9 in every case.
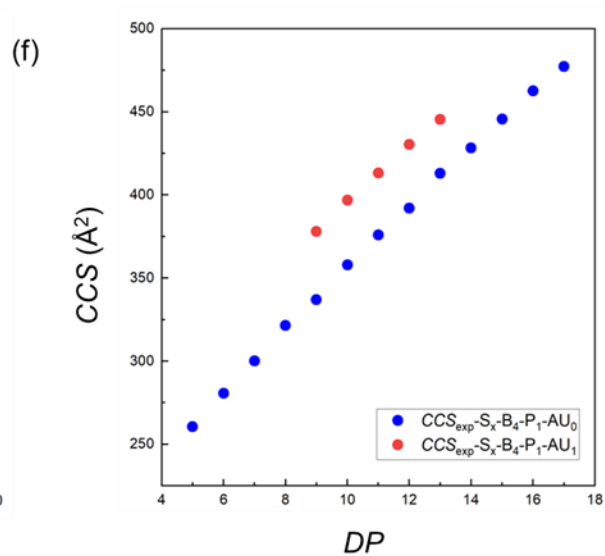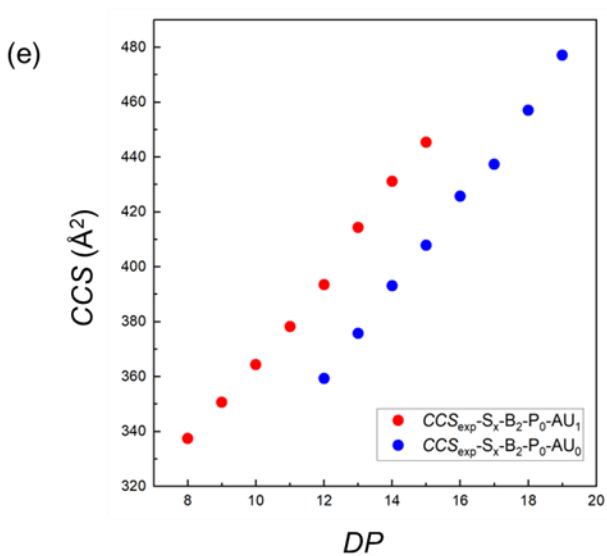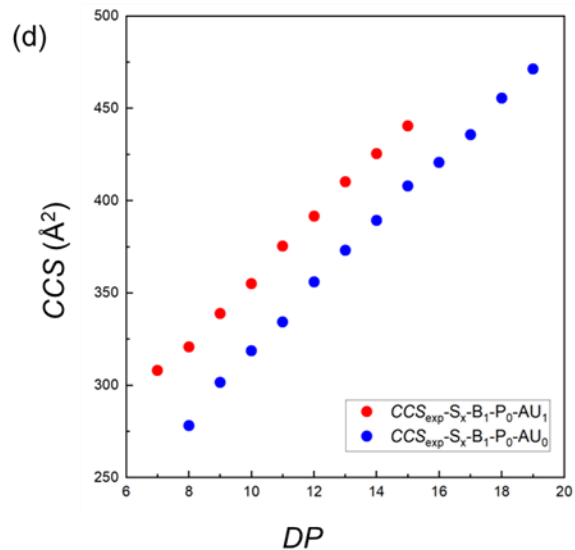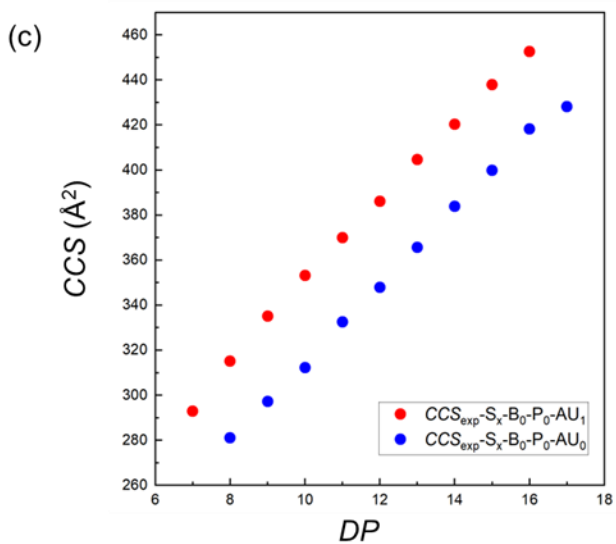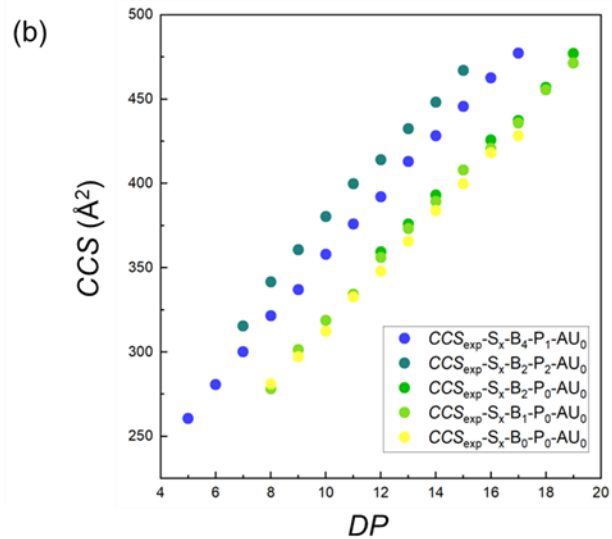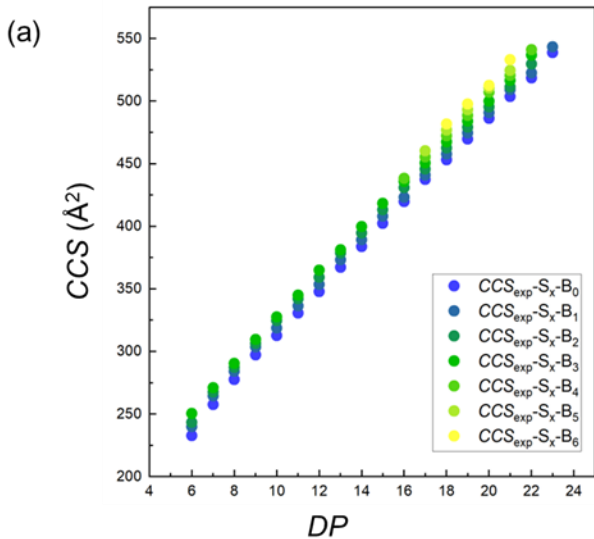
Figure A7. Ion mobility mass spectrometry analysis of copolymer (0.01 mg mL^{-1}) in acetonitrile/ tetrahydrofuran (80/20) (*v/v*); (a)TEMPO-(styrene)$_x$-(styrene-CH$_2$-OH)$_y$ and (b) TEMPO-(styrene)$_x$-(styrene-CH$_2$-OH)$_y$-(styrene-PPh$_2$)$_w$-(styrene-PPh$_2$-AuCl)$_0$ ions, (a) and (b) are represent by the blue-green-yellow palette, (c) TEMPO-(styrene)$_x$-(styrene-CH$_2$-OH)$_0$-(styrene-PPh$_2$)$_0$-(styrene-PPh$_2$-AuCl)$_{0/1}$ (d) TEMPO-(styrene)$_x$-(styrene-CH$_2$-OH)$_1$-(styrene-PPh$_2$)$_0$-(styrene-PPh$_2$-AuCl)$_{0/1}$, (e) TEMPO-(styrene)$_x$-(styrene-CH$_2$-OH)$_2$-(styrene-PPh$_2$)$_0$-(styrene-PPh$_2$-AuCl)$_{0/1}$ and (f) TEMPO-(styrene)$_x$-(styrene-CH$_2$-OH)$_4$-(styrene-PPh$_2$)$_1$-(styrene-PPh$_2$-AuCl)$_{0/1}$; in this case ((c) to (f)), blue colour used to represent (styrene-PPh$_2$-AuCl)$_0$ containing copolymer and red colour corresponds to the copolymer containing (styrene-PPh$_2$-AuCl)$_1$ units.

Sequence of E-S6-B6	CCS (Å^2)	SD
EB2S6B4	366	7
EB3S6B3	369	7
EB6S6	371	5
EB1S1B1S1B2S2B1S2B1	373	6
EB4S6B2	376	9
ES6B6	376	6
EB1S6B5	376	6
ES3B6S3	377	6
ES2B3S2B3S2	378	8
EB5S6B1	380	7
ES2B2S1B2S1B2S2	383	6
ES1B1S1B1S1B1S1B1S1B1S1B1	386	6

Sequence of E-S12-B6	CCS (Å^2)	SD
ES6B4S6B2	457	6
ES2B1S2B1S2B1S2B1S2B1S2B1	466	6
ES4B2S2B3S2B1S4	468	6
EB1S12B5	470	10
ES6B6S6	473	6
EB4S12B2	475	6
ES4B1S2B3S2B2S4	476	9
EB2S12B4	476	8
ES2B1S2B1S2B1S2B1S2B2S2	477	7
ES6B2S6B4	477	8
ES6B5S2B1S4	479	8
EB5S12B1	480	7
ES4B3S4B3S4	481	8
EB6S12	481	7
EB3S12B3	482	7
ES12B6	484	7
ES6B5S6B1	485	5
ES4B1S2B5S6	485	8
ES6B1S6B5	489	9
ES4B1S2B4S2B1S4	490	6
ES4B2S2B2S2B2S4	491	8

Figure A8: Theoretical *CCS* estimation using molecular dynamics simulation of the TEMPO-(styrene)$_x$-(styrene-CH$_2$-OH)$_y$: (a) theoretical *CCS* evolution for different sequences of S6B6 and (b) theoretical *CCS* evolution for different sequences of S12B6.
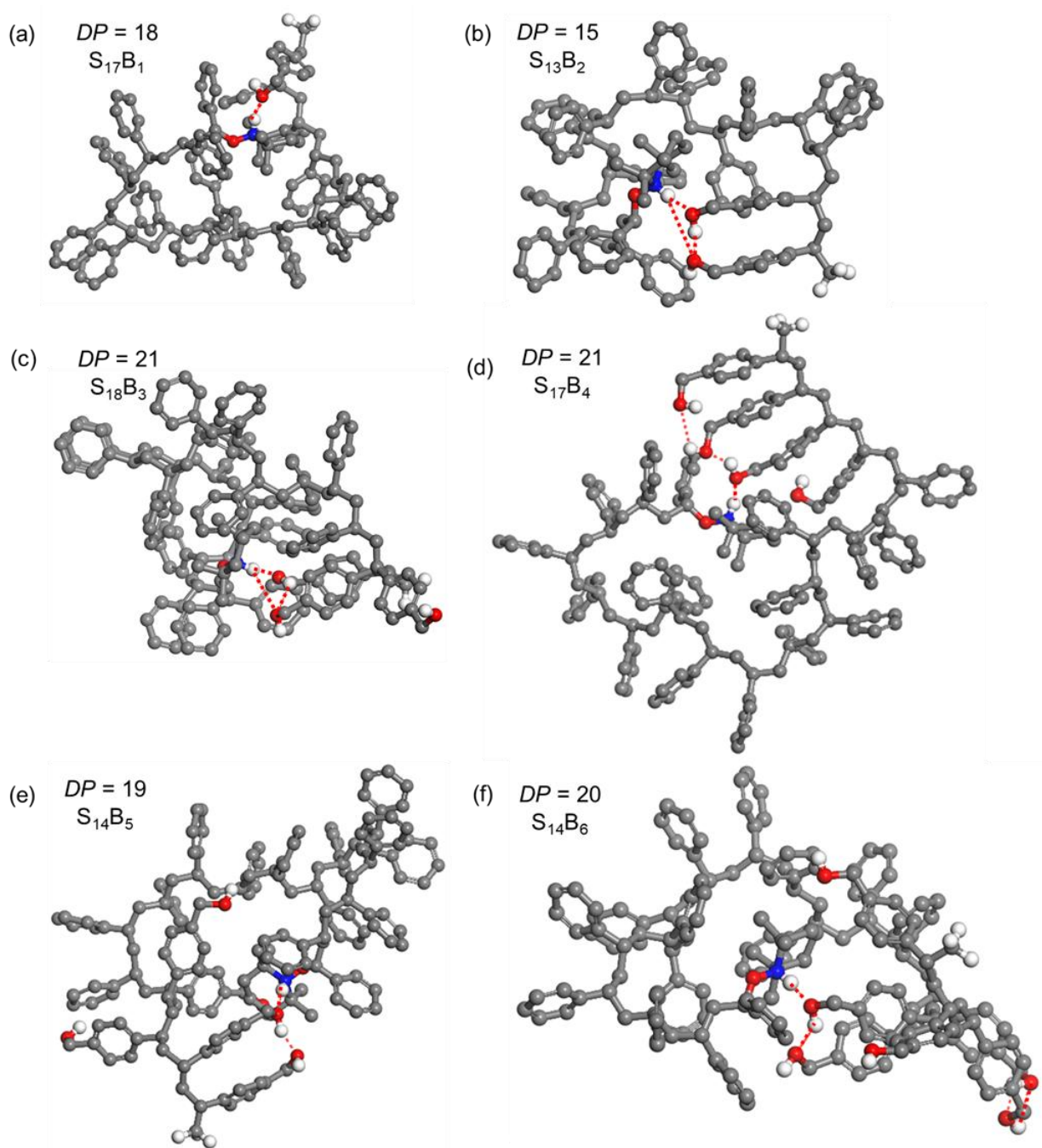
Figure A9. Molecular Dynamics simulations (PCFF force field, 298K, 25 ns) of [TEMPO-(styrene)$_x$-(styrene-CH$_2$-OH)$_y$ + H]$^+$ ions, snapshot of the last frame of the MD that represent the hydrogen bond by red colour : (a) *DP* = 18 (x = 17,

y = 1), (b) *DP* = 15 (x = 13, y = 2), (c) *DP* = 21 (x = 18, y = 3), (d) *DP* = 21 (x = 17, y = 4), (e) *DP* = 19 (x = 14, y = 5) and (f) *DP* = 20 (x = 14, y = 6).
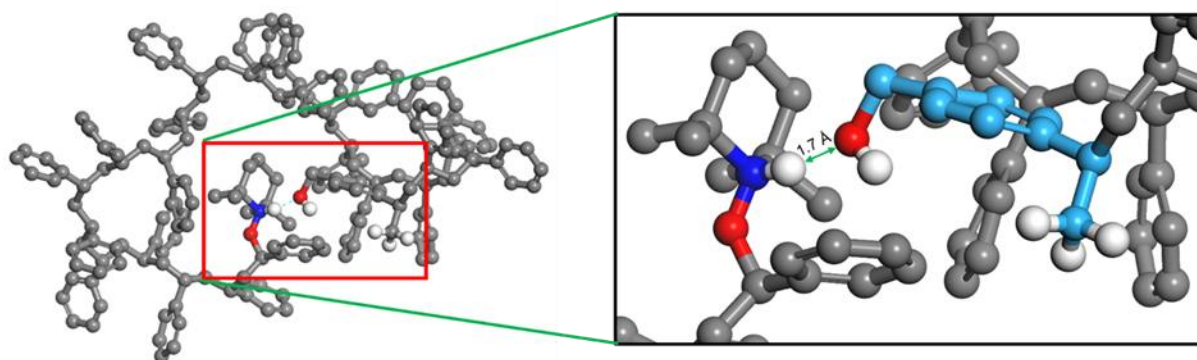
Figure A10. Molecular Dynamics simulations (PCFF force field, 300 K, 25 ns) of [TEMPO-(styrene)$_{22}$-(styrene-CH$_2$-OH)$_1$ + H]$^+$ ions (*DP* = 23, x = 22, y = 1). Snapshot of the last frame of the MD with enlarged views of the charged centers : H-bonding interaction between the protonated TEMPO end group and hydroxyl group of the styrene-CH$_2$-OH unit. Here in the zoom section, the light blue represents the styrene-CH$_2$ unit of styrene-CH$_2$-OH, while the conventional color represents the remaining portion.
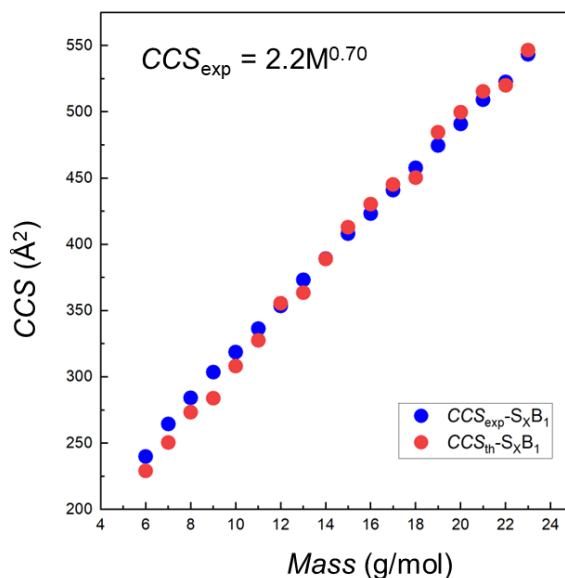
Figure A11. Ion mobility mass spectrometry analysis and Molecular Dynamics simulations of [TEMPO-(styrene)$_x$-(styrene-CH$_2$-OH)$_1$ + H]$^+$ ions: comparison between the *CCS*$_{exp}$ and *CCS*$_{th}$ over the full mass range.

(a)

(b)
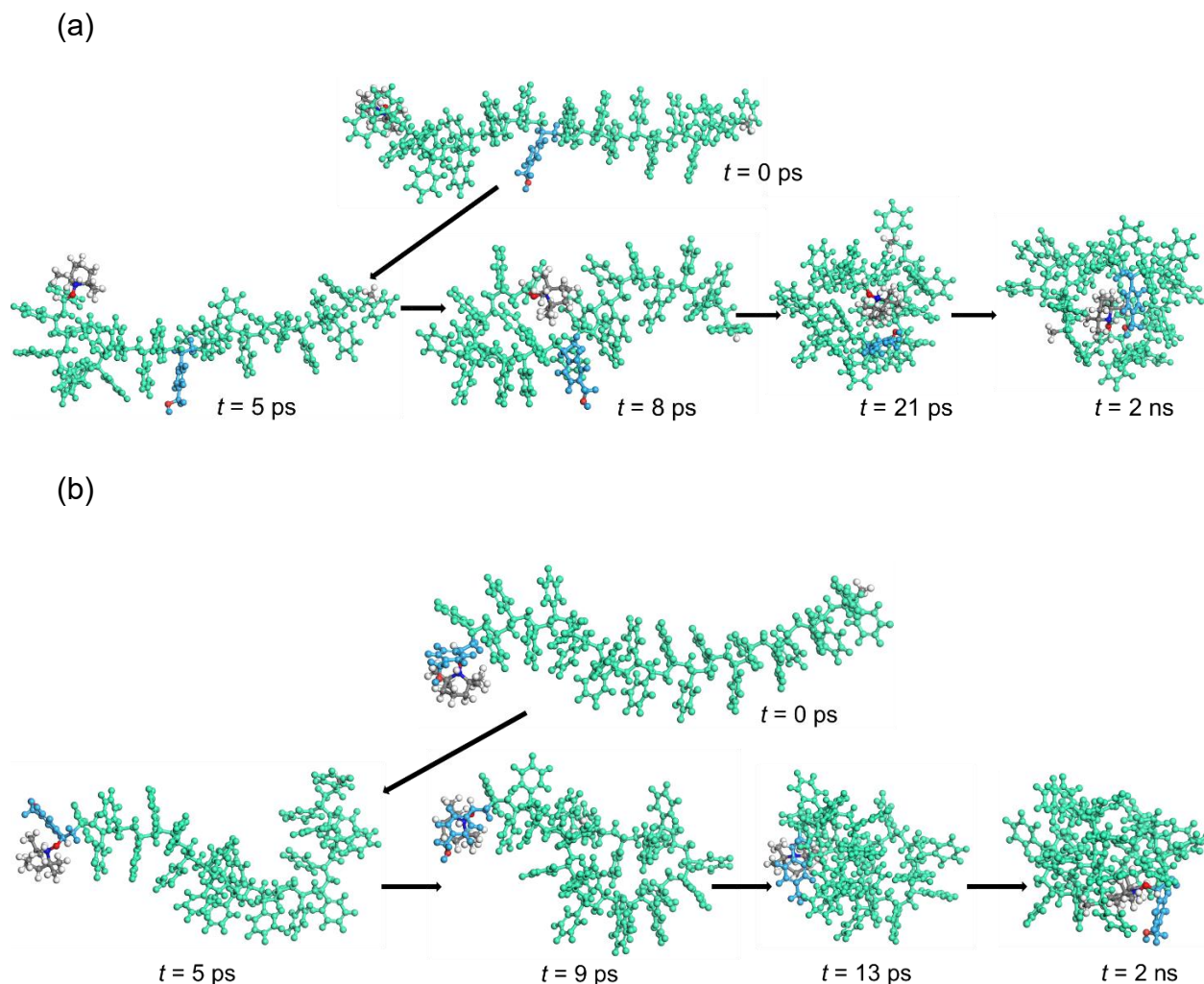
Figure A12. Molecular Dynamics simulations (PCFF force field, 300 K, 2 ns) of (a) [E-S_{11}-B_1-S_{11} + H]$^+$ ions and (b) [E-B_1-S_{22} + H]$^+$ ions (DP = 23): snapshots at different times of the trajectory revealing that the folding process is mostly initiated by π-π interactions between phenyl rings (a) with the H-bonded protonated TEMPO and styrene-CH_2-OH for the E-S_{11}-B_1-S_{11} ions ultimately being incorporated in the core of the equilibrated structure and (b) the TEMPO / styrene-CH_2-OH sequence remaining at the surface of the globular ion. The styrene-CH_2-OH and the TEMPO residues are highlighted in blue and grey for visualisation.

Universal Force Field (UFF) and PCFF Comparison

Since the parameters for the gold metal are not incorporated into the PCFF force field used successfully in our first study,[165] we turned to UFF (Universal Force Field) with charges assigned on the different atoms using the Gasteiger method for the Au-containing copolymer ions. We calculated – using both UFF and PCFF – the CCS_{th} for TEMPO-initiated polystyrene homopolymer ions (DP = 8-17) and TEMPO-initiated

styrene/styrene-CH$_2$-OH copolymer ions (DP = 8-19) in order to check whether PCFF will reproduce the UFF data without further parametrization or validation. The UFF and PCFF-computed CCS_{th} were further compared with the CCS_{exp} (refer to Figure S13). Since the three different CCS are nearly identical over the investigated DP-ranges, we will consider that both force fields are able to generate reliable molecular structures.
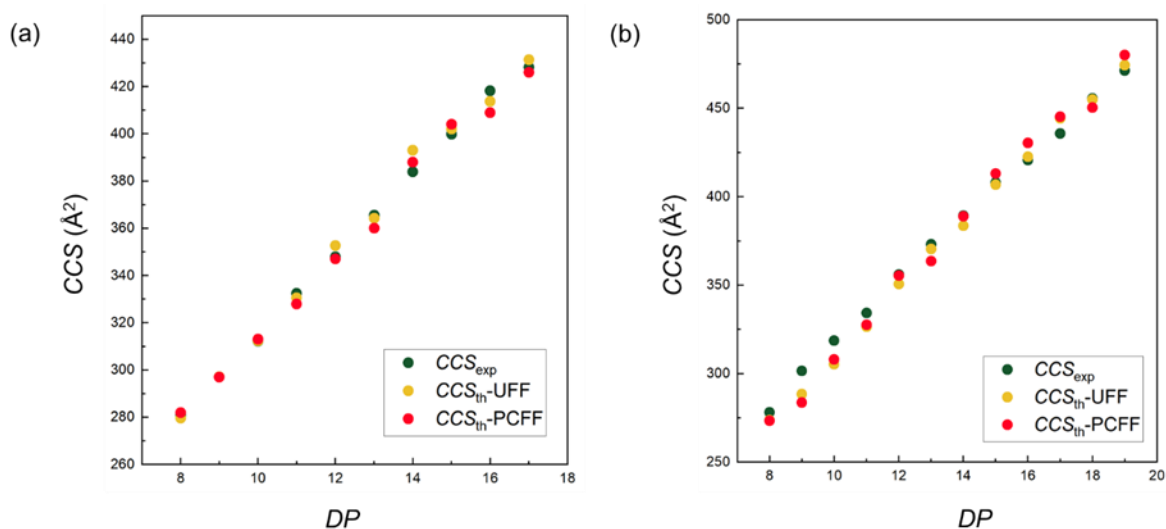
Figure A13. Ion mobility mass spectrometry and molecular dynamics simulations using (PCFF and UFF) force fields for TEMPO-initiated styrene homopolymer ions and TEMPO-initiated styrene/styrene-CH$_2$-OH copolymer ions : (a) CCS evolution with DP for [TEMPO-PS + H]$^+$ and (b) CCS evolution with DP for [TEMPO-(styrene)$_x$-(styrene-CH$_2$-OH)$_1$ + H]$^+$ ions.
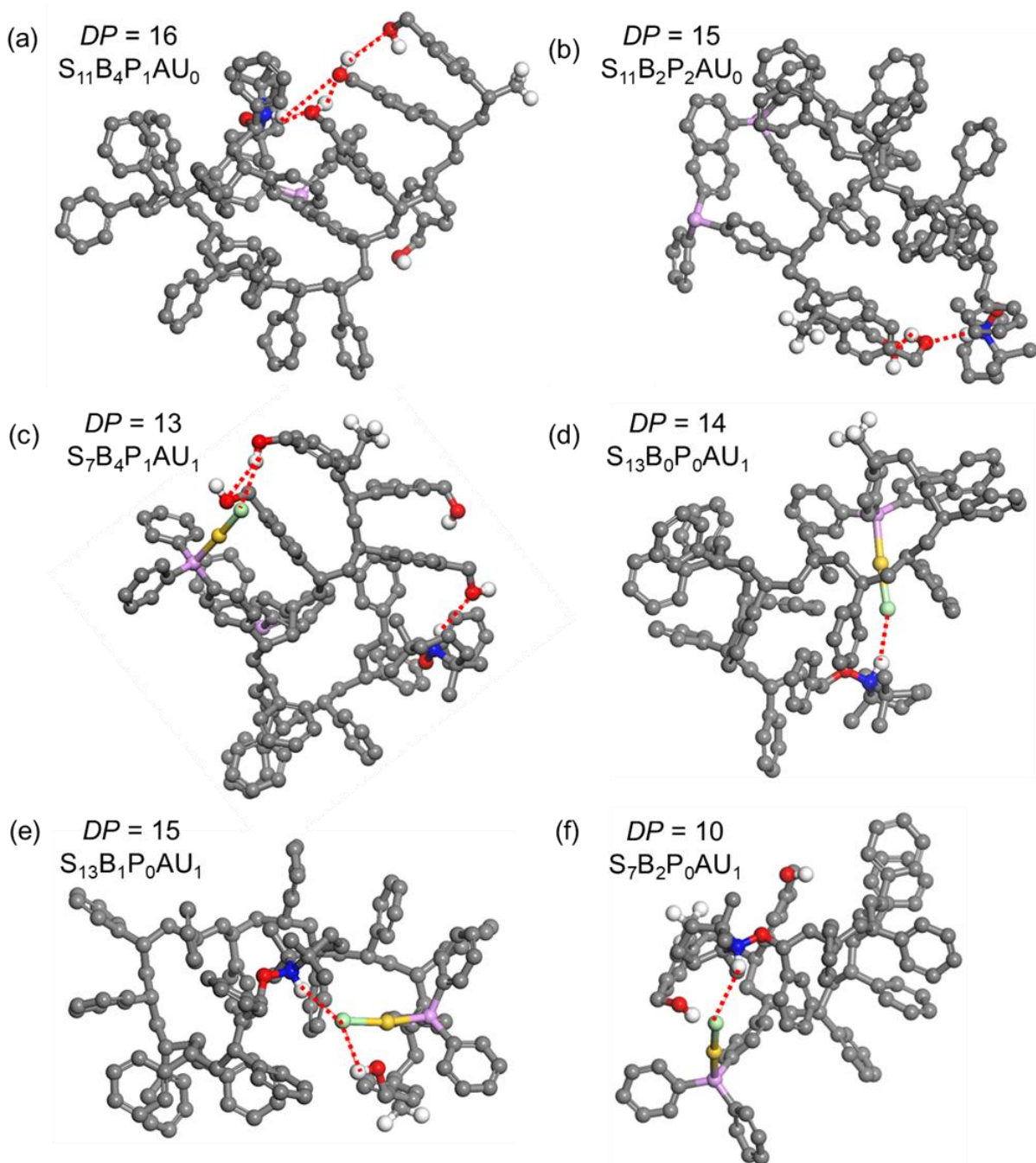
Figure A14. Molecular Dynamics simulations (UFF force field, 298K, 25 ns) of [TEMPO-(styrene)$_x$-(styrene-CH$_2$-OH)$_y$-(styrene-PPh$_2$)$_w$-(styrene-PPh$_2$-AuCl)$_z$ + H]$^+$ions, snapshot of the last frame of the MD that represent the hydrogen bond by red colour : (a) DP = 16 (x = 11, y = 4, w = 1, z = 0), (b) DP = 15 (x = 11, y = 2, w = 2, z = 0), (c) DP = 13 (x = 7, y = 4, w = 1, z = 1), (d) DP = 14 (x = 13, y = 0, w = 0, z = 1), (e) DP = 15 (x = 13, y = 1, w = 0, z = 1) and (f) DP = 10 (x = 7, y = 2, w = 0, z = 1).
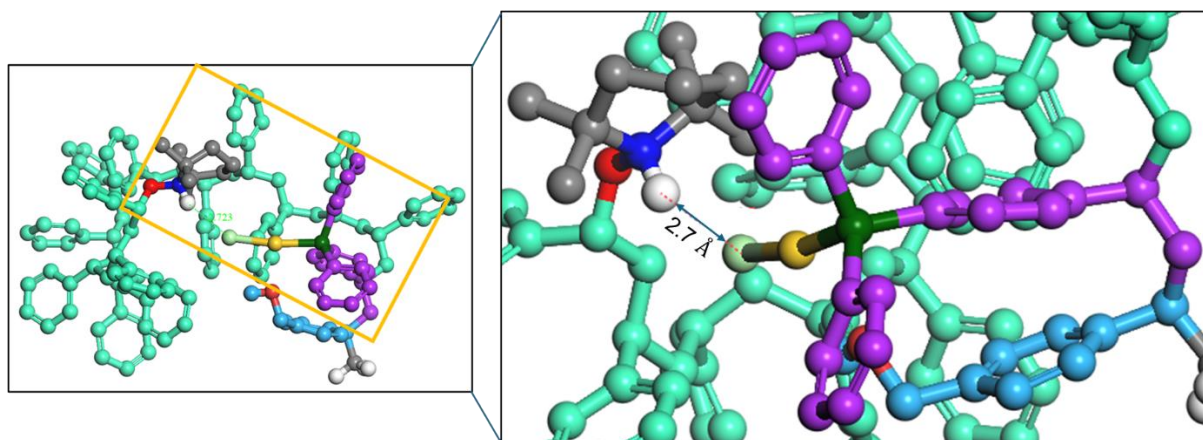
Figure A15. Molecular Dynamics simulations (UFF force field, 298K, 25 ns) of [TEMPO-(styrene)$_{13}$-(styrene-CH$_2$-OH)$_1$-(styrene-PPh$_2$-AuCl)$_1$ + H]$^+$ions (DP = 15, x = 13, y = 1, z = 1). Snapshot of the last frame of the MD with enlarged views of the charged center : H-bonding interaction between the protonated TEMPO end group and chloride group of the styrene-PPh$_2$-AuCl unit. Here, the styrene monomer unit is indicated by dark green, the styrene-CH$_2$-OH is indicated by light blue, styrene-PPh$_2$ represent by the plum and the end group is indicated by grey.

On the discrimination between regio- and stereoisomeric photo-products using Cyclic Ion Mobility Mass Spectrometry in combination with Molecular Dynamics Simulations

Introduction

Light-driven reactions are very important for biology,[172] green chemistry, and modern industry.[173] However, their large-scale application in industry is limited due to low yields, poor selectivity, and scalability challenges. Photoreactivity is typically assessed by the quantum yield,[174] which depends on factors such as solvent,[175] temperature,[176] and wavelength.[177] The efficiency of photochemical reactions can be increased using confinement in nanoreactors.[178] Further, self-assemblies can enhance efficiency by controlling local concentration and geometry. However, the influence of molecular architecture in solution has not been systematically addressed. Our group reported the enhancement of the efficiency of photochemical reactions by increasing local concentrations.[179] A library of monodisperse, trifunctional macromolecules with variable spacers between photoreactive units was designed and synthesized. The study revealed a "goldilocks zone" where steric and entropic factors balance to maximize quantum yields.[179] Importantly, these findings are translated into two-photon microprinting, directly linking molecular design to material performance and print quality. The materials synthesized mostly using chalcone derivatives as chalcone has good light controlling properties.

Chalcone derivatives substituted with simple π-conjugated units, such as pyrene and anthracene, display moderate non-linear optical responses.[180,181] Among these, pyrene is regarded as a highly promising nonlinear optical building block for π-extended derivatives, owing to its strong π-electron delocalization that can markedly enhance two-photon absorption processes.[182] Pyrene-containing chalcone derivatives exhibit enhanced nonlinear optical effects, rendering them well-suited for applications in all-optical switching and optical limiting.[183,184] The activity of the molecules is generally governed by their architecture. However, precise monitoring of their activity may remain challenging due to limited knowledge of the structure–activity relationship.

Photopolymerization employs light as a clean and non-invasive stimulus for macromolecular synthesis, offering spatiotemporal control[185] and compatibility with green chemistry. In general, photoreactive molecules can initiate chain-growth mechanisms[186] (radical,[187–189] ionic,[190–192] or ring-opening[193]), but more recently, catalyst-free systems using direct light activation have emerged. Step-growth photopolymerizations via [2+2] and [4+4] cycloadditions[194–197] (e.g., cinnamates,[194,195] coumarins,[196,197] anthracenes,[198] chalcones[199]) enable the preparation of controlled macromolecular assemblies, with a key importance being their reversibility. Shorter-wavelength irradiation can trigger cycloreversion,[200] enabling depolymerization and recyclability of photopolymers.

In general, (cyclization) reactions form only a single bond. An important advantage of photocycloaddition reactions is that they can form two or more bonds successively.[201] For example, the [2+2] photocycloaddition reaction is one of the most well-known transformations of this type. Here, two olefins undergo [2+2] photocycloaddition to form a cyclobutane ring in the presence of visible or ultraviolet (UV) light. Upon irradiation, one of the olefins is excited from its ground state (S_0) to the first excited state (S_1), where it can react with another olefin in the ground state to yield the cyclobutane product.[202–205]

Pyrene-substituted chalcone derivatives also undergo [2+2] photocycloaddition reactions. When more than one pyrene-substituted chalcone unit is present within the same molecule, both intramolecular and intermolecular [2+2] photocycloaddition can occur. The pyrene chalcone-based system that will be investigated in the present chapter contains three pyrene-substituted chalcone units (refer to Scheme 1). The left and right sides of the molecule are identical, with equal bridge lengths, whereas the head segment differs due to a difference in linker length. This molecule is designated as trifunctional photoactive ene (TPE), indicating that the bridge chains on the left and right sides consists each of three monomer units.[179]
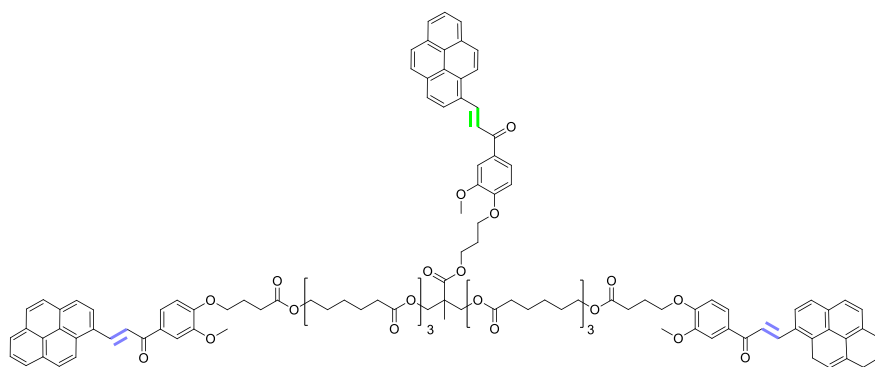
Scheme 1. Chemical structure of the investigated molecule, designated as TPE.[179]

The TPE molecule contains a total of three double bonds: two located on the left and right sides, highlighted in blue, and one in the head segment, highlighted in green. Upon exposure to light, the TPE molecule undergoes both intramolecular and intermolecular [2+2] photocycloaddition reactions. Due to its asymmetric structure, multiple isomers can be formed through these photocycloaddition processes. In the current chapter, a photocycloaddition between the left and right sides of the molecule (*i.e.,* between the two blue double bonds) will be designated as "Q," while a photocycloaddition between either the left or right side and the head unit (*i.e.,* between one blue and one green double bonds) will be referred as "P" (refer to Scheme 2).
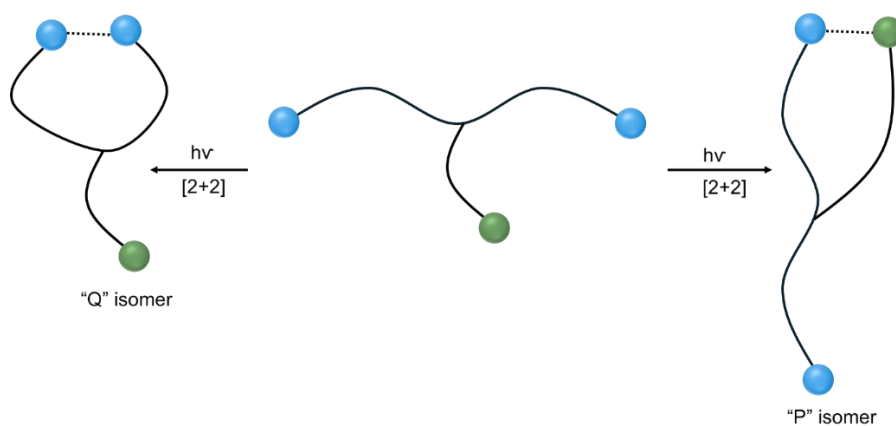
Scheme 2. Schematic representation of the "P" and "Q" isomers.

In addition to the "P" and "Q" isomers, two configurations may be generated during the cycloaddition process, *i.e.* a head-to-head and a head-to-tail arrangements. In the head-to-head configuration, both pyrene rings are positioned on the same side, whereas in the

head-to-tail configuration, the two pyrene rings are located on opposite sides (refer to scheme 3). In addition, both head-to-head and head-to-tail configurations can give rise to multiple possible stereoisomers, such as *cis–cis*, *cis–trans*, and *trans–trans*, depending on the relative positions of the substituents.

Head-to-head   Head-to-tail
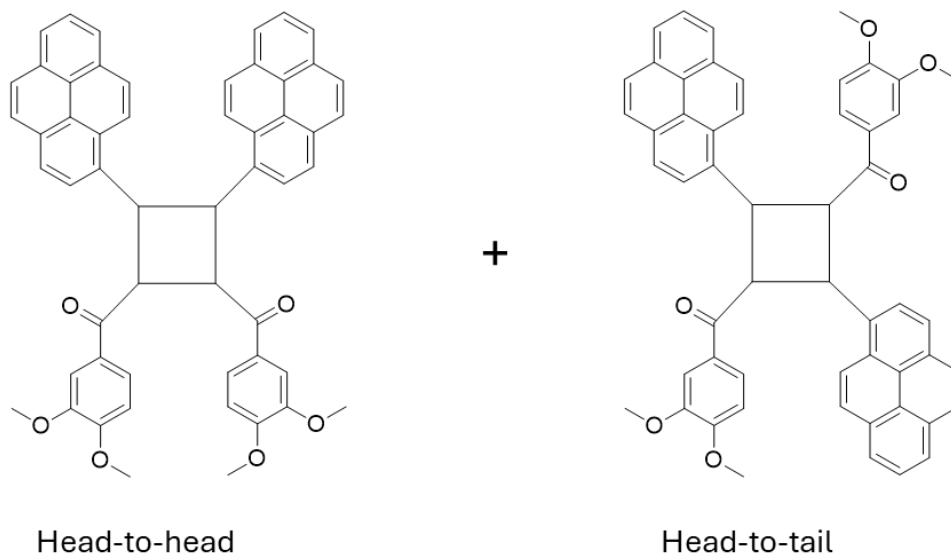
Scheme 3. Head-to-head and head-to-tail isomers.

Consequently, numerous isomers are formed upon intramolecular [2+2] photocycloaddition of the TPE molecule. Identifying the specific isomers produced by this reaction is challenging. In the current chapter, we will challenge ion mobility mass spectrometry (IM-MS), cyclic ion mobility spectrometry (cyclic IMS), molecular dynamics simulations, and density functional theory (DFT) map the isomeric diversity of the photo-adduct products.

Experimental section

Synthesis of parent TPE molecules and cyclic molecules

The TPE molecule – prepared at the Queensland University of Technology (QUT) by Fred Pashley-Johnson – was mainly designed for investigating how two-photon microprinting is influenced by intramolecular photocycloadditions.[179,206,207] ε-Caprolactone was used as a tether between the photoreactive units.[208,209]

Initially, the cyclic TPE species were prepared by [2+2] photocycloaddition. Both parent and cyclic TPE molecules were characterized using SEC (refer to Figure 1) and NMR (refer to Figure A1). The SEC chromatogram of the cyclic TPE molecules was shifted slightly towards the lower molecular weight after irradiation. The SEC trace shows a bimodal curve (refer to Figure 1a) that corresponds to two different hydrodynamic volumina, suggesting that two different types of cyclic molecules are formed (refer to Figure 1b). Here, the pink curve corresponds to one isomer and blue curve corresponds to another curve (refer to Figure 1b).
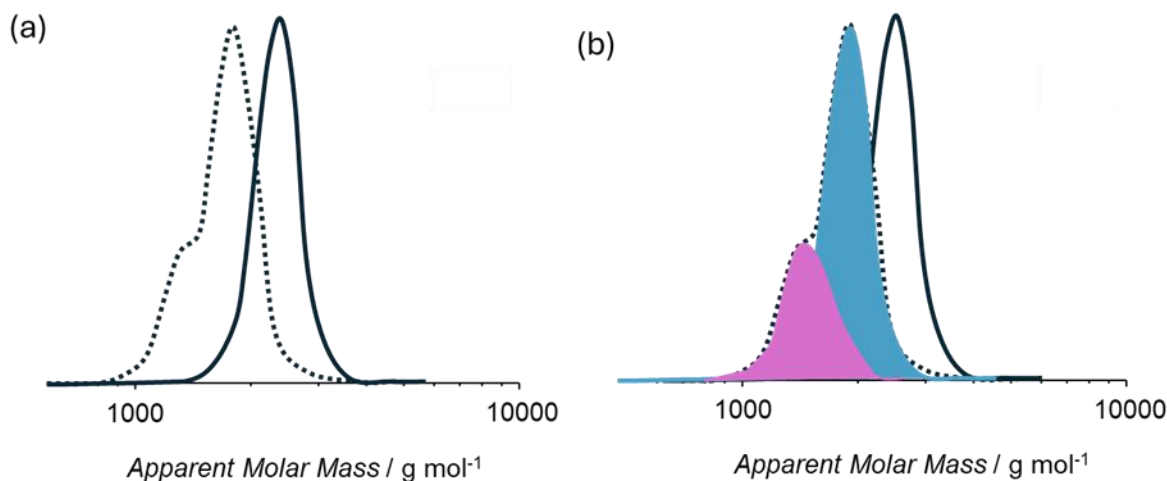
Figure 1. Size Exclusion Chromatographs of TPE recorded in THF. (a) Size-exclusion chromatographs of the TPE macromolecules: solid curve corresponds to the parent TPE molecules and the dashed curve corresponds the cyclic molecules created due to intramolecular folding upon irradiation of a 12.5 μM solution of the analyte in acetonitrile with a 10 W LED, λ_{max} = 445 nm; (b) Deconvolution of SEC traces by fitting with two monodisperse peaks to show the large

and the small isomer that form upon irradiation: here pink curve and blue curve correspond to the two different isomers.

Results and discussions

ESI-MS analysis of the TPE molecules

The parent TPE molecule (*i.e.,* the reactant) and their [2+2] photocyclization products (cyclic molecules, *i.e.,* the products) were initially analyzed by electrospray ionization mass spectrometry (ESI-MS) to evaluate whether they can be detected by MS and to determine what the nature of the detected ions is. TPE ionizes most effectively by Na$^+$ ion capture, generating [M + Na]$^+$ and [M + 2Na]$^{2+}$ ions, likely due to favorable interactions between Na$^+$ and the oxygen atoms of either the C=O carbonyl groups or the CH$_3$-O-methoxy groups (refer to Figure 2 and Figure 3).
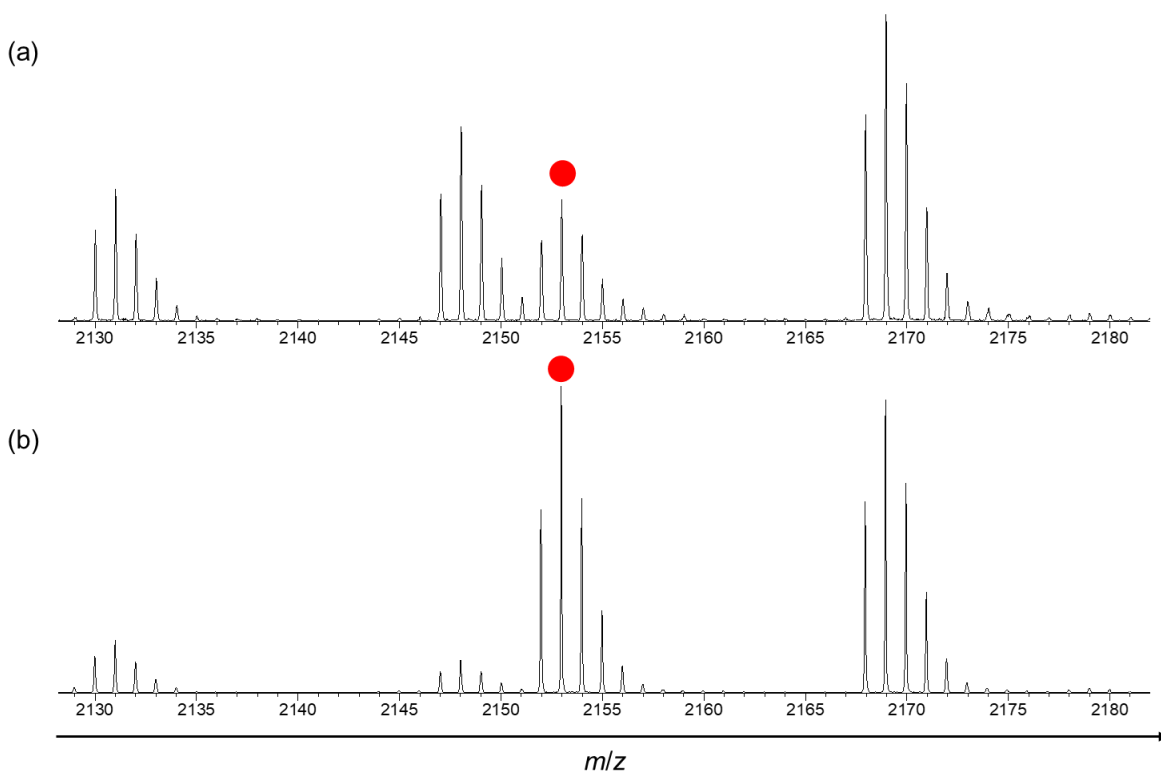
Figure 2. ESI-MS spectra of singly charged [M + Na]$^+$ (a) Cyclic TPE molecules (*i.e.*, product) at 0.01 mg mL^{-1} in acetonitrile/tetrahydrofuran (80/20) (*v/v*), and (b) parent TPE molecules (*i.e.*, reactant) at 0.01 mg mL^{-1} in acetonitrile/tetrahydrofuran (80/20) (*v/v*) with NaI (0.0002 mg mL^{-1}). Red circles indicate singly charged [M + Na]$^+$ ions.
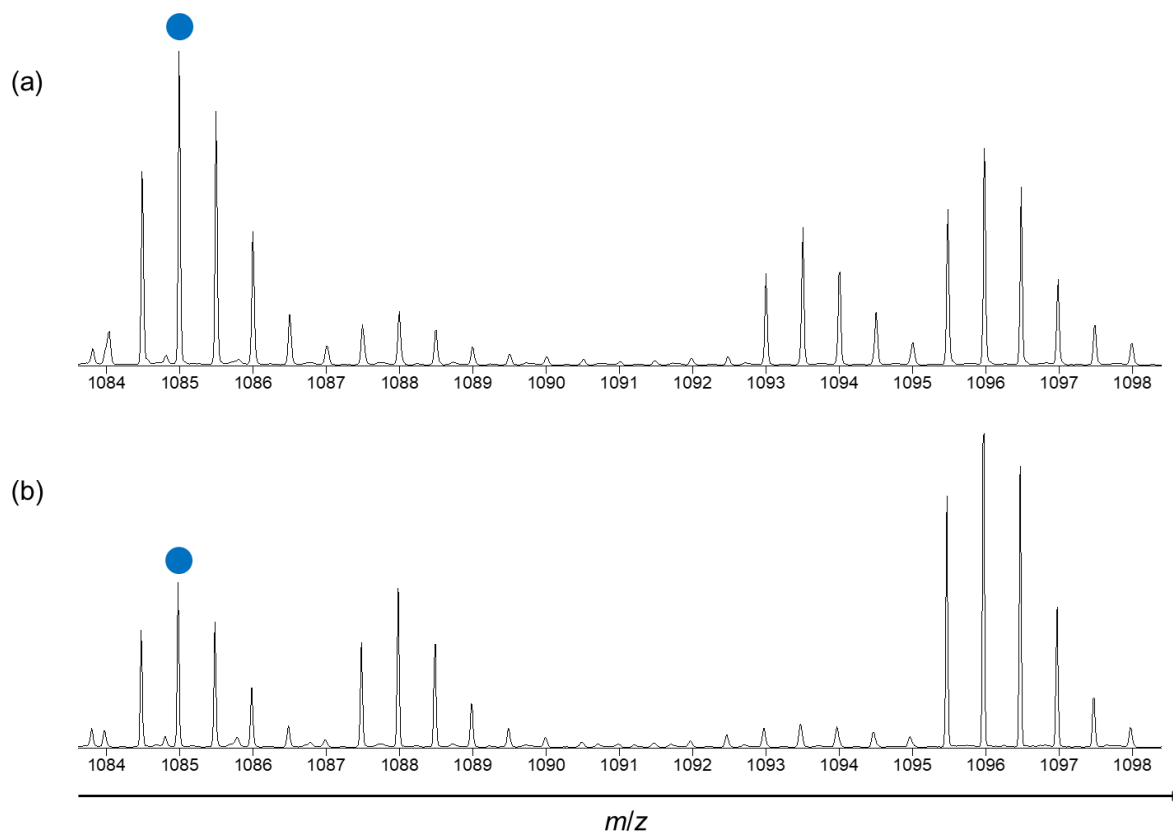
Figure 3. ESI-MS spectra of doubly charged [M + 2Na]$^{2+}$ (a) Cyclic TPE molecules (*i.e.*, product) at 0.01 mg mL^{-1} in acetonitrile/tetrahydrofuran (80/20) (*v/v*), and (b) parent TPE molecules (*i.e.*, reactant) at 0.01 mg mL^{-1} in acetonitrile/tetrahydrofuran (80/20) (*v/v*) with NaI (0.0002 mg mL^{-1}). Blue circles indicate doubly charged [M + 2Na]$^{2+}$ ions.

As shown in Figure 2 and Figure 3, both parent TPE molecules and cyclic molecules generate two characteristic ion species: singly charged [TPE + Na]$^+$ and doubly charged [TPE + 2Na]$^{2+}$ ions. The consistent generation of singly and doubly charged states confirms robust sodium coordination for both cyclic isomer and parent molecules. In this chapter, the discussion will focus on the doubly charged [TPE + 2Na]$^{2+}$ ions for both the parent TPE molecules and cyclic molecules. The entire ESI-MS spectrum of the parent TPE molecules and cyclic TPE molecules is provided in the Annexes (refer to Figure A2). The isotopic distribution of the simulated spectrum, parent TPE molecules and the cyclic TPE molecules is also shown in the Annexes (refer to Figure A3 for [TPE + Na]$^+$ and

Figure A4 for [TPE + 2Na]$^{2+}$ ions). All ions detected in the ESI-MS are listed in the Annexes (refer to Table 1 in the Annexes).

IMS experiments on gaseous parent TPE molecules and cyclic molecules

Following the ESI-ToF mass spectrometric analysis of parent TPE molecules and cyclic molecules (*i.e.*, reactant and product), the doubly charged TPE ions, [TPE + 2Na]$^{2+}$, were subjected to ion mobility measurements (refer to Figure 4) on a Waters Synapt G2-*Si* mass spectrometer to attempt a separation of the isomeric folded ions.
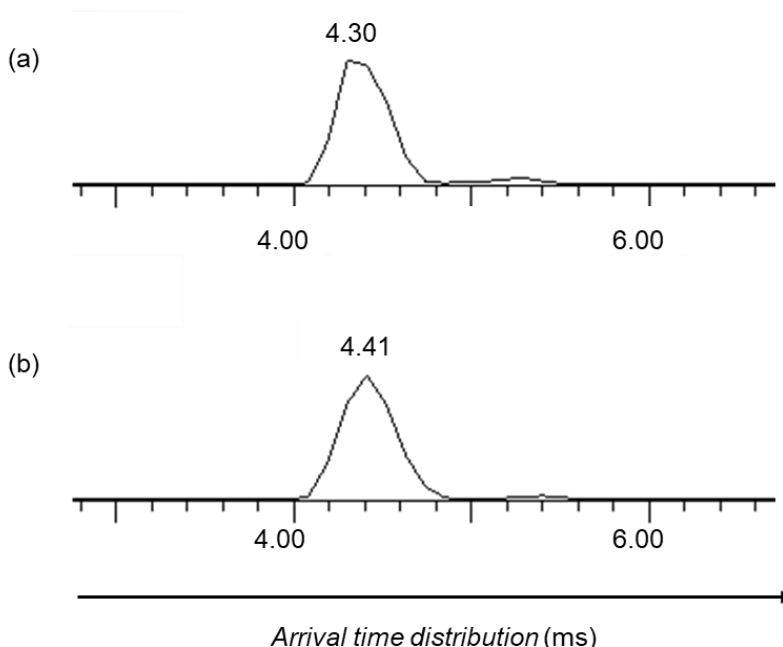
Figure 4. Ion mobility–mass spectrometry analysis of TPE molecules (0.01 mg mL^{-1} in acetonitrile/tetrahydrofuran, 80/20) (*v/v*) using a Waters Synapt G2-*Si* mass spectrometer: (a) arrival time distribution (*ATD*) of cyclic isomer [TPE + 2Na]$^{2+}$ ions, and (b) arrival time distribution (*ATD*) of parent [TPE + 2Na]$^{2+}$ ions.

Figure 4 depicts the arrival time distributions (*ATDs*) of the cyclic isomer and parent [*M* + 2Na]$^{2+}$ TPE ions that are nearly indistinguishable, indicating that IM-MS is unable to separate the cyclic isomeric and parent ions, likely due to the weak resolution of the

Waters Synapt G2-*Si* instrument.[149] Further, it is not possible to detect any isomers formed via the [2+2] photocycloaddition. Therefore, cyclic IMS analysis is required to achieve separation of the different isomers (refer to Figure 5). Cyclic ion mobility mass spectrometry (cIM-MS) experiments were performed on the same ion using a SELECT SERIES Cyclic IMS instrument (Waters Corporation, Wilmslow, UK). The number of passes through the cIMS cell was optimized to maximize separation (30 passes in this case). MassLynx exported the *ATD* as plain text files, which were subsequently fitted using Igor Pro (Version 8.02, 64-bit). Additional experimental details are provided in the Annexes. Cyclic IMS allows multiple passes of ions through the mobility cell, thereby increasing resolving power. After 30 passes through the cIMS, the ion mobilogram of the parent TPE molecules [TPE + 2Na]$^{2+}$, *m/z* 1087.48, displayed a single peak, whereas the cyclic TPE molecules [TPE + 2Na]$^{2+}$, *m/z* = 1087.49, showed two distinct peaks. This observation indicates the formation of at least two different isomers as a result of the [2+2] photocycloaddition of the TPE molecules (refer to Figure 5). Although the parent molecules show a very small peak at 30.5 ms, its intensity is negligible compared to the others; therefore, we exclude it from our discussion.
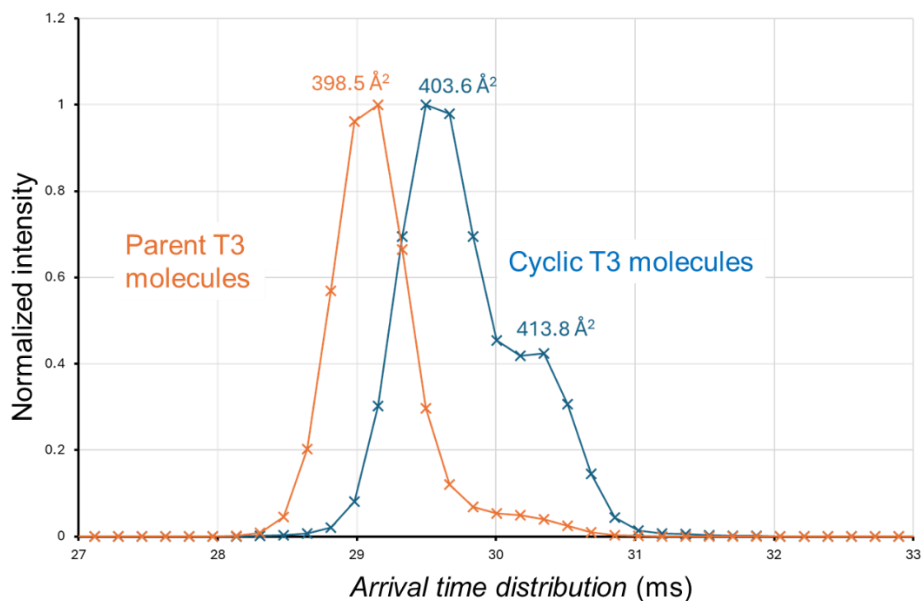
Figure 5. Cyclic ion mobility–mass spectrometry analysis of TPE molecules (0.01 mg mL^{-1} in MeOH); arrival time distribution (*ATD*) of cyclic TPE molecules [TPE + 2Na]$^{2+}$ ions shown in blue and arrival time distribution (*ATD*) of parent TPE molecules [TPE + 2Na]$^{2+}$ ions shown in orange after 30 pass.

In Figure 5, two distinct *ATD* peaks are observed for the cyclic isomer (*i.e.*, product) doubly charged TPE ions using cyclic IMS, whereas only a single *ATD* peak is detected for the parent (*i.e.*, reactant) doubly charged TPE ions. The Collisional Cross Section (*CCS*) values were calculated from the arrival times obtained in the cyclic IMS analysis. The *CCS* value for the parent (*i.e.*, reactant) doubly charged TPE ions is 398.5 $Å^2$, while the cyclic isomer (*i.e.*, product) doubly charged TPE ions exhibit two *CCS* values at 403.6 $Å^2$ and 413.8 $Å^2$. The size order obtained from cyclic ion mobility mass spectrometry (cIMS) does not match the order observed in SEC or TWIMS. This discrepancy arises from differences in physical environment, operating principles, timescales, path lengths, and ion heating. SEC measures hydrodynamic size in solution and is therefore influenced by intramolecular solvation and polymer–solvent interactions. TWIMS, uses a shorter drift path and travelling waves that can introduce varying degrees of ion heating and compaction. These differences influence the distribution of gas-phase conformers and can change the observed arrival-time order. In contrast, cIMS employs a cyclic, extended path length—often with multiple passes (e.g., 30)—which enables high-resolution sampling of ion conformational ensembles. However, it remains difficult to assign the specific isomers formed via [2+2] photocycloaddition based solely on this analysis. Therefore, DFT calculations and molecular dynamics simulations will be performed to identify the isomers detected by cyclic IMS.

Density Functional Theory (DFT) calculations

Initially, DFT calculations were performed to identify the most stable isomer for the *cis* and *trans* pyrene-substituted chalcone derivatives. All calculations were carried out using the B3LYP functional and the 6-31G** basis set. The results indicated that the *trans* isomer is energetically more stable than the *cis* isomer by 9.5 kcal mol^{-1} (refer to Figure 6).
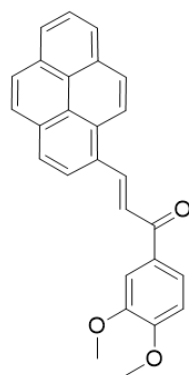
Trans isomer

E = 0 kcal/mol
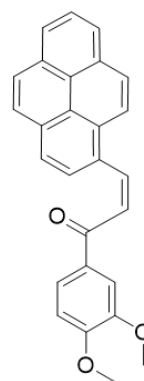
Cis isomer

E = 9.5 kcal/mol

Figure 6. DFT calculations were performed using B3LYP functional and 6-31G** basis set to determine the energetically more stable isomer of the pyrene-substituted chalcone derivative. The *trans* isomer was found to be 9.5 kcal mol^{-1} more stable than the *cis* isomer.

The above DFT calculations established that the *trans* isomer is energetically more stable than the *cis* isomer. Therefore, the *cis* isomer was excluded, and all subsequent calculations were performed using the *trans* isomer. For both the "P" and "Q" isomers, two possibilities exist: head-to-head and head-to-tail connectivity. Subsequently, DFT calculations were carried out to identify the most stable isomer between the head-to-head and head-to-tail configurations (refer to Figure 7).
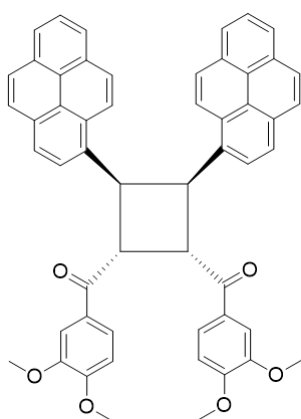
Head-to-head

E = 8.27 kcal/mol
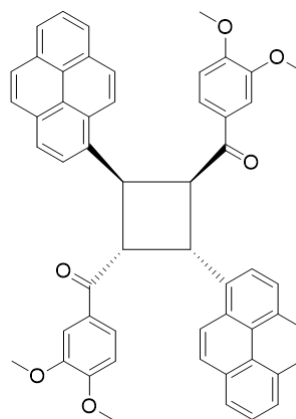
Head-to-tail

E = 0 kcal/mol

Figure 7. DFT calculations were performed using B3LYP functional and 6-31G** basis set to determine the energetically more stable isomer resulting from the [2+2] photocycloaddition of the pyrene-substituted chalcone derivative. The head-to-tail isomer was found to be 8.27 kcal mol^{-1} more stable than the head-to-head isomer.

The DFT calculations show that the head-to-tail isomer is 8.27 kcal mol^{-1} more stable than the head-to-head isomer. However, it is important to note that these results were obtained using a small fragment of the molecule. When the calculations were performed using the full TPE molecule, but with a shorter bridge chain (*i.e.*, one monomer in the bridge instead of three), the results were completely reversed. For the "P" isomer, the head-to-head configuration is 13.38 kcal·mol^{-1} more stable than the head-to-tail configuration. Similarly, for the "Q" isomer, the head-to-head isomer is 15.79 kcal·mol^{-1} more stable than the head-to-tail isomer. In the full molecules, steric hindrance and π–π stacking interactions stabilize the head-to-head isomer compared to the head-to-tail isomer.

Therefore, DFT calculations provide two important pieces of information: the *trans* isomer is more stable than the *cis* isomer, and the head-to-head isomer is more stable than the head-to-tail isomer. Following the DFT calculations, molecular dynamics (MD) simulations were performed to assign the peaks observed in the cyclic IMS analysis.

**Molecular dynamics simulation and theoretical *CCS* calculation**

To further assign experimental peaks, *i.e.* the peak in the cyclic IMS mobilogram, molecular dynamics (MD) simulations are performed starting from four different isomers of the cyclic TPE molecules, *i.e.*, the isomers formed via [2+2] photocycloaddition of TPE. The selected isomers for the MD simulations include the head-to-head and head-to-tail isomers for both "P" and "Q." MD simulations were also performed on the parent TPE molecules (*i.e.*, the reactant). The simulations employed a modified DREIDING force field, which has been previously established by our group.[105,210] In the modified DREIDING force field, the van der Waals equilibrium distance (R_0) for hydrogen was adjusted. An equilibrium distance of 2.83 Å was used instead of the default value of 3.195 Å. All molecular dynamics simulations were performed using this modified DREIDING force field. After the molecular dynamics simulation, Collisional Cross Section (*CCS*) calculations were performed. The *CCS* values for all different isomers are presented below (refer to Table 1). Please go through the Annexes for details about the MD simulation procedure.

Table 1. Molecular dynamics simulations of [TPE + 2Na]$^{2+}$ ions (modified DREIDING force field, 300 K, 25 ns): theoretical collision cross sections and standard deviation for all isomers

Name of the isomer	CCS_{th} (Å^2)	SD
"P" head-to-head	400	6
"P" head-to-tail	404	5
"Q" head-to-head	412	5
"Q" head-to-tail	415	7
Parent TPE	408	7

From the theoretical *CCS* calculations, it is observed that the "P" isomers are systematically more compact than the "Q" isomers, whereas the head-to-head isomers are characterized by weaker *CCS* than the head-to-tail isomers. These theoretical *CCS* values are then compared with those obtained from cyclic IMS in Figure 5.

The parent TPE ions are characterized by only one peak, with an experimental *CCS* value at 398.5 Å^2, the theoretical value (CCS_{th} = 408 Å^2) being 2.3% higher than the experimental one. Three-dimensional structures of the doubly charged TPE molecules are shown in Figure 8. Doubly charged cyclic TPE molecules present two peaks in the cyclic IMS spectrum, with *CCS* values at 403.6 Å^2 and 413.8 Å^2. Since the theoretical *CCS* values are very close to each other, it is difficult to assign the peaks based solely on theory. It is here proposed that the 403.6 Å^2 peak corresponds to the "P" head-to-head isomer (404 Å^2) and that the 413.8 Å^2 peak corresponds to the "Q" head-to-head isomer as the head-to-head configurations are calculated more stable than the head-to-tail ones due to π-π stacking interactions between two pyrene rings.
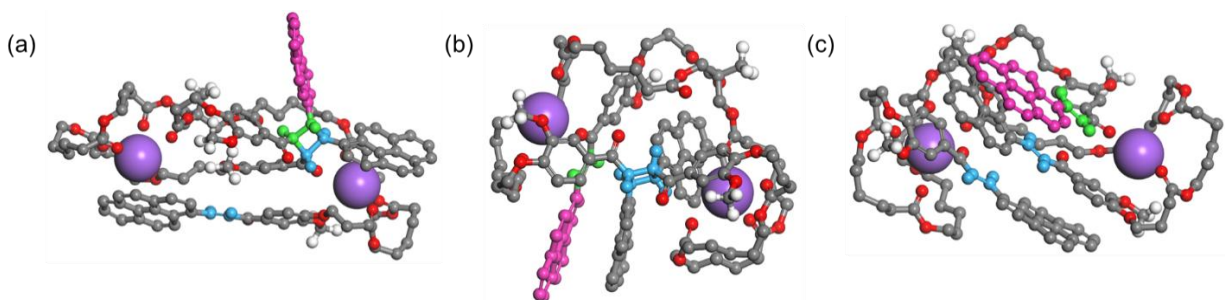
Figure 8. Molecular dynamics simulations (modified DREIDING force field, 300 K, 25 ns) of [TPE + 2Na]$^{2+}$ ions: snapshots from the last frame of the MD simulation showing (a) the head-to-head isomer of "P", (b) the head-to-head isomer of "Q", and (c) the parent (*i.e.*, reactant) TPE molecules.

DFT calculations only consider thermodynamics and are not suitable for photoreactions. We started with three trans bonds initially, then gradually decreased the number of *trans* bonds while increasing the number of *cis* bonds—for example, combinations of 2 *trans* + 1 *cis*, 1 *trans* + 2 *cis*, and 3 *cis*. However, when shifting from trans to cis, the *CCS* value increased significantly (the combinations of the two *trans* and one *cis* units are provided in Table 2). Therefore, we excluded the *cis* isomers from further consideration.

Table 2. Molecular dynamics simulations of [TPE + 2Na]$^{2+}$ ions (modified DREIDING force field, 300 K, 25 ns): the resulting theoretical collision cross sections and standard deviations for all isomers containing two *trans* and one *cis* units are summarized. In the notation used, "L" denotes the left side, "R" the right side, "H" the head region (refer to Scheme 1), "C" represents the *cis* configuration, and "T" represents the *trans* configuration.

Name of the isomer (2 *trans* and 1 *cis*)	CCS_{th}	SD
"P" head-to-head (LC_HT_RT)	434	6
"P" head-to-tail (LC_HT_RT)	416	8
"P" head-to-head (LT_HT_RC)	423	6
"P" head-to-tail (LT_HT_RC)	425	8
"Q" head-to-head (LC_RT_HT)	426	6
"Q" head-to-tail (LC_RT_HT)	421	5

"Q" head-to-head (LT_RT_HC)	418	6
"Q" head-to-tail (LT_RT_HC)	439	7
Unfolded (LC_RT_HT)	417	6
Unfolded (LT_RT_HC)	420	6

Conclusion

The current study demonstrates that intramolecular [2+2] photocycloaddition in TPE generates multiple folded isomers that cannot be distinguished by standard IM-MS. However, it can be resolved by cyclic IMS. DFT calculations and MD simulation reveal that the predominant species are the 'P' and 'Q' head-to-head isomers, stabilized by favorable π–π stacking interactions. These findings provide new insights into the structure–function relationship of pyrene-substituted chalcone derivatives, underscoring the role of molecular architecture in governing photoreactivity and conformational diversity.

Annexes

On the discrimination between regio- and stereoisomeric photo-products using Cyclic Ion Mobility Mass Spectrometry in combination with Molecular Dynamics Simulations

Synthesis of the parent TPE molecules and cyclic TPE molecules:

The compound was synthesized in Queensland University of Technology by Pashley-Johnson et al[179]. Initially, a difunctional alcohol containing a PyChal was synthesized, which will serve as the initiator for subsequent stepwise additions. An acid with a protected hydroxyl group was then coupled to this initiator, yielding a doubly protected diol with an additional linker unit. Importantly, the intrinsic hydrophobicity of the chalcone initiator—and the resulting oligomers—enabled purification solely by aqueous extraction from the organic reaction mixture, thereby eliminating the need for labor-intensive and costly column chromatography throughout the sequence.

The terminal protected diol of the growing macromolecule could be rapidly and efficiently deprotected using tetrabutylammonium fluoride, affording a free diol that was readily available for further chain extension.

After synthesizing linkers of the desired length, the chain end was capped by coupling with a carboxylic acid–functionalized PyChal. This afforded a trifunctional macromolecule, that was characterized by NMR.[179]

[2+2] photocycloaddition of the parent TPE molecules was performed using a 25 μM solution in acetonitrile of the parent TPE molecules and irradiating by a tunable monochromatic pulsed laser. The formation of the cyclic isomer was characterized using NMR (refer to Figure A1), investigating the resonance of the proton of cyclobutane ring. However, in that case both intermolecular and intramolecular [2+2] photocycloaddition happened together. Another different [2+2] photocycloaddition reaction was performed using a low concentration of the parent TPE molecules to suppress the intermolecular reactions and to make intramolecular reactions dominant for a small timescale. The

reaction was performed using 12.5 µM solution in acetonitrile of the parent TPE molecules and irradiating using a light emitting diode of 10W at λ_{max} = 445 nm.

Confirmation of parent TPE molecules and cyclic TPE molecules

TPE (1 mg) was dissolved in acetonitrile to obtain a 12.5 µM solution and irradiated with a 10 W LED light source (λ_{max} = 445 nm) for 3.5 min. Following irradiation, the solvent was removed, and the resulting residue was subjected to NMR analysis (refer to Figure A1).
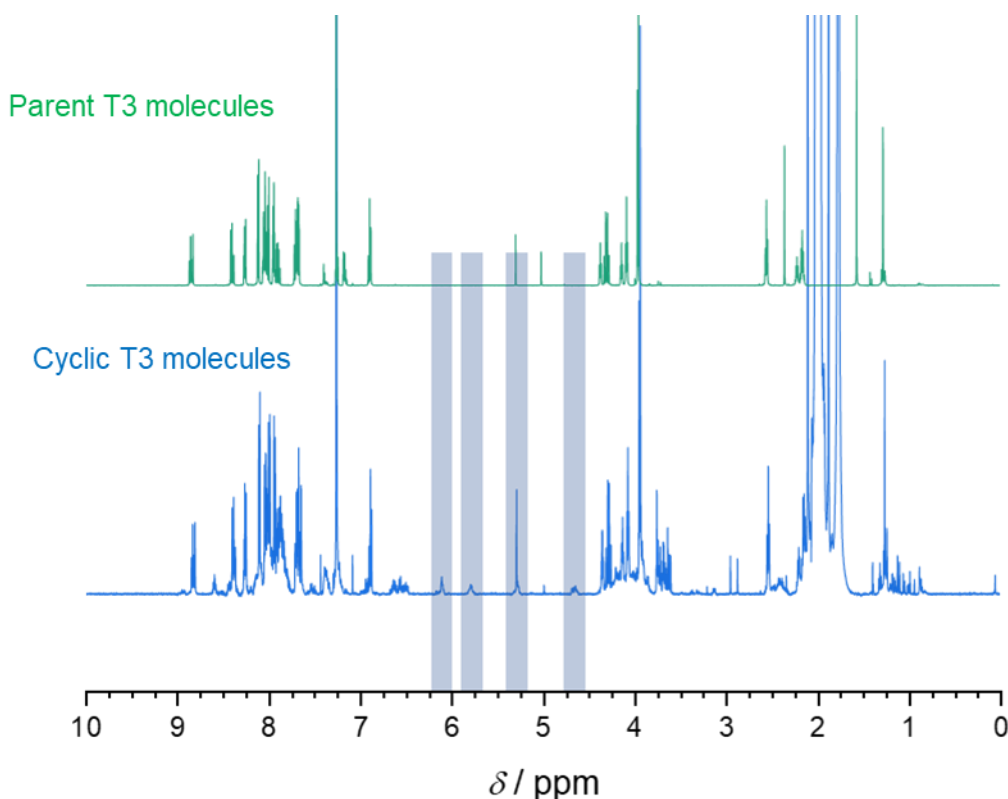
Figure A1. ^{1}H NMR spectra of TPE before (green) and after (blue) irradiation, with blue highlights showing the formation of cyclobutane resonances.

Ion Mobility Experiments

Stock solutions of parent and cyclic TPE molecules of 0.01 mg mL^{-1} were prepared in tetrahydrofuran and acetonitrile (20:80, *v/v*). Both molecules was characterized using NaI (0.0002 mg mL^{-1}) as a ionization agent. The stock solutions were 100x diluted with acetonitrile and tetrahydrofuran (80:20, *v/v*) before analysis.

MS spectra and *CCS* measurements were performed on a Waters Synapt G2-*Si* mass spectrometer in positive ion mode. The solutions were infused at a flow rate of 5 µL min⁻¹ with a capillary voltage of 3.1 kV, a source temperature of 100 °C and a desolvation temperature of 150 °C. The standard IMS-MS parameters were : wave height = 40 V, wave velocities = 350 or 600 or 800 m s⁻¹, mass range = *m/z* 50-4,000; N_2 flow rate = 60 mL min⁻¹, He flow rate = 180 mL min⁻¹ and trap bias = 45.0 V. A pre-established calibration procedure[158] was used to convert the experimentally determined arrival time distributions to $^{TW}CCS_{N2 \rightarrow He}$,[159] which will be referred to as CCS_{exp}.

Figure A2. ESI-MS spectra of (a) Cyclic TPE molecules (*i.e.*, product) at 0.01 mg mL⁻¹ in acetonitrile/tetrahydrofuran (80/20) (*v/v*), and (b) parent TPE molecules (*i.e.*, reactant) at 0.01 mg mL⁻¹ in acetonitrile/tetrahydrofuran (80/20) (*v/v*) with NaI (0.0002 mg mL⁻¹). Red circles indicate singly charged [*M* + Na]⁺ ions, and blue circles indicate doubly charged [*M* + 2Na]²⁺ ions.
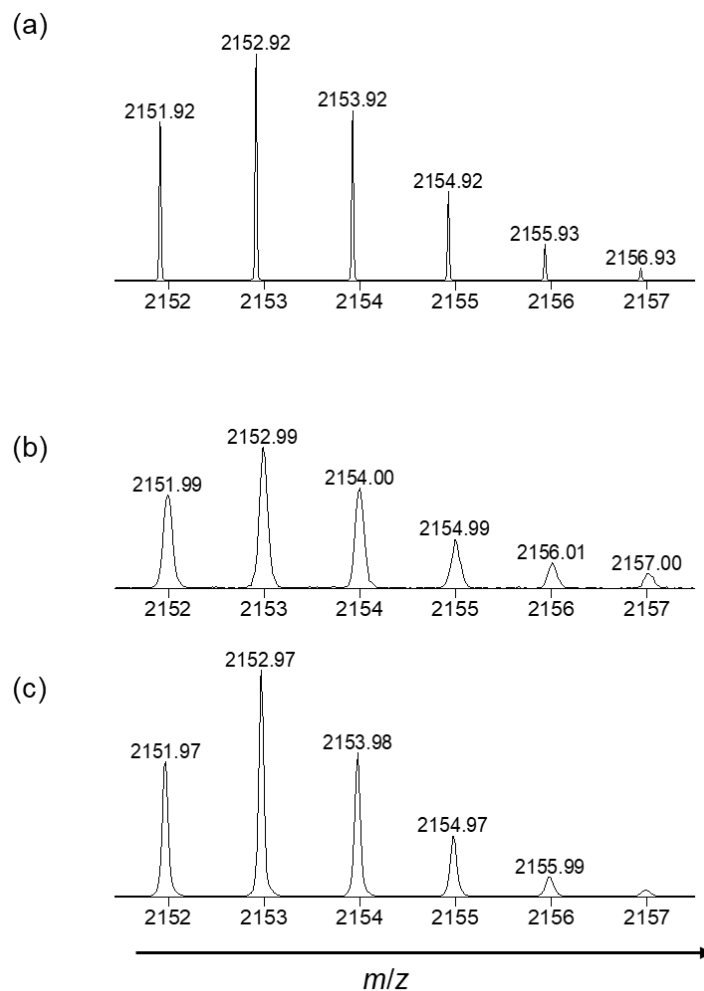
Figure A3. ESI-MS mass spectra of singly charged [TPE + Na]$^+$ (0.01 mg mL^{-1}) in acetonitrile/tetrahydrofuran (80/20) (*v/v*) with NaI (0.0002 mg mL^{-1}); comparison between experimental and simulated isotope patterns: (a) simulated spectrum of [TPE + Na]$^+$, (b) experimental spectrum of cyclic TPE molecules (*i.e.* product) and (c) experimental spectrum of parent TPE molecules (*i.e.* reactant).
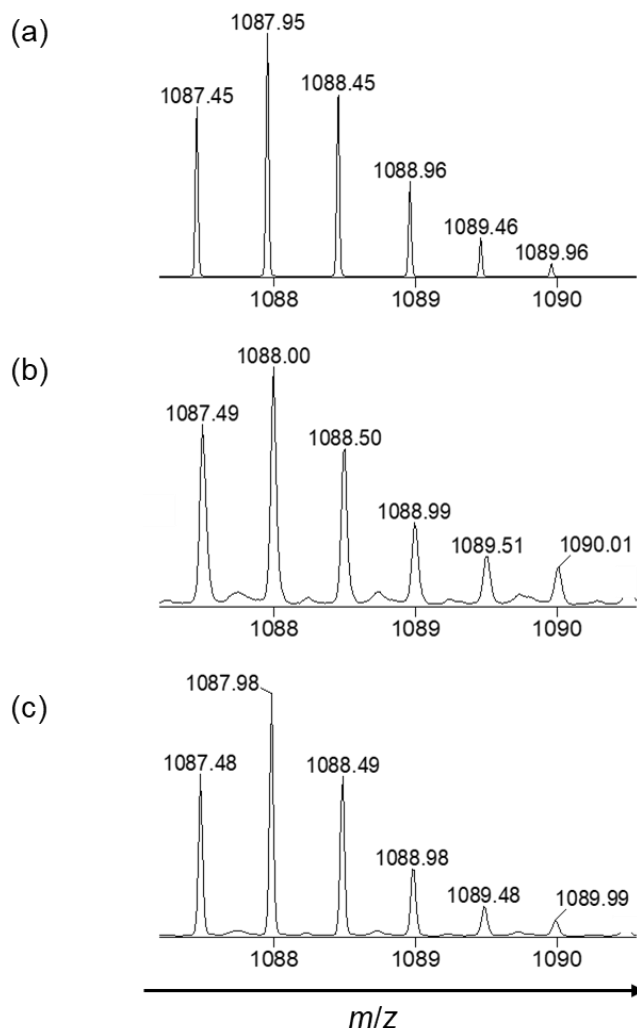
Figure A4. ESI-MS mass spectra of doubly charged [TPE + 2Na]$^{2+}$ (0.01 mg mL^{-1}) in acetonitrile/ tetrahydrofuran (80/20) (*v/v*) with NaI (0.0002 mg mL^{-1}); comparison between experimental and simulated isotope patterns: (a) simulated spectrum of [TPE + 2Na]$^{2+}$, (b) experimental spectrum of cyclic TPE molecules (*i.e.* product) and (c) experimental spectrum of parent TPE molecules (*i.e.* reactant).

Table 1. ESI-MS mass spectra of TPE molecules (0.01 mg mL^{-1}) in acetonitrile/tetrahydrofuran (80/20) (*v/v*) with NaI (0.0002 mg mL^{-1}): The ions that were detected, along with their simulated and experimental *m/z* values, are reported for both the parent TPE molecules and the cyclic TPE molecules

Name of the isomer	Simulated *m/z*	Experimental *m/z* (Parent TPE molecules)	Experimental *m/z* (Cyclic TPE molecules)
[*M* + H]$^+$	2129.99	2129.98	2130.02
[*M* + Na]$^+$	2151.92	2151.97	2151.99

$[M + K]^+$	2167.89	2167.94	2167.96
$[M + 2H]^{2+}$	1065.47	1065.49	1065.51
$[M + 2Na]^{2+}$	1087.45	1087.48	1087.49
$[M + 2K]^{2+}$	1103.43	1103.46	1103.46
$[M + H + Na]^{2+}$	1076.46	1076.49	1076.51
$[M + H + K]^{2+}$	1084.45	1084.47	1084.49
$[M + Na + K]^{2+}$	1095.44	1095.47	1095.48
$[M + K + NH_4]^{2+}$	1092.96	1092.97	1093.00

Cyclic Ion Mobility Experiments

Solutions of TPE molecules (both parent and cyclic forms, 0.05 mg mL^{-1} in methanol) containing sodium acetate were infused into the MS system at a constant flow rate of 5 µL min^{-1} using a syringe pump (Pump 11 Elite, Harvard Apparatus). Data were acquired in positive ion mode under the following conditions: capillary voltage = +4 kV; cone voltage = 140 V; desolvation gas flow = 800 L h^{-1}; desolvation temperature = 250 °C; source temperature = 120 °C; helium cell pressure = 2.3 mbar; and cIM cell pressure = 1.7 mbar. The traveling wave amplitude and velocity were set at 22.0 V and 600 m s^{-1}, respectively.

Calibration Procedure of Cyclic Ion Mobility Mass Spectrometry

Cyclic ion mobility mass spectrometer (cIM-MS) (Waters Select Series; Wilmslow, UK),[211] was utilized in both positive and negative ion modes. Samples of concentrations 0.1 – 1 µM were loop injected into the instrument using the Waters Acquity Premier UPLC, with injections of 10 µL into a flow of 0.1 mL/min of methanol for the positive ions or 10 mM ammonium acetate in methanol to assist the negative ion visibility. *CCS* calibrations included the infusion of major mix through the onboard sample fluidics at a flow rate of 1 µL/min, mimicking the experimental process outlined in recent publications.[212]

Density Functional Theory (DFT) calculations

Density functional theory (DFT) calculations were carried out with Gaussian 09 (Revision D.01).[162] The B3LYP functional[213–215] in combination with the 6-31G** double zeta basis set was employed. To account for dispersion interactions, Grimme's empirical dispersion correction (GD3BJ) was included.[164]

Molecular Dynamics Simulations

All calculations were carried out for a run lasting 25 ns with 1 fs time step in the *NVT* ensemble at 300 K (as temperature does not create much effect due to the high pressure in the IMS chamber) with the Materials Studio software (BIOVIA, San Diego, CA).[160] The modified DREIDING force field was used for all calculations. At first, Charges were assigned using the COMPASS force field for the initial polymer chain. Subsequently, two sodium ions were added, followed by geometry optimization. Next, a quenched dynamics was then executed for 25 ns using 1 fs timestep and 100 Å van der Waals and electrostatic interaction cutoff at 450 K. After that, a second quenched dynamics was then executed for 10 ns using 1 fs timestep and 100 Å van der Waals and electrostatic interaction cutoff at 300 K using the lowest-energy structure obtained from the first quench dynamics. A MD run was then performed starting from the most stable structure obtained from the second quenched dynamics until the calculated radius of gyration reaches equilibrium. The *CCS* calculations were carried out by taking average of 500 frames utilizing the trajectory method[161] (TM) model implemented within the Collidoscope software.[154]

Conclusion and Outlook

The objective of the current thesis was to evaluate the potential of ion mobility–mass spectrometry (IM-MS), in combination with molecular dynamics (MD) simulations, as a method for characterizing pre-polymers that can lead to single-chain polymer nanoparticles (SCNP). Conventionally, SCNPs and their precursors are studied using techniques such as nuclear magnetic resonance (NMR) spectroscopy, dynamic light scattering (DLS), and size-exclusion chromatography (SEC). More recently, our group has extended this toolbox by applying electrospray ionization mass spectrometry (ESI-MS) to SCNP characterization. To the best of our knowledge, however, the use of IM-MS for the analysis of SCNPs and their precursor polymers has not yet been reported.

The current PhD thesis study demonstrates the power of combining ion mobility–mass spectrometry (IM-MS) with molecular dynamics (MD) simulations to unravel the three-dimensional structures of polymer ions and their functional derivatives such as precursor SCNP. For polystyrene (PS) ions, we established that the rigid aromatic backbone collapses into compact, elliptic globular structures with effective densities comparable to the density of bulk polystyrene. Solvent accessible surface area (*SASA*) analyses revealed that these globular forms are densely packed, with minimal internal void volume, emphasizing the role of backbone rigidity in enforcing compaction. Importantly, the positive charges in both singly and doubly charged ions consistently localize at the periphery of the ions aggregate, in sharp contrast to polyethylene glycol ions where sodium ions are deeply buried within the core of the ions aggregate. This distinction reflects two fundamentally different folding mechanisms: in polystyrene, cation-π interaction in addition with the π-π staking interaction between styrene unit drive backbone collapse while simultaneously excluding charges from the interior due to the hydrophobic nature of the polymer chain, whereas in polyethylene glycol, flexible polymer chains fold around the cation, encapsulating it in the core. Furthermore, MD simulations initiated from diverse starting conformations revealed that PS chains can fold into multiple U- and S-shaped motifs that nevertheless display nearly identical *CCS* values, underscoring a degeneracy of gas-phase conformations reminiscent of random coil ensembles in solution. For larger PS ions, we further demonstrated that cations such as Ag^+ are not

167

simply sandwiched between two phenyl rings but instead participate in three-dimensional coordination, ultimately promoting global tertiary collapse of the ion.

Extending these insights to styrene-based copolymers (STY and STY-CH$_2$-OH) and precursor SCNP (STY, STY-CH$_2$-OH, STY-PPh$_2$ and STY-PPh$_2$-AuCl) revealed how hydrogen bonding, end-group polarity, and steric effects govern charge localization and polymer folding. In STY and STY-CH$_2$-OH containing copolymers, strong hydrogen bonding between protonated TEMPO and hydroxyl groups of STY-CH$_2$-OH monomer unit stabilize the folded structures, with the charge center gradually migrating towards the center of the ion aggregate as the degree of polymerization increases. In contrast, for gold-functionalized copolymers *i.e.* precursor SCNP, an N–H⋯Cl hydrogen bond was identified (confirmed by DFT), but steric hindrance from the bulky PPh$_3$ moiety prevents charge migration, the charge remaining localized at the edge of the ion aggregate. These investigations establish how the nature of the monomer unit directly impacts folding processes, charge distribution, and ultimately the accessibility of functional groups in SCNP precursors, with clear implications for their catalytic performance.

Finally, application of this integrative methodology to pyrene-substituted chalcone derivatives underscores its broad applicability beyond polymer systems. Here, intramolecular [2+2] photocycloaddition generates multiple folded isomers that cannot be distinguished by conventional IM-MS due to the resolution limitation of SYNAPT-G2-*Si*. However, isomers were successfully resolved using cyclic IMS. Complementary MD and DFT calculations revealed that the predominant conformations correspond to head-to-head "P" and "Q" isomers stabilized by favorable π–π stacking interactions, thereby providing detailed insight into the structural origins of their photoreactivity and conformational diversity.

In general, these studies provide a unifying framework for understanding how backbone rigidity, end-group polarity (hydrophobic/hydrophilic), charge localization, hydrogen bonding (O–H⋯H/ N–H⋯Cl), steric effects, and secondary interactions dictate the folding and collapse of polymer ions. By bridging experiment with atomistic simulations, IM-MS/MD emerges as a uniquely powerful platform for mapping hidden structure–function relationships across a broad range of macromolecular and supramolecular systems

including precursor SCNP. This comprehensive approach not only deepens our understanding of polymer collapse and conformational diversity in the gas phase but also lays the foundation for the rational design of functional SCNPs and advanced polymeric nanomaterials with tailored catalytic, responsive, and photochemical properties.

On the way of detecting intact SCNP ions in the gas phase, charge detection mass spectrometry (CD-MS) may be envisaged as an innovative method for large ion detection, including the charge and mass analysis. In CD-MS, the charge of the ions is measured directly as they pass through the analyzer, enabling the determination of the true charge state. This technique is particularly powerful for ionized molecules with very high molecular weights and could,[216] therefore, be applied in the future for the characterization of single-chain polymeric nanoparticles (SCNPs).

In the future, we aim to investigate the SCNPs previously reported by our group (refer to Figure 1),[131] which exhibit catalytic activity. A particularly intriguing possibility is that the catalytic activity of the SCNPs can potentially be regulated by changing its compaction state around the catalytically active metal-complex due to the *cis*/*trans* isomerization of the azobenzene units that are installed during the compaction process. This raises an important research question: how do the folding process and structural features of SCNPs govern the catalytic behavior of the e.g. *trans* isomer dominated SCNP, and to what extent can catalytic activity be modulated by the reversible shaping of the catalytic pocket? Addressing this question using the methodology developed in the present thesis will yield valuable information regarding the position and accessibility of functional groups within different morphological states, each of which exhibits distinct catalytic activities. Such insights into the accessibility of functional groups across varying morphologies will provide a fundamental understanding of the structure–function relationship in photo-switchable SCNPs.
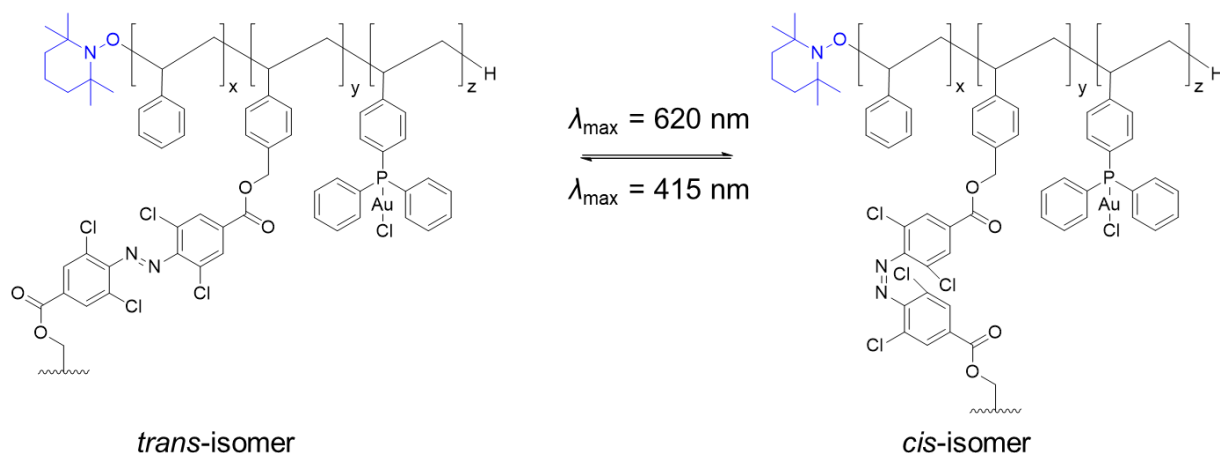
Figure 1. Structure of the light induced catalytically active SCNPs.[131] Reproduced with permission from reference [131].

Beyond our future plan of examining the more complex SCNPs described above (refer to Figure 1), we also carried out some preliminary investigations using a simple model SCNP. This model SCNP was created by coupling azobenzene-4,4'-dicarbonyl dichloride with the copolymer TEMPO-(styrene)$_x$-(styrene-CH$_2$-OH)$_y$, which has already been investigated in detail using ion mobility–mass spectrometry (IM-MS) in combination with molecular dynamics (MD) simulations (refer to Chapter 2). Our preliminary study was based solely on molecular dynamics simulations. Since no experimental results are yet available, we did not include this work in the main chapter; instead, we present it here in the Outlook section.

To gain deeper insight into the folding process, as well as the position and role of functional groups in a copolymer compared to a single-chain nanoparticle (SCNP), this model system was analyzed. Specifically, we investigated a model SCNP by MD simulations in which the TEMPO-(styrene)$_x$-(styrene-CH$_2$-OH)$_y$ copolymer was intramolecularly cross-linked through azobenzene units. In this design, the azobenzene moieties serve as dynamic crosslinkers, bridging two STY-CH$_2$-OH units along the polymer backbone.
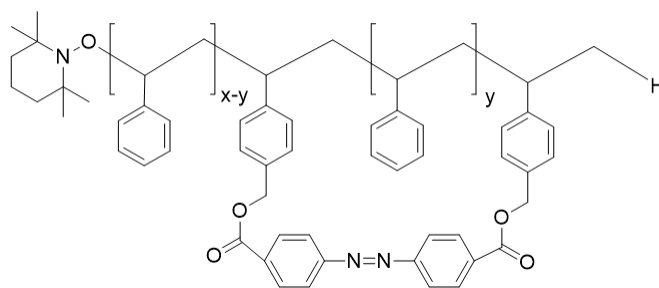
Figure 2. Model structure of an SCNP prepared by bridging the TEMPO-(STY)$_x$-(STY-CH$_2$-OH)$_y$ copolymer with an azobenzene-4,4'-dicarbonyl dichloride. The bond lengths and angles shown in the structure do not represent the actual relative bond lengths and angles.

Molecular dynamics (MD) simulations were carried out using the PCFF force field according to the following procedure. First, geometry optimization was performed starting from linear model molecules using forcefield assigned charge. After introducing a proton (H$^+$) to the optimized polymer chain, an additional geometry optimization was conducted. The TEMPO group was selected as the proton carrier due to the presence of its basic nitrogen atom. Subsequently, quenched dynamics were performed for 20 ns at 300 K, with frames quenched every 5 ps, a time step of 1 fs, and a cutoff of 100 Å for both van der Waals and electrostatic interactions. The most stable structure obtained from this quenched dynamics run was subsequently used as the starting configuration for a 25 ns MD simulation in the *NVT* ensemble (constant number of particles, volume, and temperature, with T = 300 K) using a 1 fs time step and a cutoff of 100 Å for both van der Waals and electrostatic interactions.

Preliminary MD simulations reveal that the *cis–trans* isomeric state of the azobenzene unit is governed by the spacing of the bridging monomer unit (STY-CH$_2$-OH) within the polymer chain. When the two STY-CH$_2$-OH groups are separated by up to three monomer units (y = 3), the azobenzene preferentially adopts the *cis* configuration, whereas for larger separations (y > 3), the *trans* configuration is stabilized. These results demonstrate a direct correlation between local chain architecture and the possible photochemical state of the azobenzene linker, highlighting how the folding pattern of the polymer influences the configuration of the cross-linking units.

171

Importantly, this structural dependence also provides a mechanistic basis for understanding the link between the SCNP morphology and its potential catalytic performance. Since the *cis* and *trans* isomers differ in their steric and electronic environments, their distribution directly impacts the accessibility and organization of catalytic sites within the nanoparticle. Thus, the ability to modulate azobenzene configuration through polymer folding and photo-switching establishes a clear structure–function relationship, offering a strategy to regulate catalytic activity and selectivity in photo-switchable SCNPs. This investigation provides insights into the folding process of the molecules as well as the *cis–trans* isomerization of the azobenzene unit.

In future work, we are also interested in investigating the following molecules in addition to the SCNPs developed our team earlier.[131] Pomposo and colleagues (2014),[14] developed single-chain polymer nanoparticles (SCNPs) that fold around Cu(II) ions, forming compact, enzyme-like structures. These soft nanoparticles act as catalysts, showing substrate selectivity in oxidative coupling of terminal acetylenes — something that simple Cu salts (like $CuCl_2$ or $Cu(OAc)_2$) cannot achieve (refer to Figure 3).

The selectivity is likely associated with the presence of multiple local catalytic sites, specifically $Cu(AEMA)_2$ complexes, which are structurally shielded by the surrounding polymer environment. This environment is thought to stabilize certain reaction transition states more effectively than others. The SCNPs therefore exhibit highly selective catalytic activity, with the selectivity being intrinsically linked to the polymer folding and overall morphology. The position of the catalytic centers and their local polymer environment can be systematically investigated using the methodology developed in the present thesis. The above approach enables a deeper understanding of the folding process, morphological features, and polymer environment, thereby providing critical insights into the origins of catalytic selectivity in SCNPs.
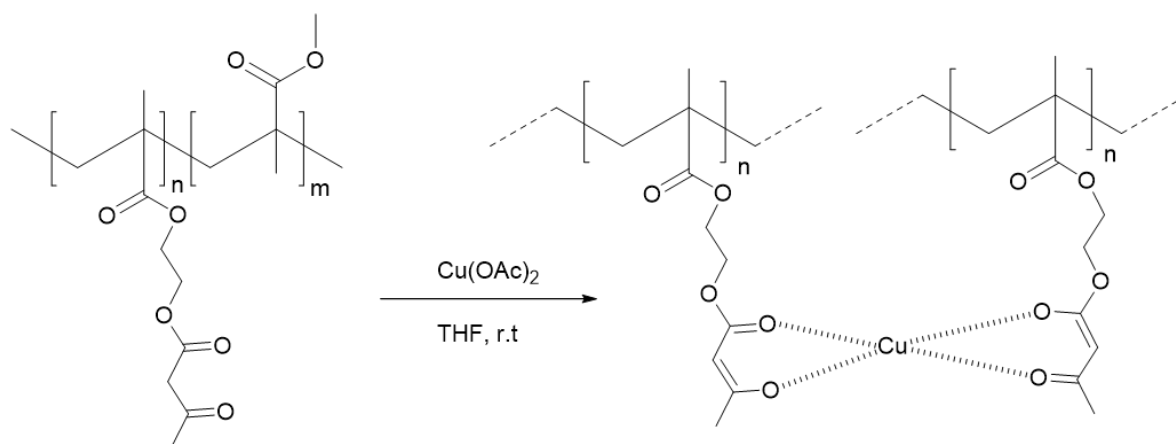
Figure 3. Structure of the catalytically active metallo-folded SCNPs.[14] Reproduced with permission from reference [14].

Furthermore, we are interested in investigating SCNPs developed by our group, specifically heterobimetallic single-chain polymeric nanoparticles (SCNPs) that exhibit recyclable homogeneous catalytic activity.[217] The design of this system is based on three distinct monomer units: STY, STY-PPh$_2$ and STY-CO$_2$H (refer to Figure 4). STY-PPh$_2$ and STY-CO$_2$H showing selective binding affinity for different metal ions. The STY-CO$_2$H unit coordinates with Eu(III) ions, which induces intramolecular chain collapse and thereby drives the formation of SCNPs. In contrast, the STY-PPh$_2$ unit binds selectively to AuCl, generating well-defined STY-PPh$_2$-AuCl complexes that serve as catalytically active centers, displaying high activity in hydroamination reactions.

A particularly attractive feature of this system is that it operates as a homogeneous catalyst while being readily recyclable. The two types of monomer units thus fulfill entirely different functions: one acts as a catalytic site, while the other dictates SCNP formation through metal coordination. As a result, both the catalytic activity and selectivity are intimately linked to the morphology of the SCNPs.

The close connection between morphology and function makes it ideal to understand the polymer architecture surrounding the different metal ions. However, conventional characterization techniques are often unable to provide precise information about these local environments. In this context, the methodology developed in the present thesis

offers a powerful approach to probe such architectures and to rationalize the relationship between SCNP morphology, catalytic activity, and selectivity.
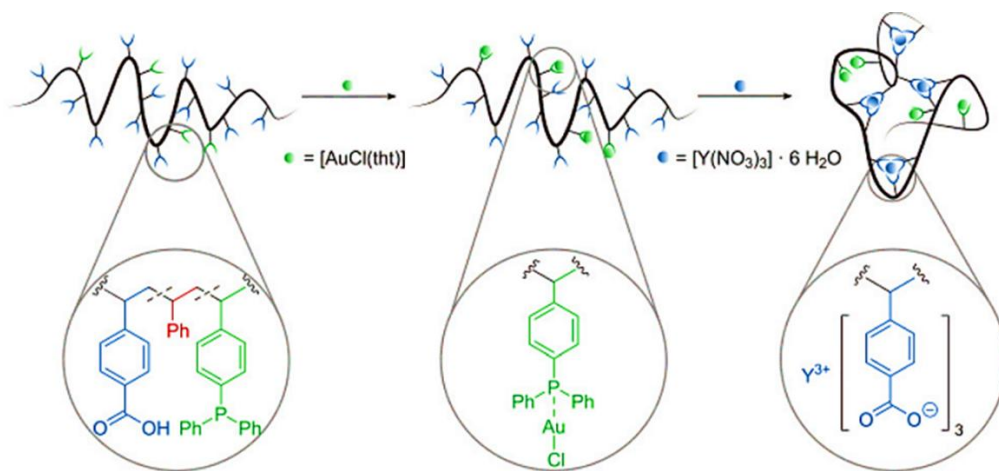
Figure 4. Schematic structure of the heterobimetallic catalytically active Au(I)/Y(III)-SCNPs.[217] Reproduced with permission from reference [217].

In summary, the current thesis presents a detailed investigation of precursor single-chain nanoparticles and photochemically driven SCNPs using ion mobility–mass spectrometry (IM-MS) in combination with molecular dynamics (MD) simulations provides a fascinating and highly resolved view of the folding mechanisms of such macromolecules. As research on single-chain nanoparticles is expanding, the IM-MS/MD protocols established herein are expected to significantly extend the toolbox of conventional characterization techniques—including size exclusion chromatography (SEC), dynamic light scattering (DLS), diffusion-ordered NMR spectroscopy (DOSY NMR) and small-angle X-ray scattering (SAXS)—by offering a unique perspective on chain folding processes, the position of functional groups and end groups, as well as the influence of sequence on SCNP architecture, this approach facilitates understanding of the relationship between structure and catalytic activity. Such insights are essential for the rational design of more efficient, externally stimuli-responsive SCNPs.

List of Publications

1. <u>**S. Naskar**</u>, A. Minoia, Q. Duez, A. Izuagbe, J. De Winter, S. J. Blanksby, C. Barner- Kowollik, J. Cornil, P. Gerbaux. **"*Polystyrene Chain Geometry Probed by Ion Mobility Mass Spectrometry and Molecular Dynamics Simulations*"**. *J. Am. Soc. Mass Spectrom. 2024, 35, 10, 2408–2419* https://doi.org/10.1021/jasms.4c00231

Citation = 1

This paper is presented in chapter 1

2. <u>**S. Naskar**</u>, A. Izuagbe, V. Lemaur, Q. Duez, A. Minoia, J. De Winter, S. Blanksby, J. Cornil, C. Barner- Kowollik, P. Gerbaux. **"*Ion Mobility Mass Spectrometry Coupled with Molecular Dynamics Simulations: In- depth Structural Analysis of Polystyrene-based Au-Containing Copolymers*"**. *Polym. Chem., 2025* https://doi.org/10.1039/D5PY00194C

This paper is presented in chapter 2

3. **"*On the discrimination between regio- and stereoisomeric photo-products using Cyclic Ion Mobility Mass Spectrometry in combination with Molecular Dynamics Simulations*"**. *(Ongoing project).*

This work is presented in chapter 3

References

(1) Lyon, C. K.; Prasher, A.; Hanlon, A. M.; Tuten, B. T.; Tooley, C. A.; Frank, P. G.; Berda, E. B. A Brief User's Guide to Single-Chain Nanoparticles. *Polym. Chem.* **2015**, *6* (2), 181–197. https://doi.org/10.1039/C4PY01217H.

(2) Wegner, M. All Purpose Sox: The Many Roles of Sox Proteins in Gene Expression. *The International Journal of Biochemistry & Cell Biology* **2010**, *42* (3), 381–390. https://doi.org/10.1016/j.biocel.2009.07.006.

(3) Raynal, M.; Ballester, P.; Vidal-Ferran, A.; Van Leeuwen, P. W. N. M. Supramolecular Catalysis. Part 2: Artificial Enzyme Mimics. *Chem. Soc. Rev.* **2014**, *43* (5), 1734–1787. https://doi.org/10.1039/C3CS60037H.

(4) Ryu, J.-H.; Chacko, R. T.; Jiwpanich, S.; Bickerton, S.; Babu, R. P.; Thayumanavan, S. Self-Cross-Linked Polymer Nanogels: A Versatile Nanoscopic Drug Delivery Platform. *J. Am. Chem. Soc.* **2010**, *132* (48), 17227–17235. https://doi.org/10.1021/ja1069932.

(5) Njikang, G.; Liu, G.; Hong, L. Chiral Imprinting of Diblock Copolymer Single-Chain Particles. *Langmuir* **2011**, *27* (11), 7176–7184. https://doi.org/10.1021/la2006887.

(6) Tamura, A.; Oishi, M.; Nagasaki, Y. Enhanced Cytoplasmic Delivery of siRNA Using a Stabilized Polyion Complex Based on PEGylated Nanogels with a Cross-Linked Polyamine Structure. *Biomacromolecules* **2009**, *10* (7), 1818–1827. https://doi.org/10.1021/bm900252d.

(7) Hamilton, S. K.; Harth, E. Molecular Dendritic Transporter Nanoparticle Vectors Provide Efficient Intracellular Delivery of Peptides. *ACS Nano* **2009**, *3* (2), 402–410. https://doi.org/10.1021/nn800679z.

(8) Gillissen, M. A. J.; Voets, I. K.; Meijer, E. W.; Palmans, Anja. R. A. Single Chain Polymeric Nanoparticles as Compartmentalised Sensors for Metal Ions. *Polym. Chem.* **2012**, *3* (11), 3166. https://doi.org/10.1039/c2py20350b.

(9) Latorre-Sanchez, A.; Pomposo, J. A. A Simple, Fast and Highly Sensitive Colorimetric Detection of Zein in Aqueous Ethanol via Zein–Pyridine–Gold Interactions. *Chem. Commun.* **2015**, *51* (86), 15736–15738. https://doi.org/10.1039/C5CC06083D.

(10) Terashima, T.; Mes, T.; De Greef, T. F. A.; Gillissen, M. A. J.; Besenius, P.; Palmans, A. R. A.; Meijer, E. W. Single-Chain Folding of Polymers for Catalytic Systems in Water. *J. Am. Chem. Soc.* **2011**, *133* (13), 4742–4745. https://doi.org/10.1021/ja2004494.

(11) Perez-Baena, I.; Loinaz, I.; Padro, D.; García, I.; Grande, H. J.; Odriozola, I. Single-Chain Polyacrylic Nanoparticles with Multiple Gd(Iii) Centres as Potential MRI Contrast Agents. *J. Mater. Chem.* **2010**, *20* (33), 6916. https://doi.org/10.1039/c0jm01025a.

(12) Rubio-Cervilla, J.; González, E.; Pomposo, J. Advances in Single-Chain Nanoparticles for Catalysis Applications. *Nanomaterials* **2017**, *7* (10), 341. https://doi.org/10.3390/nano7100341.

(13) Rothfuss, H.; Knöfel, N. D.; Roesky, P. W.; Barner-Kowollik, C. Single-Chain Nanoparticles as Catalytic Nanoreactors. *J. Am. Chem. Soc.* **2018**, *140* (18), 5875–5881. https://doi.org/10.1021/jacs.8b02135.

(14) Sanchez-Sanchez, A.; Arbe, A.; Colmenero, J.; Pomposo, J. A. Metallo-Folded Single-Chain Nanoparticles with Catalytic Selectivity. *ACS Macro Lett.* **2014**, *3* (5), 439–443. https://doi.org/10.1021/mz5001477.

(15) Mavila, S.; Rozenberg, I.; Lemcoff, N. G. A General Approach to Mono- and Bimetallic Organometallic Nanoparticles. *Chem. Sci.* **2014**, *5* (11), 4196–4203. https://doi.org/10.1039/C4SC01231C.

(16) Knöfel, N. D.; Rothfuss, H.; Willenbacher, J.; Barner-Kowollik, C.; Roesky, P. W. Platinum(II)-Crosslinked Single-Chain Nanoparticles: An Approach towards Recyclable Homogeneous Catalysts. *Angew Chem Int Ed* **2017**, *56* (18), 4950–4954. https://doi.org/10.1002/anie.201700718.

(17) Wang, W.; Wang, J.; Li, S.; Li, C.; Tan, R.; Yin, D. Iron(Ⅱ)-Folded Single-Chain Nanoparticles: A Metalloenzyme Mimicking Sustainable Catalyst for Highly Enantioselective Sulfa-Michael Addition in Water. *Green Chem.* **2020**, *22* (14), 4645–4655. https://doi.org/10.1039/D0GC00949K.

(18) Smith, D. P.; Knapman, T. W.; Campuzano, I.; Malham, R. W.; Berryman, J. T.; Radford, S. E.; Ashcroft, A. E. Deciphering Drift Time Measurements from Travelling

Wave Ion Mobility Spectrometry-Mass Spectrometry Studies. *Eur J Mass Spectrom (Chichester)* **2009**, *15* (2), 113–130. https://doi.org/10.1255/ejms.947.

(19) Lanucara, F.; Holman, S. W.; Gray, C. J.; Eyers, C. E. The Power of Ion Mobility-Mass Spectrometry for Structural Characterization and the Study of Conformational Dynamics. *Nature Chem* **2014**, *6* (4), 281–294. https://doi.org/10.1038/nchem.1889.

(20) Mack, E. AVERAGE CROSS-SECTIONAL AREAS OF MOLECULES BY GASEOUS DIFFUSION METHODS. *J. Am. Chem. Soc.* **1925**, *47* (10), 2468–2482. https://doi.org/10.1021/ja01687a007.

(21) D'Atri, V.; Porrini, M.; Rosu, F.; Gabelica, V. Linking Molecular Models with Ion Mobility Experiments. Illustration with a Rigid Nucleic Acid Structure. *J. Mass Spectrom.* **2015**, *50* (5), 711–726. https://doi.org/10.1002/jms.3590.

(22) Metwally, H.; Konermann, L. Crown Ether Effects on the Location of Charge Carriers in Electrospray Droplets: Implications for the Mechanism of Protein Charging and Supercharging. *Anal. Chem.* **2018**, *90* (6), 4126–4134. https://doi.org/10.1021/acs.analchem.8b00099.

(23) Marklund, E. G.; Benesch, J. L. Weighing-up Protein Dynamics: The Combination of Native Mass Spectrometry and Molecular Dynamics Simulations. *Current Opinion in Structural Biology* **2019**, *54*, 50–58. https://doi.org/10.1016/j.sbi.2018.12.011.

(24) Wendland, M. S.; Zimmerman, S. C. Synthesis of Cored Dendrimers. *J. Am. Chem. Soc.* **1999**, *121* (6), 1389–1390. https://doi.org/10.1021/ja983097m.

(25) Altintas, O.; Barner-Kowollik, C. Single-Chain Folding of Synthetic Polymers: A Critical Update. *Macromol. Rapid Commun.* **2016**, *37* (1), 29–46. https://doi.org/10.1002/marc.201500547.

(26) Tuten, B. T.; Chao, D.; Lyon, C. K.; Berda, E. B. Single-Chain Polymer Nanoparticles via Reversible Disulfide Bridges. *Polym. Chem.* **2012**, *3* (11), 3068. https://doi.org/10.1039/c2py20308a.

(27) Oria, L.; Aguado, R.; Pomposo, J. A.; Colmenero, J. A Versatile "Click" Chemistry Precursor of Functional Polystyrene Nanoparticles. *Advanced Materials* **2010**, *22* (28), 3038–3041. https://doi.org/10.1002/adma.201000243.

(28) Mahon, C. S.; McGurk, C. J.; Watson, S. M. D.; Fascione, M. A.; Sakonsinsiri, C.; Turnbull, W. B.; Fulton, D. A. Molecular Recognition-Mediated Transformation of

Single-Chain Polymer Nanoparticles into Crosslinked Polymer Films. *Angew Chem Int Ed* **2017**, *56* (42), 12913–12918. https://doi.org/10.1002/anie.201706379.

(29) Murray, B. S.; Fulton, D. A. Dynamic Covalent Single-Chain Polymer Nanoparticles. *Macromolecules* **2011**, *44* (18), 7242–7252. https://doi.org/10.1021/ma201331f.

(30) Gasparini, G.; Dal Molin, M.; Lovato, A.; Prins, L. J. Dynamic Covalent Chemistry. In *Supramolecular Chemistry*; Gale, P. A., Steed, J. W., Eds.; Wiley, 2012. https://doi.org/10.1002/9780470661345.smc161.

(31) Davankov, V. A.; Ilyin, M. M.; Tsyurupa, M. P.; Timofeeva, G. I.; Dubrovina, L. V. From a Dissolved Polystyrene Coil to an Intramolecularly-Hyper-Cross-Linked "Nanosponge." *Macromolecules* **1996**, *29* (26), 8398–8403. https://doi.org/10.1021/ma951673i.

(32) Harth, E.; Horn, B. V.; Lee, V. Y.; Germack, D. S.; Gonzales, C. P.; Miller, R. D.; Hawker, C. J. A Facile Approach to Architecturally Defined Nanoparticles via Intramolecular Chain Collapse. *J. Am. Chem. Soc.* **2002**, *124* (29), 8653–8660. https://doi.org/10.1021/ja026208x.

(33) Tuteja, A.; Mackay, M. E.; Hawker, C. J.; Van Horn, B.; Ho, D. L. Molecular Architecture and Rheological Characterization of Novel Intramolecularly Crosslinked Polystyrene Nanoparticles. *J Polym Sci B Polym Phys* **2006**, *44* (14), 1930–1947. https://doi.org/10.1002/polb.20826.

(34) Dobish, J. N.; Hamilton, S. K.; Harth, E. Synthesis of Low-Temperature Benzocyclobutene Cross-Linker and Utilization. *Polym. Chem.* **2012**, *3* (4), 857. https://doi.org/10.1039/c2py00606e.

(35) Dukette, T. E.; Mackay, M. E.; Van Horn, B.; Wooley, K. L.; Drockenmuller, E.; Malkoch, M.; Hawker, C. J. Conformation of Intramolecularly Cross-Linked Polymer Nanoparticles on Solid Substrates. *Nano Lett.* **2005**, *5* (9), 1704–1709. https://doi.org/10.1021/nl050941f.

(36) Jiang, J.; Thayumanavan, S. Synthesis and Characterization of Amine-Functionalized Polystyrene Nanoparticles. *Macromolecules* **2005**, *38* (14), 5886–5891. https://doi.org/10.1021/ma0507286.

(37) Mecerreyes, D.; Lee, V.; Hawker, C. J.; Hedrick, J. L.; Wursch, A.; Volksen, W.; Magbitang, T.; Huang, E.; Miller, R. D. A Novel Approach to Functionalized

Nanoparticles: Self-Crosslinking of Macromolecules in Ultradilute Solution. *Adv. Mater.* **2001**, *13* (3), 204–208. https://doi.org/10.1002/1521-4095(200102)13:3%253C204::AID-ADMA204%253E3.0.CO;2-9.

(38) Altintas, O.; Willenbacher, J.; Wuest, K. N. R.; Oehlenschlaeger, K. K.; Krolla-Sidenstein, P.; Gliemann, H.; Barner-Kowollik, C. A Mild and Efficient Approach to Functional Single-Chain Polymeric Nanoparticles via Photoinduced Diels–Alder Ligation. *Macromolecules* **2013**, *46* (20), 8092–8101. https://doi.org/10.1021/ma4015033.

(39) Altintas, O.; Gerstel, P.; Dingenouts, N.; Barner-Kowollik, C. Single Chain Self-Assembly: Preparation of α,ω-Donor–Acceptor Chains via Living Radical Polymerization and Orthogonal Conjugation. *Chem. Commun.* **2010**, *46* (34), 6291. https://doi.org/10.1039/c0cc00702a.

(40) Altintas, O.; Lejeune, E.; Gerstel, P.; Barner-Kowollik, C. Bioinspired Dual Self-Folding of Single Polymer Chains via Reversible Hydrogen Bonding. *Polym. Chem.* **2012**, *3* (3), 640–651. https://doi.org/10.1039/C1PY00392E.

(41) Altintas, O.; Rudolph, T.; Barner-Kowollik, C. Single Chain Self-assembly of Well-defined Heterotelechelic Polymers Generated by ATRP and Click Chemistry Revisited. *J. Polym. Sci. A Polym. Chem.* **2011**, *49* (12), 2566–2576. https://doi.org/10.1002/pola.24688.

(42) Foster, E. J.; Berda, E. B.; Meijer, E. W. Metastable Supramolecular Polymer Nanoparticles via Intramolecular Collapse of Single Polymer Chains. *J. Am. Chem. Soc.* **2009**, *131* (20), 6964–6966. https://doi.org/10.1021/ja901687d.

(43) Berda, E. B.; Foster, E. J.; Meijer, E. W. Toward Controlling Folding in Synthetic Polymers: Fabricating and Characterizing Supramolecular Single-Chain Nanoparticles. *Macromolecules* **2010**, *43* (3), 1430–1437. https://doi.org/10.1021/ma902393h.

(44) Foster, E. J.; Berda, E. B.; Meijer, E. W. Tuning the Size of Supramolecular Single-chain Polymer Nanoparticles. *J. Polym. Sci. A Polym. Chem.* **2011**, *49* (1), 118–126. https://doi.org/10.1002/pola.24426.

(45) Hosono, N.; Gillissen, M. A. J.; Li, Y.; Sheiko, S. S.; Palmans, A. R. A.; Meijer, E. W. Orthogonal Self-Assembly in Folding Block Copolymers. *J. Am. Chem. Soc.* **2013**, *135* (1), 501–510. https://doi.org/10.1021/ja310422w.

(46) Stals, P. J. M.; Gillissen, M. A. J.; Nicolaÿ, R.; Palmans, A. R. A.; Meijer, E. W. The Balance between Intramolecular Hydrogen Bonding, Polymer Solubility and Rigidity in Single-Chain Polymeric Nanoparticles. *Polym. Chem.* **2013**, *4* (8), 2584. https://doi.org/10.1039/c3py00094j.

(47) De Luzuriaga, A. R.; Ormategui, N.; Grande, H. J.; Odriozola, I.; Pomposo, J. A.; Loinaz, I. Intramolecular Click Cycloaddition: An Efficient Room-Temperature Route towards Bioconjugable Polymeric Nanoparticles. *Macromol. Rapid Commun.* **2008**, *29* (12–13), 1156–1160. https://doi.org/10.1002/marc.200700877.

(48) Ormategui, N.; García, I.; Padro, D.; Cabañero, G.; Grande, H. J.; Loinaz, I. Synthesis of Single Chain Thermoresponsive Polymernanoparticles. *Soft Matter* **2012**, *8* (3), 734–740. https://doi.org/10.1039/C1SM06310C.

(49) De Luzuriaga, A. R.; Perez-Baena, I.; Montes, S.; Loinaz, I.; Odriozola, I.; García, I.; Pomposo, J. A. New Route to Polymeric Nanoparticles by Click Chemistry Using Bifunctional Cross-Linkers. *Macromolecular Symposia* **2010**, *296* (1), 303–310. https://doi.org/10.1002/masy.201051042.

(50) Stevens, D. M.; Tempelaar, S.; Dove, A. P.; Harth, E. Nanosponge Formation from Organocatalytically Synthesized Poly(Carbonate) Copolymers. *ACS Macro Lett.* **2012**, *1* (7), 915–918. https://doi.org/10.1021/mz300179r.

(51) Chao, D.; Jia, X.; Tuten, B.; Wang, C.; Berda, E. B. Controlled Folding of a Novel Electroactive Polyolefin via Multiple Sequential Orthogonal Intra-Chain Interactions. *Chem. Commun.* **2013**, *49* (39), 4178–4180. https://doi.org/10.1039/C2CC37157J.

(52) Perez-Baena, I.; Asenjo-Sanz, I.; Arbe, A.; Moreno, A. J.; Lo Verso, F.; Colmenero, J.; Pomposo, J. A. Efficient Route to Compact Single-Chain Nanoparticles: Photoactivated Synthesis via Thiol–Yne Coupling Reaction. *Macromolecules* **2014**, *47* (23), 8270–8280. https://doi.org/10.1021/ma5017133.

(53) Willenbacher, J.; Wuest, K. N. R.; Mueller, J. O.; Kaupp, M.; Wagenknecht, H.-A.; Barner-Kowollik, C. Photochemical Design of Functional Fluorescent Single-Chain

Nanoparticles. *ACS Macro Lett.* **2014**, *3* (6), 574–579. https://doi.org/10.1021/mz500292e.

(54) He, J.; Tremblay, L.; Lacelle, S.; Zhao, Y. Preparation of Polymer Single Chain Nanoparticles Using Intramolecular Photodimerization of Coumarin. *Soft Matter* **2011**, *7* (6), 2380. https://doi.org/10.1039/c0sm01383h.

(55) Frank, P. G.; Tuten, B. T.; Prasher, A.; Chao, D.; Berda, E. B. Intra-Chain Photodimerization of Pendant Anthracene Units as an Efficient Route to Single-Chain Nanoparticle Fabrication. *Macromol. Rapid Commun.* **2014**, *35* (2), 249–253. https://doi.org/10.1002/marc.201300677.

(56) Ter Huurne, G. M.; Palmans, A. R. A.; Meijer, E. W. Supramolecular Single-Chain Polymeric Nanoparticles. *CCS Chem* **2019**, *1* (1), 64–82. https://doi.org/10.31635/ccschem.019.20180036.

(57) Christianson, D. W.; Fierke, C. A. Carbonic Anhydrase: Evolution of the Zinc Binding Site by Nature and by Design. *Acc. Chem. Res.* **1996**, *29* (7), 331–339. https://doi.org/10.1021/ar9501232.

(58) Lukin, J. A.; Ho, C. The Structure−Function Relationship of Hemoglobin in Solution at Atomic Resolution. *Chem. Rev.* **2004**, *104* (3), 1219–1230. https://doi.org/10.1021/cr940325w.

(59) Decker, H.; Tuczek, F. Tyrosinase/Catecholoxidase Activity of Hemocyanins: Structural Basis and Molecular Mechanism. *Trends in Biochemical Sciences* **2000**, *25* (8), 392–397. https://doi.org/10.1016/S0968-0004(00)01602-9.

(60) Willenbacher, J.; Altintas, O.; Roesky, P. W.; Barner-Kowollik, C. Single-Chain Self-Folding of Synthetic Polymers Induced by Metal–Ligand Complexation. *Macromol. Rapid Commun.* **2014**, *35* (1), 45–51. https://doi.org/10.1002/marc.201300594.

(61) Khabibulin, V. R.; Kulik, A. V.; Oshanina, I. V.; Bruk, L. G.; Temkin, O. N.; Nosova, V. M.; Ustynyuk, Yu. A.; Bel'skii, V. K.; Stash, A. I.; Lysenko, K. A.; Antipin, M. Yu. Mechanism of the Oxidative Carbonylation of Terminal Alkynes at the ≡C-H Bond in Solutions of Palladium Complexes. *Kinet Catal* **2007**, *48* (2), 228–244. https://doi.org/10.1134/S0023158407020073.

(62) Willenbacher, J.; Altintas, O.; Trouillet, V.; Knöfel, N.; Monteiro, M. J.; Roesky, P. W.; Barner-Kowollik, C. Pd-Complex Driven Formation of Single-Chain Nanoparticles. *Polym. Chem.* **2015**, *6* (24), 4358–4365. https://doi.org/10.1039/C5PY00389J.

(63) Wang, F.; Pu, H.; Jin, M.; Wan, D. Supramolecular Nanoparticles via Single-Chain Folding Driven by Ferrous Ions. *Macromol. Rapid Commun.* **2016**, *37* (4), 330–336. https://doi.org/10.1002/marc.201500616.

(64) Sanchez-Sanchez, A.; Fulton, D. A.; Pomposo, J. A. pH-Responsive Single-Chain Polymer Nanoparticles Utilising Dynamic Covalent Enamine Bonds. *Chem. Commun.* **2014**, *50* (15), 1871–1874. https://doi.org/10.1039/C3CC48733D.

(65) Tooley, C. A.; Pazicni, S.; Berda, E. B. Toward a Tunable Synthetic [FeFe] Hydrogenase Mimic: Single-Chain Nanoparticles Functionalized with a Single Diiron Cluster. *Polym. Chem.* **2015**, *6* (44), 7646–7651. https://doi.org/10.1039/C5PY01196E.

(66) Zhu, Z.; Xu, N.; Yu, Q.; Guo, L.; Cao, H.; Lu, X.; Cai, Y. Construction and Self-Assembly of Single-Chain Polymer Nanoparticles via Coordination Association and Electrostatic Repulsion in Water. *Macromol. Rapid Commun.* **2015**, *36* (16), 1521–1527. https://doi.org/10.1002/marc.201500281.

(67) Ng, Y.-H.; Di Lena, F.; Chai, C. L. L. PolyPEGA with Predetermined Molecular Weights from Enzyme-Mediated Radical Polymerization in Water. *Chem. Commun.* **2011**, *47* (22), 6464. https://doi.org/10.1039/c1cc10989h.

(68) Ng, Y.-H.; Di Lena, F.; Chai, C. L. L. Metalloenzymatic Radical Polymerization Using Alkyl Halides as Initiators. *Polym. Chem.* **2011**, *2* (3), 589–594. https://doi.org/10.1039/C0PY00139B.

(69) Sanchez-Sanchez, A.; Arbe, A.; Kohlbrecher, J.; Colmenero, J.; Pomposo, J. A. Efficient Synthesis of Single-Chain Globules Mimicking the Morphology and Polymerase Activity of Metalloenzymes. *Macromol. Rapid Commun.* **2015**, *36* (17), 1592–1597. https://doi.org/10.1002/marc.201500252.

(70) Artar, M.; Souren, E. R. J.; Terashima, T.; Meijer, E. W.; Palmans, A. R. A. Single Chain Polymeric Nanoparticles as Selective Hydrophobic Reaction Spaces in Water. *ACS Macro Lett.* **2015**, *4* (10), 1099–1103. https://doi.org/10.1021/acsmacrolett.5b00652.

(71) Chambers, L. C.; Barner-Kowollik, C.; Barner, L.; Michalek, L.; Frisch, H. Photostationary State in Dynamic Covalent Networks. *ACS Macro Lett.* **2022**, *11* (4), 532–536. https://doi.org/10.1021/acsmacrolett.2c00097.

(72) Frisch, H.; Bloesser, F. R.; Barner-Kowollik, C. Controlling Chain Coupling and Single-Chain Ligation by Two Colours of Visible Light. *Angew Chem Int Ed* **2019**, *58* (11), 3604–3609. https://doi.org/10.1002/anie.201811541.

(73) Maag, P. H.; Feist, F.; Truong, V. X.; Frisch, H.; Roesky, P. W.; Barner-Kowollik, C. Visible-Light-Induced Control over Reversible Single-Chain Nanoparticle Folding. *Angew Chem Int Ed* **2023**, *62* (37), e202309259. https://doi.org/10.1002/anie.202309259.

(74) Wen, W.; Chen, A. The Self-Assembly of Single Chain Janus Nanoparticles from Azobenzene-Containing Block Copolymers and Reversible Photoinduced Morphology Transitions. *Polym. Chem.* **2021**, *12* (16), 2447–2456. https://doi.org/10.1039/D1PY00223F.

(75) Yu, H. Recent Advances in Photoresponsive Liquid-Crystalline Polymers Containing Azobenzene Chromophores. *J. Mater. Chem. C* **2014**, *2* (17), 3047–3054. https://doi.org/10.1039/C3TC31991A.

(76) Gohy, J.-F.; Zhao, Y. Photo-Responsive Block Copolymer Micelles: Design and Behavior. *Chem. Soc. Rev.* **2013**, *42* (17), 7117. https://doi.org/10.1039/c3cs35469e.

(77) Greb, L.; Mutlu, H.; Barner-Kowollik, C.; Lehn, J.-M. Photo- and Metallo-Responsive *N* -Alkyl α-Bisimines as Orthogonally Addressable Main-Chain Functional Groups in Metathesis Polymers. *J. Am. Chem. Soc.* **2016**, *138* (4), 1142–1145. https://doi.org/10.1021/jacs.5b12198.

(78) Moore, J. C. Gel Permeation Chromatography. I. A New Method for Molecular Weight Distribution of High Polymers. *J. Polym. Sci. A Gen. Pap.* **1964**, *2* (2), 835–843. https://doi.org/10.1002/pol.1964.100020220.

(79) Striegel, A. M.; Yau, W. W.; Kirkland, J. J.; Bly, D. D. *Modern Size‑Exclusion Liquid Chromatography: Practice of Gel Permeation and Gel Filtration Chromatography*, 1st ed.; Wiley, 2009. https://doi.org/10.1002/9780470442876.

(80) Teraoka, I. Calibration of Retention Volume in Size Exclusion Chromatography by Hydrodynamic Radius. *Macromolecules* **2004**, *37* (17), 6632–6639. https://doi.org/10.1021/ma0494939.

(81) Latorre-Sánchez, A.; Alegría, A.; Lo Verso, F.; Moreno, A. J.; Arbe, A.; Colmenero, J.; Pomposo, J. A. A Useful Methodology for Determining the Compaction Degree of Single-Chain Nanoparticles by Conventional SEC. *Part & Part Syst Charact* **2016**, *33* (7), 373–381. https://doi.org/10.1002/ppsc.201500210.

(82) Gonzalez-Burgos, M.; Latorre-Sanchez, A.; Pomposo, J. A. Advances in Single Chain Technology. *Chem. Soc. Rev.* **2015**, *44* (17), 6122–6142. https://doi.org/10.1039/C5CS00209E.

(83) Wong, E. H. H.; Qiao, G. G. Factors Influencing the Formation of Single-Chain Polymeric Nanoparticles Prepared via Ring-Opening Polymerization. *Macromolecules* **2015**, *48* (5), 1371–1379. https://doi.org/10.1021/ma502526c.

(84) Cole, J. P.; Lyon, C. K.; Berda, E. B. Single-Chain Nanoparticles. In *Bio-inspired Polymers*; Bruns, N., Kilbinger, A. F. M., Eds.; The Royal Society of Chemistry, 2016; pp 107–140. https://doi.org/10.1039/9781782626664-00107.

(85) Wang, F.; Pu, H.; Che, X. Voltage-Responsive Single-Chain Polymer Nanoparticles via Host–Guest Interaction. *Chem. Commun.* **2016**, *52* (17), 3516–3519. https://doi.org/10.1039/C5CC09984F.

(86) Kalmer, H.; Sbordone, F.; Frisch, H. Peptide Based Folding and Function of Single Polymer Chains. *Polym. Chem.* **2022**, *13* (38), 5458–5462. https://doi.org/10.1039/D2PY00717G.

(87) Purcell, E. M.; Torrey, H. C.; Pound, R. V. Resonance Absorption by Nuclear Magnetic Moments in a Solid. *Phys. Rev.* **1946**, *69* (1–2), 37–38. https://doi.org/10.1103/PhysRev.69.37.

(88) Bloch, F.; Hansen, W. W.; Packard, M. Nuclear Induction. *Phys. Rev.* **1946**, *69* (3–4), 127–127. https://doi.org/10.1103/PhysRev.69.127.

(89) Gillhuber, S.; Holloway, J. O.; Mundsinger, K.; Kammerer, J. A.; Harmer, J. R.; Frisch, H.; Barner-Kowollik, C.; Roesky, P. W. Visible Light Photoflow Synthesis of a Cu(II) Single-Chain Polymer Nanoparticle Catalyst. *Chem. Sci.* **2024**, *15* (37), 15280–15290. https://doi.org/10.1039/D4SC03079F.

(90) Griffiths, J. A Brief History of Mass Spectrometry. *Anal. Chem.* **2008**, *80* (15), 5678–5683. https://doi.org/10.1021/ac8013065.

(91) Squires, G. Francis Aston and the Mass Spectrograph. *J. Chem. Soc., Dalton Trans.* **1998**, No. 23, 3893–3900. https://doi.org/10.1039/a804629h.

(92) Coon, J. J.; Syka, J. E. P.; Shabanowitz, J.; Hunt, D. F. Tandem Mass Spectrometry for Peptide and Protein Sequence Analysis. *BioTechniques* **2005**, *38* (4), 519–523. https://doi.org/10.2144/05384TE01.

(93) Steinkoenig, J.; Rothfuss, H.; Lauer, A.; Tuten, B. T.; Barner-Kowollik, C. Imaging Single-Chain Nanoparticle Folding via High-Resolution Mass Spectrometry. *J. Am. Chem. Soc.* **2017**, *139* (1), 51–54. https://doi.org/10.1021/jacs.6b10952.

(94) Steinkoenig, J.; Nitsche, T.; Tuten, B. T.; Barner-Kowollik, C. Radical-Induced Single-Chain Collapse of Passerini Sequence-Regulated Polymers Assessed by High-Resolution Mass Spectrometry. *Macromolecules* **2018**, *51* (11), 3967–3974. https://doi.org/10.1021/acs.macromol.8b00577.

(95) Hunt, D. F.; Yates, J. R.; Shabanowitz, J.; Winston, S.; Hauer, C. R. Protein Sequencing by Tandem Mass Spectrometry. *Proc. Natl. Acad. Sci. U.S.A.* **1986**, *83* (17), 6233–6237. https://doi.org/10.1073/pnas.83.17.6233.

(96) Ahrens, A.; Möhle, J.; Hitzemann, M.; Zimmermann, S. Novel Ion Drift Tube for High-Performance Ion Mobility Spectrometers Based on a Composite Material. *Int. J. Ion Mobil. Spec.* **2020**, *23* (2), 75–81. https://doi.org/10.1007/s12127-020-00265-0.

(97) Kanu, A. B.; Dwivedi, P.; Tam, M.; Matz, L.; Hill, H. H. Ion Mobility–Mass Spectrometry. *J. Mass Spectrom.* **2008**, *43* (1), 1–22. https://doi.org/10.1002/jms.1383.

(98) Ridgeway, M. E.; Lubeck, M.; Jordens, J.; Mann, M.; Park, M. A. Trapped Ion Mobility Spectrometry: A Short Review. *International Journal of Mass Spectrometry* **2018**, *425*, 22–35. https://doi.org/10.1016/j.ijms.2018.01.006.

(99) Crotty, S.; Gerişlioğlu, S.; Endres, K. J.; Wesdemiotis, C.; Schubert, U. S. Polymer Architectures via Mass Spectrometry and Hyphenated Techniques: A Review. *Analytica Chimica Acta* **2016**, *932*, 1–21. https://doi.org/10.1016/j.aca.2016.05.024.

(100) Montaudo, G.; Samperi, F.; Montaudo, M. S. Characterization of Synthetic Polymers by MALDI-MS. *Progress in Polymer Science* **2006**, *31* (3), 277–357. https://doi.org/10.1016/j.progpolymsci.2005.12.001.

(101) Weidner, S. M.; Trimpin, S. Mass Spectrometry of Synthetic Polymers. *Anal. Chem.* **2008**, *80* (12), 4349–4361. https://doi.org/10.1021/ac8006413.

(102) Duez, Q.; Josse, T.; Lemaur, V.; Chirot, F.; Choi, C. M.; Dubois, P.; Dugourd, P.; Cornil, J.; Gerbaux, P.; De Winter, J. Correlation between the Shape of the Ion Mobility Signals and the Stepwise Folding Process of Polylactide Ions: Stepwise Folding Process of Polylactide Ions. *J. Mass Spectrom.* **2017**, *52* (3), 133–138. https://doi.org/10.1002/jms.3915.

(103) De Winter, J.; Lemaur, V.; Ballivian, R.; Chirot, F.; Coulembier, O.; Antoine, R.; Lemoine, J.; Cornil, J.; Dubois, P.; Dugourd, P.; Gerbaux, P. Size Dependence of the Folding of Multiply Charged Sodium Cationized Polylactides Revealed by Ion Mobility Mass Spectrometry and Molecular Modelling. *Chemistry A European J* **2011**, *17* (35), 9738–9745. https://doi.org/10.1002/chem.201100383.

(104) Lapthorn, C.; Dines, T. J.; Chowdhry, B. Z.; Perkins, G. L.; Pullen, F. S. Can Ion Mobility Mass Spectrometry and Density Functional Theory Help Elucidate Protonation Sites in "small" Molecules? *Rapid Comm Mass Spectrometry* **2013**, *27* (21), 2399–2410. https://doi.org/10.1002/rcm.6700.

(105) Hoyas, S.; Lemaur, V.; Duez, Q.; Saintmont, F.; Halin, E.; De Winter, J.; Gerbaux, P.; Cornil, J. PEPDROID: Development of a Generic DREIDING-Based Force Field for the Assessment of Peptoid Secondary Structures. *Advcd Theory and Sims* **2018**, *1* (12), 1800089. https://doi.org/10.1002/adts.201800089.

(106) Bleiholder, C.; Wyttenbach, T.; Bowers, M. T. A Novel Projection Approximation Algorithm for the Fast and Accurate Computation of Molecular Collision Cross Sections (I). Method. *International Journal of Mass Spectrometry* **2011**, *308* (1), 1–10. https://doi.org/10.1016/j.ijms.2011.06.014.

(107) Zanotto, L.; Heerdt, G.; Souza, P. C. T.; Araujo, G.; Skaf, M. S. High Performance Collision Cross Section Calculation—HPCCS. *J Comput Chem* **2018**, *39* (21), 1675–1681. https://doi.org/10.1002/jcc.25199.

(108) Wang, X.; Norgate, E.; Dai, J.; Benoit, F.; Bristow, T.; England, R. M.; Kalapothakis, J. M. D.; Barran, P. E. Conformational Landscapes of Rigid and Flexible Molecules Explored with Variable Temperature Ion Mobility-Mass Spectrometry. *Nat Commun* **2025**, *16* (1), 4183. https://doi.org/10.1038/s41467-025-59065-x.

(109) *Single-Chain Polymer Nanoparticles: Synthesis, Characterization, Simulations, and Applications*, 1. Auflage.; Pomposo, J. A., Pomposo, J. A., Eds.; Wiley-VCH Verlag GmbH & Co. KGaA: Weinheim, 2017.

(110) Wyttenbach, T.; Von Helden, G.; Bowers, M. T. Conformations of Alkali Ion Cationized Polyethers in the Gas Phase: Polyethylene Glycol and Bis[(Benzo-15-Crown-5)-15-Ylmethyl] Pimelate. *International Journal of Mass Spectrometry and Ion Processes* **1997**, *165–166*, 377–390. https://doi.org/10.1016/S0168-1176(97)00179-1.

(111) Gidden, J.; Bushnell, J. E.; Bowers, M. T. Gas-Phase Conformations and Folding Energetics of Oligonucleotides: dTG$^-$ and dGT$^-$. *J. Am. Chem. Soc.* **2001**, *123* (23), 5610–5611. https://doi.org/10.1021/ja015940d.

(112) Von Helden, G.; Wyttenbach, T.; Bowers, M. T. Conformation of Macromolecules in the Gas Phase: Use of Matrix-Assisted Laser Desorption Methods in Ion Chromatography. *Science* **1995**, *267* (5203), 1483–1485. https://doi.org/10.1126/science.267.5203.1483.

(113) Jackson, A. T.; Scrivens, J. H.; Williams, J. P.; Baker, E. S.; Gidden, J.; Bowers, M. T. Microstructural and Conformational Studies of Polyether Copolymers. *International Journal of Mass Spectrometry* **2004**, *238* (3), 287–297. https://doi.org/10.1016/j.ijms.2004.09.025.

(114) Wyttenbach, T.; Bowers, M. T. Structural Stability from Solution to the Gas Phase: Native Solution Structure of Ubiquitin Survives Analysis in a Solvent-Free Ion Mobility–Mass Spectrometry Environment. *J. Phys. Chem. B* **2011**, *115* (42), 12266–12275. https://doi.org/10.1021/jp206867a.

(115) Fenn, J. B. Electrospray Wings for Molecular Elephants (Nobel Lecture). *Angew Chem Int Ed* **2003**, *42* (33), 3871–3894. https://doi.org/10.1002/anie.200300605.

(116) Vijay-kumar, S.; Bugg, C. E.; Cook, W. J. Structure of Ubiquitin Refined at 1.8 Å Resolution. *Journal of Molecular Biology* **1987**, *194* (3), 531–544. https://doi.org/10.1016/0022-2836(87)90679-6.

(117) Cornilescu, G.; Marquardt, J. L.; Ottiger, M.; Bax, A. Validation of Protein Structure from Anisotropic Carbonyl Chemical Shifts in a Dilute Liquid Crystalline Phase. *J. Am. Chem. Soc.* **1998**, *120* (27), 6836–6837. https://doi.org/10.1021/ja9812610.

(118) Weber, P. L.; Brown, S. C.; Mueller, L. Sequential Proton NMR Assignments and Secondary Structure Identification of Human Ubiquitin. *Biochemistry* **1987**, *26* (23), 7282–7290. https://doi.org/10.1021/bi00397a013.

(119) Di Stefano, D. L.; Wand, A. J. Two-Dimensional Proton NMR Study of Human Ubiquitin: A Main Chain Directed Assignment and Structure Analysis. *Biochemistry* **1987**, *26* (23), 7272–7281. https://doi.org/10.1021/bi00397a012.

(120) Stockman, BrianJ.; Euvrard, A.; Scahill, TerrenceA. Heteronuclear Three-Dimensional NMR Spectroscopy of a Partially Denatured Protein: The A-State of Human Ubiquitin. *J Biomol NMR* **1993**, *3* (3), 285–296. https://doi.org/10.1007/BF00212515.

(121) Brutscher, B.; Brüschweiler, R.; Ernst, R. R. Backbone Dynamics and Structural Characterization of the Partially Folded A State of Ubiquitin by[1] H,[13] C, and[15] N Nuclear Magnetic Resonance Spectroscopy. *Biochemistry* **1997**, *36* (42), 13043–13053. https://doi.org/10.1021/bi971538t.

(122) Cox, M. J.; Haas, A. L.; Wilkinson, K. D. Role of Ubiquitin Conformations in the Specificity of Protein Degradation: Iodinated Derivatives with Altered Conformations and Activities. *Archives of Biochemistry and Biophysics* **1986**, *250* (2), 400–409. https://doi.org/10.1016/0003-9861(86)90742-3.

(123) Segev, E.; Wyttenbach, T.; Bowers, M. T.; Gerber, R. B. Conformational Evolution of Ubiquitin Ions in Electrospray Mass Spectrometry: Molecular Dynamics Simulations at Gradually Increasing Temperatures. *Phys. Chem. Chem. Phys.* **2008**, *10* (21), 3077. https://doi.org/10.1039/b718610j.

(124) Wyttenbach, T.; Bowers, M. T. Gas-Phase Conformations: The Ion Mobility/Ion Chromatography Method. In *Modern Mass Spectrometry*; Schalley, C. A., Ed.; Topics

in Current Chemistry; Springer Berlin Heidelberg: Berlin, Heidelberg, 2003; Vol. 225, pp 207–232. https://doi.org/10.1007/3-540-36113-8_6.

(125) Mason, E. A.; McDaniel, E. W. *Transport Properties of Ions in Gases*, 1st ed.; Wiley, 1988. https://doi.org/10.1002/3527602852.

(126) Case, D. A.; Cheatham, T. E.; Darden, T.; Gohlke, H.; Luo, R.; Merz, K. M.; Onufriev, A.; Simmerling, C.; Wang, B.; Woods, R. J. The Amber Biomolecular Simulation Programs. *J Comput Chem* **2005**, *26* (16), 1668–1688. https://doi.org/10.1002/jcc.20290.

(127) Hanlon, A. M.; Lyon, C. K.; Berda, E. B. What Is Next in Single-Chain Nanoparticles? *Macromolecules* **2016**, *49* (1), 2–14. https://doi.org/10.1021/acs.macromol.5b01456.

(128) Blasco, E.; Tuten, B. T.; Frisch, H.; Lederer, A.; Barner-Kowollik, C. Characterizing Single Chain Nanoparticles (SCNPs): A Critical Survey. *Polym. Chem.* **2017**, *8* (38), 5845–5851. https://doi.org/10.1039/C7PY01278K.

(129) Engelke, J.; Brandt, J.; Barner-Kowollik, C.; Lederer, A. Strengths and Limitations of Size Exclusion Chromatography for Investigating Single Chain Folding – Current Status and Future Perspectives. *Polym. Chem.* **2019**, *10* (25), 3410–3425. https://doi.org/10.1039/C9PY00336C.

(130) Steinkoenig, J.; Rothfuss, H.; Lauer, A.; Tuten, B. T.; Barner-Kowollik, C. Imaging Single-Chain Nanoparticle Folding via High-Resolution Mass Spectrometry. *J. Am. Chem. Soc.* **2017**, *139* (1), 51–54. https://doi.org/10.1021/jacs.6b10952.

(131) Izuagbe, A. E.; Truong, V. X.; Tuten, B. T.; Roesky, P. W.; Barner-Kowollik, C. Visible Light Switchable Single-Chain Nanoparticles. *Macromolecules* **2022**, *55* (20), 9242–9248. https://doi.org/10.1021/acs.macromol.2c01467.

(132) Pashley-Johnson, F.; Munaweera, R.; Hossain, S. I.; Gauci, S. C.; Delafresnaye, L.; Frisch, H.; O'Mara, M. L.; Du Prez, F. E.; Barner-Kowollik, C. How Molecular Architecture Defines Quantum Yields. *Nat Commun* **2024**, *15* (1), 6033. https://doi.org/10.1038/s41467-024-50366-1.

(133) Itagaki, H.; Yoshida, N.; Sano, T.; Yokoyama, M.; Iba, N.; Sugiyama, R.; Kuroki, M. Electrically Conductive Gels Prepared from Syndiotactic Polystyrene and an Ionic

Liquid. *ACS Omega* **2019**, *4* (14), 16125–16129. https://doi.org/10.1021/acsomega.9b02310.

(134) Zatorska-Płachta, M.; Łazarski, G.; Maziarz, U.; Foryś, A.; Trzebicka, B.; Wnuk, D.; Chołuj, K.; Karewicz, A.; Michalik, M.; Jamróz, D.; Kepczynski, M. Encapsulation of Curcumin in Polystyrene-Based Nanoparticles—Drug Loading Capacity and Cytotoxicity. *ACS Omega* **2021**, *6* (18), 12168–12178. https://doi.org/10.1021/acsomega.1c00867.

(135) Burguière, C.; Dourges, M.-A.; Charleux, B.; Vairon, J.-P. Synthesis and Characterization of ω-Unsaturated Poly(Styrene- *b* - *n* -Butyl Methacrylate) Block Copolymers Using TEMPO-Mediated Controlled Radical Polymerization. *Macromolecules* **1999**, *32* (12), 3883–3890. https://doi.org/10.1021/ma982037y.

(136) Ladavière, C.; Lacroix-Desmazes, P.; Delolme, F. First Systematic MALDI/ESI Mass Spectrometry Comparison to Characterize Polystyrene Synthesized by Different Controlled Radical Polymerizations. *Macromolecules* **2009**, *42* (1), 70–84. https://doi.org/10.1021/ma8013788.

(137) Gruendling, T.; Hart-Smith, G.; Davis, T. P.; Stenzel, M. H.; Barner-Kowollik, C. Enhanced Ionization in Electrospray Ionization Mass Spectrometry of Labile End-Group-Containing Polystyrenes Using Silver(I) Tetrafluoroborate as Doping Salt. *Macromolecules* **2008**, *41* (6), 1966–1971. https://doi.org/10.1021/ma702163v.

(138) Altintas, O.; Josse, T.; De Winter, J.; Matsumoto, N. M.; Gerbaux, P.; Wilhelm, M.; Barner-Kowollik, C. Ready Access to End-Functional Polystyrenes via a Combination of ARGET ATRP and Thiol–Ene Chemistry. *Polym. Chem.* **2015**, *6* (39), 6931–6935. https://doi.org/10.1039/C5PY01048A.

(139) Gidden, J.; Bowers, M. T.; Jackson, A. T.; Scrivens, J. H. Gas-Phase Conformations of Cationized Poly(Styrene) Oligomers. *J. Am. Soc. Mass Spectrom.* **2002**, *13* (5), 499–505. https://doi.org/10.1016/S1044-0305(02)00367-7.

(140) Guillaneuf, Y.; Dufils, P.-E.; Autissier, L.; Rollet, M.; Gigmes, D.; Bertin, D. Radical Chain End Chemical Transformation of SG1-Based Polystyrenes. *Macromolecules* **2010**, *43* (1), 91–100. https://doi.org/10.1021/ma901838m.

(141) Dourges, M.-A.; Charleux, B.; Vairon, J.-P.; Blais, J.-C.; Bolbach, G.; Tabet, J.-C. MALDI-TOF Mass Spectrometry Analysis of TEMPO-Capped Polystyrene. *Macromolecules* **1999**, *32* (8), 2495–2502. https://doi.org/10.1021/ma981513h.

(142) Gidden, J.; Bowers, M. T.; Jackson, A. T.; Scrivens, J. H. Gas-Phase Conformations of Cationized Poly(Styrene) Oligomers. *J. Am. Soc. Mass Spectrom.* **2002**, *13* (5), 499–505. https://doi.org/10.1016/S1044-0305(02)00367-7.

(143) Gibson, H. W.; Ge, Z.; Huang, F.; Jones, J. W.; Lefebvre, H.; Vergne, M. J.; Hercules, D. M. Syntheses and Model Complexation Studies of Well-Defined Crown Terminated Polymers. *Macromolecules* **2005**, *38* (7), 2626–2637. https://doi.org/10.1021/ma047811y.

(144) Shoeib, T.; Cunje, A.; Hopkinson, A. C.; Siu, K. W. M. Gas-Phase Fragmentation of the Ag $^+$ —Phenylalanine Complex: Cation—π Interactions and Radical Cation Formation. *J. Am. Soc. Mass Spectrom.* **2002**, *13* (4), 408–416. https://doi.org/10.1016/S1044-0305(02)00353-7.

(145) Saintmont, F.; De Winter, J.; Chirot, F.; Halin, E.; Dugourd, P.; Brocorens, P.; Gerbaux, P. How Spherical Are Gaseous Low Charged Dendrimer Ions: A Molecular Dynamics/Ion Mobility Study? *J. Am. Soc. Mass Spectrom.* **2020**, *31* (8), 1673–1683. https://doi.org/10.1021/jasms.0c00113.

(146) Weber, P.; Hoyas, S.; Halin, É.; Coulembier, O.; De Winter, J.; Cornil, J.; Gerbaux, P. On the Conformation of Anionic Peptoids in the Gas Phase. *Biomacromolecules* **2022**, *23* (3), 1138–1147. https://doi.org/10.1021/acs.biomac.1c01442.

(147) Hoyas, S.; Halin, E.; Lemaur, V.; De Winter, J.; Gerbaux, P.; Cornil, J. Helicity of Peptoid Ions in the Gas Phase. *Biomacromolecules* **2020**, *21* (2), 903–909. https://doi.org/10.1021/acs.biomac.9b01567.

(148) Hoyas, S.; Weber, P.; Halin, E.; Coulembier, O.; De Winter, J.; Cornil, J.; Gerbaux, P. Helical Peptoid Ions in the Gas Phase: Thwarting the Charge Solvation Effect by H-Bond Compensation. *Biomacromolecules* **2021**, *22* (8), 3543–3551. https://doi.org/10.1021/acs.biomac.1c00623.

(149) Giles, K.; Williams, J. P.; Campuzano, I. Enhancements in Travelling Wave Ion Mobility Resolution. *Rapid Comm Mass Spectrometry* **2011**, *25* (11), 1559–1566. https://doi.org/10.1002/rcm.5013.

(150) Ruotolo, B. T.; Benesch, J. L. P.; Sandercock, A. M.; Hyung, S.-J.; Robinson, C. V. Ion Mobility–Mass Spectrometry Analysis of Large Protein Complexes. *Nat Protoc* **2008**, *3* (7), 1139–1152. https://doi.org/10.1038/nprot.2008.78.

(151) Pugh, T. L.; Heller, W. Density of Polystyrene and Polyvinyltoluene Latex Particles. *Journal of Colloid Science* **1957**, *12* (2), 173–180. https://doi.org/10.1016/0095-8522(57)90004-1.

(152) Gidden, J.; Wyttenbach, T.; Jackson, A. T.; Scrivens, J. H.; Bowers, M. T. Gas-Phase Conformations of Synthetic Polymers: Poly(Ethylene Glycol), Poly(Propylene Glycol), and Poly(Tetramethylene Glycol). *J. Am. Chem. Soc.* **2000**, *122* (19), 4692–4699. https://doi.org/10.1021/ja993096+.

(153) Duez, Q.; Hoyas, S.; Josse, T.; Cornil, J.; Gerbaux, P.; De Winter, J. Gas-phase Structure of Polymer Ions: Tying Together Theoretical Approaches and Ion Mobility Spectrometry. *Mass Spectrometry Reviews* **2023**, *42* (4), 1129–1151. https://doi.org/10.1002/mas.21745.

(154) Ewing, S. A.; Donor, M. T.; Wilson, J. W.; Prell, J. S. Collidoscope: An Improved Tool for Computing Collisional Cross-Sections with the Trajectory Method. *J. Am. Soc. Mass Spectrom.* **2017**, *28* (4), 587–596. https://doi.org/10.1007/s13361-017-1594-2.

(155) Lee, B.; Richards, F. M. The Interpretation of Protein Structures: Estimation of Static Accessibility. *Journal of Molecular Biology* **1971**, *55* (3), 379-IN4. https://doi.org/10.1016/0022-2836(71)90324-X.

(156) Mahadevi, A. S.; Sastry, G. N. Cation−π Interaction: Its Role and Relevance in Chemistry, Biology, and Material Science. *Chem. Rev.* **2013**, *113* (3), 2100–2138. https://doi.org/10.1021/cr300222d.

(157) Gerber, J.; Radke, W. Topological Separation of Linear and Star-Shaped Polystyrenes by off-Line 2D Chromatography. Stars Having High Molar Mass Arms and Quantification of the Star Fraction. *Polymer* **2005**, *46* (22), 9224–9229. https://doi.org/10.1016/j.polymer.2005.07.038.

(158) Duez, Q.; Chirot, F.; Liénard, R.; Josse, T.; Choi, C.; Coulembier, O.; Dugourd, P.; Cornil, J.; Gerbaux, P.; De Winter, J. Polymers for Traveling Wave Ion Mobility

Spectrometry Calibration. *J. Am. Soc. Mass Spectrom.* **2017**, *28* (11), 2483–2491. https://doi.org/10.1007/s13361-017-1762-4.

(159) Gabelica, V.; Shvartsburg, A. A.; Afonso, C.; Barran, P.; Benesch, J. L. P.; Bleiholder, C.; Bowers, M. T.; Bilbao, A.; Bush, M. F.; Campbell, J. L.; Campuzano, I. D. G.; Causon, T.; Clowers, B. H.; Creaser, C. S.; De Pauw, E.; Far, J.; Fernandez-Lima, F.; Fjeldsted, J. C.; Giles, K.; Groessl, M.; Hogan, C. J.; Hann, S.; Kim, H. I.; Kurulugama, R. T.; May, J. C.; McLean, J. A.; Pagel, K.; Richardson, K.; Ridgeway, M. E.; Rosu, F.; Sobott, F.; Thalassinos, K.; Valentine, S. J.; Wyttenbach, T. Recommendations for Reporting Ion Mobility Mass Spectrometry Measurements. *Mass Spectrometry Reviews* **2019**, *38* (3), 291–320. https://doi.org/10.1002/mas.21585.

(160) BIOVA - San Diego: Dassault Systèmes, Materials Studio, (2022).

(161) Mesleh, M. F.; Hunter, J. M.; Shvartsburg, A. A.; Schatz, G. C.; Jarrold, M. F. Structural Information from Ion Mobility Measurements: Effects of the Long-Range Potential. *J. Phys. Chem.* **1996**, *100* (40), 16082–16086. https://doi.org/10.1021/jp961623v.

(162) M.J. Frisch, G.W. Trucks, H.B. Schlegel, G.E. Scuseria, M.A. Robb, J.R.Cheeseman, G. Scalmani, V. Barone, B. Mennucci, G.A. Petersson, Gaussian2009, 2009.

(163) Duez, Q.; Van Huizen, N. A.; Lemaur, V.; De Winter, J.; Cornil, J.; Burgers, P. C.; Gerbaux, P. Silver Ion Induced Folding of Alkylamines Observed by Ion Mobility Experiments. *International Journal of Mass Spectrometry* **2019**, *435*, 34–41. https://doi.org/10.1016/j.ijms.2018.10.016.

(164) Grimme, S.; Antony, J.; Ehrlich, S.; Krieg, H. A Consistent and Accurate *Ab Initio* Parametrization of Density Functional Dispersion Correction (DFT-D) for the 94 Elements H-Pu. *The Journal of Chemical Physics* **2010**, *132* (15), 154104. https://doi.org/10.1063/1.3382344.

(165) Naskar, S.; Minoia, A.; Duez, Q.; Izuagbe, A.; De Winter, J.; Blanksby, S. J.; Barner-Kowollik, C.; Cornil, J.; Gerbaux, P. Polystyrene Chain Geometry Probed by Ion Mobility Mass Spectrometry and Molecular Dynamics Simulations. *J. Am. Soc. Mass Spectrom.* **2024**, *35* (10), 2408–2419. https://doi.org/10.1021/jasms.4c00231.

(166) Gasteiger, J.; Marsili, M. A New Model for Calculating Atomic Charges in Molecules. *Tetrahedron Letters* **1978**, *19* (34), 3181–3184. https://doi.org/10.1016/S0040-4039(01)94977-9.

(167) Steiner, T. The Hydrogen Bond in the Solid State. *Angew. Chem. Int. Ed.* **2002**, *41* (1), 48–76. https://doi.org/10.1002/1521-3773(20020104)41:1%253C48::AID-ANIE48%253E3.0.CO;2-U.

(168) Boehmke Amoruso, A.; Boto, R. A.; Elliot, E.; De Nijs, B.; Esteban, R.; Földes, T.; Aguilar-Galindo, F.; Rosta, E.; Aizpurua, J.; Baumberg, J. J. Uncovering Low-Frequency Vibrations in Surface-Enhanced Raman of Organic Molecules. *Nat Commun* **2024**, *15* (1), 6733. https://doi.org/10.1038/s41467-024-50823-x.

(169) Mentel, Ł. M.; Baerends, E. J. Can the Counterpoise Correction for Basis Set Superposition Effect Be Justified? *J. Chem. Theory Comput.* **2014**, *10* (1), 252–267. https://doi.org/10.1021/ct400990u.

(170) Ohno, K.; Izu, Y.; Tsujii, Y.; Fukuda, T.; Kitano, H. Some Aspects of Nitroxide-Mediated Living Radical Polymerization of N-(p-Vinylbenzyl)Phthalimide. *European Polymer Journal* **2004**, *40* (1), 81–88. https://doi.org/10.1016/j.eurpolymj.2003.08.002.

(171) Stals, P. J. M.; Phan, T. N. T.; Gigmes, D.; Paffen, T. F. E.; Meijer, E. W.; Palmans, A. R. A. Nitroxide-mediated Controlled Radical Polymerizations of Styrene Derivatives. *J. Polym. Sci. A Polym. Chem.* **2012**, *50* (4), 780–791. https://doi.org/10.1002/pola.25833.

(172) Rohatgi-Mukherjee, K. K. *Fundamentals of Photochemistry*; Wiley: New Delhi, 1978.

(173) Oelgemöller, M.; Jung, C.; Mattay, J. Green Photochemistry: Production of Fine Chemicals with Sunlight. *Pure and Applied Chemistry* **2007**, *79* (11), 1939–1947. https://doi.org/10.1351/pac200779111939.

(174) Braslavsky, S. E. Glossary of Terms Used in Photochemistry, 3rd Edition (IUPAC Recommendations 2006). *Pure and Applied Chemistry* **2007**, *79* (3), 293–465. https://doi.org/10.1351/pac200779030293.

(175) Steen, H. B. Wavelength Dependence of the Quantum Yield of Fluorescence and Photoionization of Indoles. *The Journal of Chemical Physics* **1974**, *61* (10), 3997–4002. https://doi.org/10.1063/1.1681692.

(176) Kubin, R. F.; Fletcher, A. N. Fluorescence Quantum Yields of Some Rhodamine Dyes. *Journal of Luminescence* **1982**, *27* (4), 455–462. https://doi.org/10.1016/0022-2313(82)90045-X.

(177) Köhler, G.; Getoff, N. Wavelength Dependence of the Fluorescence Quantum Yield of Some Substituted Phenols. *J. Chem. Soc., Faraday Trans. 1* **1976**, *72* (0), 2101. https://doi.org/10.1039/f19767202101.

(178) Zhou, Q.; Wirtz, B. M.; Schloemer, T. H.; Burroughs, M. C.; Hu, M.; Narayanan, P.; Lyu, J.; Gallegos, A. O.; Layton, C.; Mai, D. J.; Congreve, D. N. Spatially Controlled UV Light Generation at Depth Using Upconversion Micelles. *Advanced Materials* **2023**, *35* (46), 2301563. https://doi.org/10.1002/adma.202301563.

(179) Pashley-Johnson, F.; Munaweera, R.; Hossain, S. I.; Gauci, S. C.; Delafresnaye, L.; Frisch, H.; O'Mara, M. L.; Du Prez, F. E.; Barner-Kowollik, C. How Molecular Architecture Defines Quantum Yields. *Nat Commun* **2024**, *15* (1), 6033. https://doi.org/10.1038/s41467-024-50366-1.

(180) Maidur, S. R.; Jahagirdar, J. R.; Patil, P. S.; Chia, T. S.; Quah, C. K. Structural Characterizations, Hirshfeld Surface Analyses, and Third-Order Nonlinear Optical Properties of Two Novel Chalcone Derivatives. *Optical Materials* **2018**, *75*, 580–594. https://doi.org/10.1016/j.optmat.2017.11.008.

(181) Xiao, Z.; Shi, Y.; Sun, R.; Ge, J.; Li, Z.; Fang, Y.; Wu, X.; Yang, J.; Zhao, M.; Song, Y. Ultrafast Broadband Optical Limiting in Simple Pyrene-Based Molecules with High Transmittance from Visible to Infrared Regions. *J. Mater. Chem. C* **2016**, *4* (21), 4647–4653. https://doi.org/10.1039/C5TC04047G.

(182) Li, J.; Chen, S.; Wang, Z.; Zhang, Q. Pyrene-Fused Acenes and Azaacenes: Synthesis and Applications. *The Chemical Record* **2016**, *16* (3), 1518–1530. https://doi.org/10.1002/tcr.201600015.

(183) Zhan, X.; Zhang, J.; Tang, S.; Lin, Y.; Zhao, M.; Yang, J.; Zhang, H.-L.; Peng, Q.; Yu, G.; Li, Z. Pyrene Fused Perylene Diimides: Synthesis, Characterization and Applications in Organic Field-Effect Transistors and Optical Limiting with High

Performance. *Chem. Commun.* **2015**, *51* (33), 7156–7159. https://doi.org/10.1039/C5CC00966A.

(184) Ballestas-Barrientos, A. R.; Woodward, A. W.; Moreshead, W. V.; Bondar, M. V.; Belfield, K. D. Synthesis and Linear and Nonlinear Photophysical Characterization of Two Symmetrical Pyrene-Terminated Squaraine Derivatives. *J. Phys. Chem. C* **2016**, *120* (14), 7829–7838. https://doi.org/10.1021/acs.jpcc.6b00143.

(185) Jung, K.; Corrigan, N.; Ciftci, M.; Xu, J.; Seo, S. E.; Hawker, C. J.; Boyer, C. Designing with Light: Advanced 2D, 3D, and 4D Materials. *Advanced Materials* **2020**, *32* (18), 1903850. https://doi.org/10.1002/adma.201903850.

(186) Corrigan, N.; Yeow, J.; Judzewitsch, P.; Xu, J.; Boyer, C. Seeing the Light: Advancing Materials Chemistry through Photopolymerization. *Angew Chem Int Ed* **2019**, *58* (16), 5170–5189. https://doi.org/10.1002/anie.201805473.

(187) Pan, X.; Tasdelen, M. A.; Laun, J.; Junkers, T.; Yagci, Y.; Matyjaszewski, K. Photomediated Controlled Radical Polymerization. *Progress in Polymer Science* **2016**, *62*, 73–125. https://doi.org/10.1016/j.progpolymsci.2016.06.005.

(188) Dadashi-Silab, S.; Doran, S.; Yagci, Y. Photoinduced Electron Transfer Reactions for Macromolecular Syntheses. *Chem. Rev.* **2016**, *116* (17), 10212–10275. https://doi.org/10.1021/acs.chemrev.5b00586.

(189) Chen, M.; Zhong, M.; Johnson, J. A. Light-Controlled Radical Polymerization: Mechanisms, Methods, and Applications. *Chem. Rev.* **2016**, *116* (17), 10167–10211. https://doi.org/10.1021/acs.chemrev.5b00671.

(190) Lai, H.; Zhang, J.; Xing, F.; Xiao, P. Recent Advances in Light-Regulated Non-Radical Polymerisations. *Chem. Soc. Rev.* **2020**, *49* (6), 1867–1886. https://doi.org/10.1039/C9CS00731H.

(191) Shi, S.; Croutxé-Barghorn, C.; Allonas, X. Photoinitiating Systems for Cationic Photopolymerization: Ongoing Push toward Long Wavelengths and Low Light Intensities. *Progress in Polymer Science* **2017**, *65*, 1–41. https://doi.org/10.1016/j.progpolymsci.2016.09.007.

(192) Michaudel, Q.; Kottisch, V.; Fors, B. P. Cationic Polymerization: From Photoinitiation to Photocontrol. *Angew Chem Int Ed* **2017**, *56* (33), 9670–9679. https://doi.org/10.1002/anie.201701425.

(193) Eivgi, O.; Lemcoff, N. Turning the Light On: Recent Developments in Photoinduced Olefin Metathesis. *Synthesis* **2018**, *50* (01), 49–63. https://doi.org/10.1055/s-0036-1589113.

(194) Gupta, P.; Trenor, S. R.; Long, T. E.; Wilkes, G. L. In Situ Photo-Cross-Linking of Cinnamate Functionalized Poly(Methyl Methacrylate- *Co* -2-Hydroxyethyl Acrylate) Fibers during Electrospinning. *Macromolecules* **2004**, *37* (24), 9211–9218. https://doi.org/10.1021/ma048844g.

(195) Trenor, S. R.; Shultz, A. R.; Love, B. J.; Long, T. E. Coumarins in Polymers: From Light Harvesting to Photo-Cross-Linkable Tissue Scaffolds. *Chem. Rev.* **2004**, *104* (6), 3059–3078. https://doi.org/10.1021/cr030037c.

(196) Xu, J.-F.; Chen, Y.-Z.; Wu, L.-Z.; Tung, C.-H.; Yang, Q.-Z. Dynamic Covalent Bond Based on Reversible Photo [4 + 4] Cycloaddition of Anthracene for Construction of Double-Dynamic Polymers. *Org. Lett.* **2013**, *15* (24), 6148–6151. https://doi.org/10.1021/ol403015s.

(197) Van Damme, J.; Van Den Berg, O.; Brancart, J.; Vlaminck, L.; Huyck, C.; Van Assche, G.; Van Mele, B.; Du Prez, F. Anthracene-Based Thiol–Ene Networks with Thermo-Degradable and Photo-Reversible Properties. *Macromolecules* **2017**, *50* (5), 1930–1938. https://doi.org/10.1021/acs.macromol.6b02400.

(198) Kaur, G.; Johnston, P.; Saito, K. Photo-Reversible Dimerisation Reactions and Their Applications in Polymeric Systems. *Polym. Chem.* **2014**, *5* (7), 2171–2186. https://doi.org/10.1039/C3PY01234D.

(199) Van De Walle, M.; Petit, C.; Blinco, J. P.; Barner-Kowollik, C. Visible-Light Reversible Photopolymerisation: Insights *via* Online Photoflow – Electrospray Ionisation – Mass Spectrometry. *Polym. Chem.* **2020**, *11* (40), 6435–6440. https://doi.org/10.1039/D0PY01119C.

(200) Frisch, H.; Mundsinger, K.; Poad, B. L. J.; Blanksby, S. J.; Barner-Kowollik, C. Wavelength-Gated Photoreversible Polymerization and Topology Control. *Chem. Sci.* **2020**, *11* (10), 2834–2842. https://doi.org/10.1039/C9SC05381F.

(201) Poplata, S.; Tröster, A.; Zou, Y.-Q.; Bach, T. Recent Advances in the Synthesis of Cyclobutanes by Olefin [2 + 2] Photocycloaddition Reactions. *Chem. Rev.* **2016**, *116* (17), 9748–9815. https://doi.org/10.1021/acs.chemrev.5b00723.

(202) Klán, P.; Wirz, J. *Photochemistry of Organic Compounds: From Concepts to Practice*, 1st ed.; Wiley, 2009. https://doi.org/10.1002/9781444300017.

(203) Turro, N. J.; Ramamurthy, V.; Scaiano, J. C.; Ramamurthy, V. *Modern Molecular Photochemistry of Organic Molecules*; University Science Books: Sausalito, California, 2010.

(204) Kopecký, J. *Organic Photochemistry: A Visual Approach*; VCH: New York, 1992.

(205) Gilbert, A.; Baggott, J. E. *Essentials of Molecular Photochemistry*; Blackwell Scientific Publications: Oxford ; Boston, 1991.

(206) Irshadeen, I. M.; De Bruycker, K.; Micallef, A. S.; Walden, S. L.; Frisch, H.; Barner-Kowollik, C. Green Light LED Activated Ligation of a Scalable, Versatile Chalcone Chromophore. *Polym. Chem.* **2021**, *12* (34), 4903–4909. https://doi.org/10.1039/D1PY00533B.

(207) Van De Walle, M.; De Bruycker, K.; Blinco, J. P.; Barner-Kowollik, C. Two Colour Photoflow Chemistry for Macromolecular Design. *Angew Chem Int Ed* **2020**, *59* (33), 14143–14147. https://doi.org/10.1002/anie.202003130.

(208) Arif, Z. U.; Khalid, M. Y.; Noroozi, R.; Sadeghianmaryan, A.; Jalalvand, M.; Hossain, M. Recent Advances in 3D-Printed Polylactide and Polycaprolactone-Based Biomaterials for Tissue Engineering Applications. *International Journal of Biological Macromolecules* **2022**, *218*, 930–968. https://doi.org/10.1016/j.ijbiomac.2022.07.140.

(209) Cook, C. C.; Fong, E. J.; Schwartz, J. J.; Porcincula, D. H.; Kaczmarek, A. C.; Oakdale, J. S.; Moran, B. D.; Champley, K. M.; Rackson, C. M.; Muralidharan, A.; McLeod, R. R.; Shusteff, M. Highly Tunable Thiol-Ene Photoresins for Volumetric Additive Manufacturing. *Advanced Materials* **2020**, *32* (47), 2003376. https://doi.org/10.1002/adma.202003376.

(210) Decroo, C.; Colson, E.; Demeyer, M.; Lemaur, V.; Caulier, G.; Eeckhaut, I.; Cornil, J.; Flammang, P.; Gerbaux, P. Tackling Saponin Diversity in Marine Animals by Mass Spectrometry: Data Acquisition and Integration. *Anal Bioanal Chem* **2017**, *409* (12), 3115–3126. https://doi.org/10.1007/s00216-017-0252-7.

(211) Giles, K.; Ujma, J.; Wildgoose, J.; Pringle, S.; Richardson, K.; Langridge, D.; Green, M. A Cyclic Ion Mobility-Mass Spectrometry System. *Anal. Chem.* **2019**, *91* (13), 8564–8573. https://doi.org/10.1021/acs.analchem.9b01838.

(212) Xia, C.; Mernie, E.; Zaia, J.; Costello, C. E.; Lin, C. Accurate Collisional Cross Section Measurement by Multipass Cyclic Ion Mobility Spectrometry. *Anal. Chem.* **2024**, *96* (29), 11959–11968. https://doi.org/10.1021/acs.analchem.4c01758.

(213) Becke, A. D. A New Mixing of Hartree–Fock and Local Density-Functional Theories. *The Journal of Chemical Physics* **1993**, *98* (2), 1372–1377. https://doi.org/10.1063/1.464304.

(214) Lee, C.; Yang, W.; Parr, R. G. Development of the Colle-Salvetti Correlation-Energy Formula into a Functional of the Electron Density. *Phys. Rev. B* **1988**, *37* (2), 785–789. https://doi.org/10.1103/PhysRevB.37.785.

(215) Becke, A. D. Density-Functional Exchange-Energy Approximation with Correct Asymptotic Behavior. *Phys. Rev. A* **1988**, *38* (6), 3098–3100. https://doi.org/10.1103/PhysRevA.38.3098.

(216) Jarrold, M. F. Applications of Charge Detection Mass Spectrometry in Molecular Biology and Biotechnology. *Chem. Rev.* **2022**, *122* (8), 7415–7441. https://doi.org/10.1021/acs.chemrev.1c00377.

(217) Bohlen, J. L.; Kulendran, B.; Rothfuss, H.; Barner-Kowollik, C.; Roesky, P. W. Heterobimetallic Au(Ⅰ)/Y(Ⅲ) Single Chain Nanoparticles as Recyclable Homogenous Catalysts. *Polym. Chem.* **2021**, *12* (28), 4016–4021. https://doi.org/10.1039/D1PY00552A.